A HARMONIC AND STATISTICAL ANALYSIS OF THE TOPOGRAPHY OF THE EARTH, MOON AND MARS

Thesis by

Bruce Gordon Bills

In Partial Fulfillment of the Requirements
for the Degree of
Doctor of Philosophy

California Institute of Technology
Pasadena, California
1978
(Submitted October 11, 1977)

ACKNOWLEDGMENTS

Many people have contributed to the research reported in this thesis. I am particularly indebted to Dr. Alfred J. Ferrari for his continued support and encouragement during the course of this investigation. Indeed, the first three chapters of this thesis report the results of work on which we have collaborated for the better part of the last three years. I would also like to express appreciation to Prof. Duane O. Muhleman and Dr. Roger J. Phillips of the Jet Propulsion Laboratory (J.P.L.) for support and valuable discussion during various phases of this investigation.

L.A. Schimerman of the Defense Mapping Agency and E.J. Christensen of J.P.L. provided us with magnetic tapes of lunar and martian topographic data, respectively. R.W. Wimberly, also of J.P.L., assisted in adapting these data to our computational facilities.

I have benefitted from discussions with Professors H.J. Melosh, R.P. Sharp and E.M. Shoemaker concerning geological implications of this research. S.S.C. Wu of the U.S. Geological Survey and M.E. Davies of the Rand Corporation were helpful in the early phases of the martian data analysis. E.C. Posner of J.P.L. improved my understanding of stochastic processes.

I have also enjoyed lively discussions and debates with my fellow students Dave Diner, John Dvorak, Bill McKinnon and particularly Tony Dobrovolskis.

I would like to thank Kay Campbell and Brenda Parson for their help in the preparation of several early drafts and the final manuscript of this thesis.

The first two chapters of this thesis have been previously published in *Icarus* **31**, 244-259 (1977) and *Journal of Geophysical Research* **82**, 1306-1314 (1977), respectively. I thank Academic Press and the American Geophysical Union for permission to include them here. Figure 4.3 is adapted from T.H. Bell's paper in *Deep-Sea Research* **22**, 883-891 (1975). I am grateful to Pergamon Press for permission to use this material.

This research was performed at both the California Institute of Technology and the Jet Propulsion Laboratory under NASA contract NAS 7-100.

ABSTRACT

In chapter I a global lunar topographic map is derived from Earth-based and orbital observations supplemented in areas without data by a linear autocovariance predictor. Of 2592 bins, each 5° square, 1380 (64.7% by area) contain at least one measurement. A spherical harmonic analysis to degree 12 yields a mean radius of (1737.53 ± 0.03) km (formal standard error) and an offset of the center of figure of (1.98 ± 0.06) km toward $(19 \pm 2)^\circ$S, $(194 \pm 1)^\circ$E. A Bouguer gravity map is also presented. It is confirmed that the low-degree gravity harmonics are caused primarily by surface height variations and only secondarily by lateral density variations.

In chapter II a series of models of the lunar interior are derived from topographic, gravitational, librational and seismic data. The moon departs from isostasy, even for the low-degree harmonics, with a maximum superisostatic stress of 200 bars under the major mascon basins. The mean crustal thicknesses under different physiographic regions are: mascons, 30-35 km; irregular maria, 50-60 km; and highlands, 90-110 km. A significant correlation between lunar surface chemistry and crustal thickness suggests that regions of thicker crust are more highly differentiated. A possible mean composition consistent with our model is an anorthositic crust, underlain by a predominantly forsterite upper mantle which grades into a refractory rich lower mantle surrounding a pyrrhotite core.

In chapter III a model of martian global topography is obtained by fitting a spherical harmonic series of degree 16 to occultation, radar, spectral and photogrammetric measurements. The existing observations are supplemented in areas without data by emperical elevation estimates based on photographic data. The mean radius is (3389.92 ± 0.04) km. The corresponding mean density is (3.933 ± 0.002) g cm^{-3}. The center of figure is displaced from the center of mass by (2.50 ± 0.07) km towards $(62 \pm 3)^{\circ}$S, $(272 \pm 3)^{\circ}$W. The geometric flattening [$f_g = (6.12 \pm 0.04)\ 10^{-3}$] is too great and the dynamic flattening [$f_d = (5.22 \pm 0.03)\ 10^{-3}$] is too small for Mars to be homogeneous and hydrostatic. It is confirmed that, similar to the Moon, the martian low-degree gravity harmonics are produced primarily by surface height variations and only secondarily by lateral density variations. Maps of the global topography and Bouguer gravity are presented. These are interpreted in terms of a crustal thickness map which is consistent with gravity, topography and recent preliminary Viking seismic results. Using plausible density contrasts and an assumed zero crustal thickness at Hellas, the inferred minimum mean crustal thickness is (28 ± 4) km.

In chapter IV it is shown that the topographic variance spectra of the Earth, Moon, Mars and Venus are all very similar. The variance per harmonic degree V(H;n) decreases roughly as the inverse square of the degree, or more precisely $V(H;n) \doteq V(H;0)/(n)(n+1)$. On the Earth and Moon this relationship has been confirmed down to scale lengths as

small as $L \doteq 100$ m. At the other end of the spectrum, the variance appears to be deficient relative to this model for scale lengths greater than $L \doteq 2000$ km. The most satisfactory explanation for this phenomenon appears to be a simple equilibrium between constructional or "tectonic" processes which tend to roughen the surface uniformly at all scales, and destructional or erosive processes which tend to smooth the surface preferentially at small scales. The deficiency in the low-degree variances is attributable to visco-elastic deformation.

CONTENTS

CONTENTS

CONTENTS

FIGURES

FIGURES

TABLES

PREFACE

The surface topography of a planet is one of its most important characteristics, since it reflects the complex history of interaction between exogenic and endogenic processes which have formed and subsequently modified the planet. Topographic data can also be used in conjunction with gravity observations to estimate the lateral variation of subsurface density and the stress distribution which maintains the gravity anomalies.

The initial objective of this investigation was to obtain spherical harmonic representations of lunar and martian topography of sufficient resolution and fidelity to be of use in performing global Bouguer analyses and in internal density modeling. The results of these efforts are reported in the first three chapters.

In the course of this research it was discovered that the topographic variance spectra of the Moon and Mars are very similar to the Earth's. The statistical similarity of these surfaces which have been subjected to vastly different formative processes seems to require some explanation. In the fourth chapter we investigate this phenomenon and find a simple explanation in terms of equilibrium between constructional and erosive activity. The statistical aspects of the resultant surface are largely independent of the details of the processes producing it.

I. A HARMONIC ANALYSIS OF LUNAR TOPOGRAPHY

A. INTRODUCTION

The objective of this investigation has been to obtain a lunar topography model that resolves basin-sized features, and can be used with a gravity model of equivalent resolution to perform global Bouguer analyses. A variety of elevation data types have been used to derive a spherical harmonic representation of the lunar figure. Previous analyses of lunar topography (Goudas, 1971; Jones, 1973; Chuikova, 1976) have suffered from inadequate data coverage and insufficient model resolution.

This chapter presents a discussion of the data used in the analysis, its selenographic distribution, and associated errors. A development is also presented of the analysis technique used to compensate for the irregular data distribution.

Maps of the global topography and its formal uncertainty are presented, along with a Bouguer anomaly map. The implications of some of the low-degree harmonics are considered separately.

B. DATA

The determination of the figure of the Moon has had a long and interesting history (see, e.g., Kopal and Carder, 1974). The measurements have been referred to several similar, but fundamentally different, coordinate systems. All measures are of the basic form $R(\theta,\varphi)$, where R is the radial distance from the origin, θ is the latitude, and φ is the (east) longitude. The angles are measured from the mean sub-Earth point.

The basic difference between the various reference systems used is in the location of their respective coordinate origins. For analytical purposes, the most convenient coordinate origin is the lunar center of mass. Before combining the various data types used in this analysis, we will refer them to this selenodetic coordinate system.

The data used which are already selenodetically referenced consist of Apollo laser altimetry (Roberson and Kaula, 1972; Wollenhaupt and Sjogren, 1972; Wollenhaupt *et al.*, 1974; Kaula *et al.*, 1972, 1973, 1974), vertical and oblique metric photogrammetry (Schimerman, 1975, personal communication), and landmark tracking data (Wollenhaupt *et al.*, 1972).

The data which were not initially in a selenodetic coordinate system consists of Watts' (1963) limb profiles (sampled at $2\overset{\circ}{.}5$ intervals in the libration frame) and ground-based stereoscopic photogrammetry (Hopmann, 1967; Mills and Sudbury, 1968; Arthur and Bates, 1968). These limb and photogrammetric data were referred to the selenodetic system by means of transformations determined by Van Flandern (1970) and Schimerman *et al.* (1973), respectively.

Other recent data which we have examined but have not used (either because of redundancy with the above data or because of ambiguity in the associated coordinate systems) include more ground-based photogrammetry (Baldwin, 1963), Zond-6 limb profiles (Rodionov *et al.*, 1971), lunar orbiter photogrammetry (Jones, 1973), radar interferometry (Zisk, 1972), and Apollo radar altimetry (Brown et al., 1974).

Table 1.1 is a summary of the various data types used, the number of points measured, and their estimated accuracies. Figure 1.1 indicates the approximate distribution of the data, summarized according to 5° x 5° bins. The most important aspect of this distribution is the complete lack of data for large regions on the far side. This situation considerably complicates our analysis.

TABLE 1.1

DATA SOURCES

Data type	Number of points	Error (km)
Inertial		
Laser altimeter		
Apollo 15	919	0.30
Apollo 16	1 353	0.30
Apollo 17	3 359	0.30
Orbital photogrammetry	12 432	0.30
Landmark tracking	31	0.50
Noninertial		
Earth-based photogrammetry		
Hopmann	1 049	0.80
Mills and Sudbury	906	0.40[a]
Arthur and Bates	1 356	0.90[a]
Limb profile	483	0.38

[a] Errors are estimated for each point separately. Number quoted is the mean of the individual errors.

FIGURE 1.1 - Data Distribution. The lunar surface is shown divided into 2592 bins, each 5° x 5°. The dot pattern indicates those bins (1380) which contain at least one measurement. A linear autocovariance analysis was used to estimate elevations in remaining bins.

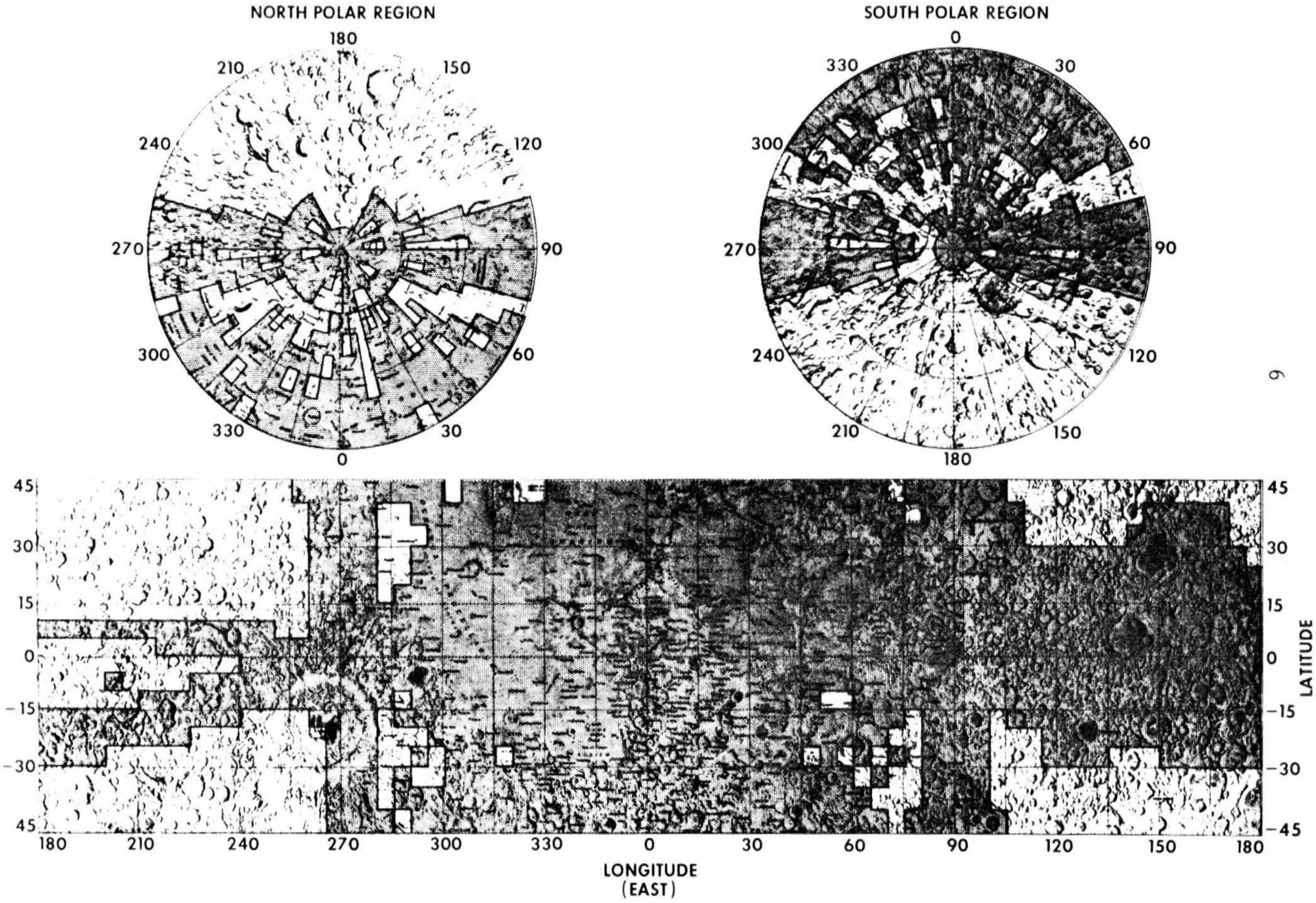
NORTH POLAR REGION
180
210
150
240
120
270
90
300
60
330
30
0
SOUTH POLAR REGION
0
330
30
300
60
270
90
240
120
210
150
180
45
30
15
0
-15
-30
45
180
210
240
270
300
330
0
30
60
90
120
150
180
45
30
15
0
-15
-30
-45
LATITUDE
LONGITUDE
(EAST)

In addition to the spherical coordinates (R,θ,φ), we will have occasion to use a Cartesian coordinate system (X_1,X_2,X_3), with its origin at the lunar center of mass. This system is right-handed and oriented such that the X_1 axis lies along the mean Earth-Moon line (positive toward Earth), the X_2 axis points east along the orbit (positive away from direction of orbital motion), and the X_3 axis lies along the rotation axis (positive toward north).

C. ANALYSIS

Given the data discussed in the previous section, we now have the problem of how best to estimate a set of harmonic coefficients which characterize the shape of the lunar surface. We will be interested not only in the complete ensemble of harmonics and the global lunar configuration which they represent, but also in some of the low-degree harmonics, considered separately. Therefore, it is imperative that we obtain harmonic coefficient estimates which not only accurately represent the data, but are also optimally uncorrelated with one another, consistent with the uneven data distribution. An intimately related problem is that we desire to avoid unreasonable values for our harmonic model in regions containing no direct measurements. We will now formulate this problem more rigorously and present our solution thereto.

Given a collection of topographic data F, with standard deviation σ, distributed on a sphere

$$R(\theta_i,\varphi_i) = F_i \pm \sigma_i \quad , \tag{1.1}$$

we desire optimally uncorrelated estimates of the harmonic coefficients H_{nm} through degree and order N.

Our basic model is of the form

$$R(\theta,\varphi) = R_o \left[1 + \sum_{n=1}^{12} \sum_{m=o}^{n} H_{nm}^{T} \Lambda_{nm} (\theta,\varphi) \right] \tag{1.2}$$

where

$$H_{nm} = \begin{bmatrix} H_{nm1} \\ H_{nm2} \end{bmatrix} \begin{matrix} = \\ = \end{matrix} \begin{bmatrix} \overline{C}_{nm} \\ \overline{S}_{nm} \end{bmatrix}$$

$$\Lambda_{nm}(\theta,\varphi) = \overline{P}_{nm}\left[\sin\ (\theta)\right] \begin{bmatrix} \cos\ (m\varphi) \\ \sin\ (m\varphi) \end{bmatrix}$$

are the normalized harmonic coefficients and surface spherical harmonic functions, respectively. These functions are defined and discussed at some length in Appendix A.

A 12-degree model was chosen since it is capable of resolving the major lunar basins. This facilitates comparison with recent gravity studies. A higher-degree model was not utilized because of the adverse effect of data gaps. For the ensemble of observations, (1.2) can be written as

$$F_i = (\partial F_i/\partial Z_j)\ Z_j = A_{ij}\ Z_j \tag{1.3}$$

where Z_j is the vector of H_{nm}. In this notation, the weighted least-squares estimator is (see, e.g., Lawson and Hanson, 1974)

$$\hat{Z} = [A^T BA]^{-1} [A^T BF] \quad , \tag{1.4}$$

where the weighting matrix B is the inverse of the data noise covariance matrix (assumed, in this analysis, to be diagonal).

To obtain uncorrelated estimates of the parameters Z_j, we must diagonalize the solution covariance matrix

$$E(ZZ^T) = [A^TBA]^{-1} \tag{1.5}$$

where E(•) is the expectation operator. Since we are assuming that B is diagonal, the problem thus reduces to the diagonalization of

$$[A^TA]_{ij} = \int_0^{2\pi} \int_{-1}^{1} \Lambda_i \Lambda_j d\mu d\varphi \tag{1.6}$$

where $\mu = \sin(\theta)$. The problem then is the optimal approximation of an integral by a finite sum. If we had data of uniform accuracy, evenly distributed over the sphere, the evaluation of this integral could be performed by any standard quadrature formula. However, the very uneven distribution of the data necessitates further analysis (Carlson and Helmsen, 1969).

The approach we have taken is to determine the weighted mean and standard deviation of all the data within each of 2592 5° x 5° bins. Actually, only 1380 of the bins, representing 64.7% of the lunar surface, contain data (see Fig. 1.1). In the remaining bins, we have used a linear autocovariance technique (see, e.g., Kaula, 1967; Heiskanen and Moritz, 1967) to estimate the most probable elevations and associated errors, consistent with the known statistical characteristics of the available data. Chapman and Pollack (1975) have applied a linear cross-covariance predictor to a very similar problem in terrestrial heat flow measurements.

In much of what follows, it will be useful to regard the surface of the Moon as a realization of a homogeneous stochastic process on a sphere (see Appendix C). A process is said to be homogeneous if its first and second moments are invariant under the group of rotations of the sphere. This is equivalent (Roy, 1973) to stationarity, i.e., constancy of the mean $E[F(\theta,\varphi)]$, and isotropy of the covariance function

$$C(\gamma) = E[F(\Omega)F(\Omega+\gamma)] \quad , \tag{1.7}$$

where $\Omega = (\theta,\varphi)$, i.e. $C(\gamma)$ depends only on the angular separation γ between the points (θ,φ) and $(\theta+\Delta\theta,\ \varphi+\Delta\varphi)$. This separation is given by

$$\begin{aligned} 2\cos(\gamma) &= (\cos(\Delta\varphi) + 1)\cos(\Delta\theta) \\ &\quad + (\cos(\Delta\varphi) - 1)\cos(\Sigma\theta) \quad . \end{aligned} \tag{1.8}$$

The predicted radii $\hat{R}$ and associated variances $\hat{\sigma}^2$ are calculated from the covariance function and the known radii F_i as follows:

$$\begin{aligned} \hat{R} &= Q^T S^{-1} F \quad , \\ \hat{\sigma}^2 &= C(0) - Q^T S^{-1} Q \quad , \end{aligned} \tag{1.9}$$

where

$$S = E(F^T F) \qquad \text{and} \qquad Q = E(F^T R),$$

the known-known and known-unknown covariance matrices, respectively, are obtained from $C(\gamma)$.

In a further effort to compensate for the extremely uneven distribution of the data, a lower bound of 0.05 km was imposed on the bin standard deviation. This measure prevents those regions in which the data are most densely concentrated from completely dominating the solution, at the expense of other regions. This censoring affected 220 bins, representing 12.9% of the lunar surface.

Finally, the weighted least-squares estimate of the harmonic coefficients was obtained by applying (1.4) to the averaged data, augmented by the predicted radii in the unsurveyed areas. The weighting of each point was proportional to the area of its bin and inversely proportional to the variance of the measurement or prediction:

$$B_{ij} = 2 \sin(\Delta\theta/2) \cos(\theta_i) \Delta\varphi \, \delta_{ij} / \sigma_i^2 \quad . \qquad (1.10)$$

The estimates of the normalized harmonic coefficients and their formal uncertainties are presented in Table 1.2.

Solutions were also obtained in which the predicted elevations were weakly weighted ($\sigma = 5$, 10 km). These solutions were characterized by unrealistically large estimates for the high-degree coefficients and large height excursions in the regions containing no data.

D. RESULTS

Figure 1.2 shows a comparison between raw laser altimeter data and the harmonic model evaluated along the ground tracks of representative orbits of Apollo missions 15, 16, and 17. The amount of high-frequency information contained in the data is indicated, as well as the fidelity of the harmonic model to the global and regional shape of the Moon. The variance of the 21 888 unaveraged data is 4.22 km^2, whereas the model variance is

TABLE 1.2

NORMALIZED LUNAR TOPOGRAPHY HARMONICS ($\times 10^6$)

n	m	$\bar{C}_{nm}$	$\bar{S}_{nm}$	$\sigma(\bar{C}_{nm})$	$\sigma(\bar{S}_{nm})$
1	0	-212.3		25.7	
1	1	-605.8	147.4	17.5	13.6
2	0	-135.9		22.1	
2	1	-149.8	-23.6	26.5	19.3
2	2	11.5	-167.1	11.5	14.5
3	0	62.2		20.5	
3	1	102.1	-53.1	28.0	18.2
3	2	47.2	-51.9	18.1	22.7
3	3	250.1	-28.9	11.1	11.4
4	0	104.2		20.5	
4	1	30.9	-57.3	26.7	17.0
4	2	-115.5	25.6	20.7	24.2
4	3	-13.1	41.0	18.0	18.5
4	4	-92.1	-20.9	9.6	10.1
5	0	0.6		20.3	
5	1	-50.6	79.2	25.4	16.2
5	2	5.5	-35.9	21.4	23.5
5	3	-48.2	-51.7	20.3	21.2
5	4	-2.0	6.6	16.0	16.0
5	5	86.9	10.5	8.2	8.7
6	0	-56.4		19.8	
6	1	-27.6	44.5	24.6	15.4
6	2	-3.5	-15.3	21.1	21.8
6	3	-1.9	-32.2	21.0	22.0
6	4	-62.6	44.2	19.3	18.5
6	5	-70.5	62.0	13.8	14.5
6	6	-30.9	-54.6	7.3	7.3

TABLE 1.2 (Cont'd)

n	m	$\bar{C}_{nm}$	$\bar{S}_{nm}$	$\sigma(\bar{C}_{nm})$	$\sigma(\bar{S}_{nm})$
7	0	-60.4		18.5	
7	1	219.4	-18.2	22.8	15.2
7	2	107.1	23.6	20.0	20.2
7	3	-76.9	12.7	20.3	21.4
7	4	-14.9	-14.0	20.1	19.3
7	5	107.5	20.2	16.4	16.8
7	6	54.0	2.2	12.2	12.3
7	7	4.1	-29.2	6.2	6.2
8	0	85.6		18.0	
8	1	-0.4	35.7	21.2	14.3
8	2	-134.3	-54.6	18.9	19.2
8	3	-23.8	-8.2	19.0	20.0
8	4	69.9	-64.9	19.8	19.6
8	5	45.6	-0.1	17.2	17.6
8	6	-156.3	0.8	14.4	14.3
8	7	-12.5	52.5	10.1	10.3
8	8	31.0	-41.5	5.1	5.1
9	0	9.8		16.9	
9	1	64.4	-28.0	19.7	13.5
9	2	13.2	56.6	17.6	16.9
9	3	-63.0	3.8	17.6	18.3
9	4	-67.3	13.9	18.2	17.9
9	5	53.4	115.6	17.4	17.7
9	6	39.5	-36.0	14.8	15.0
9	7	25.1	-14.2	12.3	12.1
9	8	48.0	-45.7	8.5	8.0
9	9	-1.2	16.8	4.0	4.0
10	0	95.0		14.2	
10	1	33.0	12.3	15.9	12.5
10	2	-55.2	6.9	14.7	14.0
10	3	-1.6	-31.3	14.9	14.7
10	4	34.5	-32.8	15.2	15.1
10	5	25.8	34.2	14.8	14.8
10	6	-75.5	-44.3	13.4	14.1
10	7	2.4	48.5	11.4	11.3
10	8	16.8	-6.0	9.4	9.5
10	9	8.5	59.6	6.5	6.4
10	10	54.9	-27.3	3.6	3.6

TABLE 1.2 (Cont'd)

n	m	$\bar{C}_{nm}$	$\bar{S}_{nm}$	$\sigma(\bar{C}_{nm})$	$\sigma(\bar{S}_{nm})$
11	0	41.2		11.9	
11	1	-99.0	-52.6	13.4	10.8
11	2	35.3	-33.6	11.4	12.2
11	3	-69.0	-98.1	12.0	12.3
11	4	-30.9	63.7	11.7	12.0
11	5	57.5	-71.8	11.6	12.0
11	6	-29.2	-63.6	10.8	11.1
11	7	43.4	-38.2	9.4	9.5
11	8	35.0	-91.5	7.5	7.2
11	9	11.9	53.6	6.5	6.4
11	10	8.6	-31.7	4.1	4.2
11	11	-17.1	-54.2	3.0	3.0
12	0	-38.8		9.5	
12	1	-33.6	8.3	10.2	8.8
12	2	15.2	2.1	9.5	9.4
12	3	-109.2	29.3	9.2	9.4
12	4	13.9	20.5	9.4	9.1
12	5	-15.8	0.6	8.8	9.1
12	6	-11.1	-10.3	8.6	9.0
12	7	9.2	9.6	8.0	8.0
12	8	-76.3	40.0	6.9	7.1
12	9	32.9	33.6	5.6	5.8
12	10	-20.0	-70.9	5.0	5.0
12	11	43.0	15.8	3.6	3.6
12	12	-35.1	-41.7	2.6	2.7

FIGURE 1.2 - Comparison of laser data and harmonic model. Elevations relative to 1738.0 km sphere. Indicates amount of high frequency information in data and general fidelity of model to global and regional scale features.

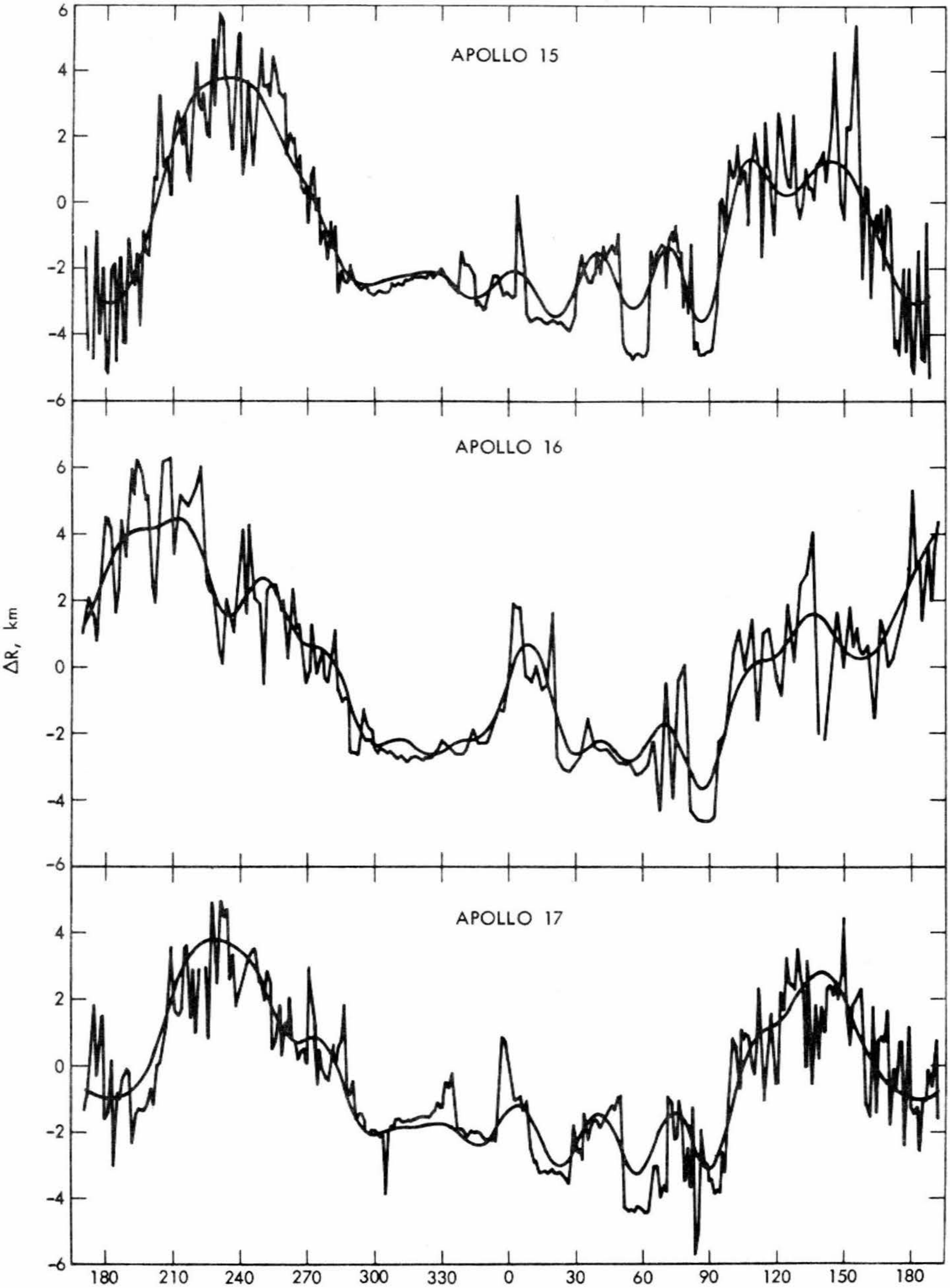
APOLLO 15
APOLLO 16
APOLLO 17
ΔR, km
6
4
2
0
-2
-4
-6
180
210
240
270
300
330
0
30
60
90
120
150
180
LONGITUDE (EAST)

$$C(0) = R_o^{\ 2} \sum_{n=1}^{12} \sum_{m=0}^{n} H_{nm}^T H_{nm}$$

$$= 3.08 \text{ km}^2 \qquad (1.11)$$

Figures 1.3 and 1.4 are maps of lunar topography, as given by our model, and the associated formal uncertainties, repectively. These are derived from the relationships (Graybill, 1961)

$$R(\theta,\varphi) = A^T(\theta,\varphi)\ Z \qquad ,$$

$$\sigma^2(\theta,\varphi) = A^T(\theta,\varphi)\ [A^T BA]^{-1}\ A(\theta,\varphi) \qquad . \qquad (1.12)$$

The error map reflects the distribution of the data, showing quite clearly the regions where we have no direct data. Since the model duplicates 73.0% of the original data variance, this computed error map should be a good first-order approximation to the actual error distribution. The topographic map, with heights relative to the lunar mean radius, resolves most major features within the areas of data coverage. This was a major objective in the construction of the model and permits comparison with equivalent-resolution gravity models for the purpose of determining the lunar internal density distribution.

Dimensionless degree variances V(H;n) of lunar topography and the associated error variances W(H;n) are listed in Table 1.3. These variances are given by:

FIGURE 1.3 - Lunar topography. Twelfth degree model. Elevations relative to 1737.53 km mean sphere. Contour interval is 1 km (solid line). Selected ½ km contours indicated (dashed line).

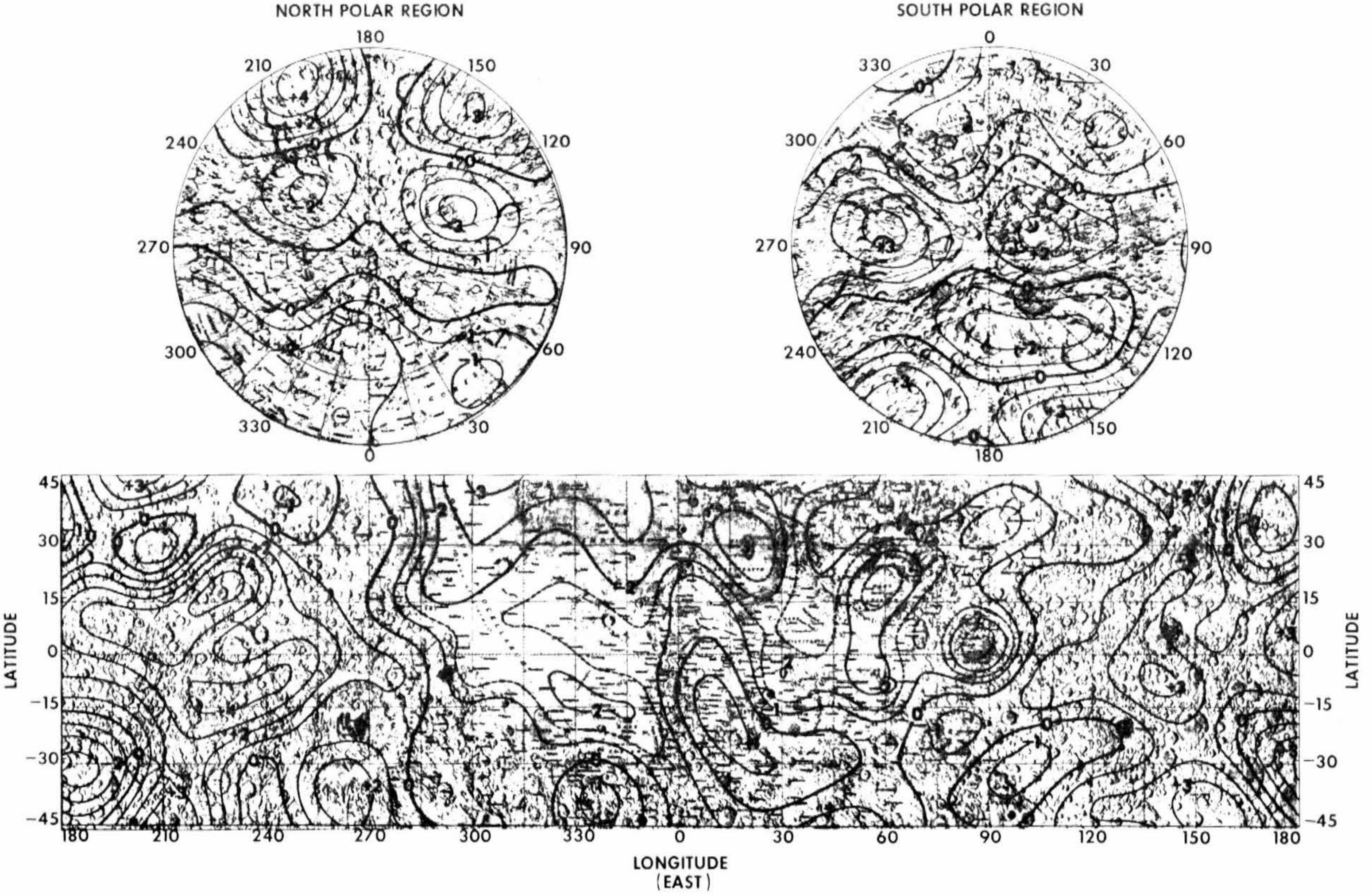
NORTH POLAR REGION
SOUTH POLAR REGION
LATITUDE
LONGITUDE (EAST)
45
30
15
0
-15
-30
-45
180
210
240
270
300
330
0
30
60
90
120
150
180

FIGURE 1.4 - Lunar topography error. Formal standard error computed from equation (1.12). Actual error can be somewhat larger. Contour interval is 0.2 km.

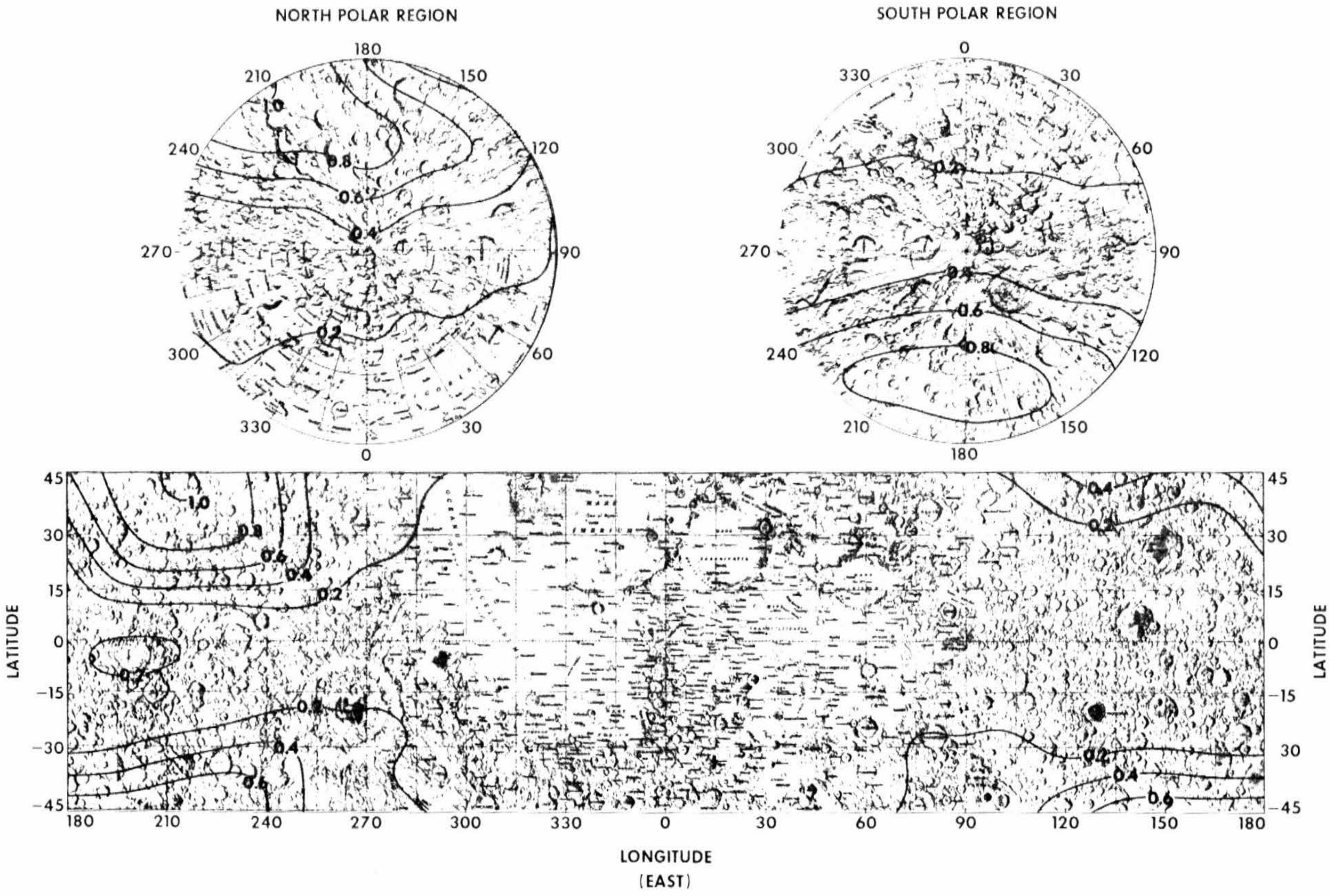
NORTH POLAR REGION
SOUTH POLAR REGION
180
150
120
90
60
30
0
330
300
270
240
210
1.0
0.8
0.6
0.4
0.2
LATITUDE
45
30
15
0
-15
-30
-45
LONGITUDE
(EAST)

TABLE 1.3

LUNAR TOPOGRAPHY AND ERROR VARIANCES $(\times 10^8)$

Degree n	Topography V(H;n)	Error W(H;n)
1	43.38	0.12
2	6.95	0.19
3	8.54	0.26
4	3.99	0.33
5	2.29	0.38
6	2.58	0.43
7	8.64	0.45
8	7.15	0.45
9	4.17	0.43
10	3.62	0.33
11	6.97	0.23
12	3.71	0.15

$$V(H;n) = \sum_{m=0}^{n} H_{nm}^{T} H_{nm}$$

$$W(H;n) = \sum_{m=0}^{n} \sigma^{T}(H_{nm})\ \sigma(H_{nm}) \tag{1.13}$$

where $\sigma^2(H_{nm})$, the variance of the error in H_{nm}, is obtained from the solution covariance matrix $[A^TBA]^{-1}$. We note that the topographic degree variances decrease in magnitude with increasing harmonic degree approximately as

$$V(H;n) \doteq \frac{V(H,0)}{(n)(n+1)} \quad . \tag{1.14}$$

We will discuss the significance of this spectral behavior at considerable length in Chapter IV. We also note that in the case of uniformly accurate data, i.e., $\sigma[R(\theta,\varphi)] = \sigma_o$, the degree error variances are (Heiskanen and Moritz, 1967)

$$W(H;n) = \frac{2n+1}{4\pi} \left(\frac{\sigma_o}{R_o}\right)^2 \quad . \tag{1.15}$$

The small departures of our error variances from this simple form are due to the irregular data distribution.

The observed gravity of a planet may be considered as the sum of contributions due to internal lateral density variations and surface topography. The topography of a planet characterized by harmonics H_{nm}, gives rise to gravitational potential perturbations ΔG_{nm}, where (MacRobert, 1967)

$$\left(\frac{2n+1}{3}\right) \bar{\rho}\, \Delta G_{nm} = \rho(R_o)\, H_{nm} \quad , \tag{1.16}$$

and $\rho(R_o)$ and $\bar{\rho}$ are the surface and mean mass densities, respectively, of the planet. The difference between the observed gravity and the topographic correction, known as the Bouguer anomaly, is thus a measure of the extent of lateral density variation.

Figure 1.5 is a map of lunar Bouguer gravity, evaluated at an elevation of 100 km above the mean lunar radius. This is calculated as the radial component of the gradient of the 12th degree Bouguer anomaly potential

$$\Delta\Phi_B(R,\theta,\varphi) = \frac{GM}{R_o} \sum_{n=1}^{12} \left(\frac{R_o}{R}\right)^{n+1} \sum_{m=0}^{n} B_{nm}\Lambda_{nm}(\theta,\varphi) \tag{1.17}$$

with

$$B_{nm} = G_{nm} - \Delta G_{nm}$$

where G is the gravitational constant, M is the planetary mass, G_{nm} is a harmonic coefficient of the observed gravitational field (Ferrari, 1977), and we have assumed a surface density $\rho(R_o) = 2.7$ g cm^{-3}. We find that the low-degree harmonics of the gravitational field are determined primarily by surface height variations and only secondarily by lateral density variations. The most striking feature of this map is the association of large positive anomalies with the mascons (Muller and Sjogren, 1968). It is also interesting to note that large regions of the farside highlands are associated with strong negative anomalies. This map, along with other data types such as librational and seismic observations, can be used to infer

FIGURE 1.5 - Lunar Bouguer gravity anomaly. Twelfth degree model. Evaluated 100 km above mean sphere. Contour interval 100 mGal = 0.1 cm sec^{-2}. Free-air gravity from Ferrari (1977). Assumed crustal density is 2.7 gm cm^{-3}.

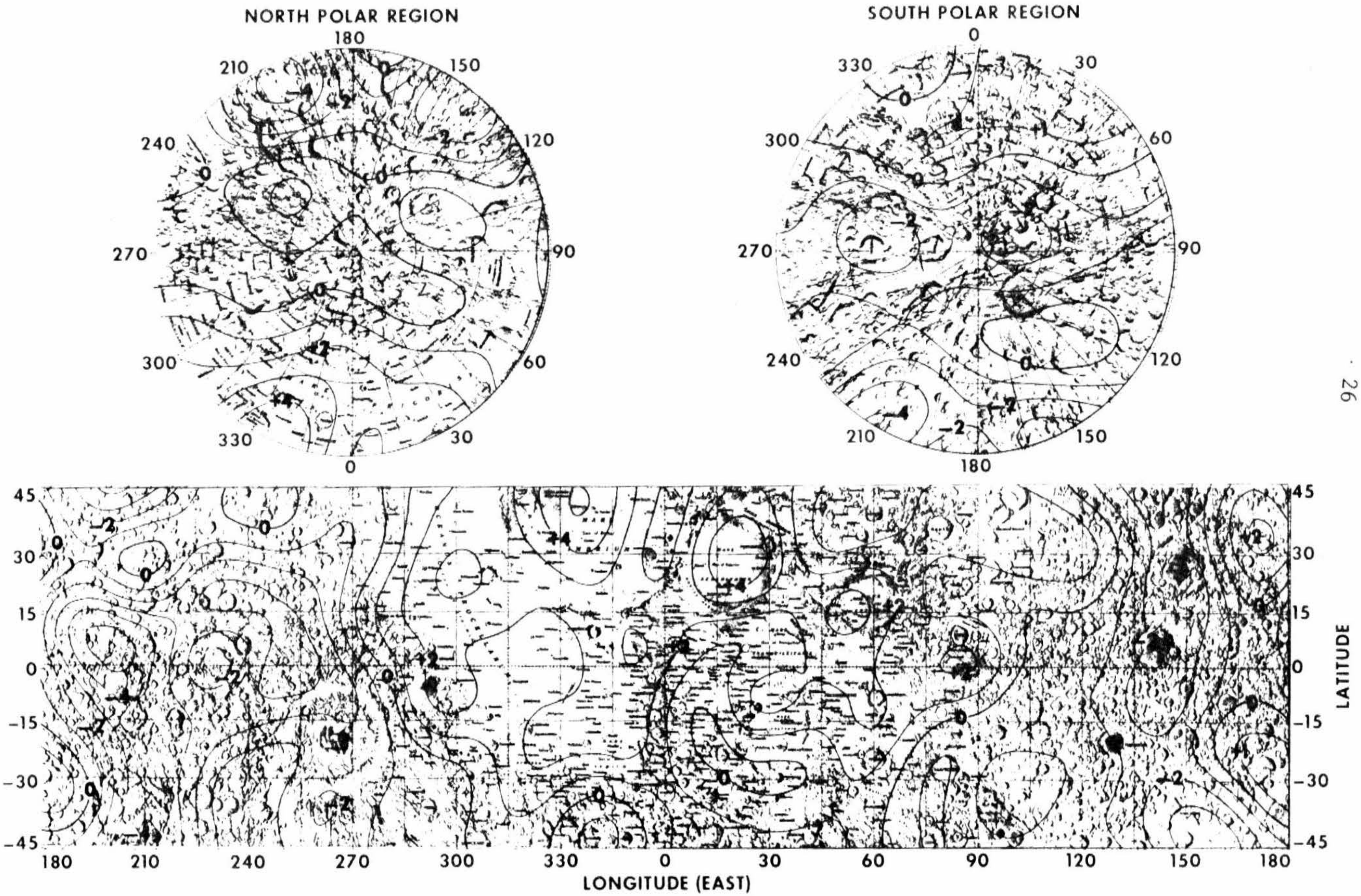
NORTH POLAR REGION
180
210
150
240
120
270
90
300
60
330
30
0
SOUTH POLAR REGION
0
330
30
300
60
270
90
240
120
210
150
180
45
30
15
0
-15
-30
-45
180
210
240
270
300
330
0
30
60
90
120
150
180
LONGITUDE (EAST)
LATITUDE
+2
+4
0
-2

lunar crustal and upper mantle structure, an effort which we discuss in the next chapter (see also, Bills and Ferrari, 1977). In that analysis a mean crustal thickness of 70 km is estimated by matching the gravimetrically derived local crustal thickness with the seismic results (Toksöz et al., 1974) from Mare Cognitum.

We now turn our attention to the harmonics of degrees 0, 1, and 2. These represent the mean radius, center of figure displacement, and triaxial figure, respectively.

The estimated lunar radius is (1737.53 ± 0.03) km. This, in conjunction with estimates of GM = $(4902.796 \pm 0.003)\ \mathrm{km}^3\ \mathrm{sec}^{-2}$ (Sinclair et al., 1976) and G = $(667.32 \pm 0.31 \times 10^{-25})\ \mathrm{km}^3\ \mathrm{g}^{-1}\ \mathrm{sec}^{-2}$ (Heyl and Chrzanowski, 1942), yields an estimate for the mean density of $\bar{\rho} = (3.3437 \pm 0.0016)\ \mathrm{g\ cm}^{-3}$. Most of this error comes from the error in G. The mean density, in conjunction with the mean inertial moment, places important constraints on models of lunar internal composition and structure (Gast and Giuli, 1972; Bills and Ferrari, 1977).

We now consider the first-degree terms in the topography. They represent a displacement of the center of figure (C.F.) from the center of mass (C.M.). In terms of rectangular coordinates, and un-normalized harmonics, the location of the C.F. is

$$\begin{bmatrix} \Delta X_1 \\ \Delta X_2 \\ \Delta X_3 \end{bmatrix} = R_o \begin{bmatrix} C_{1,1} \\ S_{1,1} \\ C_{1,0} \end{bmatrix} = \begin{bmatrix} -1.823 \pm 0.053 \\ -0.444 \pm 0.041 \\ -0.639 \pm 0.077 \end{bmatrix} \mathrm{km} \qquad (1.18)$$

or in terms of spherical coordinates,

$$\begin{bmatrix} R \\ \theta \\ \varphi \end{bmatrix} = \begin{bmatrix} (1.982 \pm 0.057)\ \text{km} \\ (18^\circ\!.8 \pm 2^\circ\!.1)\ \text{S} \\ (193^\circ\!.7 \pm 1^\circ\!.1)\ \text{E} \end{bmatrix}$$

where, as before, the origin is at the C.M.

This offset, by definition, implies a departure from spherical symmetry in the internal density distribution. Attempts have been made to explain this asymmetry in terms of two-layered models, with either an offset between the centers of the spheres comprising the model (Ransford and Sjogren, 1972; Kaula _et al._, 1972) or an outer layer of randomly varying thickness (Kobrick, 1976). Large-scale internal convection (Lingenfelter and Schubert, 1973) and asymmetric bombardment (Wood, 1973) have been suggested as possible mechanisms for the preferential thinning of the crust of the earthward hemisphere and concomitant thickening in the opposite hemisphere.

We now consider the shape and orientation of the triaxial figure represented by the second-degree harmonics. The principal axes of this figure are

$$\begin{aligned} X_1' &= (1738.43\ \text{km},\ 13^\circ\!.58\ \text{S},\ 38^\circ\!.40\ \text{E}) \quad , \\ X_2' &= (1737.50\ \text{km},\ 32^\circ\!.70\ \text{N},\ 119^\circ\!.48\ \text{E}) \quad , \qquad (1.19) \\ X_3' &= (1736.66\ \text{km},\ 53^\circ\!.91\ \text{N},\ 327^\circ\!.76\ \text{E}) \quad . \end{aligned}$$

This misalignment between these axes and the principal inertial axes implies that, if all lateral density variation occurs as undulations on the crust-mantle interface, the principal axes of the triaxial mantle must be skewed in the opposite direction. According to this simplified model, the region of minimum crustal thickness is in southern Procellarum. Many deep-focus moonquakes occur along two great circle arcs which intersect in this same area (Lammlein _et al._, 1974; Lammlein, 1977). Thus, the stresses induced by near surface mass anomalies may control the release of seismic energy at depth.

REFERENCES

Arthur, D.W.G., and Bates, P. (1968). The Tucson selenodetic triangulation. *Commun. Lunar Planet. Lab.* **7**, 313-361.

Baldwin, R.B. (1963). *The Measure of the Moon*. Univ. of Chicago Press, Chicago.

Bills, B.G., and Ferrari, A.J. (1977). A lunar density model consistent with topographic, gravitational, librational and seismic data. *J. Geophys. Res.* **82** 1306-1314.

Brown, W.E., Jr., Adams, G.F., Eggleton, R.E., Jackson, P., Jordan, R., Kobrick, M., Peeples, W.J., Phillips, R.J., Porcello, L.J., Schaber, G., Sill, W.R., Thompson, T.W., Ward, S.H., and Zelenka, J.S. (1974). Elevation profiles of the Moon. *Proc. Fifth Lunar Sci. Conf.* **3**, 3037-3048.

Carlson, A.E., and Helmsen, M. (1969). Validity of topography represented by truncated series of surface harmonics. *Icarus* **10**, 57-65.

Chapman, D.S., and Pollack, H.N. (1975). Global heat flow: A new look. *Earth Planet. Sci. Lett.* **28**, 23-31.

Chuikova, N.A. (1976). The geometrical figure of the Moon represented in the form of an expansion in spherical and sampling functions. *Sov. Astron.* **19**, 764-771.

Ferrari, A.J. (1977). Lunar gravity: A harmonic analysis. *J. Geophys. Res.* **82**, 3065-3084.

Gast, P.W., and Giuli, R.T. (1972). Density of the lunar interior. *Earth Planet. Sci. Lett.* **16**, 299-305.

Goudas, C.L. (1971). Geometrical and dynamical properties of the Moon. In *Physics and Astronomy of the Moon* (Z. Kopal, Ed.), pp. 101-152. Academic Press, New York.

Graybill, F.A. (1961). *An Introduction to Linear Statistical Models, Vol. I*. McGraw-Hill, New York.

Heiskanen, W.A., and Moritz, H. (1967). *Physical Geodesy*. Freeman, San Francisco.

Heyl, P.R., and Chrzanowski, P. (1942). A new determination of the constant of gravitation. *J. Res. Nat. Bur. Standards* **29**, 1-31.

Hopmann, J. (1967). General-Katalog absoluter Höhen auf dem Mond. *Ann. Univ. Sternw. Wien* **26**, 7 Heft.

Jones, R.H. (1963). Stochastic processes on a sphere. *Ann. Math. Statist.* **34**, 213-218.

Jones, R.L. (1973). Estimates of the Moon's geometry using lunar orbiter imagery and Apollo laser altimeter data. NASA TR R-407.

Kaula, W.M. (1967). Theory of statistical analysis of data distribution over a sphere. *Rev. Geophys.* **5**, 83-107.

Kaula, W.M., Lingenfelter, R.E., Schubert, G. Sjogren, W.L., and Wollenhaupt, W.R. (1972). Analysis and interpretation of lunar laser altimetry. *Proc. Third Lunar Sci. Conf.* **3**, 2189-2204.

Kaula, W.M., Lingenfelter, R.E., Schubert, G., Sjogren, W.L. and Wollenhaupt, W.R. (1973). Lunar topography from Apollo 15 and 16 laser altimetry. *Proc. Fourth Lunar Sci. Conf.* **3**, 2811-2819.

Kaula, W.M., Lingenfelter, R.E., Schubert, G., Sjogren, W.L., and Wollenhaupt, W.R. (1974). Apollo laser altimetry and inference as to lunar structure. *Proc. Fifth Lunar Sci. Conf.* **3**, 3049-3058.

Kobrick, M. (1976). Random processes as a cause of the lunar asymmetry. *The Moon* **15**, 83-89.

Kopal, Z., and Carder, R.W. (1974). *Mapping of the Moon*. Reidel, Dordrecht.

Lammlein, D.R., Latham, G.V., Dorman, J., Nakamura, Y., and Ewing, M. (1974). Lunar seismicity, structure and tectonics. *Rev. Geophys. Space Phys.* **12**, 1-21.

Lammlein, D.R. (1977). Lunar seismicity and tectonics, *Phys. Earth Planet. Int.* **14**, 224-273.

Lawson, C.L., and Hanson, R.J. (1974). *Solving Least Squares Problems*. Prentice-Hall, Englewood Cliffs, N.J.

Lingenfelter, R.E., and Schubert, G., (1973). Evidence for convection in planetary interiors from first-order topography. *The Moon* **7**, 172-180.

MacRobert, T.M. (1967). *Spherical Harmonics*. Pergamon Press, New York.

Mills, G.A., and Sudbury, P.V. (1968). Absolute coordinates of lunar features. *Icarus* **9**, 538-561.

Muller, P.M., and Sjogren, W.L. (1968). Mascons: Lunar mass concentrations. *Science* **161**, 680-684.

Ransford, G., and Sjogren, W.L. (1972). Moon model - An offset core. *Nature* **238**, 260-262.

Roberson, F.I., and Kaula, W.M. (1972). Apollo 15 laser altimeter. In *Apollo 15 Preliminary Science Report*, pp. 25:48-50. NASA SP-239.

Rodionov, B.N., Isavnina, I.V., Avdeev, Yu.F., Blagov, V.D., Dorofeev, A.S., Dunaev, B.S., Ziman, Ya.L., Kiselev. V.V., Krasikov, V.A., Lebedev, O.N., Mikhailovskii, A.B., Tishchenko, A.P., Nepoklonov, B.V., Samoilov, V.K., Truskov, F.M., Chesnokov, Yu.M., and Fivenskii, Yu.I. (1971). New data on the Moon's figure and relief based on results from the reduction of Zond-6 photographs. *Cosmic Res.* **9**, 410-417.

Roy, R. (1973). Estimation of the covariance function of a homogeneous process on the sphere. *Ann. Statist.* **1**, 780-785.

Schimerman, L.A., Cannel, W.D., and Meyer, D. (1973). Relationship of spacecraft and earth-based selenodetic systems. Paper presented at the 15th General Assembly of the International Astronomical Union, Sidney, Australia.

Sinclair, W.S., Sjogren, W.L., Williams, J.G., and Ferrari, A.J. (1976). The lunar moment of inertia derived from combined doppler and laser ranging data. In *Lunar Science VII*, p. 817. Lunar Science Institute, Houston.

Toksöz, M.N., Dainty, A.M., Solomon, S.C., and Anderson, K.R. (1974). Structure of the Moon. *Rev. Geophys. Space Phys.* **12**, 539-567.

Van Flandern, T.C. (1970). Some notes on the use of the Watts limb-correction charts. *Astron. J.* **75**, 744-746.

Watts, C.B. (1963). The marginal zone of the Moon. Astron. Papers Amer. Ephemer. Naut. Almanac **17**.

Wollenhaupt, W.R., Osburn, R.K., and Ransford, G.A. (1972). Comments on the figure of the Moon from Apollo landmark tracking. The Moon **5**, 149-157.

Wollenhaupt, W.R., and Sjogren, W.L. (1972). Apollo 16 laser altimeter. In Apollo 16 Preliminary Science Report, pp. 30:1-5. NASA SP-315.

Wollenhaupt, W.R., Sjogren, W.L., Lingrenfelter, R.E., Schubert, G., and Kaula, W.M. (1974). Apollo 17 laser altimeter. In Apollo 17 Preliminary Science Report, pp. 33 : 41 - 42. NASA SP-330.

Wood, J.A. (1973). Bombardment as a cause of the lunar asymmetry. The Moon **8**, 73-103

Zisk, S.H. (1972). Lunar topography: First radar-interferometer measurements of the Alphonsus-Ptolemaeus-Arzachel region. Science **178**, 977-980.

II. A LUNAR DENSITY MODEL

A. INTRODUCTION

Lunar interior models of increasing complexity are derived from topographic, gravitational, librational, and seismic data. A series of models, rather than only the final one, is presented in an effort to demonstrate the unique contribution of each data type and its effect on determining model parameters for the lunar density structure.

The various data types and their errors are discussed, and these data are cast into a form most convenient for internal model determination. The basic theory for this analysis is developed, and a series of lunar interior models are derived from the different data. Discussions are presented at each level of modeling, showing which data are satisfied and presenting the geophysical significance of that stage of the model development. Ultimately, a six-layered model is determined which satisfies all the data. The innovative aspects of this investigation are discussed in light of previous work, and the compositional implications of this lunar interior model are analyzed.

B. DATA

The topography of the Moon will be represented in this analysis by the harmonic model developed in the preceding chapter (see also Bills and Ferrari, 1977). However, in the present chapter, it will be more convenient to use the un-normalized harmonics (see Appendix A).

As a representation of lunar gravity, we will use Ferrari's (1975) model truncated to degree twelve for consistency with the topography model.

The physical librations of the Moon are dependent upon both the low-degree gravity harmonics and the parameters (α, β, γ), which are defined in terms of the principal inertial moments $A < B < C$ as

$$\alpha = \frac{C - B}{A} \qquad \beta = \frac{C - A}{B} \qquad \gamma = \frac{B - A}{C} \tag{2.1}$$

Sinclair et al. (1976) have estimated the low-degree gravity harmonics and librational parameters from a combination of Doppler and laser-ranging data. Table 2.1 presents these estimates, the low-degree topography harmonics (Bills and Ferrari, 1977), and an estimate of the gravitational constant G (Heyl and Chrzanowski, 1942).

The resulting estimates for the lunar mean density and moments are

$$\bar{\rho} = 3.3437 \pm 0.0016 \text{ g cm}^{-3}$$

$$C = (4C_{22}{}^{g}/\gamma)MR_0{}^2 = (0.3933 \pm 0.0021)MR_0{}^2 \tag{2.2}$$

$$I = \frac{A + B + C}{3} = \left[\frac{3 + \beta + \gamma - \beta\gamma}{3(1+\beta)}\right] C = (0.3931 \pm 0.0021)MR_0{}^2 \ .$$

The moments M_n of the radial density distribution are

$$M_n \equiv (n+1) \int_0^1 \rho(\xi)\xi^n \, d\xi \qquad (2.3$$

where $\xi = r/R_0$. On the basis of the values listed in (2.2), the second

TABLE 2.1

LUNAR GRAVITATIONAL, TOPOGRAPHIC AND LIBRATIONAL DATA

$G = (667.32 \pm 0.31) \times 10^{-10}\ \mathrm{cm}^{3}\ \mathrm{sec}^{-2}\ \mathrm{gm}^{-1}$

$GM = (4902.796 \pm 0.003) \times 10^{15}\ \mathrm{cm}^{3}\ \mathrm{sec}^{-2}$

$R_o = (1737.59 \pm 0.24) \times 10^{5}\ \mathrm{cm}$

$\beta = (631.68 \pm 0.13) \times 10^{-6}$

$\gamma = (227.82 \pm 0.08) \times 10^{-6}$

		TOPOGRAPHY		GRAVITY	
n	m	$C^t_{nm} \times 10^6$	$S^t_{nm} \times 10^6$	$C^g_{nm} \times 10^6$	$S^g_{nm} \times 10^6$
0	0	10^6	---	10^6	---
1	0	-367.7 ± 44.6	---	---	---
1	1	-1049.3 ± 30.3	-255.4 ± 23.6	---	---
2	0	-303.9 ± 49.5	---	-203.62 ± 1.09	---
2	1	-193.4 ± 34.2	30.4 ± 24.9	---	---
2	2	7.4 ± 7.4	107.8 ± 9.4	22.40 ± 0.12	---

NOTE: --- indicates zero by definition.

and fourth moments are

$$\begin{aligned} M_2 &= \bar{\rho} = 3.3437 \pm 0.0016 \\ M_4 &= 5\bar{\rho}I/2MR_0^{\ 2} = 3.286 \pm 0.018 \end{aligned} \tag{2.4}$$

This form will prove useful for comparison with models to be derived later.

The seismic data used consist of (1) the inferred crustal structure in the region of the Apollo seismic array including discontinuities at depths of ~20 and 50-60 km (Toksöz et al., 1974), and (2) the travel time as a function of epicentral distance for P and S waves (Nakamura et al., 1974).

C. THEORY

We will be mainly concerned with models consisting of nearly concentric nearly spherical shells of uniform density material. Each shell ℓ will be characterized by the normalized radius of its outer surface, $\xi_\ell = R_\ell/R_0$; a density contrast from the immediately overlying layer, $\Delta\rho_\ell = \rho_\ell - \rho_{\ell-1}$; and a set of spherical harmonic coefficients $H_{nm}^{\ \ell}$ which represent the shape of the outer surface of the layer. Thus the interface has the form

$$R(\theta,\varphi) = R_0\xi_\ell \sum_{n=0}^{12}\sum_{m=0}^{n} (H_{nm}^{\ \ell})^T \Lambda_{nm}(\theta,\varphi) \tag{2.5}$$

The mean density and mean inertial moment of such a model are expressed by

$$M_2 = \bar{\rho} = \sum_{\ell} \Delta\rho_\ell \xi_\ell^{\,3} \ , \quad M_4 = \frac{5\bar{\rho}I}{2MR_0^{\,2}} = \sum_{\ell} \Delta\rho_\ell \xi_\ell^{\,5} \tag{2.6}$$

The complete inertia tensor of such a configuration is given by

$$I_{ij} = \frac{8\pi R_0^{\,5}}{15} \sum_{\ell} \Delta\rho_\ell (\xi_\ell)^5 L_{ij}^{\,\ell} \tag{2.7}$$

where, in terms of un-normalized shape harmonics,

$$L_{11}^{\,\ell} = 1 + \frac{5}{2}\left[(S_{11}^{\,\ell})^2 + (C_{10}^{\,\ell})^2\right] + \frac{C_{20}^{\,\ell}}{2} - 3C_{22}^{\,\ell}$$

$$L_{22}^{\,\ell} = 1 + \frac{5}{2}\left[(C_{11}^{\,\ell})^2 + (C_{10}^{\,\ell})^2\right] + \frac{C_{20}^{\,\ell}}{2} + 3C_{22}^{\,\ell}$$

$$L_{33}^{\,\ell} = 1 + \frac{5}{2}\left[(C_{11}^{\,\ell})^2 + (S_{11}^{\,\ell})^2\right] - C_{20}^{\,\ell}$$

$$L_{12}^{\,\ell} = L_{21}^{\,\ell} = -\frac{5}{2}\,(C_{11}^{\,\ell} S_{11}^{\,\ell}) - 3S_{22}^{\,\ell}$$

$$L_{13}^{\,\ell} = L_{31}^{\,\ell} = -\frac{5}{2}\,(C_{11}^{\,\ell} C_{10}^{\,\ell}) - \frac{3}{2}\,C_{21}^{\,\ell}$$

$$L_{23}^{\,\ell} = L_{32}^{\,\ell} = -\frac{5}{2}\,(S_{11}^{\,\ell} C_{10}^{\,\ell}) - \frac{3}{2}\,S_{21}^{\,\ell}$$

The gravitational harmonics of the configuration are given by

$$\left(\frac{2n+1}{3}\right) \bar{\rho} G_{nm} = \sum_{\ell} \Delta\rho_\ell \xi_\ell^{\,n+3} H_{nm}^{\,\ell} \tag{2.8}$$

to first order in the $H_{nm}^{\,\ell}$. From the relation between the inertia tensor and the un-normalized gravity harmonics

$$
\begin{aligned}
C_{20}\,{}^{g}MR_0^{\;2} &= (I_{11}+I_{22}-2I_{33})/2 \\
C_{21}\,{}^{g}MR_0^{\;2} &= I_{13} = I_{31} \\
S_{21}\,{}^{g}MR_0^{\;2} &= I_{23} + I_{32} \\
C_{22}\,{}^{g}MR_0^{\;2} &= (I_{22}-I_{11})/4 \\
S_{22}\,{}^{g}MR_0^{\;2} &= I_{12}/2 = I_{21}/2
\end{aligned}
\tag{2.9}
$$

we note that for $n = 2$, (2.8) is merely the linear approximation to (2.7). We will thus use (2.7) in place of (2.8) for $n = 2$.

We will also be interested in the extent to which our models depart from isostatic equilibrium. This will be measured in terms of the variations about the mean of the hydrostatic pressure at the crust-mantle interface. The mean pressure at this level is approximately,

$$\bar{P} = (4\pi G R_0^{\;2}/3)\ \rho_0\bar{\rho}(1-\xi_1) \tag{2.10}$$

and the pressure deviations are

$$\Delta P(\theta,\varphi) = \frac{4\pi G R_0^{\;2}}{3}\ \rho_0\bar{\rho}\sum_{n=1}^{12}\sum_{m=0}^{n} J_{nm}{}^{T}\ \Lambda_{nm}(\theta,\varphi) \tag{2.11}$$

where

$$J_{nm} = H_{nm}{}^{0} + \left(\frac{\Delta\rho_1}{\rho_0}\right)\left(\frac{\bar{\rho}_1}{\bar{\rho}}\right)\xi_1^{\;2}\ H_{nm}{}^{1}$$

and $\bar{\rho}_1$ is the mean density of the Moon beneath the crust.

In order to use seismic data as a constraint on lunar internal structure, we will need to specify compressional and shear wave velocities V_p and V_s at each layer. These two velocities are determined by

$$V_p^{\ 2} = (K+4\mu/3)/\rho \quad , \qquad V_s^{\ 2} = \mu/\rho \tag{2.12}$$

where

$$K \equiv \rho(\partial P/\partial\rho)_S$$

is the adiabatic bulk modulus and μ is the shear modulus or rigidity. These in turn are functions of temperature and pressure for any given material. We will assume a linear dependence on temperature and pressure:

$$\begin{aligned} \rho(T,P) &= \rho_{STP} + (\partial\rho/\rho T)\Delta T + (\partial\rho/\partial P)\,\Delta P \\ K(T,P) &= K_{STP} + (\partial K/\partial T)\Delta T + (\partial K/\partial P)\Delta P \\ \mu(T,P) &= \mu_{STP} + (\partial\mu/\partial T)\Delta T + (\partial\mu/\partial P)\Delta P \end{aligned} \tag{2.13}$$

A number of estimates of the lunar internal temperature distribution are available (e.g., Toksöz and Solomon, 1973). All such models are characterized by a steep gradient near the surface and a more gradual gradient at depth. We will assume a temperature profile of the form (Nakamura and Latham, 1969)

$$T(\xi) = T(0) + \Delta T\xi^n \tag{2.14}$$

with the parameters chosen to match the near-surface gradient and deep interior temperatures. A more complex model is not justified in light of the lack of constraints on the problem.

The pressure at each level is obtained by numerically integrating the equation of hydrostatic equilibrium. The pressure and temperature are then used to estimate the ambient density and elastic moduli from their assumed STP values.

The seismic travel times T and epicentral angles Δ are calculated from the velocity profile $V(\xi)$ for a given ray path by (Bullen, 1963)

$$T = 2R_0 \int_{\xi_m}^{1} \left[\eta^2 - \eta_m^{\,2}\right]^{-1/2} \frac{\eta^2 d\xi}{\xi}$$

$$\Delta = 2\eta_m \int_{\xi_m}^{1} \left[\eta^2 - \eta_m^{\,2}\right]^{-1/2} \frac{d\xi}{\xi} \qquad (2.15)$$

where $\eta = \xi/V(\xi)$ and η_m is the value of η at the midpoint of the ray path, where it reaches its minimum radius ξ_m.

D. MODELS

The simplest model considered has a uniform density of $\bar{\rho} = 3.3437$ g cm^{-3} and the outer surface is characterized by the topography harmonics $H_{nm}^{\ 0}$. An interesting aspect of this model is that its liberational parameters are

$$\beta = (5.28 + 485.39) \times 10^{-6} = 490.67 \times 10^{-6}$$

$$\gamma = (5.65 + 45.29) \times 10^{-6} = 50.94 \times 10^{-6}$$

where the parenthetical terms are the first- and second-degree contributions, respectively. We thus conclude that the first-degree harmonics are of little consequence dynamically in comparison to the second-degree harmonics. Comparing these estimates with the values in Table 2.1, we note that the assumption of uniform density, coupled with the actual topography, gives, at least qualitatively, reasonable estimates of β and γ, whereas Kopal (1969) has shown that the rotational and tidal distortions of a hydrostatic moon would yield

$$\beta_H = 37.39 \times 10^{-6} \qquad \gamma_H = 27.97 \times 10^{-6}$$

Two basic conclusions are obtained from this comparison: first, the orientation and rotational dynamics of the Moon are intrinsically determined primarily by surface height variations and only secondarily by lateral density variations, and second, the Moon is not well approximated by a hydrostatic model (Kopal, 1969).

We now turn our attention to models with a radial density variation. The simplest such model considered consists of two concentric spherical shells having a density ρ_0 in the outer shell and a density contrast $\Delta\rho_1$ across the interface at a normalized radius of $R_1/R_0 = \xi_1$. A weak compositional constraint is imposed in that we assume

$$2.7 \le \rho(\xi) \le 5.4 \text{ g cm}^{-3}$$

where the lower bound corresponds roughly to anorthosite and the upper bound to an Fe-FeS eutectic composition (Brett, 1973) at the lunar central pressure (~50 kbar) and room temperature. These bounds are shown by the dot-dash lines Figure 2.1. If in addition, the model is constrained to have the observed mean density and density inversions with depth are not allowed, the envelope of acceptable density profiles is given by the dashed lines in Figure 2.1. When the model is subjected to the additional constraint that it have the correct mean moment of inertia, the resulting density bounds are those given by the solid lines in Figure 2.1.

FIGURE 2.1 - Envelope of plausible lunar density profiles. Successively applied model constraints: 1) $2.7 \leq \rho \leq 5.4$ (dot-dash lines); 2) observed mean density $\bar{\rho} = 3.344 \pm 0.002$ (dashed lines); 3) observed mean inertial moment $I/MR_0^2 = 0.393 \pm 0.002$ (solid lines).

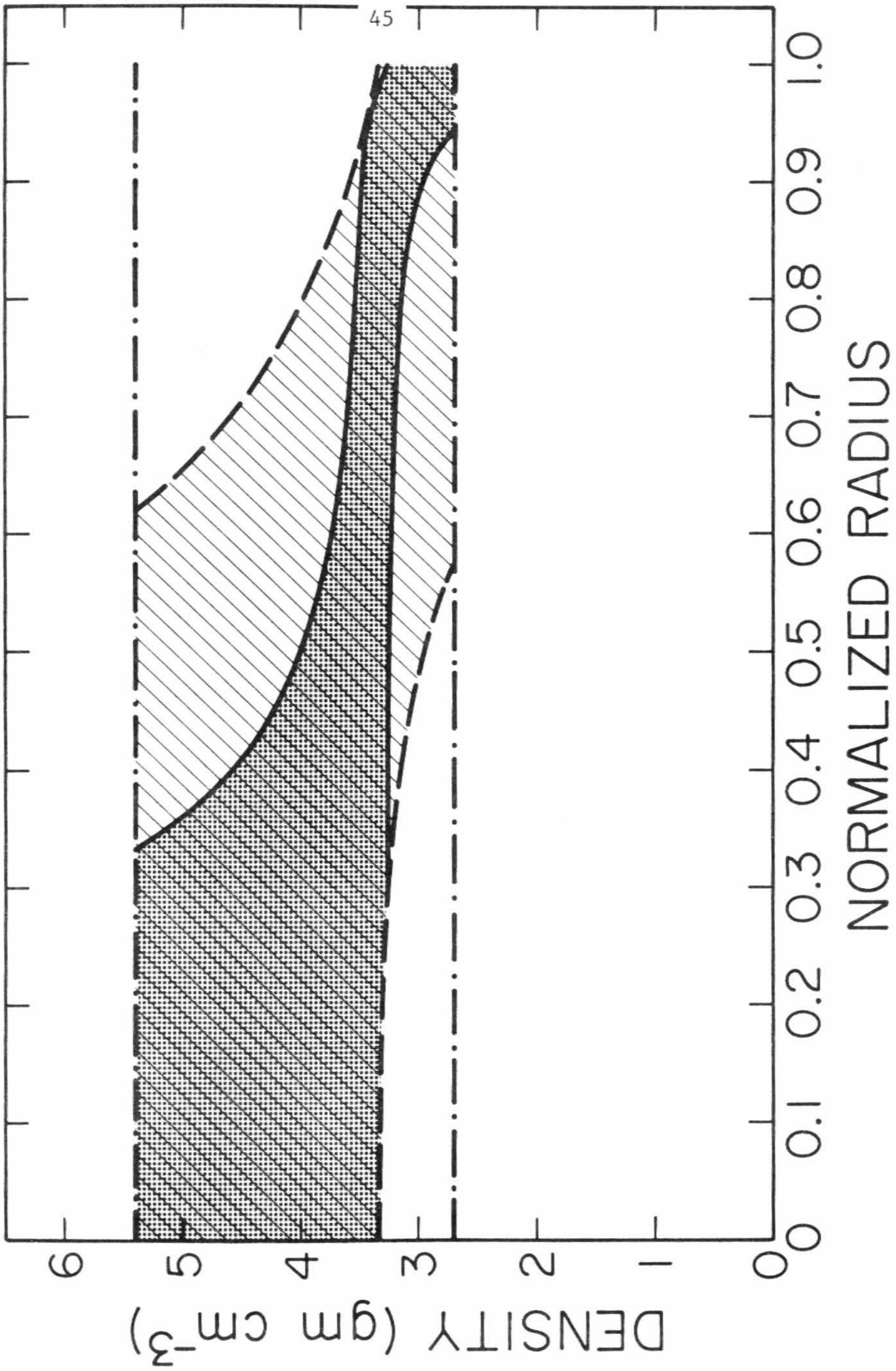
DENSITY (gm cm^{-3})
0
1
2
3
4
5
6
NORMALIZED RADIUS
0
0.1
0.2
0.3
0.4
0.5
0.6
0.7
0.8
0.9
1.0

These lower and upper bounds for the mean moment of inertia are simply the solutions for $\rho_0(\xi)$ and $\rho_0(\xi) + \Delta\rho_1(\xi)$, respectively, subject to

$$2.7 \le \rho_0 \le \rho_0 + \Delta\rho_1 \le 5.4$$

$$\rho_0 + \Delta\rho_1 \xi_1{}^3 = M_2 = 3.3437 \qquad \rho_0 + \Delta\rho_1 \xi_1{}^5 = M_4 = 3.286$$

They represent the envelope of all possible monotonic density distributions subject to the above constraints. However, not all models falling within these bounds are allowed. In particular, a uniform density model is inconsistent with these constraints. Although these bounds are not tight enough to be of real value in determining the composition of the lunar interior, they do exclude such extreme cases as either a uniform density or an Fe-Ni core with a radius of 380 km or greater. These bounds are also useful in conjunction with other data types.

The next step in complexity is to allow the model to depart from spherical symmetry in order to match not only the actual topography, as was done before, but also the gravitational potential to degree and order 12 and the entire inertia tensor, three moments and three products of inertia, rather than just the mean moment. To do this, we start by including the first- and second-degree harmonics $H_{nm}{}^{\ell}$ ($\ell = 0, 1$; $n = 1, 2$) describing the shape of the outer surface and the crust-mantle interface. The eight harmonics $H_{nm}{}^{0}$ (three first degree and five second degree) of the outer layer are known from the observed topography (Bills and Ferrari, 1977)

TABLE 2.2

TWO LAYERED LUNAR DENSITY MODEL

REPRESENTATIVE SOLUTIONS

parameter	a priori	a posteriori	a posteriori
		$R_c = 0$	$R_c = 400$ km $\rho_c = 5.4$ gm cm^{-3}
ρ_o(gm cm^{-3})	2.90 ± 0.20	2.72 ± 0.07	2.75 ± 0.06
$\Delta\rho$(gm cm^{-3})	0.50 ± 0.20	0.74 ± 0.08	0.64 ± 0.07
T_c(km)	69.5 ± 17.4	95.7 ± 15.6	73.2 ± 15.8
ΔX_1(km)	0.00 ± 1.64	8.33 ± 1.20	9.40 ± 1.30
ΔX_2 "	" "	2.53 ± 0.56	2.86 ± 0.40
ΔX_3 "	" "	1.40 ± 0.20	1.57 ± 0.22
C^1_{20}(10^{-4})	0.00 ± 10.00	-7.98 ± 0.63	-8.40 ± 0.66
C^1_{21} "	" "	10.45 ± 1.51	11.43 ± 1.59
S^1_{21} "	" "	-0.25 ± 0.04	-0.27 ± 0.04
C^1_{22} "	" "	0.45 ± 0.004	0.44 ± 0.01
S^1_{22} "	" "	-5.71 ± 0.84	-6.26 ± 0.89

(see Table 2.1), but the crustal density ρ_0 and the eight harmonics of the crust-mantle interface H_{nm}^{1}, as well as the density contrast $\Delta\rho_1$ and the normalized radius $\xi_1 = R_1/R_0$, are unknown and must be determined from (2.7) and (2.8) by constraining the inertia tensor of the model to the observed values. Equation (2.8) applied to the first-degree harmonics ensures that the center of figure of the mantle is offset in such a way as to counterbalance the center of figure displacement of the outer layer.

Such a model has 11 unknown parameters [H_{nm}^{1} (eight), ρ_0, $\Delta\rho_1$, and ξ_1], but only 10 constraints [G_{nm} (three), I_{ij} (six), and $\overline{\rho}$]. However, we have some a priori knowledge about each of the parameters, and since this makes the system effectively overdetermined, we can perform a weighted least squares inversion. See Table 2.2 for some representative results. Therein are presented the a priori and a posterior estimates and uncertainties for each of the 11 parameters for both the nominal solution and a solution with a core of radius $R_c = 400$ km and density $\rho_c = 5.4$ g cm^{-3}. The first-degree harmonics are presented in terms of the corresponding center of figure displacement

$$\Delta X = R_0 \xi_1 (C_{11}^{1}, \mathbf{S}_{11}^{1}, C_{10}^{1})$$

and the crustal thickness is $T_c = R_0(1 - \xi_1)$.

We discover two important facts from this model. First, in the case with no core the mean crustal thickness is significantly greater than that inferred from the locally derived seismic value, even though the densities are quite reasonable. This conflict can be removed by inclusion of a region of higher density at depth. Although the core model presented (R_c = 400 km and ρ_c = 5.4 g cm^{-3}) is by no means unique, the amount of density increase required is greater than can be accounted for by self-compression of a homogeneous moon for any reasonable elastic moduli and temperature profile.

Second, this model may be shown to depart from isostatic equilibrium, even for the low-degree harmonics. We shall have more to say about isostasy later.

Having established the inadequacy of a two layered model, we will now present a more detailed model in which the density, elastic moduli, and temperature are all allowed to vary more or less continuously with depth. Our analyses have shown that a three-layered model satisfies the constraints imposed by the gravitational, topographic, and librational data. However, current seismic studies (e.g., Nakamura et al., 1974) suggest a more complex internal structure. The model that we have chosen has six distinct regions. The approximate depths to the boundary interfaces are: upper and lower crust, 20 and 70 km; upper, middle, and lower mantle, 300, 800, and 1400 km. The core has a radius of 340 km. The crustal and upper mantle interfaces correspond to seismic discontinuities (Toksöz et al., 1974; Nakamura et al., 1974). The middle and lower mantle and core are inferred from deep seismic events (Nakamura et al., 1974), electrical conductivity profiles (Dyal et al., 1976), and thermal and compositional constraints (Brett, 1973). For modeling purposes the normalized radii of the interfaces are taken to be ξ_ℓ = 1.00, 0.99, 0.96, 0.83, 0.54, and 0.20.

Within each region the STP density and elastic moduli are assumed to vary linearly with depth between the values specified at the upper and lower boundaries. The ambient density and elastic moduli at each layer are then calculated from the STP values and the ambient temperature and pressure.

The assumed temperature and pressure derivativies of the density and elastic moduli correspond in the crust to anorthosite (Baldridge and Simmons, 1971), in the mantle to forsterite, and in the core to pyrite (Skinner, 1966; Birch, 1966). The STP density and bulk modulus of the core are those estimated for an Fe-FeS eutectic composition (Brett, 1973; Brett and Bell, 1969; King and Ahrens, 1973). The crustal density profile is from Gast and Giuli (1972), and the elastic moduli were chosen to duplicate a suitable average of the crustal velocity profile as given by Toksöz et al., (1974).

The lunar temperature profile is imprecisely known, particularly in the deep interior (e.g., Toksöz and Solomon, 1973). We have assumed surface and central temperatures of 250° and 1900°K, respectively, and have treated the actual temperature distribution with depth as a variable determined by the parameter n in (2.14). The value ultimately used was n = 4.0.

A family of models was generated by varying the density and elastic moduli at the mantle region interfaces (ξ = 0.96, 0.83, 0.54,

TABLE 2.3

LUNAR INTERIOR STRUCTURE MODEL

ξ	Depth, km	Temperature, °K	Pressure, kbar	ρ, g cm^{-3}	K, Mbar	σ	V_p, km s^{-1}	V_s, km s^{-1}
Upper Crust								
1.00	0	250	0.00	2.703	0.410	0.250	5.22	3.02
0.99	20	315	0.76	2.703	0.410	0.250	5.22	3.02
Lower Crust								
0.99	20	315	0.76	2.852	0.651	0.293	6.12	3.31
0.96	70	499	3.19	2.950	0.769	0.296	6.52	3.51
Upper Mantle								
0.96	70	499	3.19	3.371*	1.222*	0.246*	8.11	4.71
0.83	300	1117	14.57	3.382*	1.234*	0.275*	7.89	4.39
Middle Mantle								
0.83	300	1117	14.57	3.408*	1.234*	0.275*	7.89	4.39
0.54	800	1760	34.36	3.397*	1.691*	0.420*	7.80	2.89
Lower Mantle								
0.54	800	1760	34.36	3.399*	1.691*	0.420*	7.80	2.89
0.20	1400	1897	48.13	3.424*	1.745*	0.443*	7.68	2.46
Core								
0.20	1400	1897	48.13	5.209	1.400	0.500	5.18	0.00
0.00	1740	1900	52.95	5.223	1.423	0.500	5.22	0.00

*Parameter which was varied in search for acceptable model.

and 0.20) subject to the constraints that (1) the STP values of ρ, K, and Poisson's ratio $\sigma = (3K - 2\mu)/(6K + 2\mu)$ are all nondecreasing with depth and (2) K and σ are continuous across the interfaces at $\xi = 0.83$ and 0.54. The STP values of ρ, K, and σ at intermediate points are found by linear interpolation, and the ambient values of these parameters are found, as they were before, from the ambient temperature and pressure. These perturbations are performed until a model is found which has the desired mean density and moment as well as P and S wave travel times. The resultant temperature, pressure, density, bulk modulus, Poisson ratio, and seismic velocity profiles of such a model are given in Table 2.3. Table 2.4 gives the moments of the density distribution M_n ($n = 0, 1, \ldots, 8$). The seismic travel time as a function of epicentral distance for the model is compared with observed teleseismic data (Nakamura et al., 1974) in Figure 2.2. The seismic phases shown are identified according to the nomenclature usually applied to the earth (Jeffreys, 1959).

TABLE 2.4

MOMENTS OF DENSITY DISTRIBUTION M_n

n	M_n	n	M_n	n	M_n
0	3.7409	3	3.3101	6	3.2496
1	3.4247	4	3.2875	7	3.2322
2	3.3433	5	3.2679	8	3.2156

Observed values are $M_2 = 3.3437 \pm 0.0016$ and $M_4 = 3.2858 \pm 0.0211$.

FIGURE 2.2 - Lunar seismic travel times. Curves represent model calculations; circles represent data (Nakamura *et al*., 1974).

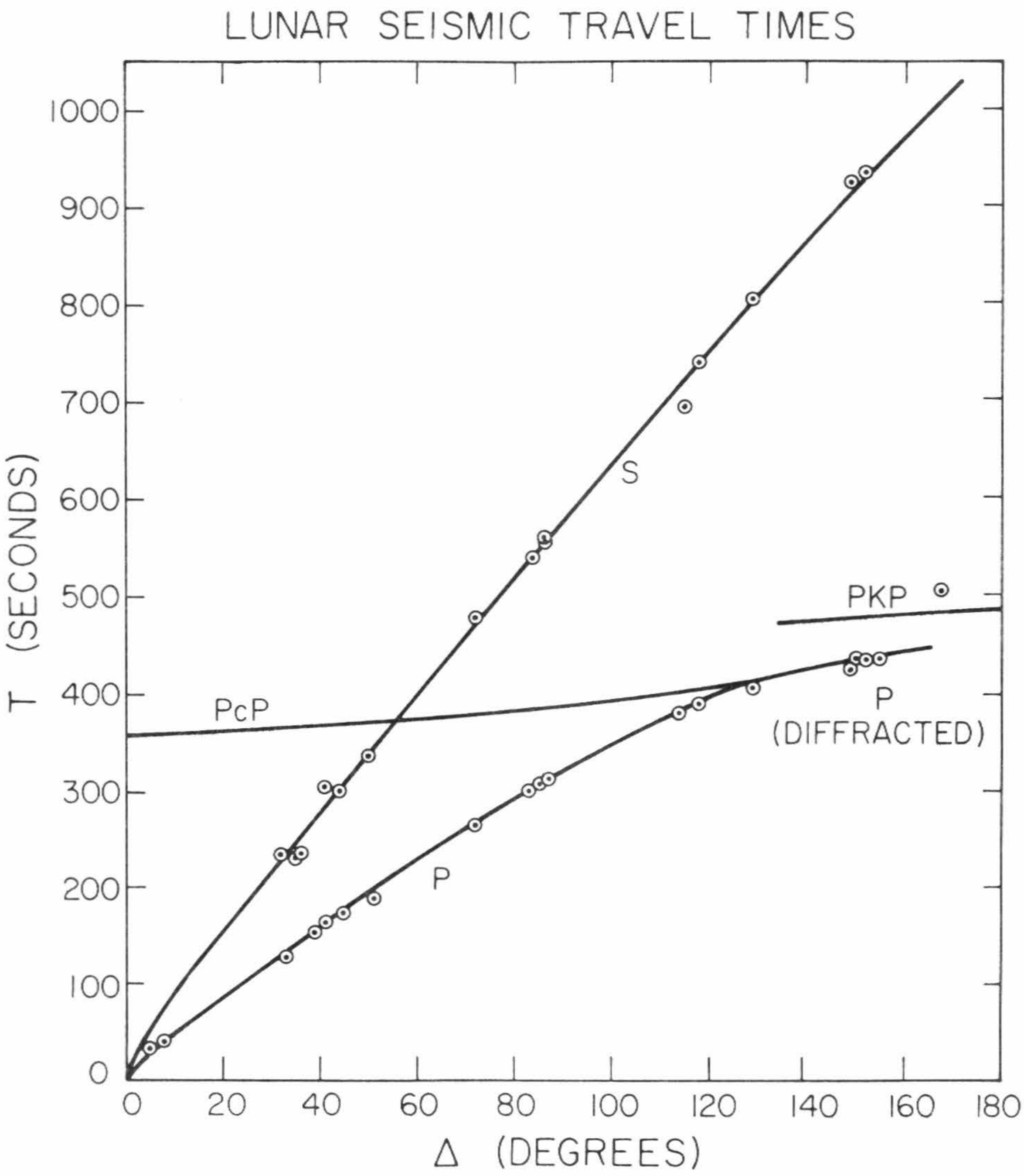
LUNAR SEISMIC TRAVEL TIMES
T (SECONDS)
0
100
200
300
400
500
600
700
800
900
1000
Δ (DEGREES)
0
20
40
60
80
100
120
140
160
180
S
P
PcP
PKP
P (DIFFRACTED)

We tentatively interpret the P wave arrivals near $\Delta = 150^\circ$ as rays diffracted around the core and the weak arrival at $\Delta = 168^\circ$ as a PKP_2 phase (not shown in the figure) due to a rapid decrease in seismic velocity at the mantle-core interface.

A comparison of the STP density and elastic moduli with those of olivine and pyroxene (Chung, 1970; Nakamura et al., 1974) reveals that a mineral assemblage consisting largely of olivine (80-85% forsterite) and some pyroxene is consistent with the upper mantle model. The increase in density and bulk modulus with depth is consistent with an increase in CaO, TiO_2, and/or Al_2O_3 (Simmons and Wang, 1971; Anderson, 1975).

Given values for the mean crustal thickness and density and the density contrast with the mantle, we can include the higher harmonics of topography and gravity in our model, solving for H_{nm}^{1} from H_{nm}^{0} and G_{nm} by (2.7) and (2.8). We are thus able to estimate the variation of crustal thickness over the planet on the assumption that all lateral density variations occur as undulations on the mantle-crust interface, which is at a depth of 50-60 km in the area of the Apollo seismic array. For the densities in our model, a mean crustal thickness of 70 km is required to match the seismic values. The resultant crustal thickness map is presented in Figures 2.3a and 2.3b. Wood (1973) has presented a similar analysis based on a more restricted data set. He inferred crustal thicknesses which are systematically less than our estimates.

FIGURE 2.3a - Crustal thickness variations. Lunar nearside. Twelfth degree model. Gravity from Ferrari (1975). Assumed mean crustal density is 2.9 gm cm^{-3} crust-mantle density contrast is 0.4 gm cm^{-3} and mean crustal thickness is 70 km.

FIGURE 2.3b - Crustal thickness variations. Lunar farside. See caption of Figure 2.3a.

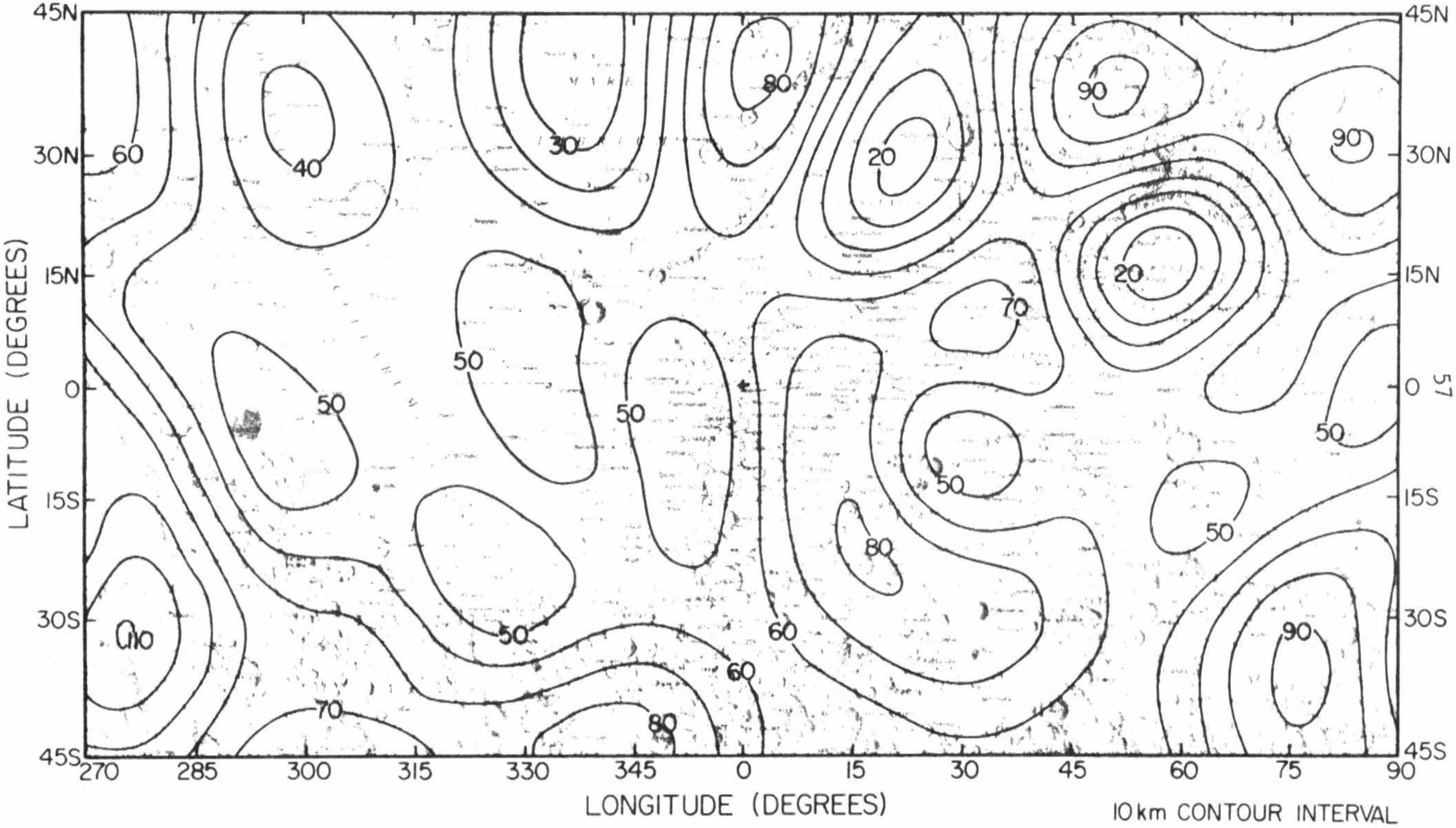
LATITUDE (DEGREES)
45N
30N
15N
0
15S
30S
45S
LONGITUDE (DEGREES)
270
285
300
315
330
345
0
15
30
45
60
75
90
10km CONTOUR INTERVAL
60
40
30
80
20
90
90
20
70
50
50
50
50
50
50
50
110
80
60
60
70
80
90

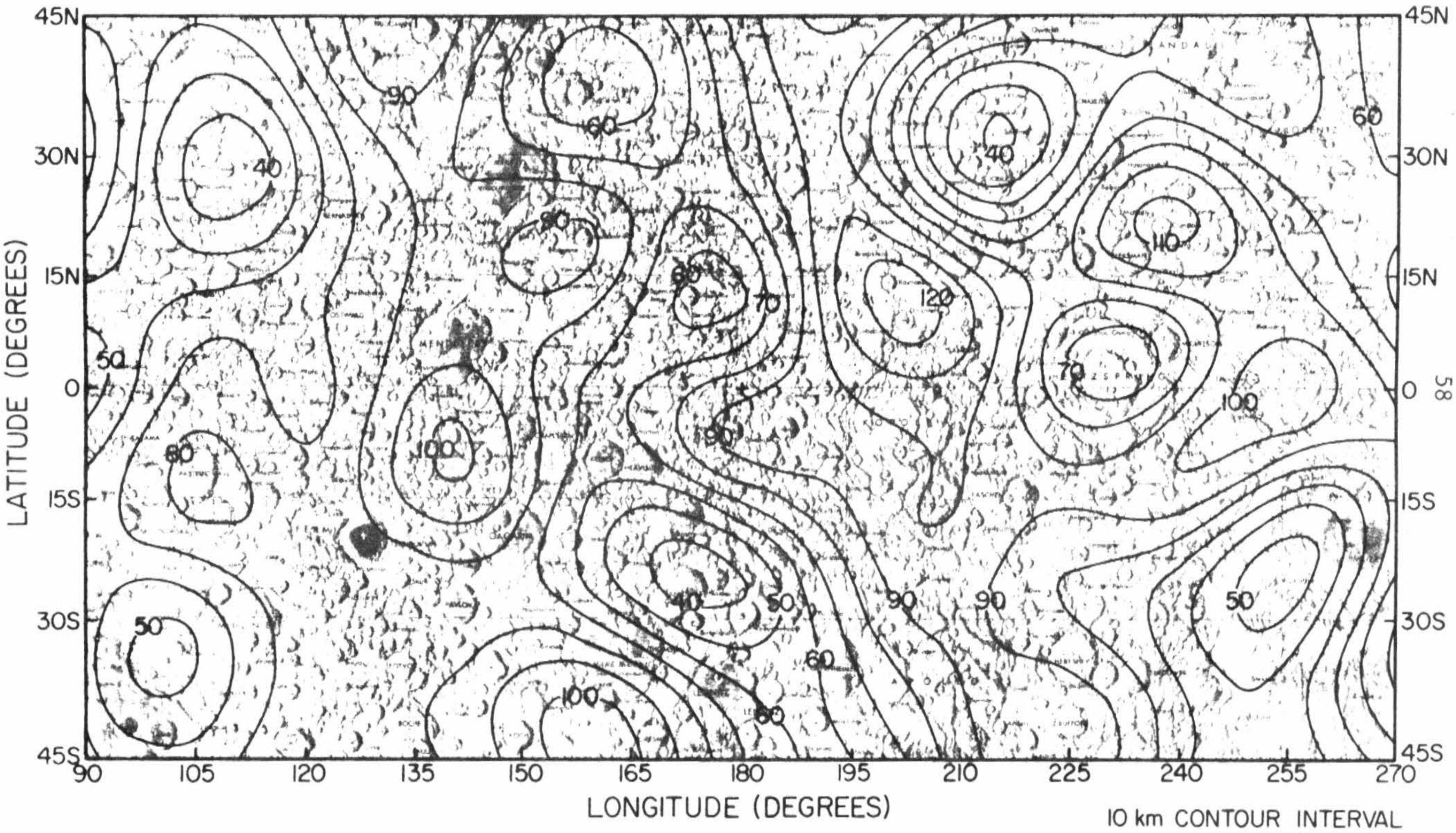
45N
30N
15N
0
15S
30S
45S
LATITUDE (DEGREES)
90
105
120
135
150
165
180
195
210
225
240
255
270
LONGITUDE (DEGREES)
10 km CONTOUR INTERVAL
90
60
40
40
60
80
110
80
70
120
50
70
100
100
80
90
50
40
50
90
90
50
60
100
60

The crustal thickness indicated in the mascon basins is somewhat of an underestimate, since the effect of a surface layer of basalt is ignored. Bowin et al. (1975) estimate that such a surface fill accounts for roughly 20% of the observed gravity anomaly. They estimate a mantle uplift in Mare Serenitatis of 12 km, compared to our estimate of roughly 50 km. However, there is a factor of 2 discrepancy between the free-air anomaly estimates used, and the fact that Bowin et al. are modeling only free-air gravity, whereas we are modeling Bouguer gravity, accounts for an additional factor of 2.

The mean crustal thicknesses under different physiographic regions are: mascons, 30-35 km; irregular maria, 50-60 km; and highlands, 90-110 km.

Schonfeld (1977) has recently shown significant correlations between lunar surface chemistry and the above crustal thickness model. From Al/Si and Mg/Si ratios determined by x-ray fluorescence measurements and Mg and Fe concentrations as determined by gamma ray spectroscopy, he has determined that, in the non-mare regions, total Al_2O_3 shows a positive correlation, whereas both total FeO and the MgO/FeO ratio are negatively correlated with crustal thickness. Though these quantities show the same type of correlation with surface elevation alone, their correlation with crustal thickness is much better.

The mere existence of compositional and thickness variations in the crust suggests that the processes of crustal formation and differentiation did not completely homogenize the surface material. The additional fact that these variations are mutually correlated requires further explanation. Recalling that magmatic differentiation leads to enrichment in Al and depletion in Fe, as well as lowering of the Mg/Fe ratio in the surface layers (Schonfeld, 1977), we see that a possible model for the observed correlations involves the simple assumption that regions of thicker crust are more highly differentiated.

As was previously mentioned, this crustal thickness model is not in isostatic equilibrium; i.e., the pressure at the crust-mantle interface varies with position about its mean value of 3.2 kbar. The maximum superisostatic stress, as calculated from (2.11), is a value, slightly in excess of 200 bars, associated with the major mascon basins Imbrium, Serenitatis, and Crisium. Other regions have smaller stresses, and the global rms stress variation is 64 bars.

It should be noted that it is possible to produce a model which satisfies both topographic and gravitational data and is also isostatically compensated at depth. However, when such models were attempted, the depth of compensation of the low-degree harmonics approached that of the presently proposed mantle-core interface. Since the superisostatic stresses implied by the above model are close to the stresses found in the Earth, it appears more reasonable to accept a nonisostatic Moon.

E. SUMMARY

We have presented a series of lunar models culminating in a six-layered model with undulations on the outer surface and at the crust-mantle interface. This model is consistent with all available topographic, gravitational, librational, and seismic data.

We have concluded that the librational parameters of the Moon are determined primarily by surface height variations and only secondarily by lateral density variations and that the surface topography is not isostatically supported, nor is it predominated by a fossil tidal or rotational bulge. The largest pressure departures from isostasy are approximately 200 bars under the major mascon basins. The crustal thickness varies from 30-35 km under mascon basins to 90-110 km under the highlands, with the irregular maria intermediate at 50-60 km.

All of the data considered are consistent with an anorthositic crust extending to a mean depth of 70 km underlain by a predominantly forsterite upper mantle grading into a refractory-rich lower mantle surrounding a pyrrhotite core. Such a composition is consistent with, but not uniquely specified by, our model calculations.

We note that a smaller estimate of the mean inertial moment would be consistent with a larger core, which in turn would simplify the interpretation of the P wave arrival times near Δ = 150 and at 168 deg, which are presently interpreted as diffracted P and PKP_2, respectively.

REFERENCES

Anderson, D.L. (1975). On the composition of the lunar interior. J. Geophys. Res. 80, 1555-1557.

Baldridge, W.S., and Simmons G. (1971). Thermal expansion of lunar rocks. Proc. Lunar Sci. Conf. 3rd, 2317-2321.

Bills, B.G., and Ferrari, A.J. (1977). A harmonic analysis of lunar topography. Icarus 31, 244-259.

Birch, F. (1966). Compressibility; Elastic constants, Handbook of Physical Constants, Geol. Soc. Amer. Mem., Sect. 7, 97-173.

Bowin, C., Simon, B., and Wollenhaupt, W.R. (1975). Mascons: A two-body solution. J. Geophys. Res. 80, 4947-4955.

Brett, R. (1973). A lunar core of Fe-Ni-S. Geochim. Cosmochim. Acta 37, 165-170.

Brett, R., and Bell, P.M. (1969). Melting relations in the Fe-rich portion of the system Fe-FeS at 30 kb pressure. Earth Planet. Sci. Lett. 6, 479-482.

Bullen, K.E. (1963). An Introduction to the Theory of Seismology. Cambridge University Press, New York, pp. 109-113.

Chung, D.H. (1970). Effects of Fe/Mg ratio on V_p and V_s in olivine. J. Geophys. Res. 75, 7353-7361.

Dyal, P., Parkin, C.W., and Daily, W.D. (1976). Structure of the lunar interior from magnetic field measurements (abstract). In Lunar Science VII, Lunar Science Institute, Houston, pp. 224-226.

Ferrari, A.J., (1975). Lunar gravity: The first farside map. *Science* **188**, 1297-1300.

Gast, P.W., and Giuli, R.T. (1972). Density of the lunar interior. *Earth Planet. Sci. Lett.* **16**, 299-305.

Heyl, P.R., and Chrzanowski, P. (1942). A new determination of the constant of gravitation. *Radio Sci.* **29**, 1-31.

Jeffreys, H. (1959). *The Earth*, Cambridge University Press, New York, pp. 87-93.

King, D.A., and Ahrens, T.J. (1973). Shock compression of FeS. *Nature Lond. Phys. Sci.* **243**, 82-83.

Kopal, Z. (1969). *The Moon*, D. Reidel, Dordrecht, Netherlands, pp. 77-90.

Nakamura, Y., and Latham, G.V. (1969). Internal constitution of the moon. *J. Geophys. Res.* **74**, 3771-3780.

Nakamura, Y., Latham, G., Lammlein, D., Ewing, M., Duennebier, F., and Dorman J. (1974). Deep lunar interior inferred from recent seismic data. *Geophys. Res. Lett.* **1**, 137-140.

Phillips, R.J., and Saunders, R.S. (1975). The isostatic state of Martian topography. *J. Geophys. Res.* **80**, 2893-2898.

Schonfeld, S. (1977). Comparison of orbital chemistry with crustal thickness and lunar sample chemistry. *Proc. Lunar Sci. Conf. 8th*, in press.

Simmons, G., and Wang, H. (1971). *Single Crystal Eleastic Constants and Calculated Aggregate Properties: A Handbook*, 2nd ed., MIT Press, Cambridge, Mass., 370 pp.

Sinclair, W.S., Sjogren, W.L., Williams, J.G., and Ferrari, A.J. (1976) The lunar moment of inertia derived from combined Doppler and laser ranging data (abstract). In Lunar Science VII, Lunar Science Institute, Houston, Tex, p. 817.

Skinner, B.J. (1966). Thermal expansion, Handbook of Physical Constants. Geol. Soc. Amer. Mem. Sect. 6 **97**, 75-96.

Toksöz, M.N., and Solomon, S.C. (1973). Thermal history and evolution of the moon. Moon **7**, 251-278.

Toksöz, M.N., Dainty, A.M., Solomon, S.C., and Anderson, K.R. (1974). Structure of the moon. Rev. Geophys. Space Phys. **12**, 539-567.

Wood, J.A. (1973). Bombardment as a cause of the lunar asymmetry. Moon **8**, 73-103.

III. A HARMONIC ANALYSIS OF MARTIAN TOPOGRAPHY

A. INTRODUCTION

The primary objective of this investigation was to obtain a spherical harmonic representation of Martian topography of sufficient resolution and fidelity to be of use in performing global Bouguer gravity analyses. Previous harmonic analyses (Pettengill et al., 1969; Cain et al., 1972; Christensen, 1975) have suffered from inadequate data coverage and insufficient model resolution. An improved model of Martian global topography has been obtained by fitting a sixteenth degree harmonic series to occultation, radar, spectral and photogrammetric measurements. The data are described by Christensen (1975) and Wu (1975). Our analysis differs from Christensen's mainly in that we have attempted to compensate for the very uneven distribution of the data by a process of interpolation similar to that used in our analysis of lunar topography in Chapter I (see also Bills and Ferrari, 1977a).

This chapter presents a brief discussion of the data used in the analysis, its spatial distribution and associated errors. The technique used to compensate for the irregular data distribution is then elaborated. The resulting harmonic estimates are presented and compared with previous analyses. Some of the low degree harmonics and their geophysical implications are discussed separately. The center-of-figure displacement and the excess topographic oblateness receive particular attention.

Maps of the global topography and the Bouguer gravity anomaly are presented, followed by a crustal thickness map consistent with gravity, topography and recent preliminary Viking seismic results.

B. DATA

The basic data used in this analysis are identical to those used by Christensen (1975). They consist of occultation and spectral measurements from Mariner 9, and Earth-based radar data. The occultation measurements yield absolute distances of surface points from the center of mass. All the other data are only relative. Christensen (1975) solved for and partially eliminated the biases between the various reference surfaces, and thus produced a more unified data set. Figure 3.1 indicates the approximate distribution of these data, summarized according to $5^\circ \times 5^\circ$ bins. An important aspect of this distribution is its uneven character. Only 1381 of the 2592 bins, representing 68.5% of the total surface area, contain any data. Even among these, the number and quality of measurements varies widely, from only one measurement per bin in some high latitude regions, to over a hundred measurements per bin in the low southern latitudes.

Carlson and Helmsen (1969) have shown that it is the unevenness, rather than the sparsity, of the data distribution which causes the greatest difficulty in obtaining reliable estimates of harmonic coefficients. It is primarily in our treatment of this problem that our analysis differs from Christensen's.

FIGURE 3.1a - Data distribution. Mid-latitudes. The Martian surface is shown divided into 2592 bins, each $5^\circ \times 5^\circ$. Shading indicates those bins (1381) which contain at least one measurement. Photographic data were used to estimate elevations in the remaining bins.

FIGURE 3.1b - Data distribution. Polar regions. See caption of Figure 3.1a.

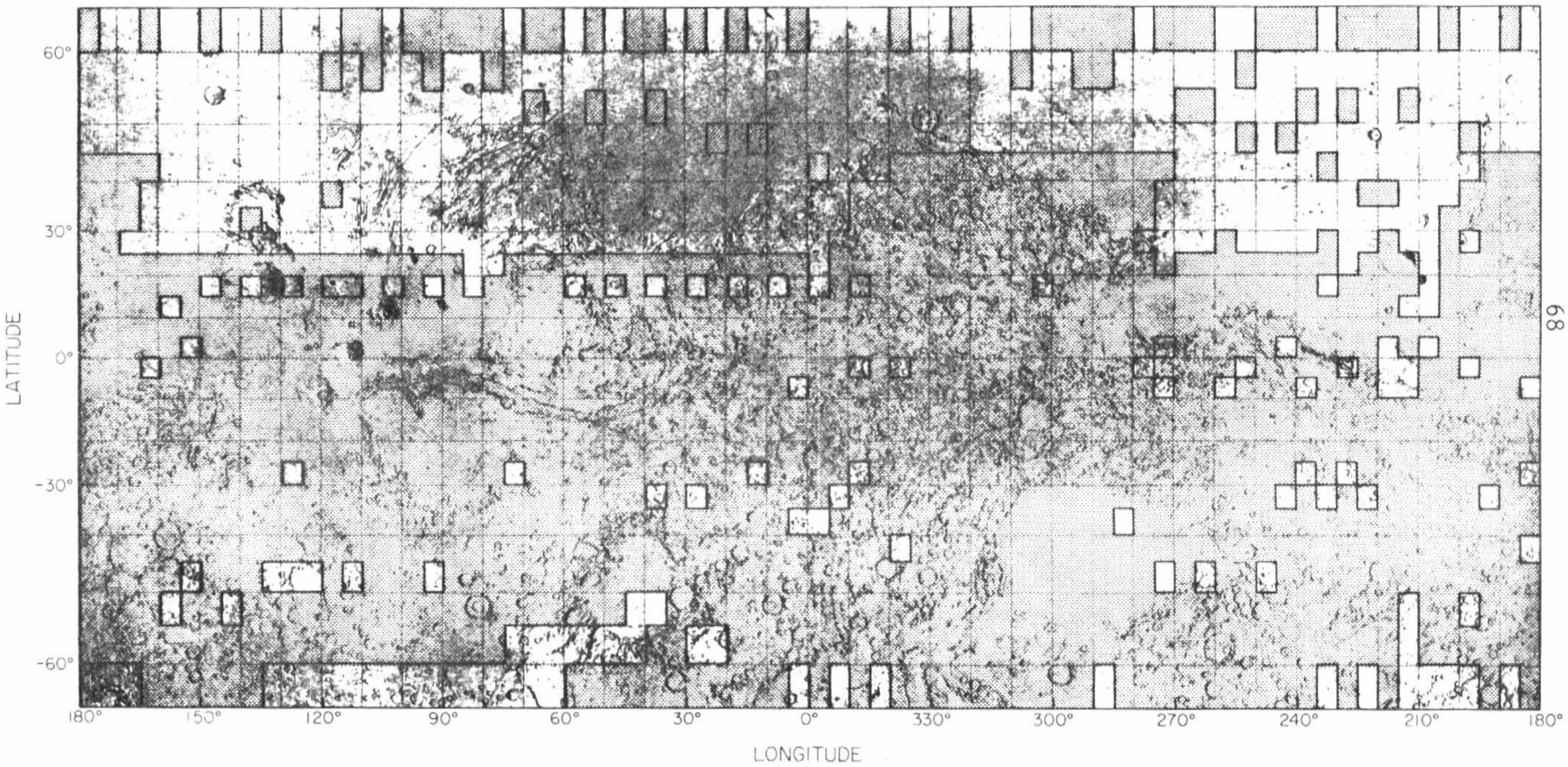
60°
30°
0°
-30°
-60°
LATITUDE
180°
150°
120°
90°
60°
30°
0°
330°
300°
270°
240°
210°
180°
LONGITUDE

NORTH POLAR REGION

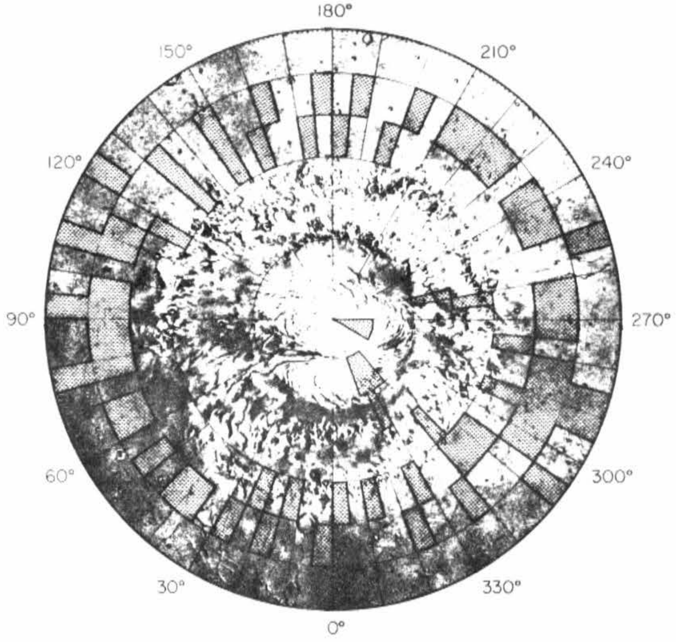

SOUTH POLAR REGION

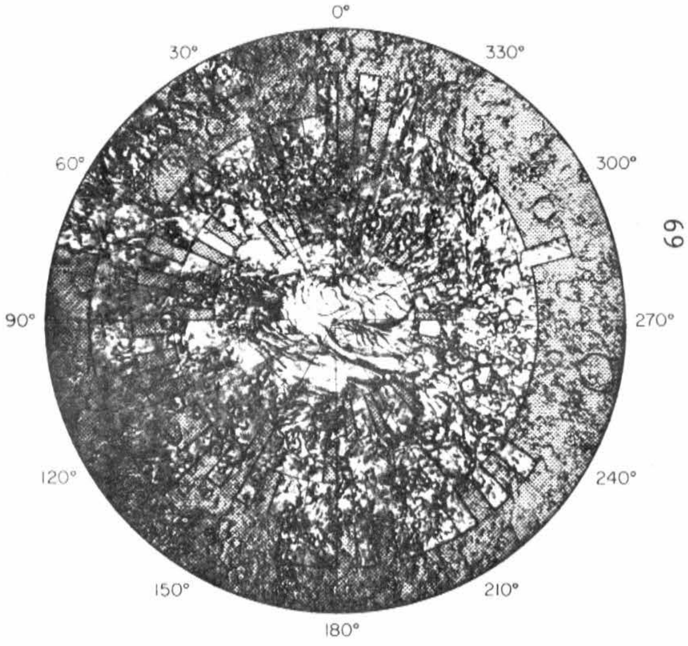

In a similar analysis of lunar topography in Chapter I, we relied on a linear auto-regressive interpolation scheme to obtain estimates, in the regions without data, of the most probable elevations and associated errors, consistent with the known statistical characteristics of the available data. This process minimizes the expected mean square error of the estimates, but, unfortunately, it totally ignores the actual topography in the unmeasured regions. Fortunately, in the case of Mars, we can do better.

Wu (1975) has used essentially this same data set, in conjunction with photographic interpretation, to produce a topographic contour map of Mars. In the regions without direct measurements, the contours have been interpolated by photogrammetric and interpretive techniques. Presumably this interpolation procedure gives a faithful representation of the high frequency components of the topography, but may suffer from low frequency distortion of bias errors.

Our complete data set thus consists of Christensen's (1975) data, where available, augmented by a bias corrected version of Wu's interpolation in the regions without direct measures. This is preferable to leaving large voids in the data distribution.

All data are of the basic form $R(\theta,\varphi)$, where R is the radial distance from the origin, θ is the latitude, and φ is the (west) longitude. In addition to the spherical coordinates (R,θ,φ), we will have occasion to use a Cartesian coordinate system (X_1, X_2, X_3) with its origin at the center of mass. This system is right-handed and oriented such that the X_1 and X_2 axes are in the equator plane with the positive X_1 axis on the $\varphi = 0^\circ$ meridian and the positive X_2 axis on the $\varphi = 270^\circ$ meridian. The X_3 axis lies along the rotation axis (positive towards north).

C. ANALYSIS

As discussed in the previous section, the greatest problem we face in the analysis of the data is compensating for their irregular spatial distribution. We will be interested, not only in the complete ensemble of harmonics which characterize the Martian surface, but also in some of the low degree harmonics considered separately. Therefore we require harmonic coefficients which not only accurately represent the data, but which are also optimally uncorrelated with one another, consistent with the uneven data distribution.

Given a collection of topographic data F_i with associated standard deviation σ_i distributed on a sphere,

$$R(\theta_i, \varphi_i) = F_i \pm \sigma_i \quad , \tag{3.1}$$

we desire optimally uncorrelated estimates of the harmonic coefficients H_{nm} through degree and order N.

Our basic model is of the form

$$R(\theta,\varphi) = R_o \left[1 + \sum_{n=1}^{16} \sum_{m=0}^{n} H_{nm}^T \Lambda_{nm}(\theta,\varphi) \right] \tag{3.2}$$

where, as before

$$H_{nm} = \begin{bmatrix} H_{nm1} \\ H_{nm2} \end{bmatrix} = \begin{bmatrix} \overline{C}_{nm} \\ \overline{S}_{nm} \end{bmatrix}$$

$$\Lambda_{nm}(\theta,\varphi) = \overline{P}_{nm}[\sin(\theta)] \begin{bmatrix} \cos(m\varphi) \\ \sin(m\varphi) \end{bmatrix}$$

are the normalized harmonic coefficients and surface harmonic functions, respectively. A sixteenth degree model was chosen as a compromise between resolution and credibility, since, as the sphere is tesselated into a finer mesh of bins, the proportion of bins containing data decreases. This model resolves many of the major physiographic features, and in fact exceeds the resolution of any presently available Martian gravity model. A higher degree model was not utilized because of the adverse effect of the data gaps.

For the ensemble of observations, equation (3.2) can be written as

$$F_i = \left(\frac{\partial F_i}{\partial Z_j}\right) Z_j = A_{ij} Z_j \tag{3.3}$$

where Z_j is the vector of harmonic coefficients H_{nm}. In this notation, the weighted least-squares estimator is (see e.g., Lawson and Hanson, 1974)

$$\hat{Z} = [A^T BA]^{-1} A^T BF \tag{3.4}$$

where the weighting matrix B is the inverse of the data noise covariance matrix (assumed, in this analysis, to be diagonal), and superscript T denotes transposition.

To obtain uncorrelated estimates of the parameters Z_j, we must diagonalize the solution covariance matrix

$$E(ZZ^T) = [A^T BA]^{-1} \tag{3.5}$$

where E(•) is the expectation operator. Since we are assuming that B is diagonal, the problem thus reduces to the optimization of the uniformity of the effective data distribution. If we had data of uniform accuracy, evenly distributed over the sphere, we would be assured of uncorrelated estimates. However, the very uneven distribution of the data necessitates further analysis.

The approach we have taken is to represent the surface of Mars, in each bin which contains data, by an average of those data, and, in the bins lacking direct measures, by elevations from Wu's (1975) map corrected for low frequency biases. The first step was to determine the weighted mean of all the data within each of the 1381 5°x 5° bins which contain data. We then sampled Wu's map at the midpoint of each of the 2592 5° x 5° data bins. The map elevations are referenced to the equipotential surface of Jordan and Lorell's (1975) gravity model with mean radius R = 3382.946 km. This approximately corresponds to the 6.1 mb equipressure level. Absolute radii were thus constructed by adding the map elevations to the radii of the corresponding points on the equipotential. These radii were then expanded in a harmonic series of degree sixteen, with coefficients H'_{nm}.

To determine the bias, if any, between the averaged data $\overline{R}$ and the map radii R, we define the difference function

$$\Delta H(\theta,\varphi) = \begin{cases} \bar{R}(\theta,\varphi) - R(\theta,\varphi) & \text{if } (\theta,\varphi) \in D \\ 0 & \text{otherwise} \end{cases} \tag{3.6}$$

where D is the set of points (θ,φ) enclosed in the 1381 bins which contain data. This difference function can be represented as

$$\Delta H = b \cdot w \tag{3.7}$$

the product of the true bias $b(\theta,\varphi)$ times a sampling window function

$$w(\theta,\varphi) = \begin{cases} 1 & \text{if } (\theta,\varphi) \in D \\ 0 & \text{otherwise.} \end{cases} \tag{3.8}$$

Therefore, in a harmonic series expansion of $\Delta H(\theta,\varphi)$, the coefficients

$$\Delta H_{nm} = b_{nm} * w_{nm} \tag{3.9}$$

are convolutions of the bias function coefficients with the window function coefficients.

We are unable to perform a direct deconvolution. However, since the detrimental effect of this convolution is greatest in the high degree harmonics, and since our a priori expectation is that most of the actual bias introduced by Wu's (1975) interpolation is of a low degree nature, we desire a low-pass filtered version of the difference function to use as our estimate of the actual bias. A candidate low-pass filter is realized by truncating the harmonic expansion at some low degree N. However, this filter is rather too abrupt for the present purpose, and the choice of cutoff degree is somewhat arbitrary. Therefore, we have chosen to convolve the difference function with a Gaussian function of angular distance γ (Roberts and Ursell, 1960)

$$G(\gamma) = \sum_{n=1}^{\infty} \frac{(2n+1)}{4\pi} e^{-(n)(n+1)\Theta/4} P_n(\cos(\gamma)) \qquad (3.10)$$

with angular variance

$$\Theta = \frac{4\pi}{(N)(N+1)} \quad , \quad N = 16$$

equivalent to the resolution of a sixteenth degree harmonic series. According to the addition theorem of spherical harmonics (see Appendix A)

$$P_n(\cos(\gamma)) = \frac{1}{2n+1} \sum_{m=0}^{n} \Lambda_{nm}^{T}(\theta,\varphi)\ \Lambda_{nm}(\theta',\varphi') \qquad (3.11)$$

where

$$\gamma = \cos^{-1}\left[\frac{\cos(\Delta\varphi) + 1}{2} \cos(\Delta\theta) + \frac{\cos\ (\Delta\varphi) - 1}{2} \cos(\Sigma\theta)\right]$$

is the angular separation between points (θ,φ) and $(\theta',\varphi') = (\theta+\Delta\theta, \varphi + \Delta\varphi)$. Therefore, the result of convolving the difference function with the specified Gaussian function and expanding the convolution in a harmonic series is

$$\Delta H'_{nm} = \Delta H_{nm}\ e^{-(n)(n+1)\Theta/4} \qquad (3.12)$$

where ΔH_{nm} is a harmonic coefficient of the difference function.

Our final bias corrected harmonic coefficient estimate is thus

$$H_{nm} = H'_{nm} + \Delta H'_{nm} \qquad (3.13)$$

where H'_{nm} is a harmonic coefficient of the elevations from Wu's (1975) map.

In performing these harmonic expansions, we have used the weighted least-squares algorithm [equation (3.4)]. The weighting of each point was proportional to the area of its bin and inversely proportional to the variance of the measurement or interpolation:

$$B_{ij} = 2 \sin(\Delta\theta/2) \cos(\theta_i) \Delta\varphi \, \delta_{ij} / \sigma_i^2 \quad . \tag{3.14}$$

The presumed errors were $\sigma = 0.3$ km for the actual data and $\sigma = 1.0$ km for the interpolation.

The estimates of the normalized harmonic coefficients and their formal uncertainties are presented in Table 3.1.

D. RESULTS

1. Low Degree Harmonics

We will now consider the harmonics of degree zero, one and two. These represent the mean radius, center of figure displacement, and tri-axial figure, respectively.

The estimated mean Martian radius is $R_0 = (3389.92 \pm 0.04)$ km. This, in conjunction with estimates of $GM = (42828.1 \pm 0.5)$ km^{3}sec^{-2} (Born, 1974) and $G = (667.32 \pm 0.31) \times 10^{-25}$ km^3 sec^{-2} gm^{-1} (Heyl and Chrzanowski, 1942) yields an estimate for the mean density of $\bar{\rho} = (3.9331 \pm 0.0018)$ gm cm^{-3}. Most of this error comes from the error in G. The mean density, in combination with the mean inertial moment, places important constraints on models of Martian internal structure and composition (see e.g., Johnston et al., 1974).

We now turn our attention to the first degree harmonics. They represent a displacement of the center of figure (C.F.) from the

TABLE 3.1

Normalized Martian Topography Harmonics (x 10^6)

R_o = 3389.916 ± 0.038 km

n	m	$\bar{C}_{nm}$	$\bar{S}_{nm}$	$\sigma(\bar{C}_{nm})$	$\sigma(\bar{S}_{nm})$
1	0	-376.0		12.7	
1	1	-8.1	-199.8	10.3	10.6
2	0	-1823.9		12.2	
2	1	71.7	103.0	11.6	11.8
2	2	-288.1	214.5	10.1	10.1
3	0	73.4		12.5	
3	1	-27.7	23.4	11.5	11.4
3	2	-37.9	68.1	11.3	11.3
3	3	111.5	250.7	9.9	10.0
4	0	19.6		12.6	
4	1	3.0	14.3	11.3	11.3
4	2	121.9	-63.2	11.3	11.3
4	3	-109.3	-4.2	10.9	11.1
4	4	-15.1	-61.0	9.8	9.8
5	0	-1.2		12.1	
5	1	7.8	16.2	11.5	11.7
5	2	-60.1	19.9	11.0	10.9
5	3	-5.9	45.4	11.1	11.3
5	4	-14.7	-95.2	10.7	10.7
5	5	-47.3	17.0	9.8	9.8
6	0	51.7		11.8	
6	1	-3.1	-64.7	11.4	11.6
6	2	-66.1	47.3	11.1	11.0
6	3	-22.3	-22.5	10.8	10.9
6	4	27.6	52.7	11.0	11.0
6	5	59.0	12.1	10.5	10.5
6	6	60.3	4.4	9.9	9.9

TABLE 3.1 (Cont'd)

n	m	$\bar{C}_{nm}$	$\bar{S}_{nm}$	$\sigma(\bar{C}_{nm})$	$\sigma(\bar{S}_{nm})$
7	0	98.2		11.4	
7	1	-8.2	29.3	11.3	11.4
7	2	48.0	-15.4	10.9	11.0
7	3	17.7	-24.4	10.8	10.8
7	4	14.9	5.0	10.8	10.7
7	5	25.7	13.2	10.9	10.8
7	6	22.6	3.6	10.4	10.4
7	7	35.1	-43.5	10.0	10.0
8	0	29.8		11.1	
8	1	-9.1	35.7	11.2	11.2
8	2	9.2	15.0	10.8	10.9
8	3	15.1	16.6	10.7	10.7
8	4	-0.6	32.6	10.7	10.6
8	5	37.4	20.5	10.7	10.7
8	6	-38.7	-15.2	10.7	10.7
8	7	33.6	7.3	10.4	10.3
8	8	-28.6	5.3	10.1	10.1
9	0	34.8		10.9	
9	1	30.6	-10.6	10.9	10.9
9	2	2.9	5.8	10.8	10.8
9	3	-9.7	-0.5	10.5	10.6
9	4	4.2	15.4	10.6	10.6
9	5	-23.8	8.1	10.6	10.6
9	6	2.9	5.6	10.6	10.6
9	7	14.2	-14.0	10.6	10.5
9	8	-33.1	-11.1	10.3	10.3
9	9	-30.2	12.2	10.2	10.2
10	0	13.6		10.8	
10	1	20.5	-1.0	10.7	10.7
10	2	9.9	-21.7	10.7	10.7
10	3	25.9	9.1	10.5	10.5
10	4	2.3	-21.0	10.5	10.5
10	5	-18.0	3.0	10.6	10.6
10	6	1.9	-14.3	10.5	10.5
10	7	-12.2	-12.9	10.6	10.5
10	8	-8.1	-9.3	10.5	10.5
10	9	-25.6	-12.7	10.3	10.3
10	10	6.7	13.5	10.3	10.3

TABLE 3.1 (Cont'd)

n	m	$\bar{C}_{nm}$	$\bar{S}_{nm}$	$\sigma(\bar{C}_{nm})$	$\sigma(\bar{S}_{nm})$
11	0	-2.7		10.6	
11	1	1.6	-8.6	10.6	10.6
11	2	-2.4	-8.9	10.6	10.6
11	3	-2.5	-14.3	10.5	10.5
11	4	-1.3	-9.3	10.5	10.5
11	5	3.3	-8.6	10.5	10.5
11	6	11.0	10.8	10.5	10.5
11	7	1.5	-1.4	10.5	10.5
11	8	0.2	11.4	10.5	10.5
11	9	-12.3	-4.4	10.4	10.5
11	10	12.1	14.6	10.4	10.4
11	11	6.9	-8.7	10.3	10.3
12	0	23.3		10.6	
12	1	2.5	-13.8	10.5	10.5
12	2	8.9	-6.0	10.5	10.5
12	3	-18.1	-0.8	10.5	10.5
12	4	-6.6	-7.7	10.5	10.5
12	5	5.7	0.5	10.4	10.4
12	6	0.7	-11.3	10.5	10.5
12	7	2.9	11.7	10.5	10.5
12	8	0.8	-10.2	10.5	10.5
12	9	3.8	2.5	10.5	10.5
12	10	15.9	17.7	10.4	10.4
12	11	-8.7	-3.6	10.4	10.4
12	12	5.3	-6.1	10.4	10.4
13	0	-5.2		10.5	
13	1	2.2	19.1	10.5	10.5
13	2	-2.9	-3.3	10.5	10.5
13	3	10.0	10.8	10.5	10.5
13	4	4.4	1.1	10.5	10.4
13	5	7.8	3.4	10.4	10.4
13	6	-2.9	3.4	10.4	10.4
13	7	-3.2	-8.4	10.4	10.4
13	8	-2.7	-8.1	10.4	10.4
13	9	0.6	2.9	10.4	10.4
13	10	8.7	0.8	10.4	10.4
13	11	-1.0	-9.3	10.4	10.4
13	12	-3.6	3.1	10.4	10.4
13	13	-21.5	-4.6	10.4	10.4

TABLE 3.1 (Cont'd)

n	m	$\bar{C}_{nm}$	$\bar{S}_{nm}$	$\sigma(\bar{C}_{nm})$	$\sigma(\bar{S}_{nm})$
14	0	4.7		10.5	
14	1	-4.0	8.8	10.5	10.5
14	2	-10.1	5.2	10.5	10.5
14	3	5.8	-3.2	10.5	10.5
14	4	3.1	5.1	10.4	10.4
14	5	3.1	-3.4	10.4	10.4
14	6	1.4	7.2	10.4	10.4
14	7	-10.1	-2.0	10.4	10.4
14	8	0.7	7.4	10.4	10.4
14	9	0.3	1.7	10.4	10.4
14	10	-1.4	-4.0	10.4	10.4
14	11	-18.3	-11.7	10.4	10.4
14	12	4.6	2.4	10.4	10.4
14	13	5.9	1.8	10.4	10.4
14	14	-1.7	10.2	10.4	10.4
15	0	-4.6		10.4	
15	1	-3.3	-12.2	10.4	10.4
15	2	-3.3	4.8	10.4	10.4
15	3	-10.6	-10.6	10.4	10.4
15	4	-2.5	4.7	10.4	10.4
15	5	-3.3	-6.2	10.4	10.4
15	6	-0.2	-1.1	10.4	10.4
15	7	-2.6	-0.5	10.4	10.4
15	8	1.0	0.4	10.4	10.4
15	9	-6.0	12.3	10.4	10.4
15	10	-4.4	-0.3	10.4	10.4
15	11	-8.0	4.0	10.4	10.4
15	12	5.5	7.0	10.4	10.4
15	13	1.9	1.6	10.4	10.4
15	14	-3.6	-6.3	10.4	10.4
15	15	5.0	5.8	10.4	10.4

TABLE 3.1 (Cont'd.)

n	m	$\overline{C}_{nm}$	$\overline{S}_{nm}$	$\sigma(\overline{C}_{nm})$	$\sigma(\overline{S}_{nm})$
16	0	15.1		10.4	
16	1	10.0	1.5	10.4	10.4
16	2	11.0	-5.0	10.4	10.4
16	3	5.8	-6.6	10.4	10.4
16	4	-0.0	-6.4	10.4	10.4
16	5	1.6	0.1	10.4	10.4
16	6	-11.1	-10.8	10.4	10.4
16	7	0.9	5.5	10.4	10.4
16	8	1.5	-7.2	10.4	10.4
16	9	4.9	8.8	10.4	10.4
16	10	0.7	9.6	10.4	10.4
16	11	2.1	-9.2	10.4	10.4
16	12	-10.7	11.0	10.4	10.4
16	13	4.4	10.8	10.4	10.4
16	14	-5.9	-10.6	10.4	10.4
16	15	1.2	18.1	10.4	10.4
16	16	-5.3	-6.7	10.4	10.4

center of mass (C.M.). In terms of rectangular coordinates, the location of the C.F. is

$$\begin{bmatrix} \Delta X_1 \\ \Delta X_2 \\ \Delta X_3 \end{bmatrix} = R_0 \begin{bmatrix} C_{1,1} \\ -S_{1,1} \\ C_{1,0} \end{bmatrix} = \begin{bmatrix} -0.047 \pm 0.061 \\ 1.173 \pm 0.062 \\ -2.208 \pm 0.075 \end{bmatrix} \text{km} \qquad (3.15)$$

or in terms of spherical coordinates

$$\begin{bmatrix} R \\ \theta \\ \varphi \end{bmatrix} = \begin{bmatrix} (2.501 \pm 0.073) & \text{km} \\ (62\overset{\circ}{.}0 \pm 3\overset{\circ}{.}7) & S \\ (272\overset{\circ}{.}3 \pm 3\overset{\circ}{.}0) & W \end{bmatrix}$$

where, as before, the origin is at the C.M. This offset, by definition, implies a departure from spherical symmetry in the internal density distribution.

Love (1911) investigated the problem of gravitational instabilities in an initially homogeneous planet. He found that if the rigidity is sufficiently small, the initial homogeneous configuration will be unstable, and the mass will redistribute itself into a more stable state. Any such displacement of mass can be expressed as a sum of spherical harmonics. The critical rigidity for the onset of instability is a decreasing function of harmonic degree. Thus, as a planet is heated during accretion, or subsequently by radiogenic processes, and the rigidity decreases, the first mode to become unstable is that of degree zero which is characterized by purely radial disturbances. In an extreme case, this may involve radial differentiaion into a core, mantle and crust. The next mode to become unstable is the first degree, which represents hemispherical disturbances. Thus, it is not surprising that all known differentiated terrestrial planets have sizable C.F. offsets. Lingenfelter and Shubert (1973) have discussed large scale thermally driven convection as a possible mechanism for the production of these offsets.

Both the Earth and Mars display a dichotomy in physiography as well as topography. Balmino et al., (1973) have determined the distribution of oceanic and continental regions, as well as the global topography of the Earth. The Earth's C.F. offset is toward ($41^\circ.6$ N, $34^\circ.7$ E), whereas the center of the continental province is (46° N, 27° E). In a coordinate system centered at the latter point, much of the boundary between continental plates and oceanic plates occurs between colatitudes of 90° and 110°. Much of the volcanic and seismic activity of the Earth occurs in this transition zone, with an additional clustering near the pole.

The surface of Mars can also be divided into two broad physiographic regions: a high, heavily cratered southern region and a low, northern region which contains smooth plains as well as the Tharsis and Elysium volcanic provinces. The direction of the C.F. offset (62°S, 272°W) is fairly close ($\gamma \doteq 30^\circ$) to the center of the southern, heavily cratered region (55°S, 335°W) as determined by Mutch and Saunders (1976). In a coordinate system centered at the latter position, the boundary between cratered uplands and smooth lowland plains approximately follows the equator. There is also a concentration of volcanoes in the colatitude band between 120° and 150°, with another grouping near the pole. In this regard, Mars is obviously very similar to the Earth.

Mutch and Saunders (1976) have suggested that this distribution may be due to convective motions under the control of rotational forces. In fact, they argued that the axis of this shifted coordinate system may have coincided with the rotation axis prior to the structural uplift in the Tharsis region. Though global scale convection may well have been responsible for the physiographic and tectonic dichotomy of Mars, and the symmetry axis may have temporarily coincided with the rotation axis, it appears doubtful that there was any causal connection between these events. The argument is as follows:

The influence of rotation on the pattern of convection in the Earth's mantle has received considerable attention (see e.g., Knopoff, 1964; McKenzie, 1968) and is known to be negligible at present. In general the effect of rotation can be estimated in terms of the Taylor number (Roberts, 1968)

$$\mathscr{T} = \left(\frac{2\Omega R_0^2}{\nu}\right)^2 \qquad (3.16)$$

where R_0 is the mean radius (cm), Ω is the rotational angular velocity (sec^{-1}) and ν is the kinematic viscosity (stoke = $cm^2 sec^{-1}$). This is essentially the square of the ratio of Coriolis to viscous forces. For rotational effects to be significant, the Taylor number must exceed unity. For the Earth and Mars, the values are $3.6 \times 10^{27}/\nu^2$ and $2.6 \times 10^{26}/\nu^2$, respectively. Weertman (1970) has estimated the effective viscosity (at a constant strain rate) as a function of depth for the present-day Earth and Mars. In both planets, the viscosity initially decreases with depth, due to increasing temperature, goes through a minimum ($\nu \doteq 2 \times 10^{20}$ stokes) and then increases due to increasing pressure. Even during initial planetary differentiation, the effective viscosity was likely no less than 10^{18} stokes (Tozer, 1972). This minimum viscosity is still great enough to preclude the rotation from influencing the pattern of convection.

Furthermore, in situations where Coriolis forces do dominate convective motion, the induced flow is often highly inclined to the rotation axis (Roberts, 1968). The motion invoked by Mutch and Saunders (1976) is parallel to their purported rotation axis.

We now consider the shape and orientation of the tri-axial figure represented by the second degree harmonics. The principal axes of this figure are:

$$X'_1 = (3394.5 \pm 0.3 \text{ km},\ 0^\circ\!.7 \pm 0^\circ\!.2\text{N},\ 18^\circ\!.5 \pm 0^\circ\!.8\text{W})$$
$$X'_2 = (3399.2 \pm 0.3 \text{ km},\ 2^\circ\!.0 \pm 0^\circ\!.2\text{S},\ 108^\circ\!.4 \pm 0^\circ\!.8\text{W}) \qquad (3.17)$$
$$X'_3 = (3376.1 \pm 0.4 \text{ km},\ 87^\circ\!.9 \pm 0^\circ\!.2\text{N},\ 128^\circ\!.8 \pm 6^\circ\!.3\text{W})$$

These differ somewhat in orientation from the principal inertial axes, as determined from the second degree gravity harmonics (Sjogren et al., 1975):

$$X''_1 = (0^\circ\!.0\text{N},\ 15^\circ\!.7 \pm 1^\circ\!.0\text{W})$$
$$X''_2 = (0^\circ\!.0\text{N},\ 105^\circ\!.7 \pm 1^\circ\!.0\text{W}) \qquad (3.18)$$
$$X''_3 = (90^\circ\!.0\text{N}).$$

This misalignment, if confirmed by subsequent analysis, implies some lateral density variation. If such variation occurs as undulations on the crust-mantle interface, the principal axes of the tri-axial mantle must be skewed in the opposite direction. We shall pursue this idea further in a subsequent section. First, we will consider the problem of Mars' excessive oblateness.

When subjected to a disturbing potential characterized by harmonic coefficients Φ_{nm}, an elastic sphere suffers a surface distortion

$$H'_{nm} = h_n \Phi_{nm} \qquad (3.19)$$

and this redistribution of mass gives rise to a further disturbance of the potential

$$G'_{nm} = k_n \Phi_{nm} \quad . \qquad (3.20)$$

The Love numbers h_n and k_n, for a homogeneous, incompressible elastic sphere are given by (Munk and MacDonald, 1960)

$$k_n = \frac{3}{2(n-1)} \left(\frac{1}{1 + N(n)\mu/P_c} \right)$$

$$h_n = \left(\frac{2n+1}{3} \right) k_n \tag{3.21}$$

where

$$N(n) = \frac{2(n+1)^2 + 1}{2n} \quad ,$$

$$P_c = \frac{3GM^2}{8\pi R_o^4}$$

is the hydrostatic pressure at the center of the sphere and μ is the elastic rigidity. See Appendix E for a more complete discussion of these matters.

The disturbing potential induced by rotation is, in terms of un-normalized harmonics,

$$\Phi_{2,0}(\Omega) = \frac{-\Omega^2 R_0^{\,3}}{3GM} = -\frac{m}{3} \tag{3.22}$$

where Ω is again the rotational angular velocity and m is the ratio of centrifugal to gravitational accelerations on the equator. We shall use the usual geodetic terminology and denote by "gravitation" the attraction due to the mass of a planet and by "gravity" the combined effect of gravitation and rotation. Thus the rotational contributions to the surface topography and to the shape of the gravity equipotential are

$$H'_{2,0} = \frac{5}{2}\left(\frac{1}{1+19\mu/4P_c}\right)\left[-\frac{\Omega^2 R_0^{\,3}}{3GM}\right] = -\frac{2f_g}{3}$$

and (3.23)

$$\Phi_{2,0}(\Omega) + G'_{2,0} = \left[1 + \frac{3}{2}\left(\frac{1}{1+19\mu/4P_d}\right)\right]\left[-\frac{\Omega^2 R_0^{\,3}}{3GM}\right] = -\frac{2f_d}{3}$$

respectively. Here f_g and f_d are the geometric and dynamic flattenings. They are defined as the fractional difference between equatorial and polar radii of the actual topography and the gravity equipotential surfaces, respectively.

If the rotation of Mars has been essentially uniform for a period longer than its second degree visco-elastic relaxation time τ'_2, where (Darwin, 1879)

$$\tau'_n = \left[\frac{N(n)}{P_c} + \frac{1}{\mu}\right]\eta$$

and $\eta = \rho\upsilon$ is the dynamic viscosity (poise = g cm^{-1} sec^{-1}), we should expect the topography to conform to an equipotential surface. Since

$\Phi_{2,0}(\Omega) = -1.523 \times 10^{-3}$, we would expect for a homogeneous, incompressible fluid Mars:

$$\begin{aligned} H'_{2,0} &= -3.808 \times 10^{-3} \\ G'_{2,0} &= -2.285 \times 10^{-3} \quad . \end{aligned} \tag{3.24}$$

However, we find

$$H_{2,0} = (-4.078 \pm 0.027) \times 10^{-3}$$

and Sjogren et al. (1975) have found

$$G_{2,0} = (-1.958 \pm 0.021) \times 10^{-3} \quad .$$

Thus the topographic oblateness is too great, and the gravitational oblateness is too small for Mars to be homogeneous and hydrostatic.

The radial variation of density inside Mars is easily incorporated into the hydrostatic theory. In the traditional notation, the flattening of a hydrostatic configuration is (Darwin, 1900)

$$f_g = f_d = \frac{5m/2}{1 + \left[\frac{5}{2}\left(1 - \frac{3C}{2MR_0{}^2}\right)\right]^2} \tag{3.25}$$

where C is the polar moment of inertia. The homogeneous case we previously considered corresponds to $C = 2MR_0^2/5$ and therefore

$$f_g = f_d = \frac{5m}{4} \quad . \tag{3.26}$$

Since the rate of precession of Mars' rotation axis is not known, all present estimates of the moment of inertia are obtained from the dynamic flattening according to the hydrostatic theory. The discrepancy between dynamic and geometric flattening makes this approach rather suspect. This problem has a long and interesting history. We will digress now to a brief discussion of the principal points.

The earliest determination of the dynamic flattening of Mars appears to be that of Struve (1895), who analyzed the precession of the orbits of Phobos and Deimos. His result was $f_d = 5.210 \times 10^{-3}$ ($G_{2,0} = -1.951 \times 10^{-3}$). Subsequent analyses (Table 3.2) of the motions of both natural and artificial satellites have essentially confirmed this result. The situation is very different regarding the geometric flattening (Table 3.3). Though the early estimates varied widely, they tended to be large. Darwin (1877) pointed out that the best estimates available to him exceeded even the flattening predicted for a homogeneous fluid planet. A summary of the best Earth-based telescopic determinations is given by de Vaucouleurs (1964). The mean of 32 polar radius determinations spanning the period 1890-1958 yields 3378 ± 3.6 km. The mean of 68 measurements of the equatorial radius from the period 1879-1958 is equivalent to 3414.2 ± 3.6 km. The corresponding flattening is $f_g = (10.6 \pm 0.5)$ 10^{-3}. It is interesting that these early polar radius estimates essentially agree with present estimates whereas the equatorial radius was consistently overestimated. It has been suggested (de Vaucouleurs, 1964) that the excess apparent equatorial radius

TABLE 3.2

Mars Dynamic Flattening

Source		$f_d \times 10^3$	$G_{2,0} \times 10^3$
Struve	(1895)	5.210	-1.951
Woolard	(1944)	5.215	-1.955
Wilkins	(1967)	5.208 ± 0.030	-1.950 ± 0.020
Sinclair	(1972)	5.232 ± 0.005	-1.966 ± 0.003
Lorell et al.	(1973)	5.223 ± 0.015	-1.960 ± 0.010
Born	(1974)	5.223 ± 0.027	-1.960 ± 0.018
Sjogren et al.	(1975)	5.220 ± 0.032	-1.958 ± 0.021
Reasenberg et al.	(1975)	5.216	-1.955

TABLE 3.3

Mars Geometric Flattening

Source		$f_g \times 10^3$	$H_{2,0} \times 10^3$
Schur	(1896)	21.5 ± 1.7	-14.3 ± 1.1
Hartwig	(1899)	8.6 ± 1.5	-5.7 ± 1.0
Trumpler	(1924)	10.4 ± 0.6	-7.1 ± 0.4
Camichel	(1954)	12.0 ± 4.7	-8.0 ± 3.1
Dollfus	(1972)	7.9 ± 1.5	-5.3 ± 1.0
Cain et al.	(1972)	5.39 ± 0.15	-3.59 ± 0.10
Christensen	(1975)	5.90	-3.93
Present work		6.117 ± 0.041	-4.078 ± 0.027

may be an atmospheric effect. In any event, it gave rise to a number of interesting theories which attempt to explain an actual excess oblateness. Darwin (1877) considered, but discarded, the idea that Mars is in hydrostatic equilibrium, but has a density which decreases with depth. Urey (1950) hypothesized an equatorial belt of isostatically supported mountains. Lamar (1962) proposed instead that the elevation of the surface increases gradually from the poles to the equator, and that this increase is isostatically compensated by variation in the crustal thickness. Runcorn (1967) suggested that second order convection cells might produce the excess flattening. This unexplained oblateness was one of the greatest Martian geophysical problems prior to spacecraft exploration (Loomis, 1965).

More recent radar (Pettengill _et al_., 1969; Downs _et al_., 1975) and spacecraft (Cain _et al_., 1972; Fjeldbo _et al_., 1972) observations have confirmed a smaller mean equatorial radius, and the problem of excess topographic oblateness has fallen into relative obscurity. The prime geophysical problem has become the support, isostatic or otherwise, of the Tharsis ridge and associated volcanic constructs (Carr, 1973). Phillips and Saunders (1975) investigated the isostatic support of three low degree harmonics ($H_{2,2}$, $H_{3,2}$ and $H_{3,3}$) which contribute significantly to the Tharsis uplift. They conclude that the Tharsis plateau and the adjacent Chryse and Amazonis lowlands are geologically young and only partially compensated, whereas the isostatic support of other, older areas is essentially complete. Recently, Reasenberg (1977) has attempted to estimate the influence of the Tharsis region on the topographic and gravitational oblateness. His basic premise is that, prior to the uplift of Tharsis, Mars was in hydrostatic equilibrium ($f_g = f_d$). By excising Tharsis and the adjacent lowlands, he obtains an estimate of the equilibrium gravitational oblateness $G_{2,0}(E) = (-1.829 \pm 0.012) \times 10^{-3} [f_d = (5.027 \pm 0.018) \times 10^{-3}]$. He then argues (but not convincingly) that the minor (rather than the mean) equatorial radius should be used in computing the topographic flattening of the pre-Tharsis Mars. Thus, based on Christensen's (1975) topography model, he finds $H_{2,0}(E) = 3.418 \times 10^{-3}$ $[f_g = 5.127 \times 10^{-3}]$. When calculated this way, the topographic and dynamic flattenings are nearly equal. If this result is correct, it is profound not only in the historical context of showing that the solution to the older excess oblateness problem is to be found in studying Tharsis, but also because this hydrostatic flattening estimate gives a substantially reduced estimate for the moment of inertia of Mars. Previous estimates of $G_{2,0} = (-1.966 \pm 0.003) \times 10^{-3}$ (Sinclair, 1972) yield $C/MR_0^2 = 0.3768 \pm 0.0003$, whereas Reasenberg's estimate yields $C/MR_0^2 = 0.3660 \pm 0.0010$. This has important implications for the internal structure of Mars. Most internal models (Jeffreys, 1937; Bullen, 1949; MacDonald, 1962; Anderson, 1972; Johnston et al., 1974) have found a high density mantle and a small core. This new estimate for the moment of inertia would imply a lower mantle density and a larger core. This would appear to be consistent with a more extensively differentiated interior than has previously been supposed.

Another effect which could contribute to the discrepancy between the geometric and dynamic flattenings is a possible secular decrease in the rotation rate of Mars. Hartmann et al. (1975) have discussed possible rotation histories for Mars and suggest on dynamical grounds that it rotated more rapidly in the past. Binder and McCarthy (1972) have suggested a despinning of Mars based on tectonic arguments.

The influx of debris from the asteroid belt could have slowed Mars' rotation at a rate which could be significant over geologic time. In order to account for the entire excess flattening as a fossil bulge left over from a period when Mars rotated more rapidly, the ancient rotation period would be 82050 sec($22^h\ 44^m\ 30^s$) as opposed to the present period of 88642.67 sec ($24^h\ 37^m\ 22\overset{s}{.}67$). The slowing of Mars to its present rotation rate by accretion of asteroidal debris would have involved the accumulation of a debris mantle some tens of kilometers thick. This would presumably tend to mask any excess oblateness due to former spin states. However, some degree of despinning by this or other mechanisms may have occurred.

2. High Degree Harmonics

In common with the Earth (Balmino et al., 1973) and the Moon (Bills and Ferrari, 1977a), the topography of Mars is dominated by the low degree harmonics. Furthermore, the rate at which the total topographic variance per degree decreases with increasing degree is similar for all three planets. Dimensionless degree variances $V(H^*;n)$, of equipotentially referenced Martian topography and the associated error variances W(H;n) are displayed in Figure 3.2. These variances are given by:

$$V(H^*;n) = \sum_{m=0}^{n} H_{nm}^{*T} H_{nm}^{*}$$

$$W(H;n) = \sum_{m=0}^{n} \sigma^T(H_{nm})\,\sigma(H_{nm}) \tag{3.27}$$

where $H^*_{nm} = H_{nm} - G_{nm}$. We note that the topographic variances decrease approximately as

$$V(H^*;n) \doteq \frac{V(H^*;0)}{(n)(n+1)} \quad .$$

We further discuss this relationship and its implications in the next chapter. We also note that, in the case of uniformly accurate data, i.e., $\sigma[R(\theta,\varphi)] = \sigma_o$, the degree error variances are (Heiskanen and Moritz, 1967):

$$W(H;n) = \frac{2n+1}{4\pi}\left(\frac{\sigma_o}{R_o}\right)^2 \tag{3.28}$$

The small departures of our calculated error variances from this simple form are due to the irregular data distribution.

In order to compare our results H_{nm}, with those of Christensen (1975) H'_{nm}, we have calculated the degree correlation coefficients (Kaula, 1967)

$$\beta_n(H,H') = \frac{V(H,H';n)}{[V(H;n)\;V(H';n)]^{1/2}} \quad . \tag{3.29}$$

FIGURE 3.2 - Martian topographic variance spectrum. The actual dimensionless variances, $V(H;n)$, of the equipotentially referenced topography follow quite well the relationship $V(H;n) = V(H;0)/(n)(n+1)$. The error variances, $W(H;n)$, are approximated by $4\pi\ W(H;n) = (2n+1)(\sigma_0/R_0)^2$.

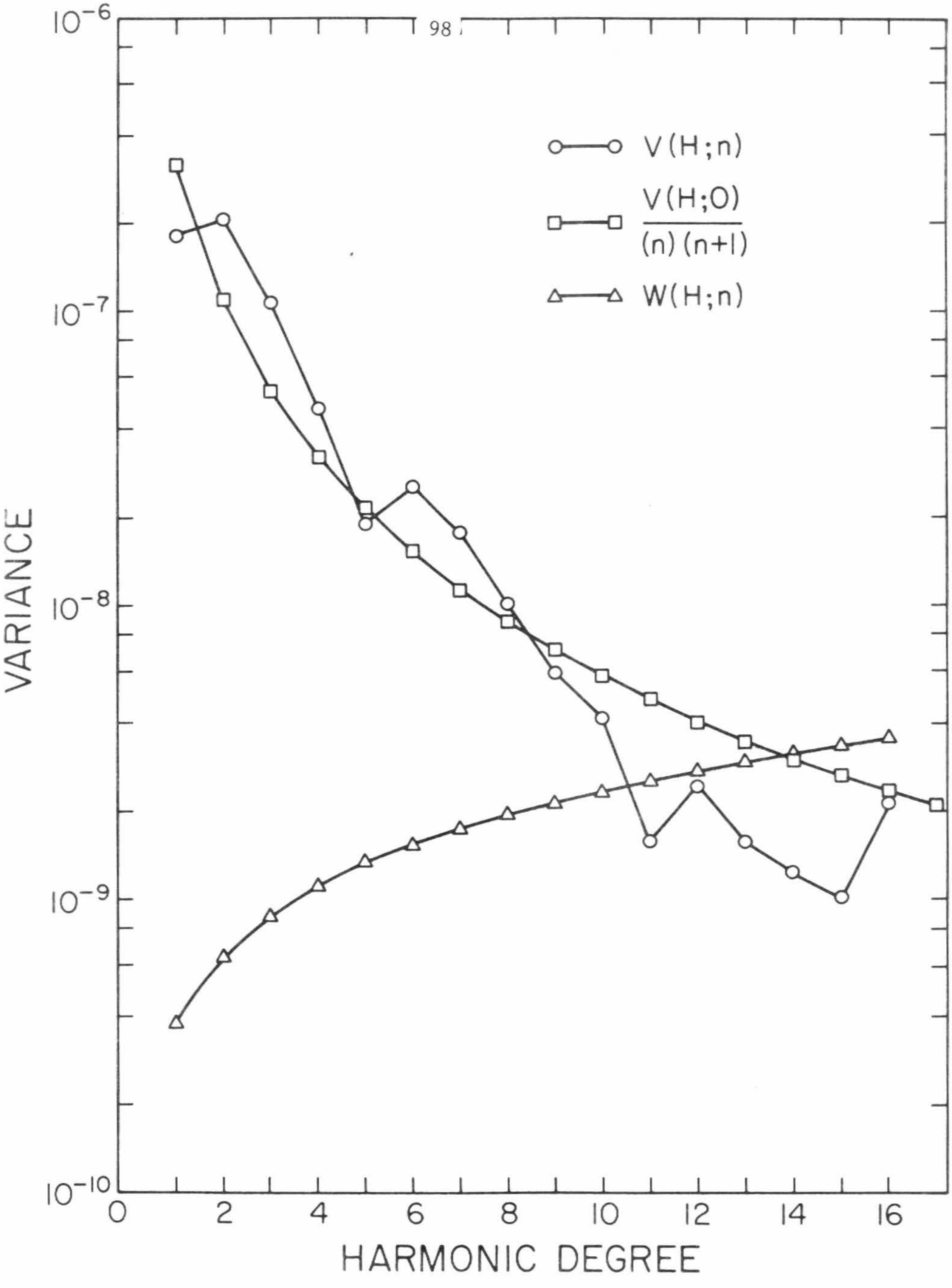
10^{-6}
10^{-7}
10^{-8}
10^{-9}
10^{-10}
VARIANCE
0
2
4
6
8
10
12
14
16
HARMONIC DEGREE
V(H;n)
$\frac{V(H;0)}{(n)(n+1)}$
W(H;n)

In Figure 3.3, we present these correlation coefficients and the critical values for various confidence levels. The correlation is seen to be very good. In computing the correlation, we have corrected two typographical errors in Christensen's original paper. The correct values for $C_{4,1}$ and $C_{4,2}$ are ten times the values listed (E.J. Christensen, personal communication, 1977).

Figure 3.4 is a map of Martian topography derived from our harmonic model. The map elevations are referenced to the 6.1 mb equipressure surface. This surface will be referred to as the reference equipotential or areoid. It is approximated by

$$R'(\theta,\varphi) = R'_o \left[1 + \frac{m}{2}\cos^2(\theta) + \sum_{n=2}^{4} \sum_{m=0}^{n} G^T_{nm} \Lambda_{nm}(\theta,\varphi) \right] \qquad (3.30)$$

where $R'_o = 3382.946$ km (Wu, 1975) and G_{nm} are the coefficients of Jordan and Lorell's (1975) gravity model. The rotational contribution can be expressed as an increase in the reference oblateness, $G'_{2,0} = G_{2,0} - m/3$, and an increase in the reference mean radius, $R''_o = R'_o(1 + m/3) = 3388.099$ km. The heights are thus $H(\theta,\varphi) = R(\theta,\varphi) - R'(\theta,\varphi)$, where R and R′ are given by equations (3.2) and (3.30) respectively.

As expected, we find a considerable increase in resolution over Christensen's (1975) eighth degree model. In fact, our model resolves most major features within areas of adequate data coverage. This was a major objective in the construction of the model and permits comparison with equivalent resolution gravity models for the purpose

FIGURE 3.3 - Correlation coefficients: topography with topography. Comparison of present model with Christensen's (1975) model. Confidence levels indicate probability of specified correlation between Gaussian random variables.

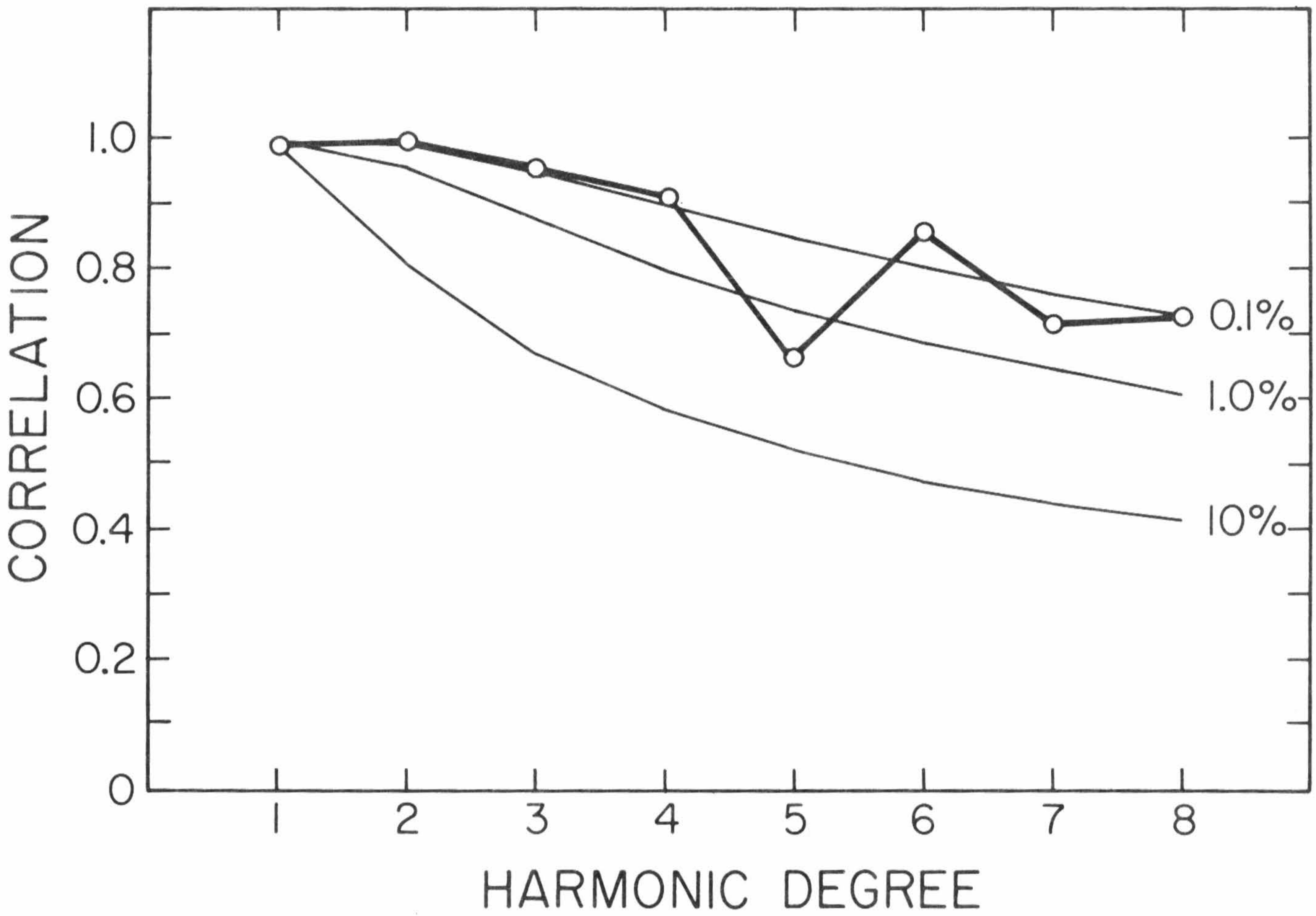
CORRELATION
1.0
0.8
0.6
0.4
0.2
0
HARMONIC DEGREE
1
2
3
4
5
6
7
8
0.1%
1.0%
10%

FIGURE 3.4a - Martian topography. Mid-latitudes. Sixteenth degree model. Elevations relative to the 6.1 mb areoid. Main contour interval is 2 km (solid line). Selected 1 km contours indicated (dashed line).

FIGURE 3.4b - Martian topography. Polar regions. See caption of Figure 3.4a.

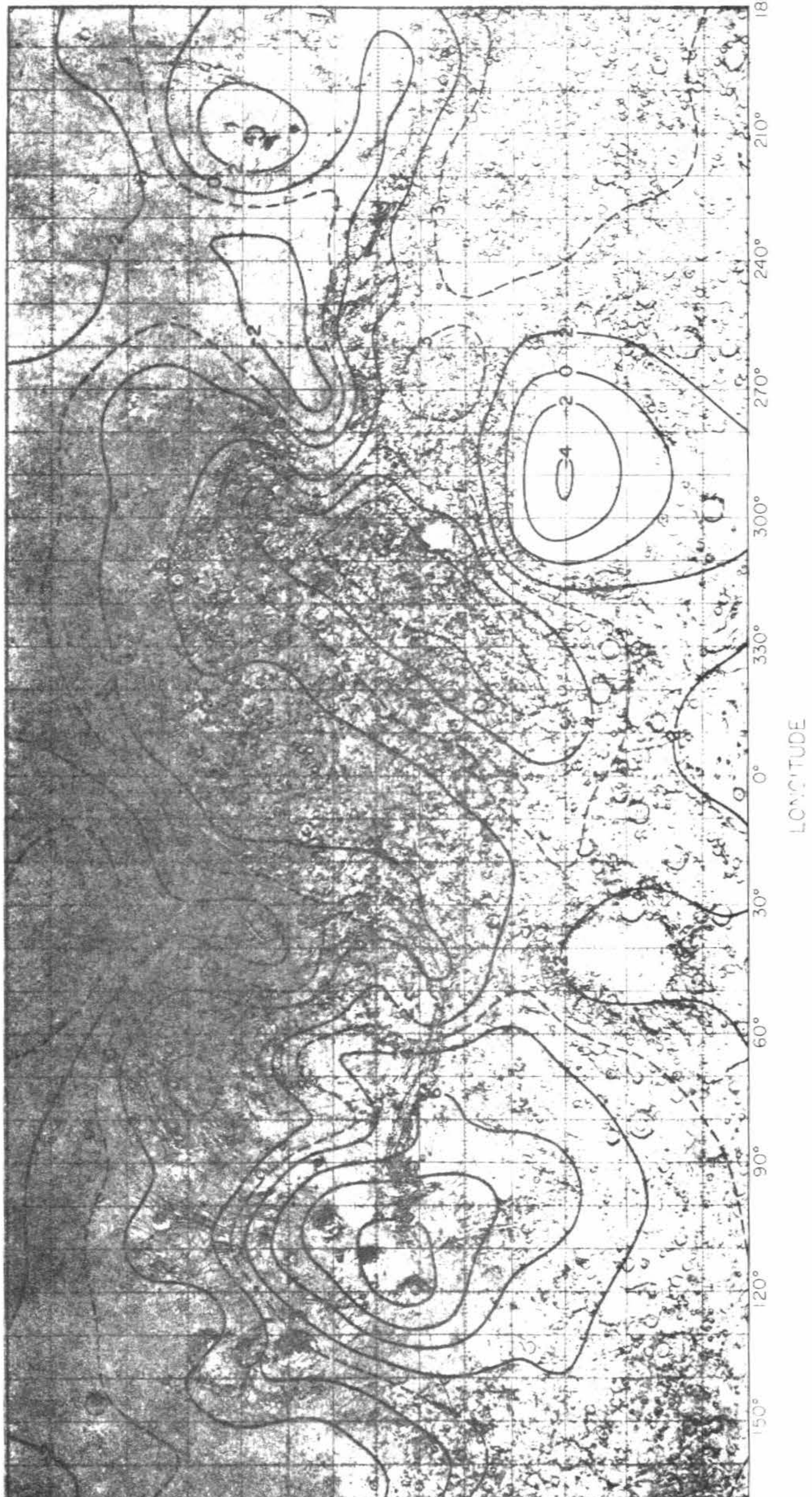
LONGITUDE
LATITUDE
180°
210°
240°
270°
300°
330°
0°
30°
60°
90°
120°
150°
180°
60°
30°
0°
-30°
-60°
-4
-2
0
2
3

NORTH POLAR REGION

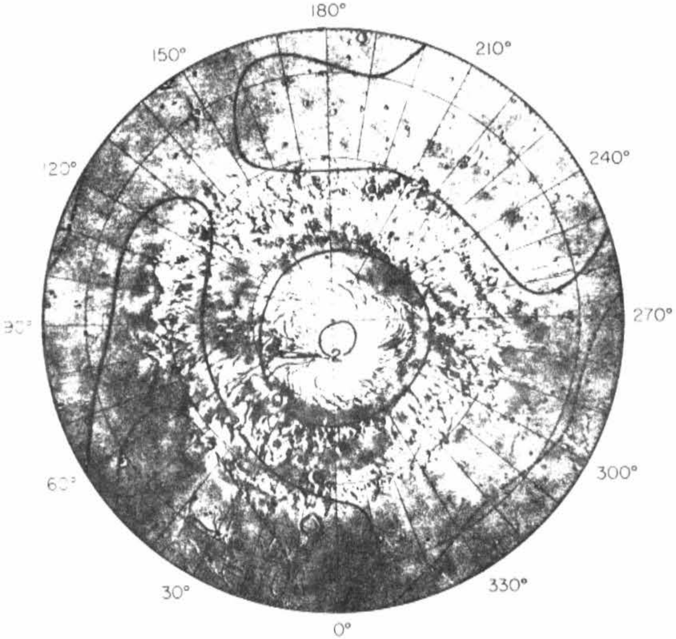

SOUTH POLAR REGION

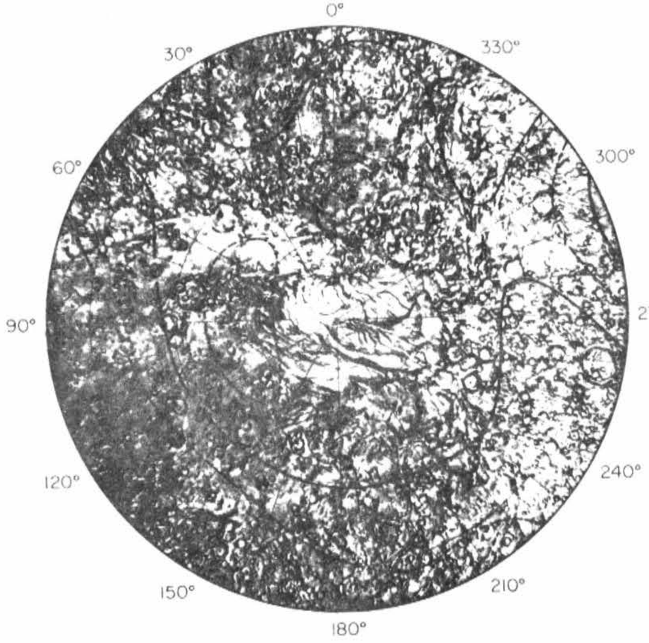

of determining the internal density. We will now attempt to do just that.

As a first step, we wish to know what correlation, if any, exists between the topography and gravity of Mars. For that purpose, we have calculated degree correlation coefficients $\beta_n(H,G)$ for $n \leq 10$ of our topography model with the gravity models of Sjogren et al. (1975) and Laing (1977, private communication). These are presented in Figure 3.5. It is seen that the low degree correlations are significant. Thus, the low degree gravity harmonics appear to be primarily due to surface height variations and only secondarily due to density anomalies. The decrease in correlation of the higher degree harmonics is presumably due to the relatively poor determination of the relevant coefficients, but may reflect an actual property of the planet.

The observed gravitational anomalies may be ascribed to contributions from both lateral density variations and surface topography. The topography of a planet with crustal density ρ_o and mean density $\bar{\rho}$ gives rise to gravitational potential perturbations (MacRobert, 1967):

$$\Delta\Phi(R,\theta,\varphi) = \frac{GM}{R_o} \sum_{n=1}^{\infty} \sum_{m=0}^{n} \left[\frac{R_o}{R}\right]^{n+1} \Delta G^T_{nm} \Lambda_{nm}(\theta,\varphi) \qquad (3.31)$$

where

$$\left(\frac{2n+1}{3}\right) \bar{\rho}\, \Delta G_{nm} = \rho_o\, H_{nm} \quad .$$

The difference between the observed gravity and the topographic

FIGURE 3.5 - Correlation coefficients: topography with gravity. Comparison of present topography model with gravity models of Sjogren et al. (1975) and P.A. Laing (1977, personal communication). The low degree harmonics are significantly correlated.

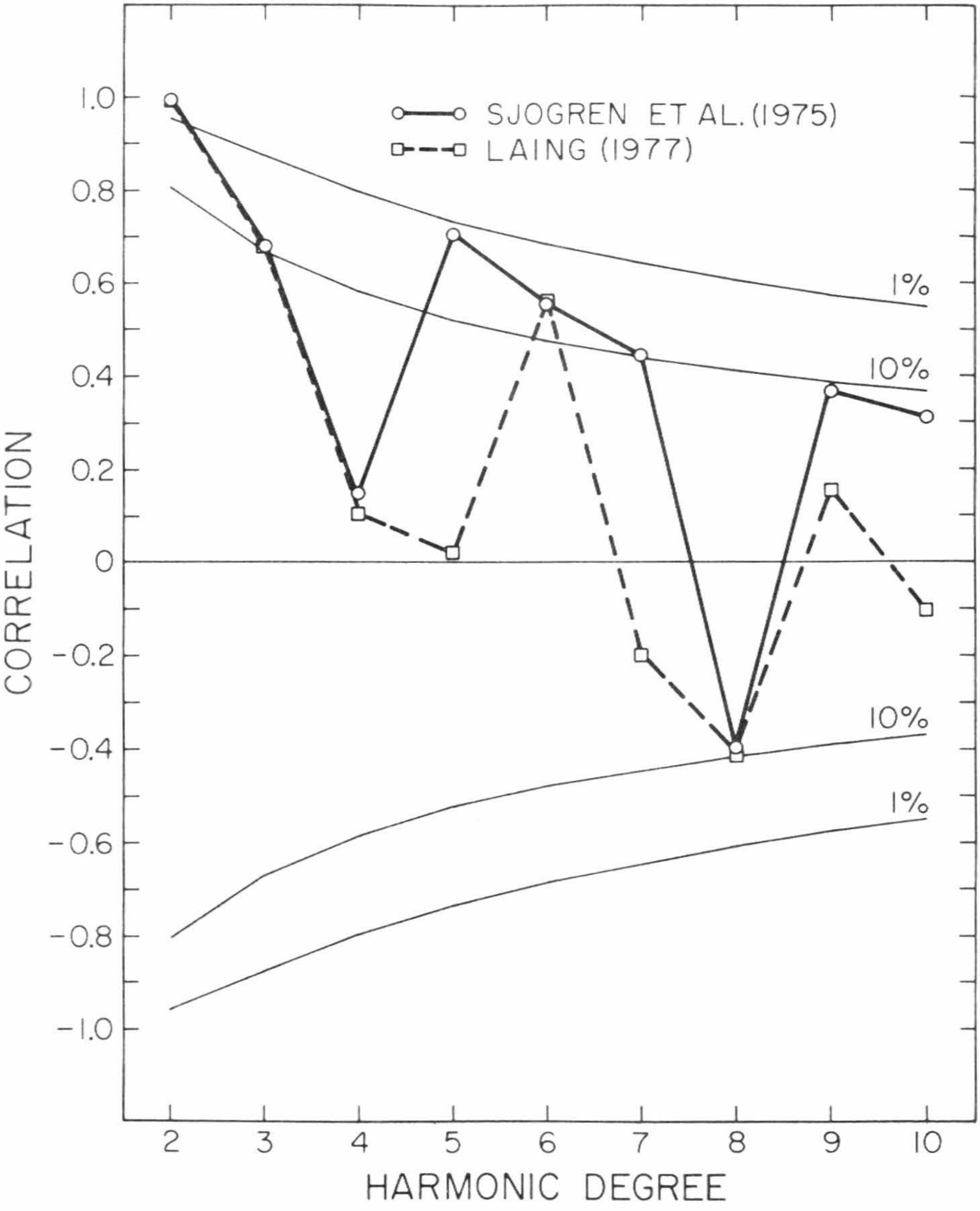
SJOGREN ET AL. (1975)
LAING (1977)
CORRELATION
1.0
0.8
0.6
0.4
0.2
0
-0.2
-0.4
-0.6
-0.8
-1.0
1%
10%
10%
1%
2
3
4
5
6
7
8
9
10
HARMONIC DEGREE

correction, known as the Bouguer anomaly, is thus a measure of the extent of lateral density variation.

Figure 3.6 is a map of the Martian Bouguer anomaly evaluated on the areoid. This is calculated as the vertical component of the gradient of the Bouger anomalous potential on the reference surface (Heiskanen and Moritz, 1967)

$$\Delta g_B(R,\theta,\varphi) = \frac{GM}{R_o^2} \sum_{n=1}^{10} \sum_{m=0}^{n} \left[\frac{R_o}{R}\right]^n (n - 1)\ B_{nm}^T \Lambda_{nm}(\theta,\varphi) \qquad (3.32)$$

where

$$B_{nm} = G_{nm} - \Delta G_{nm}$$

and we have assumed a surface density $\rho_o = 2.9$ gm cm^{-3}. The series is truncated to tenth degree because of limitations of the gravity model (Sjogren et al., 1975).

As was anticipated in our discussion of the correlation coefficients, the low degree harmonics of the gravitational field are produced primarily by surface height variations, and only secondarily by lateral density variations. However, it is interesting to note the large negative anomalies associated with Phlegra Montes (35°N, 200°W), near the Elysium volcanics, and with Tharsis Montes (5°N, 110°W) another high volcanic province. This latter feature is flanked by prominent positive anomalies in Amazonis Planitia (5°N, 160°W) and Chryse Planitia (20°N, 40°W). Other significant positive anomalies are in the low regions of Hellas Planitia (35°S, 290°W)

FIGURE 3.6 - Martian Bouguer gravity anomaly. Tenth degree model. Evaluated on areoid. Contour interval is 100 mGal = 0.1 cm sec^{-2}. Free-air gravity from Sjogren _et al_. (1975).

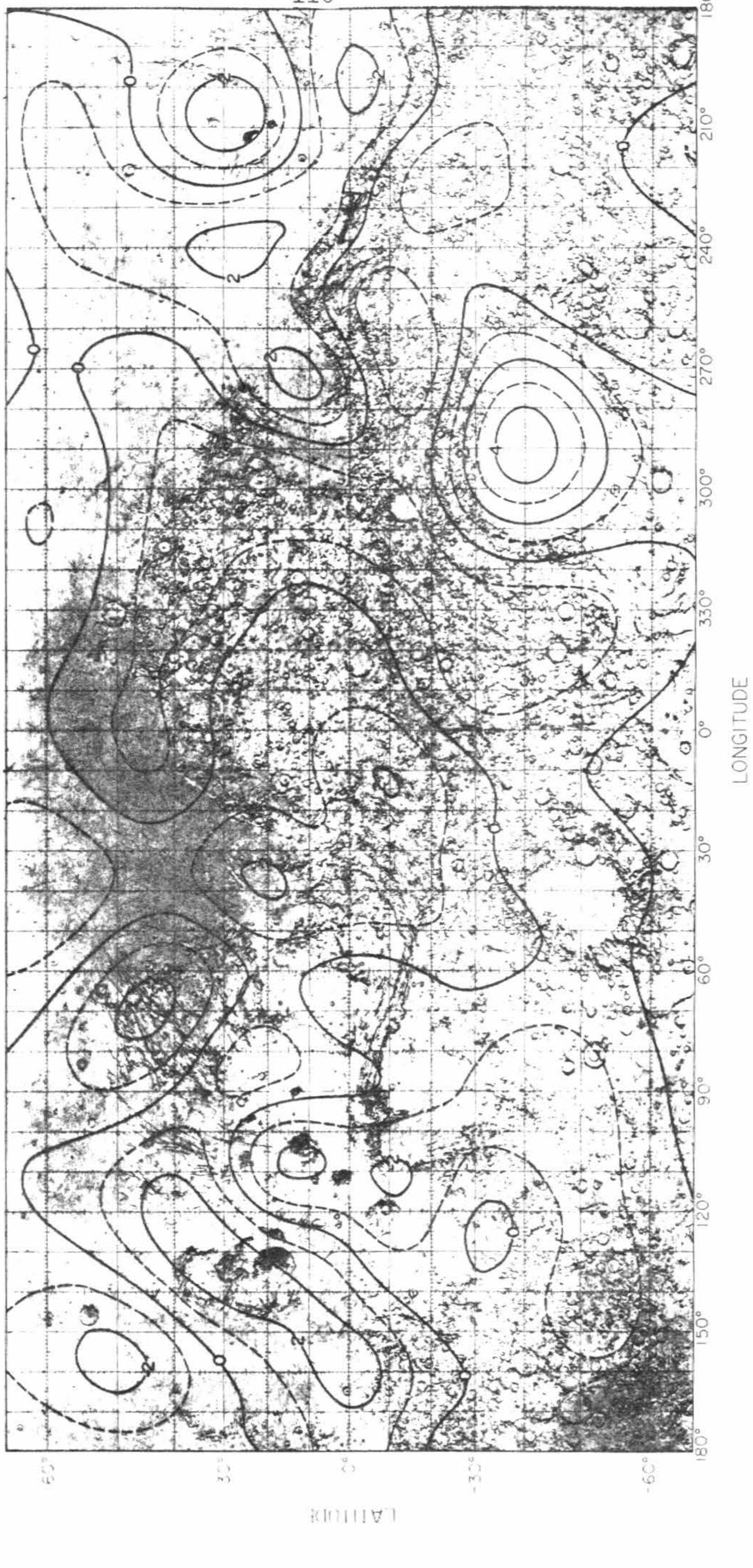
LONGITUDE
180°
210°
240°
270°
300°
330°
0°
30°
60°
90°
120°
150°
180°
LATITUDE
60°
30°
0°
-30°
-60°
0
2
4

and Isidis Planitia (15°N, 270°W). Most of the prominent negative anomalies are associated with topographic highs, and conversely. This implies some degree of isostatic compensation. To ascertain the degree of compensation, we need to know how the crustal thickness varies with elevation and location on the surface of Mars.

Recent seismic results (Anderson et al., 1977), although tentative, can be interpreted as indicative of a crustal thickness of 15 km in the vicinity of the second Viking landing site (47.°89N, 225.°86W). We can estimate the variation of crustal thickness implied by the Bouguer anomaly map on the assumption that all lateral density variations occur as undulations on the crust-mantle interface (Khan, 1977; Bills and Ferrari, 1977b). These undulations are determined from the relation

$$\left(\frac{2n+1}{3}\right)\bar{\rho}G_{nm} = \rho_o H_{nm}^{(o)} + \Delta\rho\, \xi^{n+3} H_{nm}^{(1)} \qquad (3.33)$$

where $H_{nm}^{(o)}$ and $H_{nm}^{(1)}$ define the shape of the surface topography and crust-mantle interface, respectively. The mean normalized radius of the interface is $\xi = R/R_o$. The crustal density and density contrast across the interface are ρ_o and $\Delta\rho$, respectively. These latter three parameters are unknown.

We have examined a number of cases and will discuss three of them in particular. For this discussion, we have assumed an upper mantle density of $\rho_o + \Delta\rho = 3.5$ gm cm^{-3} (Anderson, 1972). We then consider the three cases $\rho_o = 2.7, 2.8$ and 2.9 gm cm^{-3}, which span the range of probable crustal densities. The mean crustal thickness was varied in each case until a 15 km thickness was obtained at the Viking landing site. The values obtained are 34, 36 and 40 km respectively. The resulting map for the high crustal density case ($\rho_o = 2.9$ gm cm^{-3}) is shown in Figure 3.7. The maps corresponding to the other cases are qualitatively very similar. However, when the crustal density is low and the crust-mantle density contrast is accordingly high, smaller amplitude undulations on the crust-mantle interface are required to produce the observed Bouguer anomalies. For example, the maximum crustal thickness was obtained in all cases under Tharsis. These maxima were 61, 67, and 77 km, respectively. Likewise, all three models exhibited a minimum crustal thickness under Hellas (10, 9 and 8 km).

Because the Viking crustal thickness estimate (Anderson _et al._, 1977) is based on a single anomalous event that cannot be proven to be of internal origin and may, in fact, be a wind event, we have also considered models based on the assumption of zero crustal thickness in Hellas. These yield minimum mean crustal thickness estimates for a given density regime. For the densities previously considered, $\rho_o = 2.7$, 2.8 and 2.9 gm cm^{-3}, the mean crustal thickness estimates are 23, 24 and 32 km, respectively. The corresponding crustal thickness estimates under Tharsis are 50, 58 and 68 km, and at the Viking landing site 5, 6 and 7 km, respectively.

None of these models is completely isostatic. However, it was found that the mean squared super-isostatic stress at the crust

FIGURE 3.7 - Martian crustal thickness. Tenth degree model. Gravity from Sjogren et al. (1975). Assumed crustal density is 2.9 gm cm^{-3}, crust-mantle density contrast is 0.6 gm cm^{-3} and mean crustal thickness is 40 km. Second Viking landing site (47°.89N, 225°.86W) is indicated by dot. Crustal thickness at that location tentatively estimated from Viking seismic data (Anderson et al., 1977).

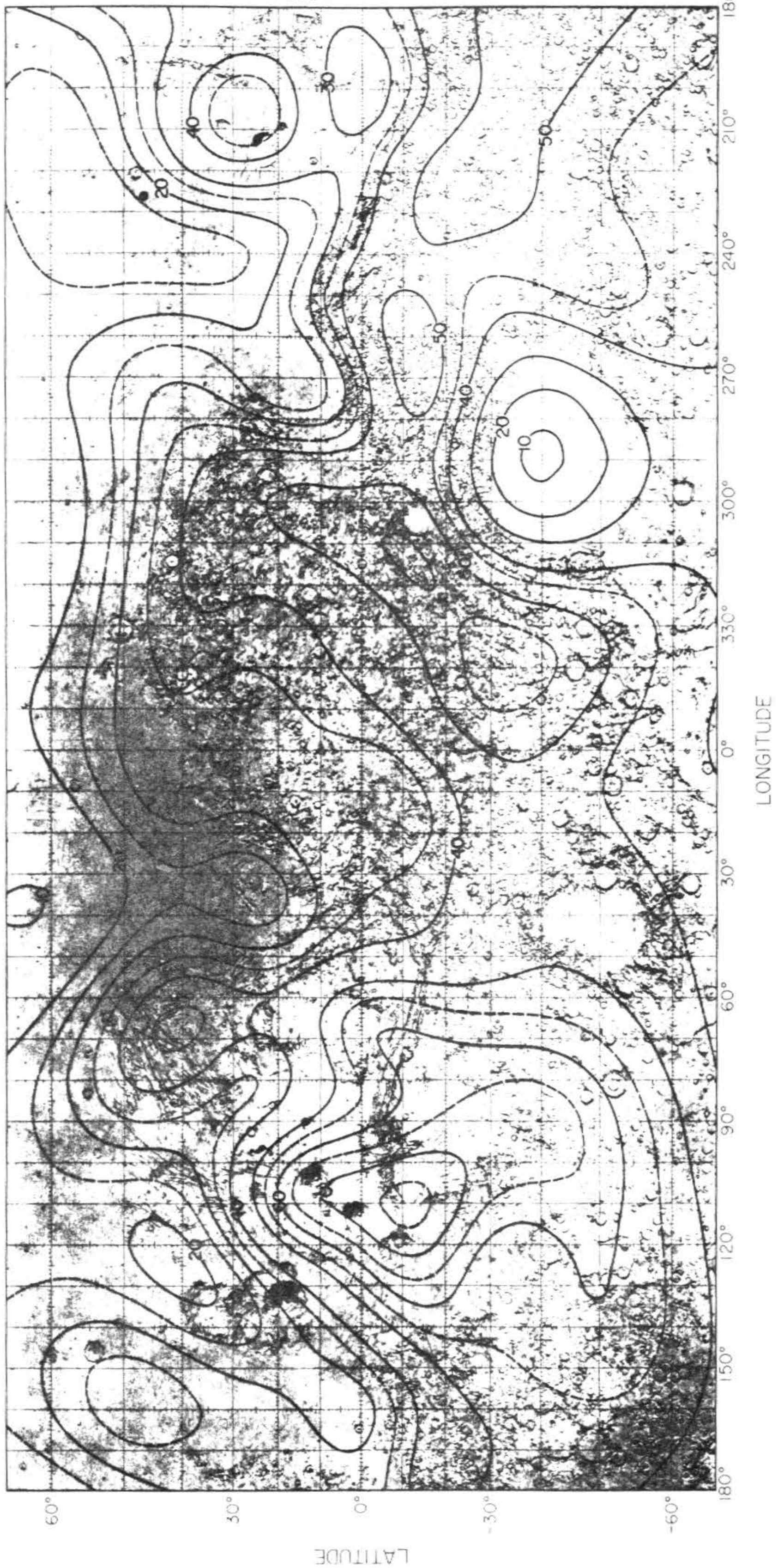
LATITUDE
60°
30°
0°
-30°
-60°
LONGITUDE
180°
210°
240°
270°
300°
330°
0°
30°
60°
90°
120°
150°
180°
10
20
30
40
50
60

mantle interface was least for models with low crustal density, thin crust and high density contrast across the interface. The range of models we considered indicate that Tharsis is 60-65% compensated, whereas, Hellas is 95-105% compensated. A complete discussion of Martian isostasy is beyond the scope of this paper.

REFERENCES

Anderson, D.L. (1972). Internal constitution of Mars. J. Geophys. Res. **77**, 789-795.

Anderson, D.L., Miller, W.F., Latham, G.V., Nakamura, Y., Duennebier, F.K., Lazarewicz, A., Toksöz, M.N., Dainty, A., Kovach, R.L., and Knight, T.C.D. (1977). Seismology on Mars. Submitted to J. Geophys. Res.

Balmino, G., Lambeck, K., and Kaula, W.M. (1973). A spherical harmonic analysis of the Earth's topography. J. Geophys. Res. **78**, 478-481.

Bills, B.G., and Ferrari, A.J. (1977a). A harmonic analysis of lunar topography. Icarus, **31**, 244-259.

Bills, B.G., and Ferrari, A.J. (1977b). A lunar density model consistent with topographic, gravitational, librational and seismic data. J. Geophys. Res. **82**, 1306-1314.

Binder, A.B., and McCarthy, D.W. (1972). Mars: The lineament systems. Science **176**, 279-281.

Born, G.H. (1974). Mars physical parameters as determined from Mariner 9 observations of the natural satellites and doppler tracking. J. Geophys. Res. **79**, 4837-4844.

Bullen, K.E. (1949). On the constitution of Mars. M. Not. Roy. Astr. Soc. **109**, 688-692.

Cain, D.L., Kliore, A.J., Seidel, B.L., and Sykes, M.J. (1972). The shape of Mars from the Mariner 9 occultations. Icarus **17**, 517-524.

Camichel, H. (1954). Determination photographique du pole de Mars, de son diamètre et des coordonnées areographiques. *Bull. Astron.* **18**, 83-191.

Carlson, A.E., and Helmsen, M. (1969). Validity of topography represented by truncated series of surface harmonics. *Icarus* **10**, 57-65.

Carr, M.H. (1973). Volcanism on Mars. *J. Geophys. Res.* **78**, 4049-4062.

Christensen, E.J. (1975). Martian topography derived from occultation, radar, spectral and optical measurements. *J. Geophys. Res.* **80**, 2909-2913.

Darwin, G.H. (1877). On an oversight in the mechanique celeste and on the internal densities of the planets. *M. Not. Roy. Astr. Soc.* **37**, 77-89.

Darwin, G.H. (1879). On the bodily tides of viscous and semi-elastic spheroids. *Phil. Trans. Roy. Soc.* **170**, 1-35.

Darwin, G.H. (1900). The theory of the figure of the Earth carried to the second order of small quantities. *M. Not. Roy. Astr. Soc.* **60**, 82-124.

Dollfus, A. (1972). New optical measurements of planetary diameters - Part IV: Mars. *Icarus* **17**, 525-539.

Downs, G.S., Reichley, P.E., and Green, R.P. (1975). Radar measurements of Martian topography and surface properties: The 1971 and 1973 oppositions. *Icarus* **26**, 273-312.

Fjeldbo, G., Kliore, A., and Seidel, B. (1972). Bistatic radar measurements of the surface of Mars with Mariner 1969. *Icarus* **16**, 502-508.

Hartmann, W.K., Davis, D.R. Chapman, C.R., Soter, S., and Greenberg, R. (1975). Mars: Satellite origin and angular momentum. *Icarus* **25**, 588-594.

Hartwig, E. (1899). Determination of the diameter and polar compression of the planet Mars. *M. Not. Roy. Astr. Soc*. **59**, 488-491.

Heiskanen, W.A., and Moritz, H. (1967). *Physical Geodesy*. W.H. Freeman, San Francisco.

Heyl, P.R., and Chrzanowski, P. (1942). A new determination of the constant of gravitation. *J. of Research of the Nat. Bur. of Standards* **29**, 1-31.

Jeffreys, H. (1937). The density distribution in the inner planets. *M. Not. Roy. Astr. Soc., Geophys. Suppl*. **4**, 62-71.

Johnston, D.H., McGetchin, T.R., and Toksöz, M.N. (1974). The thermal state and internal structure of Mars. *J. Geophys. Res*. **79**, 3959-3971.

Jordan, J.F., and Lorell, J. (1975). Mariner 9, an instrument of dynamical science. *Icarus* **25**, 146-165.

Kaula, W.M. (1967). Theory of statistical analysis of data distributed over a sphere. *Rev. Geophys*. **5**, 83-107.

Khan, M.A. (1977). Depth of sources of gravity anomalies. *Geophys. J. Roy. Astr. Soc*. **48**, 197-209.

Knopoff, L. (1964). The convection current hypothesis. Rev. Geophys. 2, 89-122.

Lamar, D.L. (1962). Optical ellipticity and internal structure of Mars. Icarus 1, 258-265.

Lawson, C.L., and Hanson, R.J. (1974). Solving Least Squares Problems. Prentice-Hall, Englewood Cliffs, N.J.

Lingenfelter, R.E., and Schubert, G. (1973). Evidence for convection in planetary interiors from first-order topography. The Moon 7, 172-180.

Loomis, A.A. (1965). Some geologic problems of Mars. Geo. Soc. Am. Bull. 76, 1083-1104.

Lorell, J., Born, G.H., Christensen, E.J., Esposito, P.B., Jordan, J.F., Laing, P.A., Sjogren, W.L., Wong, S.K., Reasenberg, R.D., Shapiro, I.I., and Slater, G.L. (1973). Gravity field of Mars from Mariner 9 Tracking Data. Icarus 18, 304-316.

Love, A.E.H. (1911). Some Problems of Geodynamics. pp. 111-125, Dover Publications Inc., New York.

MacDonald, G.J.F. (1962). On the internal constitution of the inner planets. J. Geophys. Res. 67, 2945-2974.

MacRobert, T.M. (1967). Spherical Harmonics. Pergamon Press, New York.

McKenzie, D.P. (1968). The influence of the boundary conditions and rotation on convection in the Earth's mantle. Geophys. J. Roy. Astr. Soc. 15, 457-500.

Munk, W.H., and MacDonald, G.J.F. (1960). *The Rotation of the Earth*. Cambridge Univ. Press, London.

Mutch, T.A., and Saunders, R.S. (1976). The geologic development of Mars: A review. *Space Sci. Rev*. **19**, 3-57.

Pettengill, G.H., Counselman, C.C., Rainville, L.P., and Shapiro, I.I. (1969). Radar measurement of Martian topography. *Astron. J*. **74**, 461-482.

Phillips, R.J., and Saunders, R.S. (1975). The isostatic state of Martian topography. *J. Geophys. Res*. **80**, 2893-2898.

Reasenberg, R.D. (1977). The moment of inertia and isostasy of Mars. *J. Geophys. Res*. **82**, 369-375.

Reasenberg, R.D., Shapiro, I.I., and White, R.D. (1975). The gravity field of Mars. *Geophys. Res. Lett*. **2**, 89-92.

Roberts, P.H. (1968). On the thermal instability of a rotating fluid sphere containing heat sources. *Phil. Trans. Roy. Soc. London* **A263**, 93-117.

Roberts, P.H., and Ursell, H.D. (1960). Random walk on a sphere and on a Riemannian manifold. *Phil. Trans. Roy. Soc. London* **A252**, 317-356.

Runcorn, S.K. (1967). The problem of the figure of Mars. In *Mantles of the Earth and Terrestrial Planets* (S.K. Runcorn, Ed.). pp. 425-430. Wiley, London.

Schur, W. (1897). Determination of the diameter and compression of the planet Mars. *M. Not. Roy. Astr. Soc*. **57**, 150-154.

Sinclair, A.J. (1972). The motion of the satellites of Mars. M. Not. Roy. Astr. Soc. **155**, 249-274.

Sjogren, W.L., Lorell, J., Wong, L., and Downs, W. (1975). Mars gravity field based on a short-arc technique. J. Geophys. Res. **80**, 2899-2908.

Struve, H. (1895). A determination of the oblateness and equator of Mars. Astron. Nachr. **138**, 217-228.

Tozer, D.C. (1972). The present thermal state of the terrestrial planets. Phys. Earth Planet. Interiors **6**, 182-197.

Trumpler, R.J. (1927). Observations of Mars at the opposition of 1924. Lick Obs. Bull. **13**, 19-45.

Urey, H.C. (1950). The structure and chemical composition of Mars. Phys. Rev. **80**, 295-302.

de Vaucouleurs, G. (1964). Geometric and photometric parameters of the terrestrial planets. Icarus **3**, 187-235.

Weertman, J. (1970). The creep strength of the Earth's mantle. Rev. Geophys. Space Phys. **8**, 145-168.

Wilkins, G.A. (1967). The determination of the mass and oblateness of Mars from the orbits of its satellites. In Mantles of the Earth and Terrestrial Planets (S.K. Runcorn, Ed.). pp. 77-84. Wiley, London.

Woolard, E.W. (1944). The secular perturbations of the satellites of Mars. Astron. J. **51**, 33-36.

Wu, S.S.C. (1975). Topographic mapping of Mars. U.S. Geol. Survey Interagency Report 63.

IV. TOPOGRAPHIC VARIANCE SPECTRA OF THE EARTH, MOON AND MARS: AN EQUILIBRIUM MODEL

A. INTRODUCTION

The surface topography of a solid planet or satellite may be thought of as the superposition of two components; one deterministic, the other stochastic. The nature of the deterministic component (due to influences such as rotational and tidal deformation) has been extensively studied and is rather well understood (see e.g., Kopal, 1960; Chandrasekhar, 1969). In such analyses, the solid planets are usually modeled as fluids in equilibrium with simple deformational forces possessing axial or radial symmetry. The attention this deterministic approach has received is well deserved, since for most planets and satellites, the basic spherical shape, as well as the principal departures from sphericity, are adequately understood in this paradigm. However, on a local or even regional scale, the topography is dominated by its stochastic component. Though the individual constituent features of this topography (ridges, mountains, craters, etc.) have received attention previously and are fairly well understood in isolation, it is the random superposition of many such features, each basically deterministic, which produces the stochastic nature of the topography.

A general lack of understanding and appreciation for this aspect of the problem is well illustrated by the statement of Cook (1973) that "the shape of the solid surface of the Earth is very irregular and of no scientific interest."

The principal objective of this chapter is to isolate the stochastic components in the topography of the Earth, Moon and Mars (with brief reference to Venus) and gain a better understanding of their properties. We will find interesting statistical similarities among these rather diverse surfaces. In particular, we will consider the hypothesis that the variance spectra of all solid planets have the form

$$V(H;n) = \frac{V(H;0)}{(n)(n+1)} \tag{4.1}$$

for all n such that $R_0/n \leqslant 2000$ km, and that furthermore, the individual harmonic coefficients H_{nmi} are Gaussian random variables $N(0,\sigma_n^2)$ with mean $\mu = 0$ and variance

$$\sigma_n{}^2 = \frac{V(H;n)}{2n+1} \quad . \tag{4.2}$$

For comparison with later observations, in figure 4.1 we present a topographic variance spectrum constructed according to this hypothesis. For each harmonic degree n: $1 \leq n \leq 30$, the $2n + 1$ harmonic coefficients H_{nmi} were assigned values drawn from a population of Gaussian $N(0,\sigma_n^2)$ random variables. The fluctuations of the resultant sample variances relative to the population variances are distributed as $\chi^2/(2n + 1)$, i.e., chi-square over degrees of freedom with $2n + 1$ degrees of freedom (see Appendix B). The critical values for the 90% confidence level are indicated. There is thus a 10% chance that the sample variance will fall outside these limits if the population variance is as specified by the model. The value of $V(H;0) = 10^{-6}$ was chosen to be representative of actual planetary values.

4.1 Simulated spherical topographic variance spectrum. Harmonic coefficients are $N(0,\sigma_n^2)$ Gaussian random variables with $\sigma_n^2 = 10^{-6}/(n)(n+1)$. Points are sample variances. Solid line is theoretical variance. Dotted lines indicate critical values for 90% confidence level.

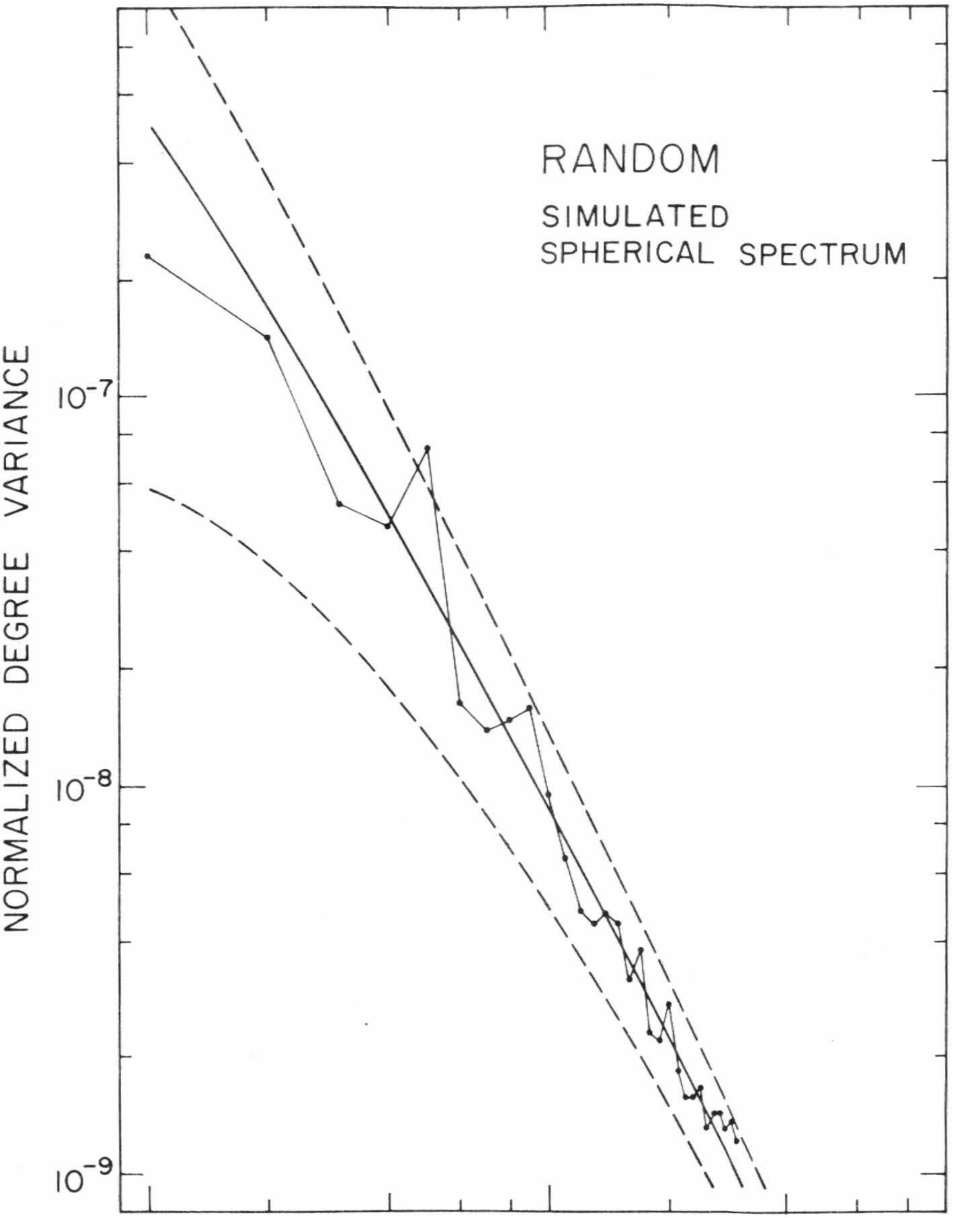
RANDOM
SIMULATED
SPHERICAL SPECTRUM
NORMALIZED DEGREE VARIANCE
10^{-7}
10^{-8}
10^{-9}
1
4
10
40
100
HARMONIC DEGREE

In the remainder of the chapter, we will discuss some observations relevant to this hypothesis, and then examine a number of possible explanations for this peculiar behavior. Lastly, we will consider some of its implications and point out some directions for future research.

B. OBSERVATIONS

1. Variance Spectra

Earth

Vening-Meinesz (1951) was apparently the first to call attention to the fact that the Earth's topographic variance spectrum, as obtained from Prey's (1922) harmonic analysis, is approximated by equation (4.1) at least for harmonic degrees n: $1 \leq n \leq 16$. We shall therefore refer to this ideal form as the Vening-Meinesz spectrum. In a later paper (Vening-Meinesz, 1962), he showed that an unpublished harmonic analysis by G.J. Bruins, with $n \leq 31$, further supports and extends the observed range of validity of his initial observation. Balmino *et al.* (1973) have performed a harmonic analysis complete through degree and order 36. In Figure 4.2, we present the degree variances from this analysis compared with the Vening-Meinesz spectrum. The value of V(H;0) was adjusted to optimize the match with the actual spectrum.

We will often loosely refer to V(H;0) as the total variance. However, this is only strictly true for the pure Vening-Meinesz spectrum. In most cases, $C(H;0) \leq R_o^2 \, V(H;0)$ (see Appendix D).

It is easily seen that the largest departures from the Vening-Meinesz spectral form are for the first few harmonic degrees. Though the confidence limits for the low degree harmonics are quite wide, it still seems significant that for the Earth, Mars and Venus, the low degree variances are consistently deficient relative to our expectations. We shall return to this point later. First, we want to find out what happens at the high frequency end of the spectrum.

For sufficiently high spatial frequencies, spherical harmonic analysis becomes computationally impractical. For small enough areas, the curvature of the earth may be neglected and a simple planar Fourier analysis is quite adequate. Several such analyses have been performed over a wide spectral range (see e.g., Cox and Sandstrom, 1962; Krause and Menard, 1965; Bretherton, 1969; Warren, 1973; Pike and Rozema, 1975). Recently, Bell (1975) has compiled the results of several previous analyses and, in conjunction with his own analysis of the oceanic abyssal hills province, has shown a rather impressive agreement between various spectral estimates over a cumulative spatial frequency range corresponding to harmonic degrees n: $1 \le n \le 300{,}000$. Even more impressive is the fact that these spectral estimates approximate the Vening-Meinesz spectrum over essentially the entire range (see Figure 4.3).

Since the topography of the Earth is dominated by the continent-ocean dichotomy, particularly in the low degree harmonics, it is possible to investigate the history of the Earth's topography spectrum from reconstructions of previous continental configurations

4.2 Earth - Spherical topographic variance spectrum. Harmonic coefficients are from Balmino <u>et al.</u> (1973). Points are computed degree variances. Solid line is Vening-Meinesz spectrum: $V(H;n) = 2.6 \times 10^{-7}/(n)(n+1)$. Dotted lines indicate critical values for 90% confidence level.

4.3 Earth - Composite topographic variance spectrum. Adapted from Bell (1975). Used by permission. The smallest scale features (harmonic degree $n \doteq 3 \times 10^{5}$) have dimensions $L = 2\pi R_o/n \doteq 120$ m.

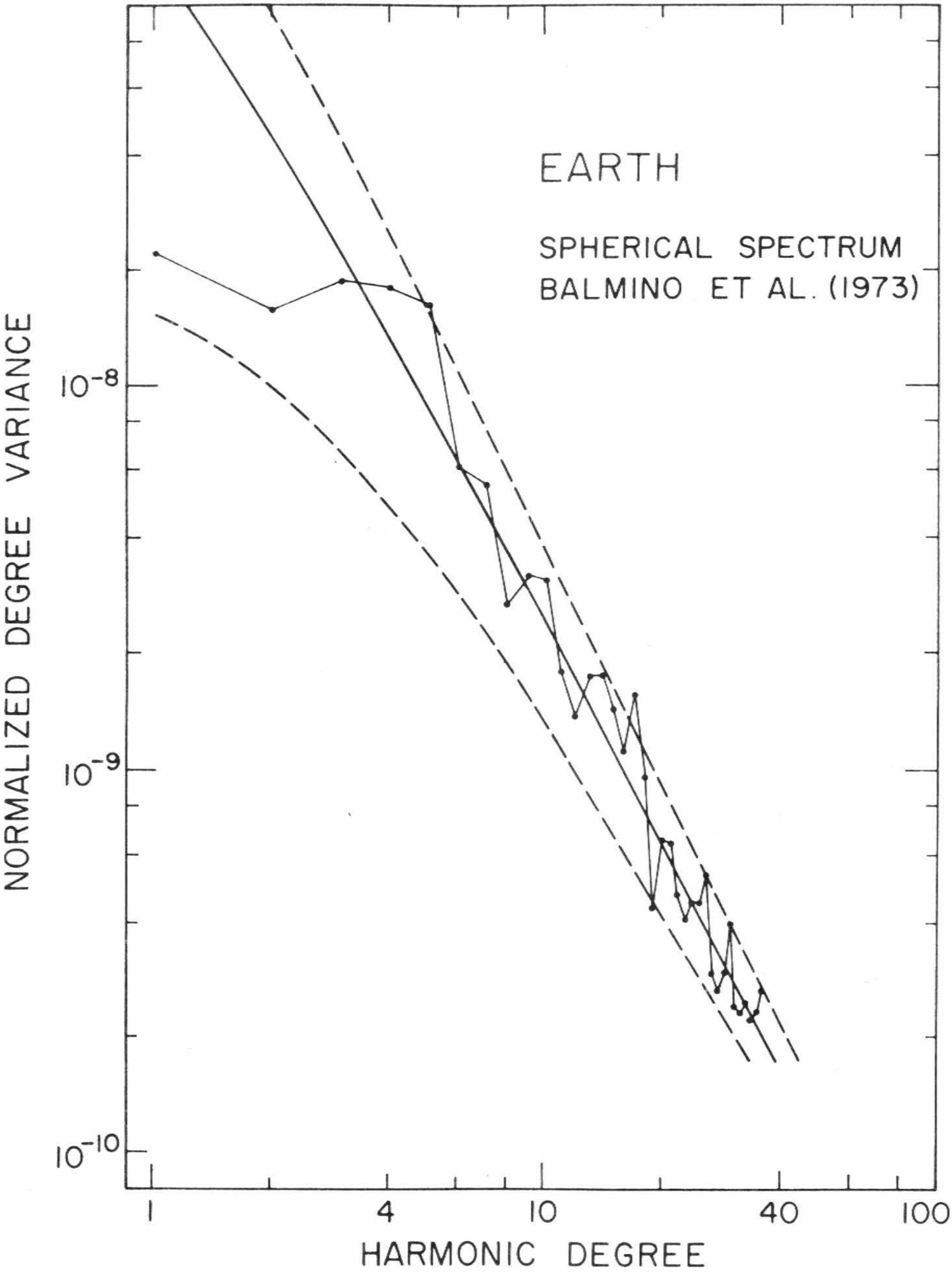
EARTH
SPHERICAL SPECTRUM
BALMINO ET AL. (1973)
NORMALIZED DEGREE VARIANCE
10^{-8}
10^{-9}
10^{-10}
1
4
10
40
100
HARMONIC DEGREE

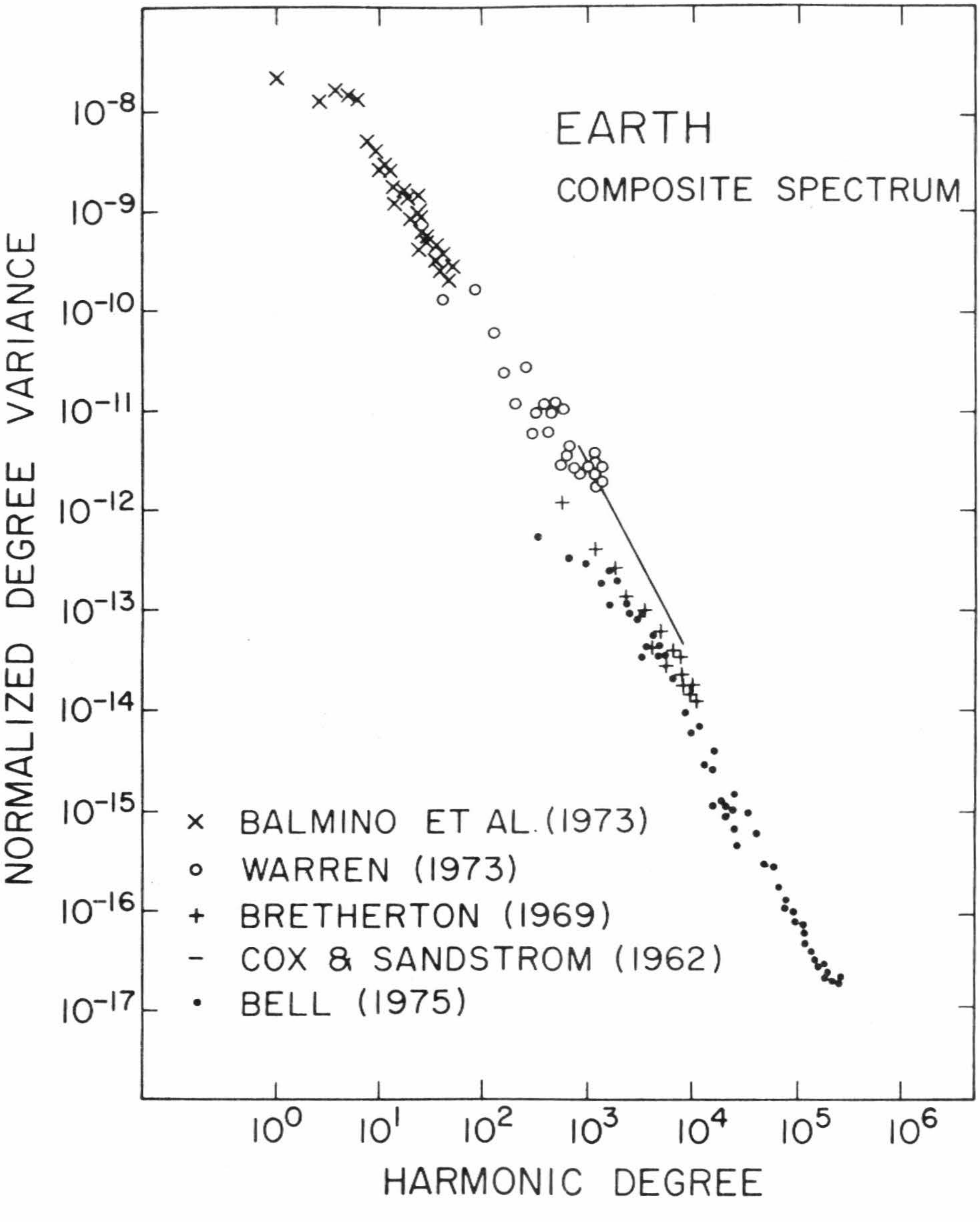
EARTH
COMPOSITE SPECTRUM
NORMALIZED DEGREE VARIANCE
HARMONIC DEGREE
10^{-8}
10^{-9}
10^{-10}
10^{-11}
10^{-12}
10^{-13}
10^{-14}
10^{-15}
10^{-16}
10^{-17}
10^{0}
10^{1}
10^{2}
10^{3}
10^{4}
10^{5}
10^{6}
× BALMINO ET AL. (1973)
o WARREN (1973)
+ BRETHERTON (1969)
– COX & SANDSTROM (1962)
• BELL (1975)

(Dietz and Holden, 1970). A preliminary analysis of this sort indicates a shift of spectral energy from the lowest degrees ($1 \le n \le 3$) to the higher harmonics as the continents have dispersed. This may be relevant to the previously mentioned fact that low degree variances are deficient relative to the higher harmonics.

Moon

Due to the paucity and uneven distribution of lunar topographic data, the variance spectrum calculated from harmonic coefficient estimates is not as representative of the true variance spectrum as was the case for the Earth. Nevertheless, recent harmonic analyses (Goudas, 1971; Chuikova, 1976; Bills and Ferrari, 1977a) indicate that lunar topography is also dominated by the low degree harmonics, and even suggest that the spectrum may approximate the Vening-Meinesz form. See Figure 4.4 for a comparison of the spectrum from Bills and Ferrari (1977a) with the Vening-Meinesz theoretical spectrum. Though the agreement is not outstanding, we should not reject the hypothesis that the Moon has a topographic variance spectrum similar to the Earth's until we examine some further evidence, particularly considering the amount of spectral distortion induced by the irregular data distribution - in spite of the efforts described in Chapter I to compensate for this effect.

As an independent estimation of the variance spectrum and to extend it to higher harmonic degree, a simple one-dimensional Fourier analysis has been performed on complete orbital segments of laser altimetry data from Apollo missions 15, 16 and 17 (Kaula et al. 1972, 1973, 1974). The resultant spectra were then averaged and are displayed in Figure 4.5. This technique of averaging raw spectra provides statistical stability at low harmonic degree, and is equivalent to smoothing the spectra with a Bartlett window (Jenkins and Watts, 1968). Since the effective domain of these data is a circle rather than a sphere, the appropriate comparison spectrum is

$$V(H;n) = \frac{V(H;0)}{n^2} \tag{4.3}$$

rather than equation (4.1) (see Appendix A). It can be seen that, at least in the range $1 \leq n \leq 32$, the variance spectrum of the Moon conforms to the Vening-Meinesz pattern.

A further, more stringent test of the applicability of the Vening-Meinesz spectrum to the Moon at high harmonic degrees involves comparison of r.m.s. slopes at various slope lengths with model values. As is shown in Appendix G, the mean square slope between points a distance $L = R_0\gamma$ apart on a planet characterized by a Vening-Meinesz spectrum is

$$S^2(\gamma) = 4\ V(H;0)\ \ln\ [1+\sin(\gamma/2)]/\gamma^2 \tag{4.4}$$

which for $\gamma \ll 1$, reduces to

$$S^2(\gamma) \doteq 2V(H;0)/\gamma \quad . \tag{4.5}$$

Thus, given an estimate for V(H;0), we can estimate values for the r.m.s. slope angle

4.4 Moon - Spherical topographic variance spectrum. Harmonic coefficients are from Bills and Ferrari (1977a). Points are computed degree variances. Solid line is Vening-Meinesz spectrum: $V(H;n) = 1.5 \times 10^{-6}/(n)(n+1)$. Dotted lines indicate critical values for 90% confidence level.

4.5 Moon - Circular topographic variance spectrum. Points are averaged degree variances from Fourier analysis of Apollo laser altimetry data. Solid line is model variance spectrum: $V(H;n) = 1.5 \times 10^{-6}/(n)^2$. This is the circular analog of the Vening-Meinesz spectrum.

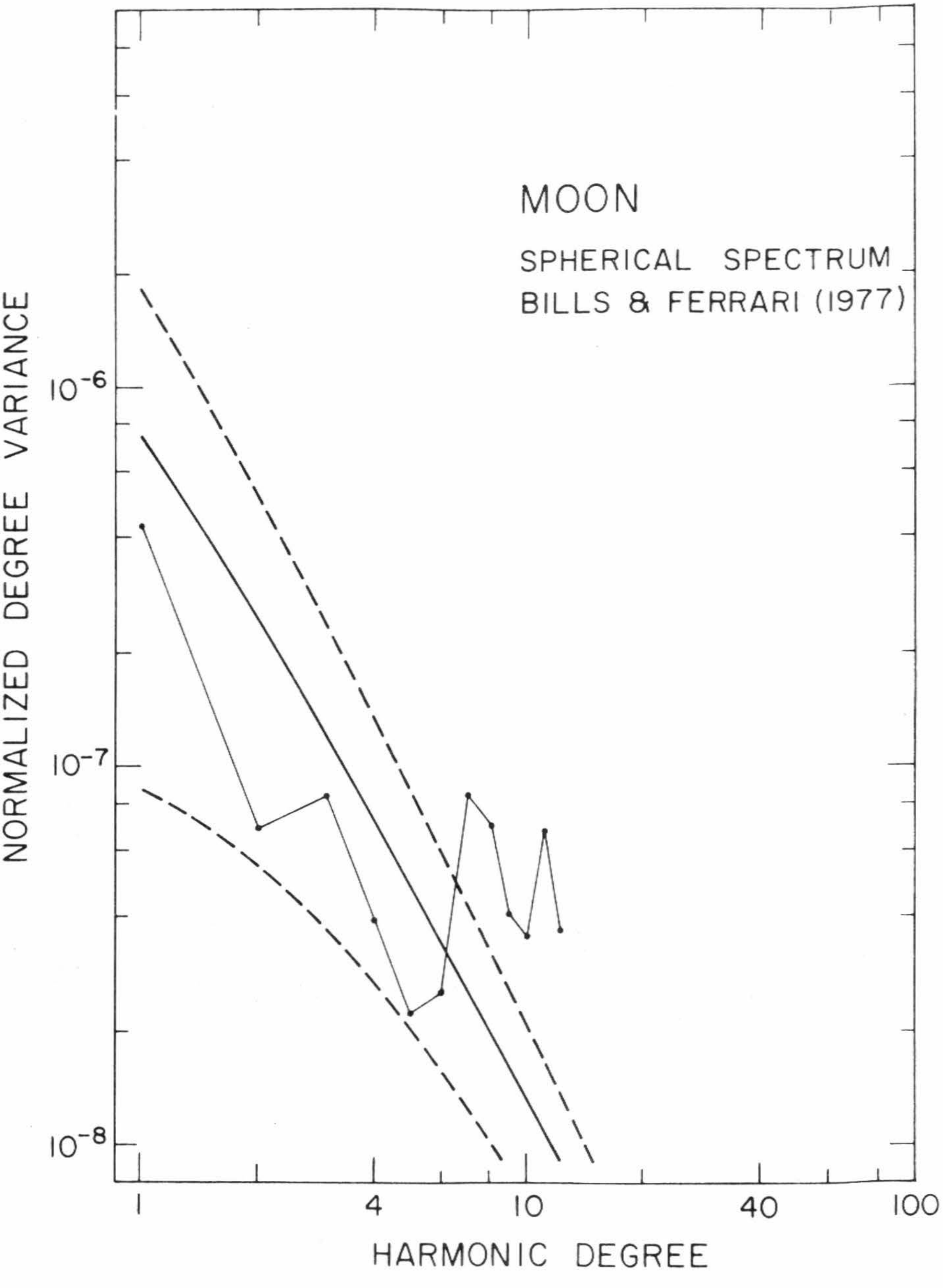
MOON
SPHERICAL SPECTRUM
BILLS & FERRARI (1977)
NORMALIZED DEGREE VARIANCE
10^{-6}
10^{-7}
10^{-8}
1
4
10
40
100
HARMONIC DEGREE

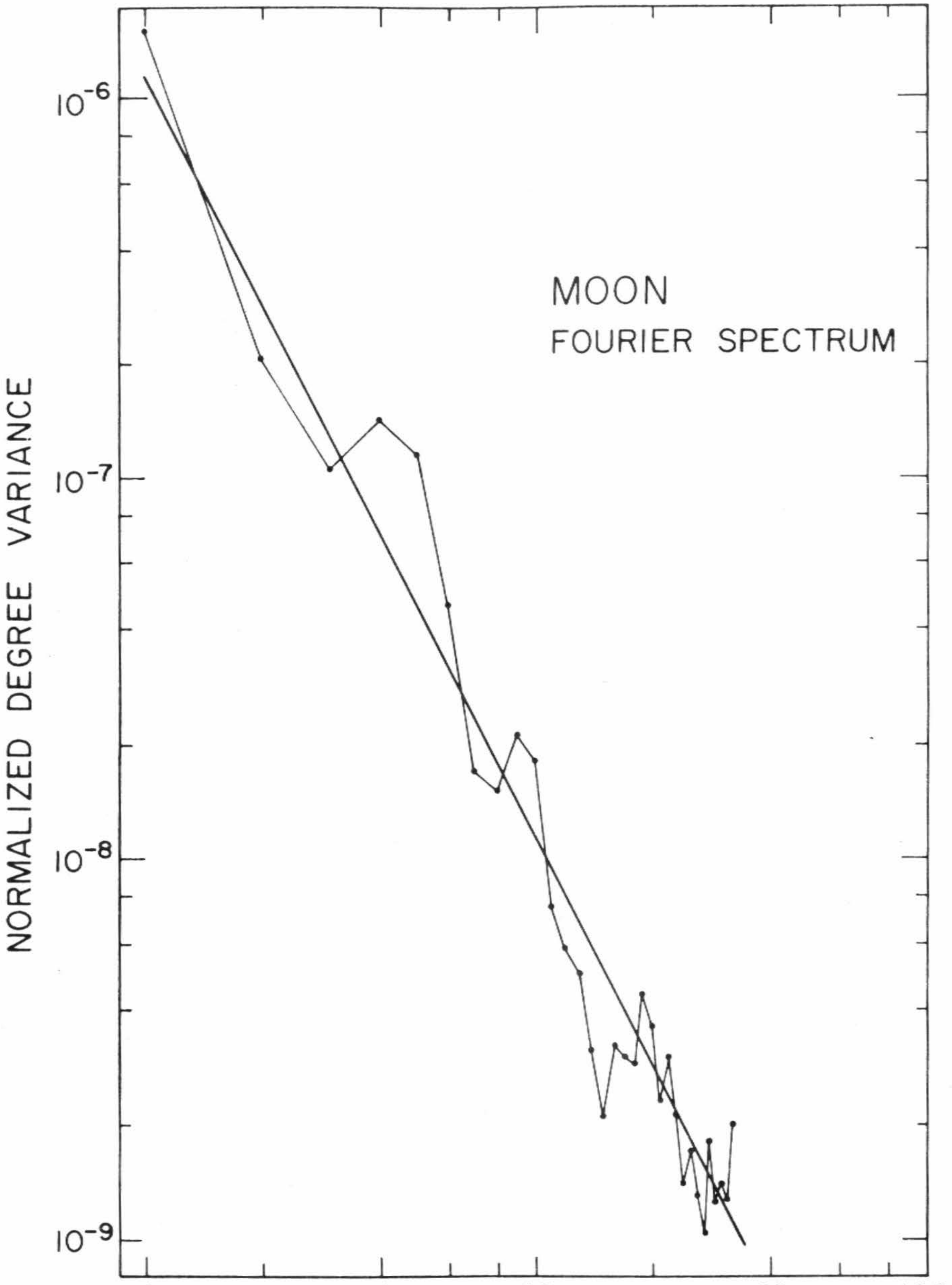
MOON
FOURIER SPECTRUM
NORMALIZED DEGREE VARIANCE
10^{-6}
10^{-7}
10^{-8}
10^{-9}
1
4
10
40
100
HARMONIC DEGREE

$$\Theta(L) = \tan^{-1} [S(L/R_0)] \tag{4.6}$$

at any linear separation L. In Figure 4.6, we compare this estimate with photogrammetrically determined r.m.s. slopes for typical highland and mare regions of the Moon over the range $25 \text{ m} \le L \le 1000 \text{ m}$ (Moore and Tyler, 1973). The agreement with these observations could be made much better by reducing the value of $V(H;0)$, however, we have used the value estimated from the spectrum in Figure 4.5. Thus, we are extrapolating from $n \le 32$ to $n = 2\pi R_o/L \doteq 40{,}000$ ($L = 250$ m). We note that our predicted slopes are intermediate between the highland and mare values and actually parallel the mare values. The highlands, though rougher than the maria at all slope lengths considered, exhibit weaker dependence of slope angle on slope length. This agreement between observed and predicted slopes is a strong confirmation of the validity of the Vening-Meinesz spectrum as applied to the Moon.

Mars

The earliest topographic spectral estimates for Mars appear to be those of Pettengill et al. (1969), who performed a Fourier analysis of elevations along the 22° N latitude parallel as determined from radar observations. They first argued from terrestrial topography data that "the Fourier spectrum of the topographic variation around any great circle (e.g., the equator), or near-equatorial parallel of latitude, will tend to approximate the spherical harmonic spectrum." They then showed that their estimated topographic

4.6 Moon - Slope analysis. Points are photogrammetrically determined r.m.s. slopes on different lunar terrain types from Moore and Tyler (1973). The solid line indicates theoretical slope angles given by equations (4.5) and (4.6) using the value $V(H;0) = 1.5 \times 10^{-6}$ determined from Figure 4.5. A representative slope length ($L = 250$ m) corresponds to a harmonic degree of $n = 2\pi R_o/L \doteq 40{,}000$.

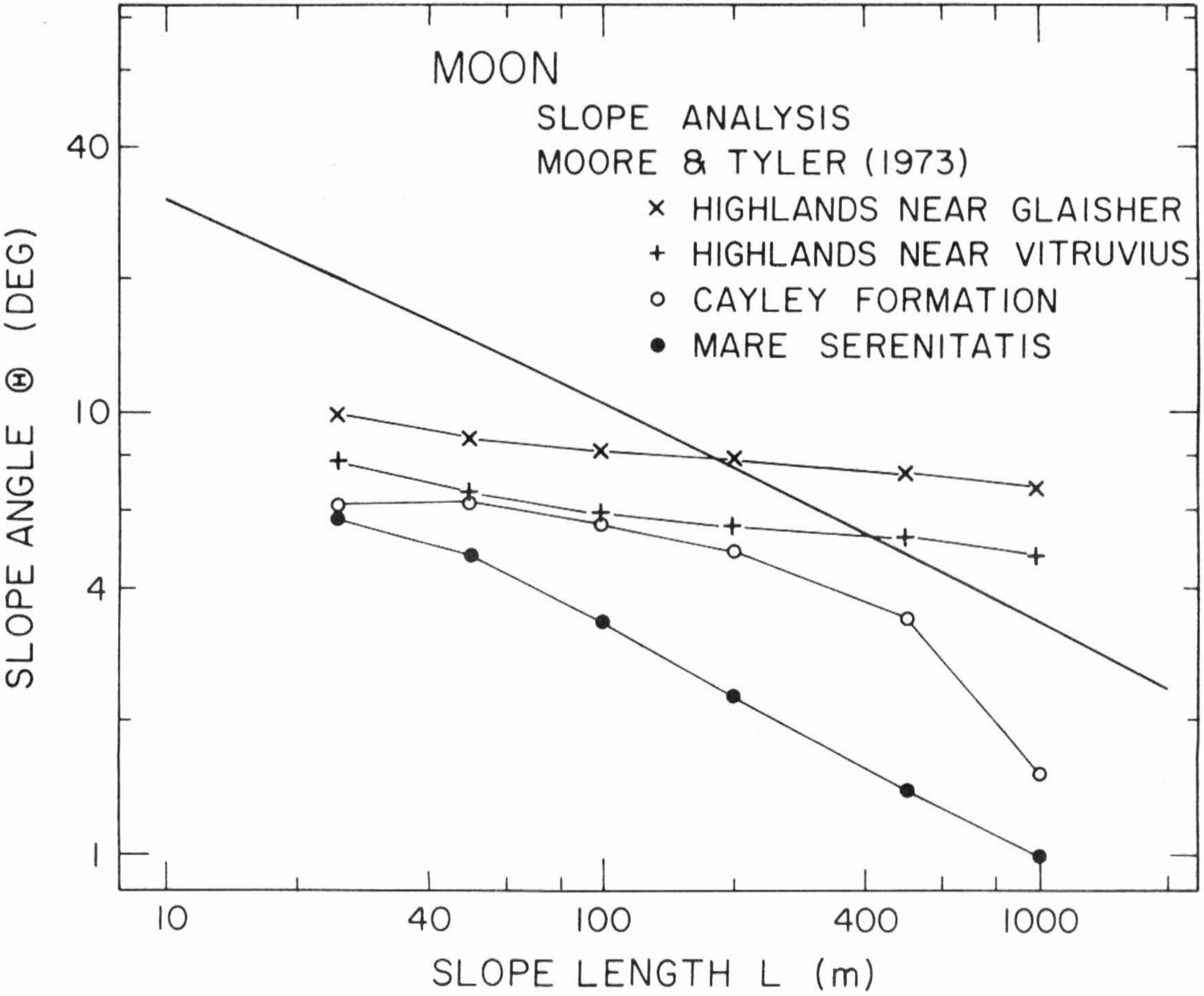
MOON
SLOPE ANALYSIS
MOORE & TYLER (1973)
× HIGHLANDS NEAR GLAISHER
+ HIGHLANDS NEAR VITRUVIUS
○ CAYLEY FORMATION
● MARE SERENITATIS
SLOPE ANGLE Θ (DEG)
40
10
4
1
10
40
100
400
1000
SLOPE LENGTH L (m)

variance spectrum for Mars, which covered the range $1 \leq n \leq 16$, is quite similar to the Earth's.

As was true of the lunar spectrum, the Martian variance spectrum as computed from spherical harmonics (Figure 4.7) is somewhat corrupted by the irregular data distribution, in spite of efforts such as those described in the last chapter. Nevertheless, harmonic analyses by Christensen (1975), with $1 \leq n \leq 8$, and by Bills and Ferrari (1977c), with $1 \leq n \leq 16$ (see Chapter III), have confirmed that the spectral behavior discovered by Pettengill et al. (1969) is indeed a feature of the entire planet rather than merely characteristic of a single latitude band.

As of this writing, r.m.s. slope determinations from Viking photogrammetry are still unavailable (H. Masursky, personal communication) for comparison with predicted slopes, as was done for the Moon.

Venus

The only topographic data presently available for Venus come from radar observations (Smith et al., 1970; Campbell et al., 1972; Shapiro et al., 1973) and are essentially restricted to the sub-Earth points. A preliminary Fourier analysis ($1 \leq n \leq 16$) of the data from Shapiro et al. (1973), which have complete longitude coverage but are severely limited in latitudinal extent, shows a distinct tendency toward decreasing variance with increasing degree (Figure 4.8). Though the spectrum is somewhat "noisy", the general trend is surprisingly consistent with the Vening-Meinesz model.

4.7 Mars - Spherical topographic variance spectrum. Harmonic coefficients are from Bills and **Ferrari** (1977c). Points are computed degree variances. Solid line is Vening-Meinesz spectrum: $V(H;n) = 5.5 \times 10^{-7}/(n)(n+1)$. Dotted lines indicate critical values for 90% confidence level.

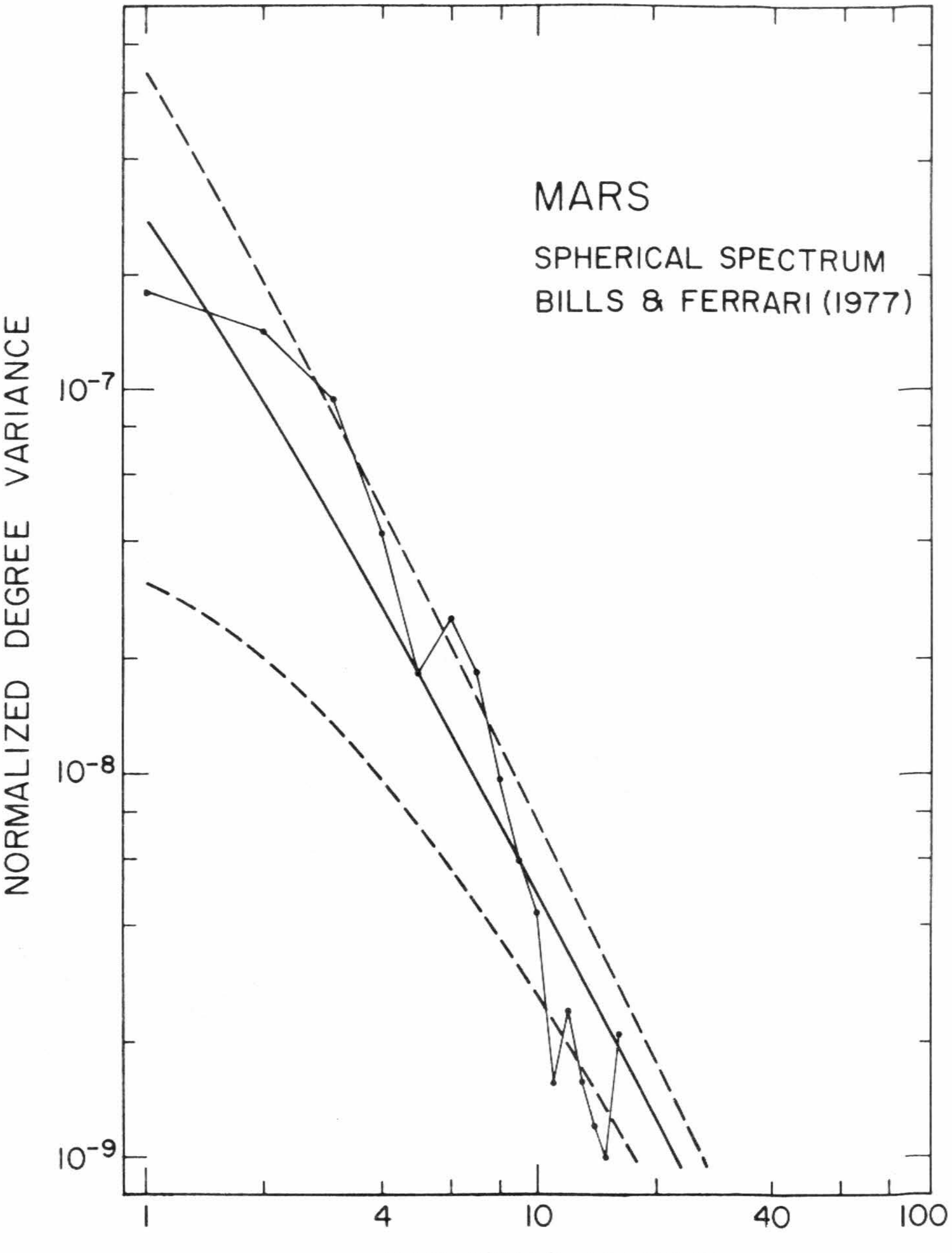
MARS
SPHERICAL SPECTRUM
BILLS & FERRARI (1977)
NORMALIZED DEGREE VARIANCE
10^{-7}
10^{-8}
10^{-9}
1
4
10
40
100
HARMONIC DEGREE

4.8 Venus - Circular topographic variance spectrum. Points are degree variances from Fourier analysis of near equatorial radar altimetry data of Shapiro *et al.* (1973). Solid line is model variance spectrum: $V(H;n) = 1.1 \times 10^{-7}/n^2$. This is the circular analog of the Vening-Meinesz spectrum.

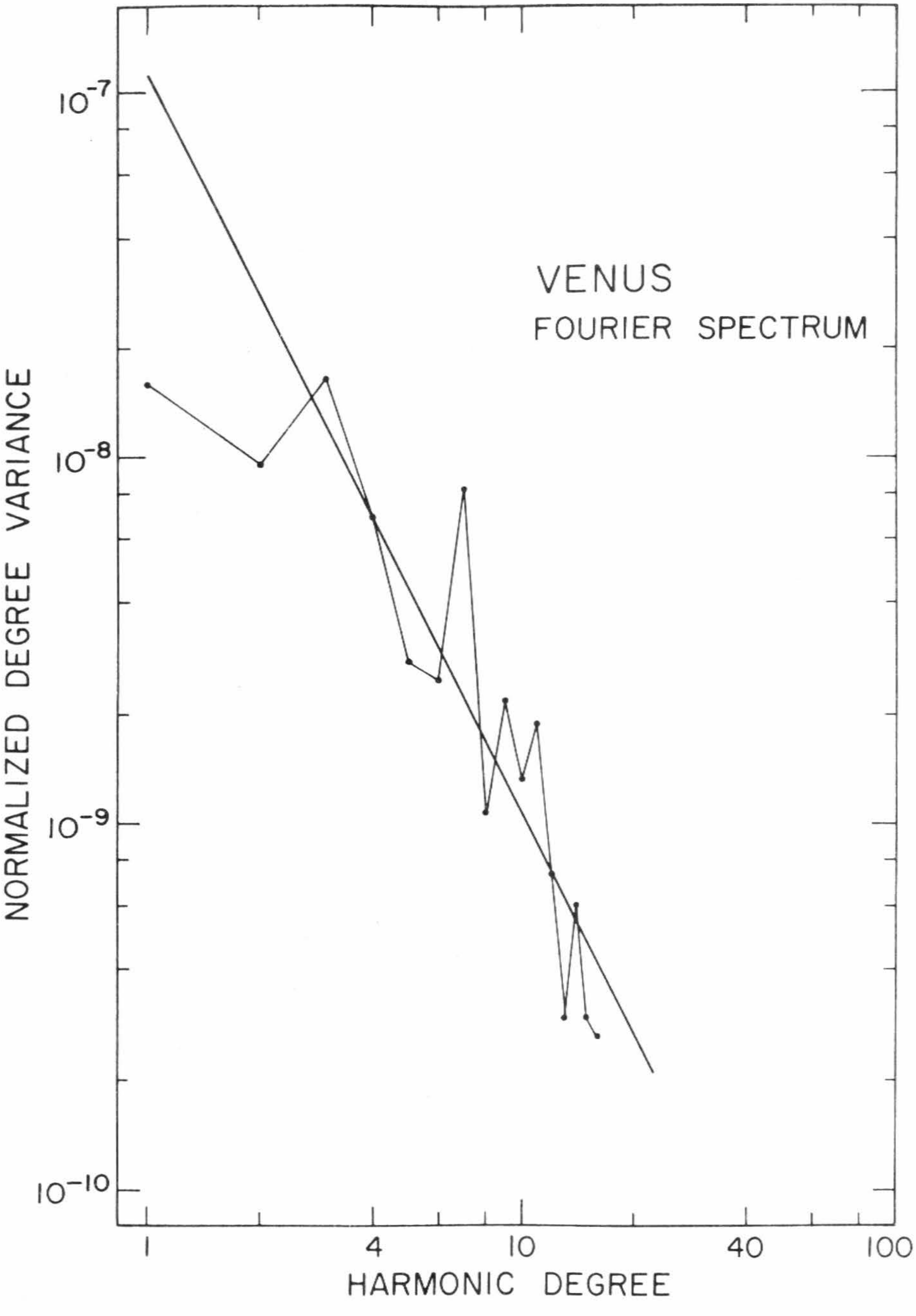
VENUS
FOURIER SPECTRUM
NORMALIZED DEGREE VARIANCE
10^{-7}
10^{-8}
10^{-9}
10^{-10}
1
4
10
40
100
HARMONIC DEGREE

2. Isotropy

Another aspect of our original hypothesis was that, apart from rotational and tidal effects, the topography should be essentially random. A convenient and informative way to check this conjecture is to measure the isotropy of the surface. As is developed in Appendix G, a necessary condition for isotropy is that the mean square east-west slope at zero slope length

$$S_\theta^2(0) = \sum_{n=1}^{\infty} T_\theta(n) \tag{4.7}$$

equals the mean square north-south slope at zero slope length

$$S_\varphi^2(0) = \sum_{n=1}^{\infty} T_\varphi(n) \tag{4.8}$$

where the degree tilts are

$$\begin{aligned} T_\theta(n) &= \sum_{m=0}^{n} \left[\frac{(2n+1)(m)}{2}\right] H_{nm}^T H_{nm} \\ T_\varphi(n) &= \sum_{m=0}^{n} \left[(n)(n+1) - \frac{(2n+1)(m)}{2}\right] H_{nm}^T H_{nm} \quad . \end{aligned} \tag{4.9}$$

A sufficient condition for mean square isotropy is the equality of the degree tilts for each harmonic degree. We thus define a degree isotropy parameter

$$\alpha_n \equiv T_\theta(n)/T_\varphi(n) \quad . \tag{4.10}$$

In Figure 4.9a, we present the isotropy spectrum for the random harmonic model previously discussed. Figures 4.9b-d are isotropy spectra calculated from spherical harmonic models of the topography of the Earth (Balmino et al., 1973), Mars (Bills and Ferrari, 1977c) and the Moon (Bills and Ferrari, 1977a), respectively. For the Earth, the topography was measured relative to the geoid, and thus the primary effect of rotation has been removed. For Mars and the Moon, the original harmonic analyses are for spherically referenced elevations, but for this analysis, the second degree terms have been corrected for rotational effects. For all three planets, we find quite consistent isotropy, with the largest departures for the low degrees.

3. Simulation

As a further, somewhat subjective criterion for judging the validity of our primary hypothesis that the topography of a solid planet or satellite is well modeled by zero-mean Gaussian random harmonic coefficients with a Vening-Meinesz variance spectrum, we would expect that a contour map produced from these coefficients would appear qualitatively similar to equivalent resolution maps of actual planetary surfaces. Figures 4.10a-c are topographic maps generated from harmonic representations of the Moon, Mars and Earth, all truncated at degree $n = 12$. For comparison, Figure 4.10d is a map of the random topography represented by the harmonic coefficients used in producing Figures 4.1 and 4.9a, also truncated

4.9a Simulated isotropy spectrum. Points are ratios $\alpha_n = T_\theta(n)/T_\varphi(n)$ of east-west degree tilts $T_\theta(n)$ to north-south degree tilts $T_\varphi(n)$ as defined in equation 4.9. Harmonic coefficients are the same random variables used in generating Figure 4.1. Solid line represents perfect isotropy $\alpha_n = 1.0$.

4.9b Earth - Isotropy spectrum. Harmonic coefficients are from Balmino *et al.* (1973). See caption to Figure 4.9a.

4.9c Mars - Isotropy spectrum. Harmonic coefficients are from Bills and Ferrari (1977c). See caption to Figure 4.9a.

4.9d Moon - Isotropy spectrum. Harmonic coefficients are from Bills and Ferrari (1977a). See caption to Figure 4.9a.

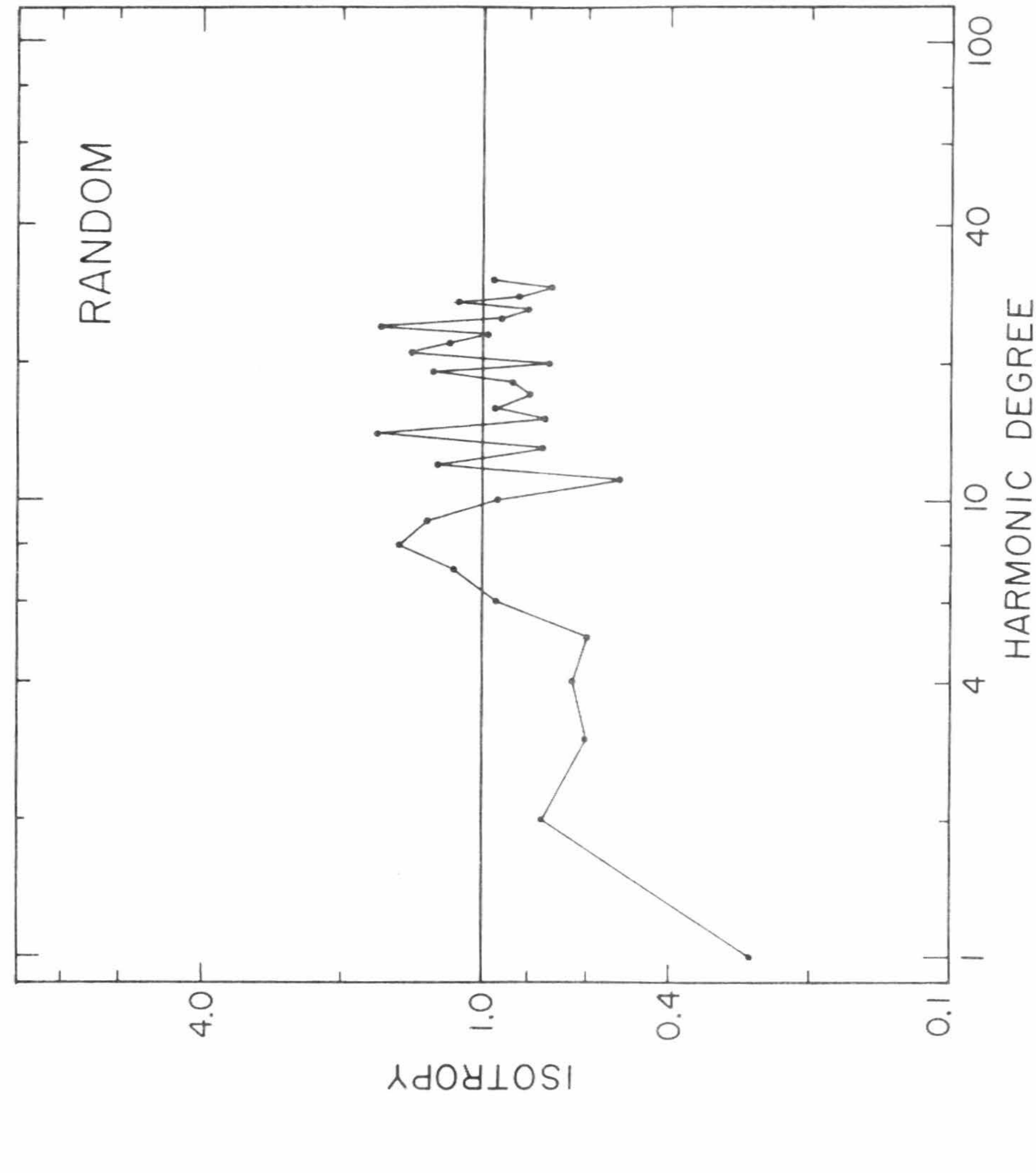
RANDOM
ISOTROPY
4.0
1.0
0.4
0.1
HARMONIC DEGREE
1
4
10
40
100

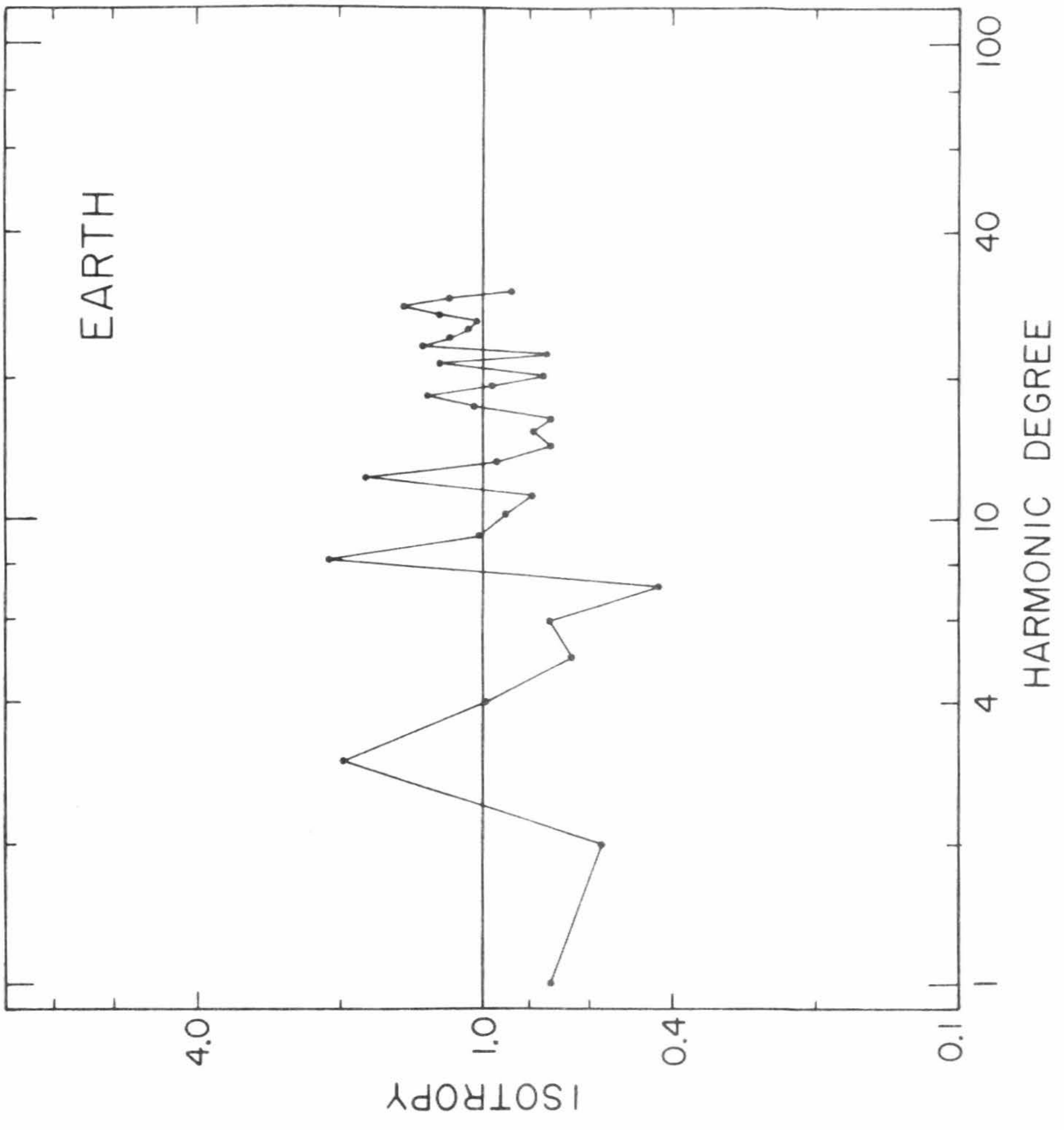
EARTH
ISOTROPY
4.0
1.0
0.4
0.1
HARMONIC DEGREE
1
4
10
40
100

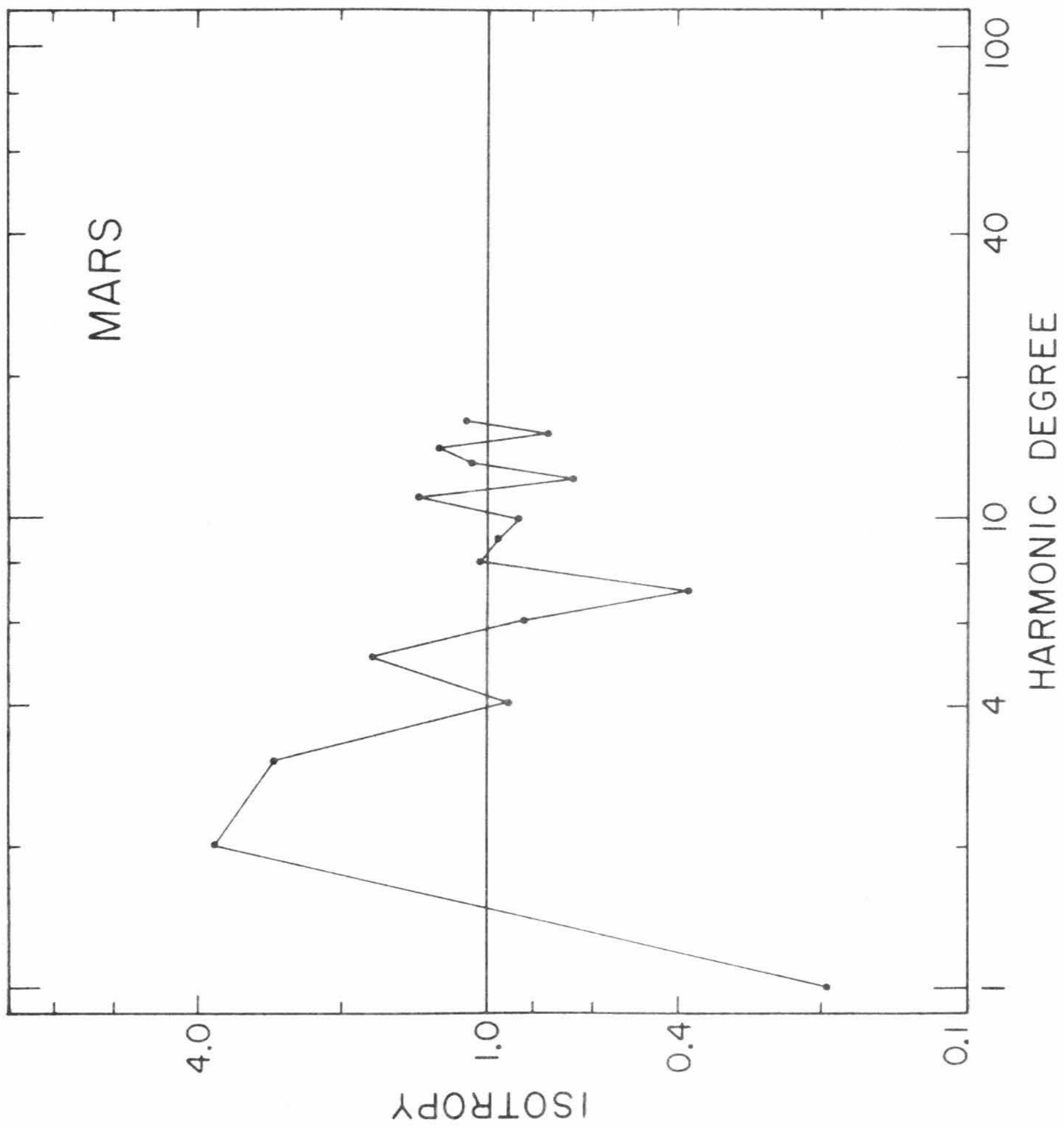
MARS
ISOTROPY
4.0
1.0
0.4
0.1
HARMONIC DEGREE
1
4
10
40
100

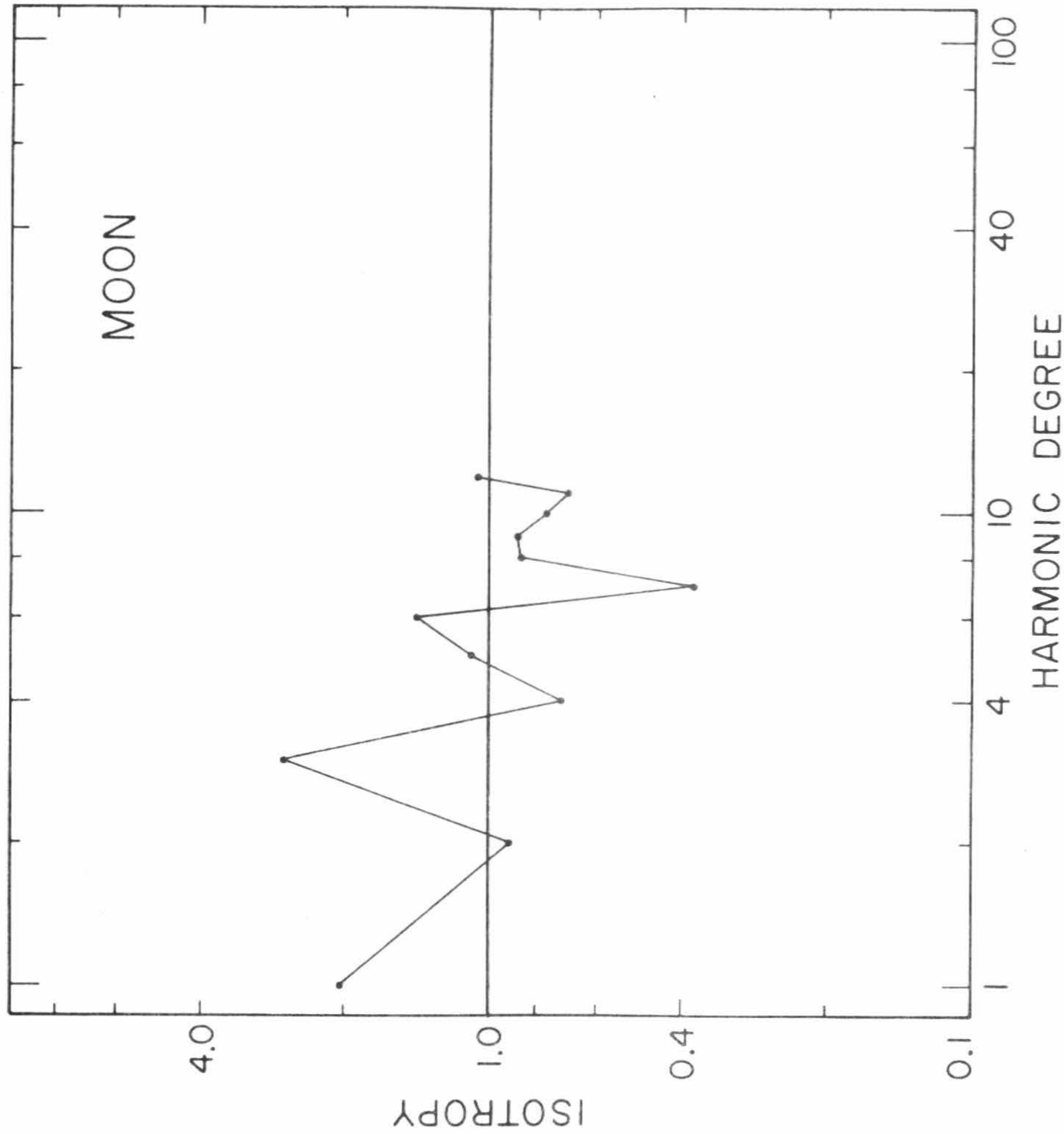
MOON
ISOTROPY
4.0
1.0
0.4
0.1
HARMONIC DEGREE
1
4
10
40
100

at n = 12. All of these figures are Mercator projections and cover the latitude range $-75^\circ \le \theta \le +75^\circ$. The contour interval in each case is 1.0 km. The mean radius of the random planet was arbitrarily taken to be $R_0 = 3000$ km. This, in conjunction with the assumption that $V(H;0) = 10^{-6}$, determines the physical variance of the surface. A decision as to the adequacy of this simulation, being rather subjective, will be left to the judgment of the reader.

4. Summary

In summary, we find that on all planets for which we have sufficient data to check our hypothesis the stochastic component of the topography is very nearly isotropic and the degree variances decrease with increasing harmonic degree consistent with the Vening-Meinesz spectrum (equation 4.1). Furthermore, we find that the largest reliably determined departures from this basic model are for the low degree harmonics. In fact, the point of incipient departure appears to correspond roughly to a scale length $L = R_0/n$ of 1700-2100 km (Earth: L = 6380/3, Venus: L=6050/3, Mars: L = 3390/2, Moon: L = 1740/1).

Since this Vening-Meinesz spectral form is applicable over such a wide range of feature sizes and on planets subject to widely differing geomorphic processes, it appears to reflect some fundamental property of the terrestrial planets. We will now attempt to gain a better theoretical understanding of this spectrum in hopes of being able to explain its ubiquity.

4.10a Moon - Topographic contour map. From harmonic coefficients of Bills and Ferrari (1977a) truncated at degree N = 12. Mean radius R_o = 1737.5 km. Contour interval ΔH = 1.0 km. Solid lines are above reference level, dashed lines are below it. Mercator projection with latitude range $-75^\circ \leq \theta \leq 75^\circ$.

4.10b Mars - Topographic contour map. From harmonic coefficients of Bills and Ferrari (1977c) truncated at degree N = 12. Mean radius R_o = 3389.9 km. Heights are referenced to 6.1 millibar level. See caption to Figure 4.10a

4.10c Earth - Topographic contour map. From harmonic coefficients of Balmino et al. (1973) truncated at degree N = 12. Mean radius = 6371.0 km. Heights are referenced to geoid. See caption to Figure 4.10a

4.10d Simulated topographic contour map. From harmonic coefficients used in figures 4.1 and 4.9 truncated at degree N = 12. Assumed mean radius R_o = 3000 km. See caption to Figure 4.10a

MOON

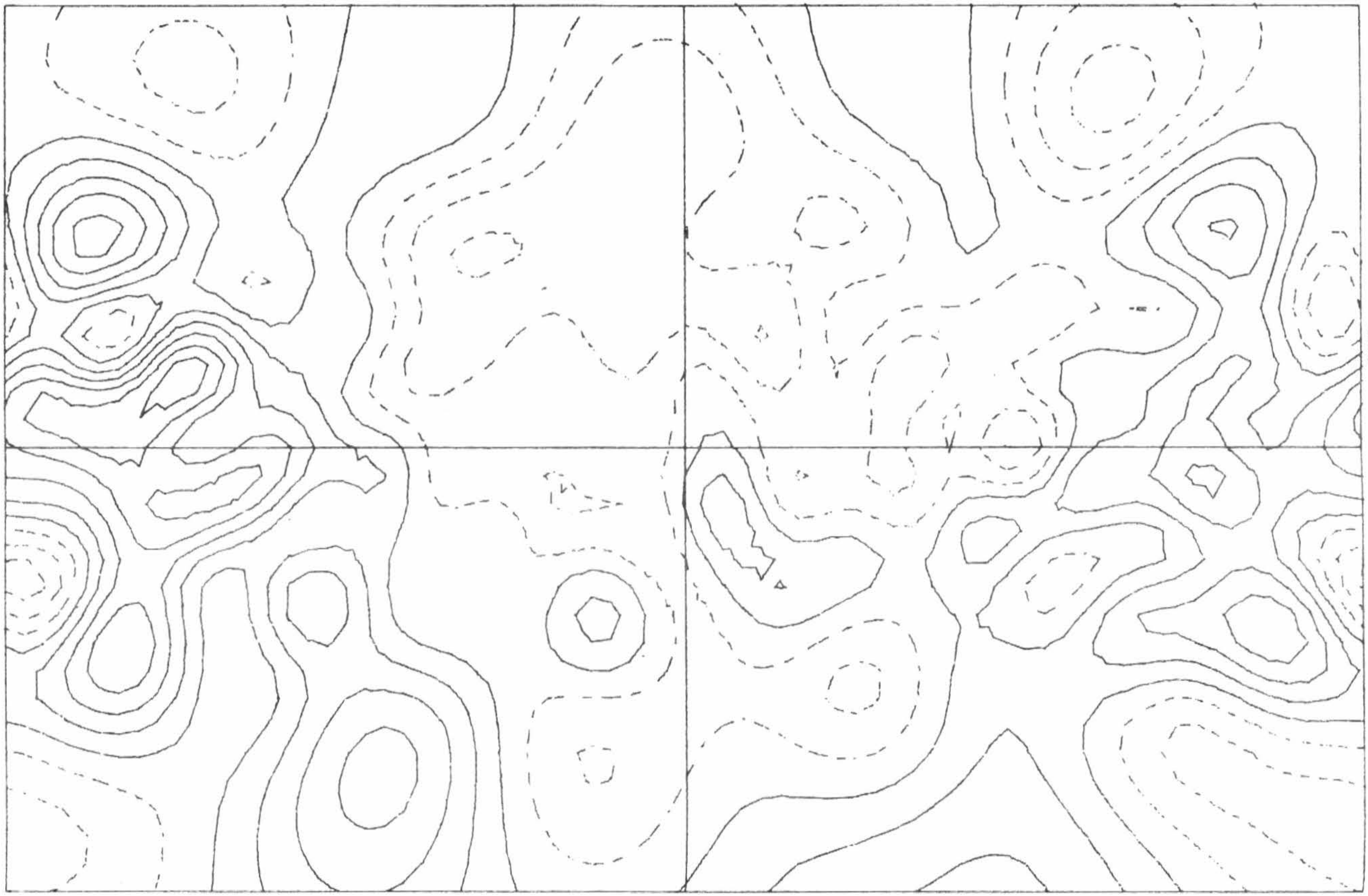

MARS

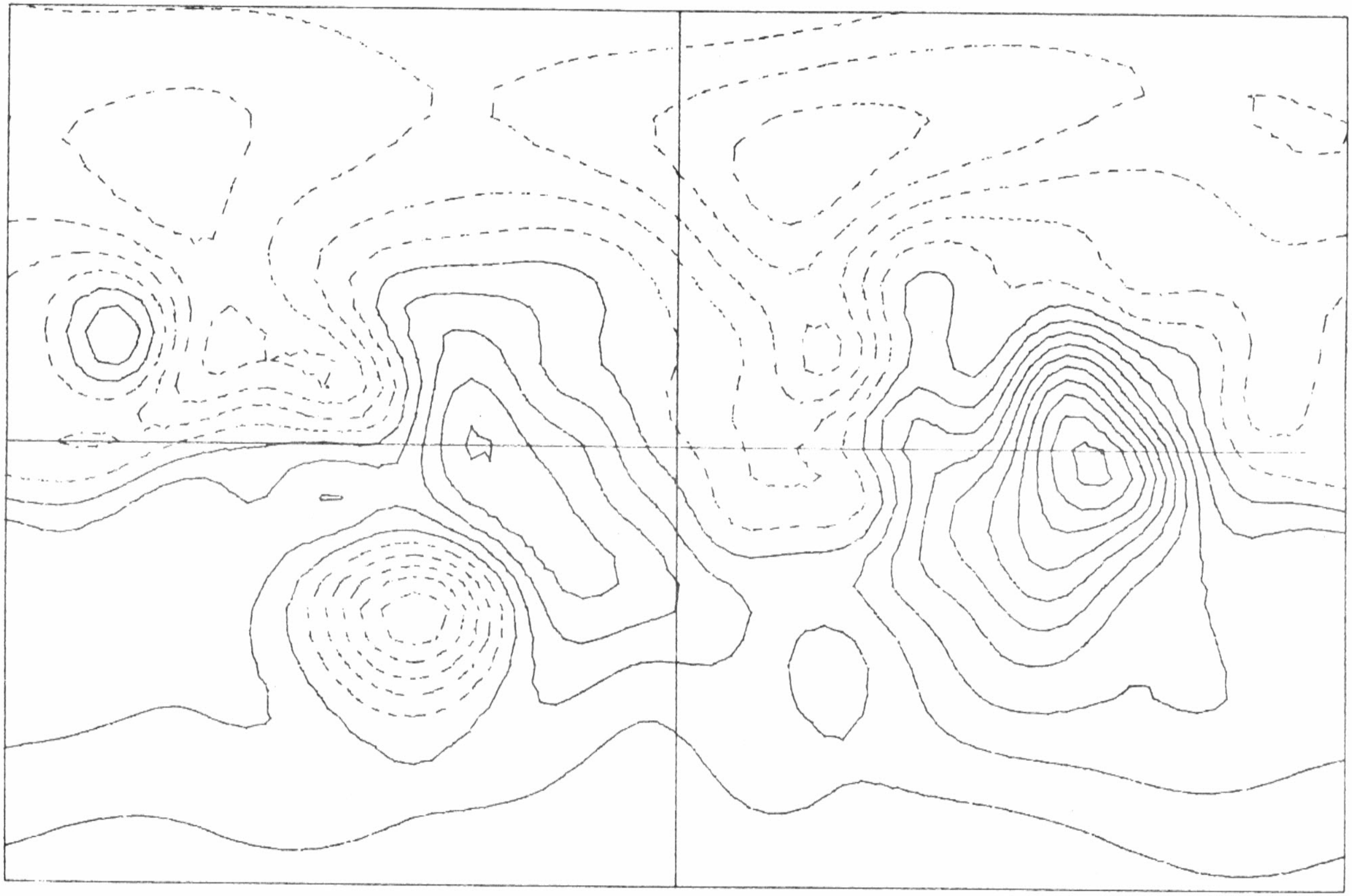

EARTH

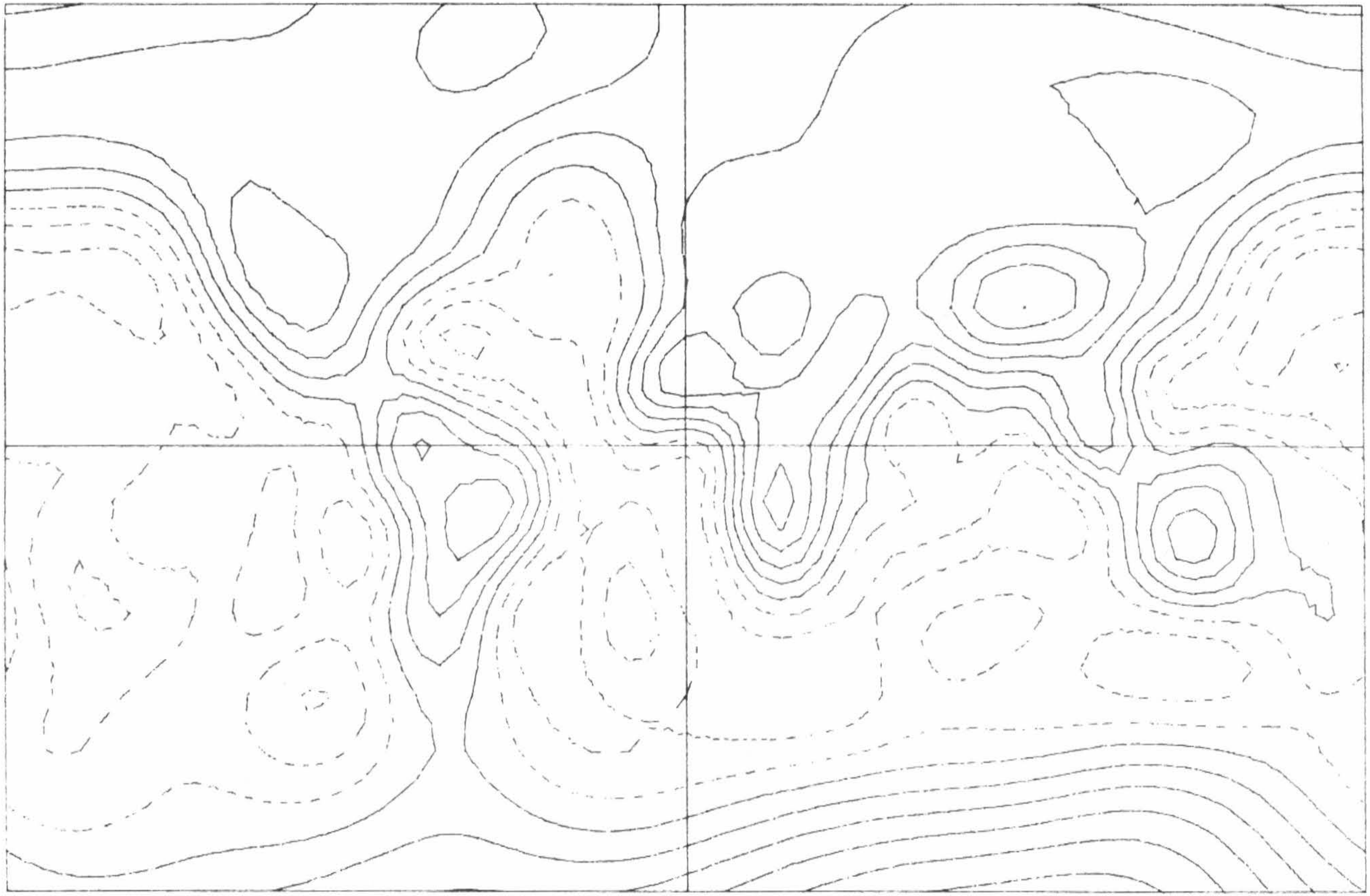

RANDOM

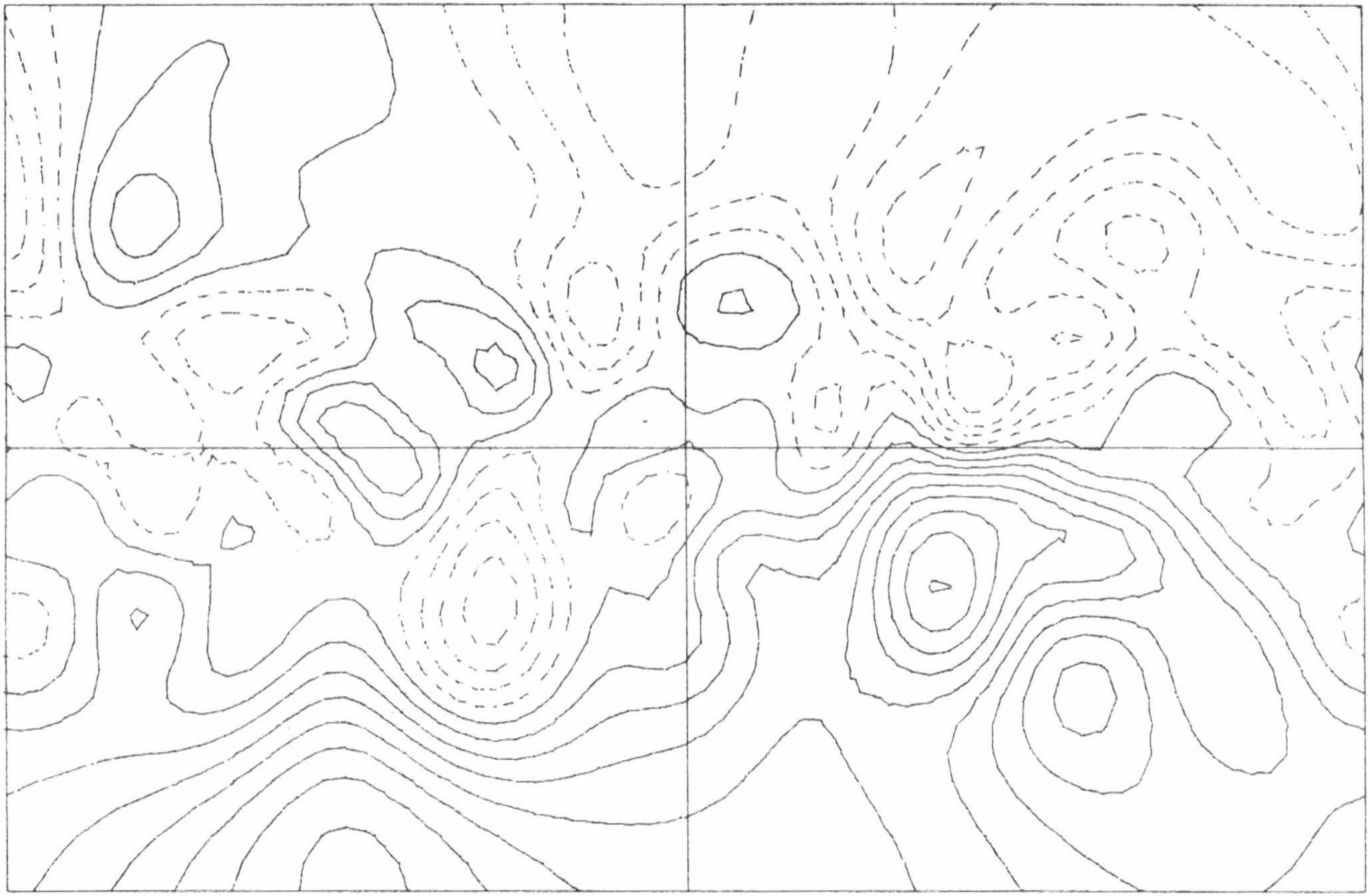

C. ANALYSIS

In this section, we will attempt to understand why planetary surfaces are characterized by the Vening-Meinesz spectral form (equ. 4.1). We will first consider (and subsequently reject) a specific physical mechanism championed by Vening-Meinesz himself - thermal convection. We will then examine some of the geometrical implications of this spectral form. This will lead to a completely equivalent reformulation of the problem in terms of a particular stochastic process rather than the variance spectrum. We then turn our attention to a number of physical systems which have analogous spectral forms to see how energy is transferred from one spectral component to another. Next, we will consider a fairly specific model for the topography which involves superposition of random pulses. We will see that the size-frequency distribution of pulses largely determines the spectral form of the resulting surface. Finally, we will consider a model which supposes only that there is a degree of equilibrium between erosive and constructional processes acting on the surface. In terms of simplicity of assumptions and verisimilitude of results, we consider this the most satisfactory explanation of the Vening-Meinesz spectral form. We close the section with a conjectured characterization of planetary surfaces in terms of continuity, fixed variance and maximal entropy.

1. Convection

Vening-Meinesz (1951) not only provided the earliest reference to the shape of the Earth's topographic variance spectrum, but also offered the earliest explanation. He argued that both the general pattern given by equation 4.1 and the principal departures therefrom are related to thermally driven convection in the mantle. The increased variance at degrees 5, 10 and 15, as best seen in the slope variance spectrum

$$V(S;n) = (n)(n+1)V(H;n) \tag{4.11}$$

were taken to be manifestations of a predominantly fifth degree convection pattern.

Walzer (1971, 1972a,b) has invoked a complex pattern of convective cells to explain the Earth's topographic variance spectrum over the range $1 \le n \le 31$. Convective models have also been proposed for the Moon (Runcorn, 1967) and Mars (Wells, 1971).

Coode (1966, 1967) showed that in a harmonic analysis of the locations of active and passive oceanic ridges and continental rift zones, the aseismic ridges have a major spectral peak at degree 4 and a secondary peak at degree 9, whereas the active seismic ridges have major and secondary spectral peaks at degrees 5 and 10 respectively. He interpreted this as evidence of a change in the dominant mode of mantle convection from degree 4 to 5. Runcorn (1965) further extended this notion in claiming that the core of the Earth has been steadily growing and that, as it has grown, the stable mode of mantle convection has been increasing. In particular, he claims that the most recent change of mode (from 4 to 5) occurred in the Permian (200 My. ago) and initiated the present era of continental drift.

Convection may very well influence the topography of the Earth and other planets. In fact, McKenzie et al. (1973) have found both positive relief features and positive gravity anomalies associated with rising convective flows in their numerical simulations. However, to infer the modes of convection in a planet from wiggles in its topographic or gravitational variance spectrum seems unjustified. Furthermore, even if convection could explain part of the spectrum, if a single explanation is sought for the form of the variance spectrum on all planets and over the entire observed spectral range, then convection is clearly inadequate.

2. Geometry

There are several interesting geometrical aspects of planetary topography which relate directly to the variance spectrum. A brief consideration of the geometry will give us better insight into the significance of the Vening-Meinesz spectral form; **and**, **in** fact, will enable us to reformulate our basic problem in different, but equivalent terms. We will be better able to say what the topography is like, but not necessarily better able to say why.

A common observation is that even those landscapes which appear quite smooth when viewed from afar, are often quite rough at a small scale. If we suppose this behavior to continue to arbitrarily small scale, we could characterize the surface as continuous but not differentiable. Based on the analyses of Beers and Dragt (1970) and of Beers (1972), we show in appendix A that a function on a sphere which is continuous, but not differentiable, has a variance spectrum which is asymptotically proportional to $1/(n)(n+1)$. Thus, if we could explain why planetary surfaces appear to be continuous, but not differentiable, we would at least understand the asymptotic behavior of the variance spectrum. However, we would still have the problem of why the low degree harmonics behave this way.

Another simple model is obtained by assuming that the surface is random and that the slope at any point is uncorrelated with the slope at any other point. In this case, the slope covariance is a delta function (Yaglom, 1962; Parzen, 1962) (see Appendix D)

$$C(S;\gamma) = S_o \, \delta(\gamma) \quad , \tag{4.12}$$

and the slope variance spectrum is constant

$$V(S;n) = S_o \quad . \tag{4.13}$$

Using the relationship between topographic variance and slope variance in equation (4.11), we see that this implies

$$V(H;n) = \frac{S_o}{(n)(n+1)} \quad . \tag{4.14}$$

The spherical Wiener process (see Appendix C) is the only stochastic process with continuous realizations which has these properties. We may, in fact, reformulate the main problem of this section. We may now ask: why are the surfaces of planets and satellites realizations of a spherical Wiener stochastic process? We will return to this notion later.

Vening-Meinesz (1951) made another interesting observation concerning the variance spectrum. He claimed that it is a result of the topography being composed of "features with elevations roughly proportional to their horizontal dimensions." As we shall see later when we consider a random pulse model for the topography, this direct proportionality is a sufficient, but not necessary, condition for the desired spectral form. However, the idea was a good one and can be developed further.

The increments

$$\Delta F(g, g+\gamma) \equiv F(g+\gamma) - F(g) \tag{4.15}$$

of a random function F: G → R are said to be self-similar with

with parameter β if, for any $\gamma > 0$ and any $g \in G$

$$\Delta F(g, g+\gamma) = \gamma^{-\beta} \Delta F(g, g+\beta\gamma) \quad , \tag{4.16}$$

where the indicated equality means that the two random variables are identically distributed. The traditional Wiener process has self-similar increments with parameter $\beta = 0.5$. Mandelbrot (1967, 1975b, 1977) has introduced the concept of fractional Weiner processes W_β which have self-similar increments with $0 \leq \beta \leq 1$. He also claims, on the basis of various landscape simulations, that the topography of the Earth is a realization of a fractional Weiner process with $\beta \doteq 0.65$. However, we note that the variance spectrum of W_β on a circle is proportional to $n^{-(2\beta+1)}$, and the observed variance spectrum of the Earth (Figure 4.3) is closer to $n^{-1.9} (\beta = 0.45)$ than to $n^{-2.3} (\beta = 0.65)$ and within probable errors is consistent with $n^{-2.0}$ $(\beta = 0.5)$.

Another interesting aspect of the Wiener and fractional Wiener processes is the extreme irregularity of their realizations. Generalizing a result of Mandelbrot (1975a) (see Appendix C), we suggest that if D[G] is the dimension of its parameter set, the dimension of a realization of $W_\beta(g)$ satisfies

$$D[W_\beta(g)] = D[G] + \beta \quad . \tag{4.17}$$

Since for our topography model $D[G] = 2$ (the surface of a sphere), we conclude that the dimension of the surface of the Earth is $2 + \beta \doteq 2.5$. It is thus intermediate between a traditional surface $(D = 2)$ and a solid $(D = 3)$.

3. Energy Redistribution

There are a number of physical systems which might serve as models for various aspects of the process or processes responsible for the observed topographic variance spectra of the terrestrial planets. A common feature of the systems we will consider is that energy is typically fed into the system over some characteristic range of spatial wavenumbers and, through non-linear interactions, this energy is redistributed across the spectrum - typically to high wavenumbers where it is dissipated.

Elastic Energy Reduction

Shaham and coworkers (Pines and Shaham, 1973; Au and Shaham, 1974) have suggested an elastic energy reduction principle for planets according to which "the direction of irreversible crustal motions must always be such as to reduce the overall elastic energy." They further suggest that an important source of elastic energy, at least for the Earth, is excess oblateness due to tidal despinning. As is shown in Appendix F, if we suppose that the total topographic variance is fixed, a shift of variance across the spectrum to higher wavenumber will in fact result in a decrease in both elastic and gravitational energy. However, at this point we have no reason to suppose that variance is conserved.

Two Dimensional Fluid Flow

There is a system in which analogs of both topographic variance and slope variance are conserved. Non-divergent two dimensional inviscid fluid flow on a sphere may be characterized by a stream function ψ in terms of which velocity v and vorticity w are

$$v = \nabla\psi \qquad (4.18)$$

$$w = \nabla^2\psi \quad . \qquad (4.19)$$

If the vorticity is expanded in a harmonic series

$$w(\theta,\varphi) = \sum_{n=1}^{\infty} \sum_{m=0}^{n} w_{nm}^{T} \; \Lambda_{nm}(\theta,\varphi) \quad , \qquad (4.20)$$

then the kinetic energy E and enstrophy F (mean square vorticity) may be expressed as (Baines, 1976),

$$E = \frac{1}{2}\int_S (\nabla\psi)^2 \; dS = \pi \sum_{n=1}^{\infty} E_n \qquad (4.21)$$

$$F = \frac{1}{2}\int_S (\nabla^2\psi)^2 \; dS = \pi \sum_{n=1}^{\infty} F_n \qquad (4.22)$$

where

$$E_n = \frac{F_n}{(n)(n+1)} \qquad (4.23)$$

and

$$F_n = \sum_{m=0}^{n} w_{nm}^{T} \; w_{nm} \quad . \qquad (4.24)$$

These quantities are clearly analogous to topographic variance and slope variance, respectively.

Fjortoft (1953) has shown that for a system in which both energy and enstrophy are conserved, any energy transfer across the spectrum must take place between components with (at least) three different values of n. Also if one of three components is a source or sink for both of the other two, its n value must be between those of the latter. The net redistribution of energy across the spectrum in such a case is rather limited.

However, in a turbulent two dimensional flow, enstrophy systematically cascades to very small scales, at which it is dissipated (Bretherton and Haidvogel, 1976). The kinetic energy, on the other hand, remains at large scales and the total kinetic energy is constant. In fact, there is an inverse energy cascade. Since the total energy

$$E = \pi \sum_{n=1}^{\infty} E_n \tag{4.25}$$

remains constant while the enstrophy

$$F = \pi \sum_{n=1}^{\infty} (n)(n+1)\, E_n \tag{4.26}$$

decreases, the energy must become more concentrated at low n. The obvious analogy is to a system in which we maintain a fixed topographic variance while reducing the mean square slope. In such a system there will be an inverse topographic variance cascade, the slope spectrum will become flatter and the topography spectrum will approach the Vening-Meinesz form. We shall return to this notion later. Incidentally, turbulence in three dimensional flows is more complicated (Hinze, 1959; Mandelbrot, 1975a).

4. Random Pulse Model

We have seen that the spherical Wiener process is an excellent model for planetary surface topography. We now hope to gain some further insight into this situation by considering representations of random processes by superposition of random pulses. The general theory of such phenomenological models for random processes is discussed by Middleton (1951).

Halford (1968) has shown that processes with variance spectra proportional to $n^{-\alpha}$ over an arbitrarily large range of frequencies can be generated from a physically realizable class of pulses only if $0 \leq \alpha \leq 2$. Bell (1974) has recently considered the inverse problem of inferring the pulse size-frequency distribution from the variance spectrum of the process and an assumed pulse shape. We shall only be directly concerned with the forward problem.

As a model for a broad class of stochastic processes on the sphere, we may consider the superposition of a collection of zero-sum binary pulses $A_k Z(\gamma,\gamma_k)$ with random amplitudes, widths and locations. These pulses represent individual topographic features and the conservation of mass requires that

$$\int_{-1}^{1} Z(\mu,\mu_k)\ d\mu = 0 \tag{4.27}$$

where γ is angular distance and $\mu = \cos(\gamma)$. See Appendix A for more about these pulses and Appendices A and D for discussion of several theorems mentioned in the following.

To facilitate the calculation of the covariance function and variance spectrum of this model, we will first consider two simpler scenarios. This will enable us to obtain valuable intermediate results. The first configuration is a Poisson distribution of unit delta functions with an average of α impulses per unit area:

$$F(\theta,\varphi) = \sum_k \delta(\theta - \theta_k, \varphi - \varphi_k) \tag{4.28}$$

where (θ_k,φ_k) is the location of the k-th impulse. By a simple application of Campbell's theorem, equation (D.23), we find that the covariance function is

$$C(F;\gamma) = \alpha\ \delta(\gamma) \tag{4.29}$$

and therefore the variance spectrum is

$$\begin{aligned} V(F;n) &= \int_{-1}^{1} C(F;\mu)\ P_n(\mu)\ d\mu \\ &= \alpha \quad . \end{aligned} \tag{4.30}$$

Obviously, this is not a very good model for topography, since the spectrum is flat.

The next model we consider consists of a Poisson distribution of zero-sum pulses with amplitude A, width γ_o and an average density of α pulses per unit area. We use the relocation property of convolution with a delta function to express this configuration as:

$$G(\theta,\varphi) = \sum_k A_o \; Z(\gamma,\gamma_o) \; * \; \delta(\theta - \theta_k, \varphi - \varphi_k) \quad . \tag{4.31}$$

The variance spectrum is, by the convolution theorem, equation (D.25),

$$\begin{aligned} V(G;n) &= \left[A_o Z_n(\mu_o)\right]^2 \, V(F;n) \\ &= 4 \, \alpha \, A_o^2 \, (1 - \mu_o)^2 \left[\frac{P_n'(\mu_o)}{(n)\,(n+1)}\right]^2 \quad . \end{aligned} \tag{4.32}$$

This is a better model in that the variance spectrum does generally decrease with increasing degree, but it is still unsatisfactory since the spectrum is quite irregular. Superimposed on the overall decrease, there are nearly periodic variations which correspond to fluctuations in $P_n'(\mu_o)$ with varying n. For $\gamma_o = 0$, the spectrum is still flat. However, as the pulse width increases the spectrum begins to fall off more rapidly and the fluctuations get closer together and generally more pronounced. Finally when $\gamma_o = \pi/2$, all the even degree harmonics are identically zero.

Finally, we consider the case where the amplitudes and widths of the pulses are also random:

$$H(\theta,\varphi) = \sum_k A_k \; Z(\gamma,\gamma_k) \; * \; \delta(\theta - \theta_k, \varphi - \varphi_k) \quad . \tag{4.33}$$

This will maintain the overall spectral decrease, but smooths out the

the fluctuations. If $p(A,\mu_o)$ is the joint probability density of pulse amplitudes and widths, then we can write the variance spectrum as

$$V(H;n) = \alpha \int_o^\infty \int_{-1}^{1} p(A,\mu_o) \left[A\ Z_n(\mu_o)\right]^2 d\mu_o dA \tag{4.34}$$

We can simplify this somewhat by noting that

$$\int_o^\infty p(A,\mu_o)\ A^2 dA = p(\mu_o)\ A^2(\mu_o) \tag{4.35}$$

where $p(\mu_o)$ is the marginal probability density of pulse widths and $A^2(\mu_o)$ is the mean square amplitude of pulses of width $\gamma_o = \cos^{-1}(\mu_o)$. We thus find

$$\begin{aligned} V(H;n) &= \alpha \int_{-1}^{1} p(\mu_o) \left[A(\mu_o)\ Z_n(\mu_o)\right]^2 d\mu_o \\ &= \frac{4\alpha}{[(n)(n+1)]^2} \int_{-1}^{1} p(\mu_o) \left[A(\mu_o)(1-\mu_o)\ P_n'(\mu_o)\right]^2 d\mu_o \quad . \end{aligned} \tag{4.36}$$

In order to make further progress with this integral, we will need to make some assumptions concerning the distribution of pulse sizes. A particularly interesting distribution results from the assumption that the product

$$p(\mu_o)\ A^2(\mu_o)\ \frac{1-\mu_o}{1+\mu_o} = \beta \tag{4.37}$$

is a constant. The resulting variance spectrum is

$$\begin{aligned} V(H;n) &= \frac{4\alpha\beta}{[(n)(n+1)]^2} \int_{-1}^{1} (1-\mu_o^2)[P_n'(\mu_o)]^2 \, d\mu_o \\ &= \frac{8\alpha\beta}{(n)(n+1)} \end{aligned} \tag{4.38}$$

since

$$\int_{-1}^{1} (1-\mu_o^2)[P_n'(\mu_o)]^2 \, d\mu_o = 2(n)(n+1) \quad . \tag{4.39}$$

If we now increase the average density of pulses α and decrease the average pulse size in such a way that the product $\alpha\beta$ remains constant, we obtain a good approximation to a spherical Weiner process. The covariance function and total variance are:

$$\begin{aligned} C(H;\gamma) &= \sum_{n=1}^{\infty} V(H;n)\ P_n[\cos(\gamma)] \\ &= 8\alpha\beta \sum_{n=1}^{\infty} \frac{P_n[\cos(\gamma)]}{(n)(n+1)} \\ &= 8\alpha\beta \left(1 - 2\,\ell n\left[1+\sin(\gamma/2)\right]\right) \\ C(H;0) &= 8\alpha\beta \end{aligned} \tag{4.40}$$

In the next few paragraphs, we will attempt to justify the assumed pulse size-frequency distribution used in the above derivation. Perhaps the strongest justification comes simply from the fact that it produces the observed variance spectrum, and , within the context of this random pulse model, it is the only way to do so. However, we should try to find out more about why it works. Paraphrasing Halford

(1968), "the crucial problem is to find the physical circumstances which cause the product $p(\mu_o)\ A^2(\mu_o)$ to vary approximately as $(1+\mu_o)/(1-\mu_o)$; the shape of the perturbation is probably irrelevant." We will therefore consider both $A^2(\mu_o)$, the relation between mean square pulse amplitude and width or horizontal extent, and $p(\mu_o)$, the pulse width-frequency distribution, in a number of different contexts.

Energy Equipartitioning

Bell (1975) has presented an interesting model which essentially argues for constancy of the product

$$\beta = p(\mu_o)\ A^2(\mu_o)\left(\frac{1-\mu_o}{1+\mu_o}\right) \tag{4.41}$$

based on putative equipartitioning of gravitational potential energy amongst various hill sizes. His analysis was set on a line rather than a sphere, and thus ignores both the curvature and two-dimensional nature of the domain; however, neither of these are serious problems. In essence, he claims that the potential energy of a binary pulse with amplitude A and width $\gamma_o = \cos^{-1}(\mu_o)$ is proportional to $A^2(1-\mu_o)/(1+\mu_o)$ and that $p(\mu_o)$ is the relative frequency of these pulses. He then claims that "the observed shape of the spectrum implies an equilibrium state of maximum disorder in which energy of formation is distributed uniformly over all hill sizes... The smaller hills may require less energy of formation, but are sufficiently more numerous than the larger hills so as to insure this equipartition of energy."

Though this argument has a certain appeal, some of which accrues from analogies with thermodynamic concepts such as entropy maximization, energy equipartitioning and statistical equilibrium, which we shall mention again later, it has at least two serious flaws. First, as is shown in Appendix F, the potential energy perturbation of a cylindrical mass on the surface of a sphere is not simply proportional to the basal area times the squared height. To assume so is to neglect the self-potential of the added mass which significantly alters the potential energy spectrum. Secondly, there is no obvious physical reason why energy should be equally partitioned among hill sizes. The thermodynamic analogy invoked would appear to be valid only for energy distribution among the normal modes of the system (Kampé de Fériet, 1962).

Slope Stability

The height of a topographic feature may be limited simply by the strength of its constituent materials. Hartmann (1972) and Johnson and McGetchin (1973) have attempted to explain the scale of planetary topographic features in this way. As shown in Appendix G, a simple slope stability analysis (Culmann, 1866) indicates that, neglecting internal friction, the maximum stable height of a slope of length L in material characterized by density ρ and cohesion c on a planet with surface gravity g is given by

$$H^2(L) = \frac{8\,c\,L}{\rho g}\left(1 + \frac{L_o}{L}\right) \tag{4.42}$$

where

$$L_o = \frac{2c}{\rho g}$$

has a value of meters to possibly tens of meters in typical terrestrial or lunar soils. Thus, at the scales in which we are interested $L \gg L_o$, and we have approximately

$$H^2(L) = \frac{8c}{\rho g} L \quad . \tag{4.43}$$

Thus, we might expect the mean square height of topographic features to be directly proportional to their horizontal extent. We shall find, in fact, that this is a reasonable approximation in several important situations.

A further implication of the above analysis is that the mean square slope between points a distance $L = R_o\gamma$ apart should be approximately

$$S^2(\gamma) = \frac{H^2(R_o\gamma)}{(R_o\gamma)^2} = \frac{8c}{\rho g R_o \gamma} \quad . \tag{4.44}$$

Comparing this result with equation 4.5, we see that our slope stability analysis has yielded not only the correct functional dependence on γ, but also an estimate of the total topographic variance

$$V(H;0) = \frac{4c}{\rho g R_o} \quad . \tag{4.45}$$

Impact Cratering

Impact cratering has been an important process on essentially all planetary surfaces. Malin and Dzurisin (1977) summarize morphology and depth/diameter relationships for craters on the Moon, Mars and Mercury. They find that the relationship between depth d and diameter D for morphologically fresh craters is adequately represented by a two part power law:

$$d = d_o (D/D_o)^b \qquad ; \qquad (4.46)$$

for craters with $D \leqslant 10$ km the exponent is approximately $b = 1.0$, whereas for $D > 10$ km, the exponent decreases to 0.25-0.45 depending upon the data set analyzed. Our slope stability analysis in the previous paragraphs would imply $b = 0.5$. If both fresh and degraded craters are considered together, there is an increased scatter, but a single power law is quite adequate to describe the entire range of crater sizes and the corresponding exponent is approximately $b = 0.6$ on all three planets.

Another important aspect of impact cratering is the resultant distribution of crater sizes. We may imagine an initially uncratered surface upon which craters are being produced at random. We further suppose that the relative frequency of craters larger than D being produced is

$$N = N_o (D/D_o)^{-c}. \qquad (4.47)$$

As the first few craters are formed, there will be little obliteration of pre-existing craters and the size-density distribution of the surface will reflect the production distribution. As more craters are formed, older craters will be destroyed, and the size-density distribution will tend more to reflect the details of the obliteration process rather than the production size distribution. Eventually a point may be reached where the size-density distribution no longer changes with the formation of additional craters. If the crater-destroying process is simply geometrical overlap, the surface will be said to have attained saturation. If, in addition to crater overlap, crater destruction occurs by processes of erosion and filling, the surface will be said to have attained equilibrium. Woronow (1977) notes that "saturation results from purely geometrical and statistical considerations, valid for any hypothetical surface anywhere, whereas equilibrium results from the interaction of the crater population with its physical environment.... The difference between the crater densities at saturation and at equilibrium on any planetary body indicates the vitality of the degradational processes present there."

The equilibrium and saturation size-density distributions have been studied through stochastic models of formation and survival of craters (Marcus, 1964, 1966, 1967, 1970b; Neukum and Dietzel, 1971) and Monte-Carlo simulations (Woronow, 1977). An interesting result is that a production distribution with $c > 2$ leads to a saturation population with $c = 2$, whereas production distributions with $1.5 \leq c \leq 2$ lead to saturation populations with c approaching 1.0. Furthermore, it is found that equilibrium populations always have $c \leq 2$, with equality only as equilibrium degenerates to saturation. Observed size-density distributions tend to have $c \doteq 1.7$ for craters larger than a kilometer (Soderblom, 1970).

We will now compare these observations with Halford's (1968) one dimensional pulse criterion for an n^{-a} spectrum. The requirement is that

$$p(D)\, A^2(D) = p_o A_o^2 (D/D_o)^{-a+1} \quad . \qquad (4.48)$$

The probability distribution p(D) corresponding to a cumulative size-frequency distribution of the form (4.47)

$$p(D) = p_o (D/D_o)^{-c-1} \qquad (4.49)$$

and the mean-square amplitude distribution corresponding to the depth-diameter relation (4.46) is

$$A^2(D) = A_o^2 (D/D_o)^{2b} \quad . \qquad (4.50)$$

In this case, Halford's criterion reduces to

$$a = 2 - 2b + c \quad . \qquad (4.51)$$

For the observed mean values of $c = 1.7$ and $b = 0.6$, we find $a = 2.4$. On the other hand, if we consider a surface saturated with small ($D \leq 10$ km) craters for which $c = 2.0$ and $b = 1.0$, we do obtain $a = 2.0$, as desired.

Though this agreement (or lack thereof) is instructive, it is not as definitive as we might hope, since the actual shape of the craters changes as a function of size, contrary to the assumption of of Halford's (1968) model. Thus, depth and diameter measurements and counts of craters do not suffice to directly estimate the spectrum of a planetary surface.

5. Equilibrium

Historical Background

At least since the work of Gilbert (1877), it has been widely recognized that most terrestrial landforms are in a state of dynamic equilibrium between the erosional and constructional processes to which they are subjected. Most of the quantitative applications of this concept have dealt with single landform elements. For example, Kirkby (1971) states that in the development of a hillslope "the influence of the initial form of the slope can be shown to decrease rapidly with time, while the slope forms tend closer and closer towards a 'characteristic form,' in which the elevation of each point continues to decline with time, but is independent of the initial form." He further notes that this equilibrium form "depends solely on the nature and relative rates of the formative process and not at all on the initial profile of the hillslope." This relationship between form and process is further developed by Carson and Kirkby (1972), again in relation to hillslopes.

Leopold and Langbein (1962) have attempted to apply the equilibrium approach to the more general problem of evolution of an entire landscape. They claim that, for example, "the most probable condition exists when energy in a river system is as uniformly distributed as may be permitted by physical constraints." An analogy is drawn with closed thermodynamic systems in which entropy is maximized at equilibrium and topographic elevation is identified as the corresponding analog of temperature. Though the analogy is enlightening, they do not rigorously justify it, and furthermore they fail to produce any quantitative results for general landscapes. However, they do examine a "most probable" river profile in which the downstream rate of entropy production is constant.

Culling (1960, 1963, 1965), in developing an analytical theory of erosion, states that "slope erosion is subject to a minimal law; that factor, whether the rate of transport or the rate of weathering, which is relatively the least efficient, controls the general course of denudation. On soil covered slopes the rate of transport is the dominant denudational control, soil creep being the responsible agency." He further concludes that the mass movement of weathered material on a hillside slope takes place at a rate proportional to the surface gradient. This leads to a diffusivity-type equation for elevation change

$$\beta' \frac{\partial H}{\partial t} = \nabla^2 H \tag{4.52}$$

This model is not only consistent with a microscopic analysis of motions of individual soil particles, but also, on a macroscopic level, it predicts slope forms actually observed on soil covered slopes. Soderblom (1970) has considered a similar model for erosion due to impact cratering.

Scheidegger and Chaudhari (1964) have examined these thermodynamic analogies in some detail. They conclude that "whenever a system is a linear combination of a large number of fluctuating systems, and in the 'large' system a certain quantity is a constant of the motion to which the component systems contribute positive-definite amounts, then, under equilibrium conditions, that quantity is canonically distributed in the component systems and, under nonequilibrium conditions, assuming linear regression of the fluctuations and microscopic reversibility, the quantity in question is subject to a diffusivity equation with symmetric diffusivity tensor." Scheidegger (1967) then attempted to develop a complete thermodynamic analogy for landscape evolution in which the conserved quantity is mass or equivalently mean topographic elevation. Local elevation is then analogous to temperature. Though the complete analogy is interesting and even extends to Carnot cycles and the like, it is not clear that anything additional of real relevance to the topographic variance spectrum emerges from this analysis. Another criticism of the model is that topographic elevation can be either positive or negative, and thus is not a suitable temperature analog. Perhaps in addition to conserving mass (mean elevation), we should consider a model in which topographic variance (mean square elevation) is conserved (Chung and Scheidegger, 1968). We shall return to this notion in our final attempt to explain the Vening-Meinesz spectrum.

Dynamic Model

Up to this point, we have paid little explicit attention to the time variation of surface topography. However, we now have all the necessary background information for our penultimate model in which we consider the dynamics of planetary surfaces. We simply suppose that the observed surface is formed by two opposing processes, erosion and uplift. We model the erosion by the diffusivity equation (Culling, 1960, 1963, 1965)

$$\beta' \frac{\partial H}{\partial t} = \nabla^2 H \tag{4.53}$$

where β', a measure of the intensity of the erosion, is assumed constant. We further suppose that linearly additive constructional or "tectonic" events occur essentially instantaneously relative to the erosive time scale and that they occur at random times and places. The times of occurence have a Poisson distribution with an average of α' events per unit time. A typical event has the form

$$f(\theta,\varphi) = R_o \sum_{n=1}^{\infty} \sum_{m=0}^{n} f_{nm}^{T} \Lambda_{nm}(\theta,\varphi) \tag{4.54}$$

where $\mathbf{f}_{nm}$ are zero-mean Gaussian random variables $N(0,\sigma_n^2)$, where

$$\sigma_n^2 = \frac{V(f;n)}{2n+1} \tag{4.55}$$

and the degree variances of the process are

$$V(f;n) = \sum_{m=0}^{n} f_{nm}^{T} f_{nm} \quad . \tag{4.56}$$

We will now determine what form the variance spectrum of the constructional process must take in order to produce the Vening-Meinesz topographic spectral form.

The spatial covariance of the topography initially produced by a single event is

$$C(f;\gamma) = R_o^2 \sum_{n=1}^{\infty} V(f;n) \; P_n \left[\cos(\gamma)\right] \quad . \tag{4.57}$$

However, erosion reduces the effect at time t of a single tectonic event which occurred at an earlier time t - τ to

$$f'(\theta,\varphi;\tau) = R_o \sum_{n=1}^{\infty} \sum_{m=0}^{n} f_{nm}^{T} \Lambda_{nm}(\theta,\varphi)\, \mathscr{E}_n(\tau) \qquad (4.58)$$

where

$$\mathscr{E}_n(\tau) = e^{-(n)(n+1)\tau/\beta'} \qquad (4.59)$$

(see Appendix A). Therefore, the spatial and temporal covariance function of the equilibrium surface produced by these processes is, by the convolution theorem,

$$\begin{aligned} C(H;\gamma,\tau) &\equiv E\,[\,H(\Omega,t)\; H(\Omega+\gamma,t+\tau)] \\ &= \alpha' R_o^2 \int_{-\infty}^{t} \sum_{n=1}^{\infty} V(f;n)\; P_n[\cos(\gamma)] \qquad (4.60) \\ &\quad \cdot \mathscr{E}_n(t-s)\, \mathscr{E}_n(t+\tau-s)\; ds. \end{aligned}$$

We can simplify this by taking terms with no time dependence outside the integral and noting that

$$\begin{aligned} &\int_{-\infty}^{t} \mathscr{E}_n(t-s)\, \mathscr{E}_n(t+\tau-s)\; ds \\ &= \mathscr{E}_n(2t+\tau) \int_{-\infty}^{t} \mathscr{E}_n(-2s)\, ds \qquad (4.61) \\ &= \frac{\beta'\, \mathscr{E}_n(\tau)}{2(n)(n+1)} \quad . \end{aligned}$$

Therefore, we obtain

$$C(H;\gamma,\tau) = \frac{\alpha'\beta'}{2} R_o^{\;2} \sum_{n=1}^{\infty} \frac{V(f,n)}{(n)(n+1)} P_n[\cos(\gamma)] \mathscr{E}_n(\tau) \qquad (4.62)$$

The resulting purely spatial ($\tau = 0$) and purely temporal ($\gamma = 0$) covariance functions are

$$C(H;\gamma) = \frac{\alpha'\beta'}{2} R_o^2 \sum_{n=1}^{\infty} \frac{V(f;n)}{(n)(n+1)} P_n [\cos(\gamma)] \qquad (4.63)$$

and

$$C(H;\tau) = \frac{\alpha'\beta'}{2} R_o^{\;2} \sum_{n=1}^{\infty} \frac{V(f;n)}{(n)(n+1)} \mathscr{E}_n(\tau) \qquad (4.64)$$

respectively, since $P_n[\cos(0)] = \mathscr{E}_n(0) = 1$. Generalizing a result of Grenander (1975), we assert that for a model of this type, given the heights at a time t

$$H(\theta,\varphi;t) = R_o \sum_{n=1}^{\infty} \sum_{m=0}^{n} H_{nm}^{\;\;T} \Lambda_{nm}(\theta,\varphi) \quad , \qquad (4.65)$$

the optimal estimate (in the sense of least-square error) of heights at an earlier or later time $t \pm \tau$ is given by

$$\hat{H}(\theta,\varphi;t \pm \tau) = R_o \sum_{n=1}^{\infty} \sum_{m=0}^{n} H_{nm}^{\;\;T} \Lambda_{nm}(\theta,\varphi) \mathscr{E}_n(\tau) \quad . \qquad (4.66)$$

The mean square error of the estimate is

$$\begin{aligned} &E\left[\left|\hat{H}(\Omega,t\pm\tau) - H(\Omega,t\pm\tau)\right|^2\right] \\ &= R_o^{\;2} \sum_{n=1}^{\infty} V(H;n) \left[1 - \mathscr{E}_n(2\tau)\right] \quad . \end{aligned} \qquad (4.67)$$

Unfortunately, unless we have independent estimates of $\alpha' V(f;n)$ or β', we cannot evaluate $\mathscr{E}_n(\tau)$, since all that is observable at one time is

$$V(H;n) = \frac{\alpha'\beta'}{2} \frac{V(f;n)}{(n)(n+1)} \quad . \tag{4.68}$$

In order to duplicate the Vening-Meinesz spectrum, we simply require that

$$V(f;n) = \frac{2}{\alpha'\beta'} V(H;0) \tag{4.69}$$

i.e. the variance spectrum of the constructional process must be constant. This has the interesting interpretation that there is no preferred scale at which tectonic or constructional processes occur.

In order to match the observed low degree variances as well, we must either allow for a decrease in constructional activity at scale lengths greater than L $\doteq$ 2000 km, or assume more erosive or attenuative activity at that scale than the diffusivity model predicts. Note that, whereas diffusive erosion is essentially a low pass filter, visco-elastic deformation acts as a high pass filter and would selectively attenuate the low degree harmonics. We will now consider this in more detail.

Visco-Elastic Deformation

Darwin (1879) determined that a homogeneous Maxwell sphere (see Appendix E) subjected to a surface load of height $f(\theta,\varphi)$ at time t will deform in such a way that, at a later time $t + \tau$, the load height will be reduced to

$$f'(\theta,\varphi;\tau) = R_o \sum_{n=1}^{\infty} \sum_{m=0}^{n} f_{nm}^{T} \Lambda_{nm}(\theta,\varphi)\, e^{-\tau/\tau'_n} \quad . \tag{4.70}$$

If the sphere of radius R_o has density ρ, viscosity η and rigidity μ, then the relaxation time will be

$$\tau_n' = \eta \left[\frac{N(n)}{P_c} + \frac{1}{\mu} \right] \tag{4.71}$$

where

$$P_c = 2\pi G \rho^2 R_o{}^2/3 \tag{4.72}$$

is the hydrostatic pressure at the center of the sphere and

$$N(n) = \frac{2(n+1)^2 + 1}{2n} \tag{4.73}$$

is a geometrical factor determined by the spherical boundary conditions. This can be rewritten as

$$\tau_n' = \tau_n + \tau_M \tag{4.74}$$

where $\tau_n = \eta\, N(n)/P_c$ is the corresponding relaxation time for a purely viscous sphere and $\tau_M = \eta/\mu$ is the Maxwell relaxation time of the material. For times $\tau < \tau_M$, the behavior is predominantly elastic, whereas for $\tau > \tau_M$, viscous behavior predominates.

If the topography of a Maxwell sphere is then subjected to erosion, the attenuating factor for the harmonics of degree n will be

$$\mathscr{E}'_n(\tau) = e^{-[(n)(n+1)\tau/\beta' + \tau/\tau_n']} \tag{4.75}$$

rather than (4.59). If we now carry through the same covariance analysis as before, substituting $\mathscr{E}'_n$ for $\mathscr{E}_n$, we find that the resultant topographic variance spectrum is

$$V(H;n) = \frac{\alpha'\beta'}{2} \frac{V(f;n)}{(n)(n+1)} A(n) \qquad 4.76)$$

where

$$A(n) = \left[1 + \frac{\beta'}{(n)(n+1)\ \tau_n'} \right]^{-1} \quad . \tag{4.77}$$

If we neglect the elastic component, this is approximately

$$A(n) \doteq \left[1 + \frac{2P_c\,\beta'/\eta}{(n+1)(2(n+1)^2+1)}\right]^{-1} \quad . \tag{4.78}$$

This model succeeds in predicting attenuation of the low degree variances. Furthermore, because of the strong dependence of P_c on R_o, it also predicts relatively more attenuation on large planets than on small planets with the same material properties. A value of $P_c\beta'/\eta \doteq 70$ yields a spectrum very similar in shape to those of the Earth and Venus.

A possible criticism of the above model is that it assumes the planets to be homogeneous. However, more sophisticated analyses of the viscous relaxation time spectrum τ_n of the Earth (e.g., Anderson and O'Connel, 1967) have shown it to be qualitatively similar to the homogeneous case. The important point is that τ_n is a rapidly increasing function of harmonic degree.

The success of this model in duplicating the entire topographic variance spectrum on all planets for which we have observations increases our confidence in the model and strengthens our earlier conclusion that there is no preferred scale of constructional activity on the planets.

In addition to duplicating the Vening-Meinesz spectral form, the models we have considered have given us three separate estimates of the total dimensionless variance. From slope stability considerations, we find

$$V(H;0) = \frac{4c}{\rho g R_o} \quad , \tag{4.79}$$

from the random pulse model, we have

$$V(H;0) = 8\alpha\, p(\mu_o)\, A^2(\mu_o) \left[\frac{1-\mu_o}{1+\mu_o}\right] \tag{4.80}$$

$$= 8\alpha\beta$$

and from the equilibrium model, we obtain

$$V(H;0) = \frac{\alpha'\beta'}{2} V(f;0) \quad . \tag{4.81}$$

We would like to use these model variances to predict the actual variance on planetary surfaces which have not yet been measured. However, the only one of these formulas with any real predictive value is the first, since we have no good a priori estimates of the parameters in the other two. The greatest uncertainty in equation (4.79) is the mean cohesion c. It turns out that a value of c between 0.2-0.8 bar gives the correct variance on all four planets we have considered. These values roughly correspond to a loosely consolidated soil.

A still better prediction comes from the observation that the physical variance C(H;0) of the four planets we have studied all fall in the range 4.0-6.5 km^2 (Moon, 4.5; Mars, 6.4; Venus, 4.0; Earth 5.6). This is perhaps suggestive of a plastic rather than visco-elastic rheology. However, we shall not pursue this matter further.

Maximum Entropy Conjecture

Our final attempt at explaining the topography of the planets focuses on the fact that planetary surfaces resemble realizations of the spherical Wiener stochastic process. First, we are going to make two conjectures concerning the Wiener process: neither of them will be proven, but we will give plausibility arguments for both. We will then discuss how this relates to planetary surfaces.

As background for our first conjecture, we note that the process which we have glibly referred to as the spherical Wiener process differs from the usual Wiener process $W(\varphi)$ in several fundamental aspects. The domain Φ of $W(\varphi)$ is usually taken to be either the real line R or some Euclidean space R^n (Levy, 1948), and on those dommains $W(\varphi)$ is not stationary. However, Levy (1954) has shown that a process defined as

$$h(\varphi) = \sum_{m=1}^{\infty} \xi_m^T \Lambda_m(\varphi) \tag{4.82}$$

where

$$\Lambda_m(\varphi) = \begin{bmatrix} \cos (m\varphi) \\ \sin (m\varphi) \end{bmatrix} \tag{4.83}$$

and

$$\xi_m = \begin{bmatrix} \xi_{m1} \\ \xi_{m2} \end{bmatrix} \tag{4.84}$$

is equivalent to

$$h(\varphi) = W(\varphi) - \frac{\varphi}{2\pi} W(2\pi) \tag{4.85}$$

and is stationary, if ξ_{mi} are Gaussian random variables $N(0,\sigma_m{}^2)$ with

$$\sigma_m^2 = \frac{V(h;0)}{2m^2} \quad . \tag{4.86}$$

Of course, this is nothing more than a great circle slice of what we have been calling a spherical Wiener process. Another stationary process which otherwise resembles the Wiener process is the Ornstein-Uhlenbeck process (see Appendix C). It is obtained from a random walk subjected to a restoring force in the limit as the step size goes to zero. Our first conjecture then is that, when the domain of the process is a sphere (or circle), the Wiener and Ornstein - Uhlenbeck processes are identical. Since these are both Gaussian processes, all that is required for the proof is a demonstration that their covariance functions are identical. Though this appears likely, we have not rigorously shown it to be so. In our discussion, we have assumed that the conjecture is true and simply refer to the process in question as a spherical (or circular) Wiener process.

Our second conjecture is that for a given variance, the spherical (or circular) Wiener process is the unique maximal entropy spherical (circular) process with continuous realizations and infinite bandwidth. As an argument for the plausibility of this conjecture, consider our random pulse model. The positions of the pulses are governed by a Poisson distribution which has the maximum entropy rate of any point process for a given intensity α (McFadden, 1965). As we let the average variance per pulse β decrease while increasing α so as to maintain a constant total variance $\alpha\beta$, the central limit theorem assures us that the distribution of heights tends to a

Gaussian, which is the maximal entropy distribution for a fixed mean and variance. This argument is suggestive only and not conclusive, since our conjecture concerns the entire process describing the surface and not merely the distribution of heights. The fact that the spherical (circular) Wiener process is a Gaussian process is probably a necessary condition, but is definitely not sufficient for our conjecture.

A proof might be developed as follows. For simplicity, we consider Levy's (1954) construction of the circular Wiener process (4.79). The system has two degrees of freedom for each harmonic degree m. The variance and entropy per degree of freedom are (Shannon, 1948)

$$v(h) = \sigma_m^2 \tag{4.87}$$

$$e(h) = \frac{1}{2}\left[1 + \ell n(2\pi\sigma_m^2)\right] \quad . \tag{4.88}$$

Therefore, the total variance and entropy are

$$V(h) = \sum_{m=1}^{\infty} 2\sigma_m^2 \tag{4.89}$$

$$E(h) = \sum_{m=1}^{\infty} 1 + \ell n(2\pi\sigma_m^2) \quad . \tag{4.90}$$

The requirement of continuous realizations for the process is essentially assured by maintaining finite total variance. This, in conjunction with the requirement of infinite bandwidth, requires

$$\sigma_m^2 = \mathcal{O}\left(m^{-2}\right) \quad . \tag{4.91}$$

Our conjecture is that the extremal value of E subject to these constraints is obtained when

$$\sigma_m^2 = \frac{3\ V(h)}{(\pi m)^2} \tag{4.92}$$

since

$$\sum_{m=1}^{\infty} \frac{1}{m^2} = \frac{\pi^2}{6} \quad . \tag{4.93}$$

The application of this conjecture to planetary topographic variance spectra is very simple, and is akin to the thermodynamic analogies of Scheidegger (1967) with the additional constraint of fixed variance. Our final model for the Vening-Meinesz spectrum merely supposes that the surface of a planet is as random or chaotic as it can be subject to the constraints of continuity and finite variance.

D. IMPLICATIONS

The simplest application of this study is to predict the form of the topographic variance spectra of other planets and satellites. Therefore, we make the following

Prediction:

The topographic variance spectra of the surfaces of all solid planets and satellites have the form

$$V(H;n) = \begin{cases} V(H;n_o) & n \le n_o \\[2ex] \dfrac{V(H;0)}{(n)(n+1)} & n \ge n_o \end{cases} \tag{4.94}$$

where $L_o = 2\pi R_o/n_o \doteq 2000$ km.

Furthermore, the total physical variance is

$$C(H;0) \equiv R_o^{\,2} \sum_{n=1}^{\infty} V(H;n) \tag{4.95}$$

$$\doteq 5 \pm 2 \text{ km}^2$$

independent of the size of the body, for all

$$R_o \geq 10 \text{ km} \quad .$$

* * *

We note that recent observations of Phobos (R_o = 11.2 km) and Deimos (R_o = 6.3 km) indicate rough, heavily cratered surfaces with variances of 2-3 km^2 about the best fitting tri-axial ellipsoids (Duxbury, 1974,1976).

Our observations concerning topographic variance spectra may contribute to another problem of current interest: determining the depth of sources of planetary gravity anomalies. The main difficulty is the inherent non-uniqueness of the density distribution

$$\rho(R,\theta,\varphi) = \bar{\rho}\left[1 + \sum_{n=1}^{\infty}\sum_{m=0}^{n} \rho^{T}_{nm}(R)\ \Lambda_{nm}(\theta,\varphi)\right] \tag{4.96}$$

associated with a given external potential

$$\Phi(R,\theta,\varphi) = \frac{GM}{R_o}\left[\frac{R_o}{R} + \sum_{n=1}^{\infty}\sum_{m=0}^{n}\left(\frac{R_o}{R}\right)^{n+1} G_{nm}^{\ \ T}\ \Lambda_{nm}(\theta,\varphi)\right] \ . \tag{4.97}$$

This non-uniqueness is evident in the relationship

$$\frac{2n + 1}{3}\ G_{nm} = \int_o^1 \rho_{nm}(\xi)\ \xi^{n+2}\ d\xi \tag{4.98}$$

where $\xi = R/R_o$, since these integral constraints can be satisfied by an infinite class of density distributions. However, if we have additional information or are willing to make some plausible assumptions, we can make some progress. It is also possible to characterize the class of admissible density distributions in terms of various extremal properties such as greatest lower bound on density contrast or least upper bound on the depth of burial of an anomalous mass (Parker, 1974,1975).

Another approach is to assume that the density anomalies are due to undulations of an interface across which there is a density contrast $\Delta\rho$. If the mean radius of the interface is $R = \xi R_o$ and the height of the undulations is

$$h(\theta,\varphi) = R \sum_{n=1}^{\infty} \sum_{m=0}^{n} h_{nm}^{T} \Lambda_{nm}(\theta,\varphi) \quad , \tag{4.99}$$

then the potential coefficients are

$$\frac{2n+1}{3} \bar{\rho}\, G_{nm} = \Delta\rho\, \xi^{n+3}\, h_{nm} \quad . \tag{4.100}$$

This approach was used to model lunar and Martian crustal thickness variations in chapters II and III respectively (Bills and Ferrari, 1977, b,c). It has also been applied to terrestrial data by Bott (1971) who attributed the gravity anomalies to undulations in the mantle phase transition boundaries, and by Hide and Horai (1968) who placed the topography on the core-mantle interface. As can be seen from equation (4.97), an increase in the depth of the interface requires an increase in either the density contrast or the amplitude of the undulations. This effect is more pronounced for high degree harmonics.

With that fact in mind, Higbie and Stacey (1970) have sought the depth at which the stresses required to support the density anomalies would be most nearly equal across the spectrum. After considering a number of different gravity models, they concluded that the most likely location of the anomalous masses is in the upper mantle.

The method which has received the most attention, though, "rests only on the assumption that the gravity anomalies arise from many independent density variations and that correlation between the density variations at different points falls to zero as the distance between the points increases" (Allan, 1972). This assumption is actually implemented through the use of a flat spectrum for the density anomalies or interface undulations. It has been widely used (Guier and Newton, 1965; Kaula, 1967; Allan, 1972; Lambeck, 1976; McQueen and Stacey, 1976; and Khan, 1977), and its practitioners consistently find two separate source depths: the low degree harmonics ($n \leq 5$) derive from depths of 800-1500 km whereas the higher harmonics have a shallower source (200-400 km). However, this result is highly suspect because of both the neglected surface topographic effect and the assumed source spectrum. Obviously, the correct spectrum to examine in seeking the depth of the source mass anomalies is the Bouguer spectrum and not the free-air spectrum. Yet every one of the above studies used the free-air spectrum. The assumed spectral behavior of the source warrants further discussion.

The models which incorporate a flat source spectrum are informative, since they yield a maximum source depth for a given potential spectrum (Naidu,1968). Furthermore, McQueen and Stacey (1976) have argued that "the superposition of sharp features on an otherwise spherically symmetrical distribution of any kind can be represented by a white spatial spectrum, that is by a sum of spherical harmonic terms of equal amplitudes. Thus if phase boundary undulations are highly localized relative to the wavelengths corresponding to the highest available harmonic terms, their spatial spectra will be white." On the other hand it might be more reasonable to suppose that all equi-density surfaces in a planet have roughly the same spectral form as the external surface topography. The resulting model potential variance for a single interface at a depth $D = R_o$ $(1 - \xi)$ is

$$\hat{V}(G;n) = \frac{9\alpha\, V(h;0)}{(n)(n+1)(2n+1)^2}\ \xi^{2n+6} \tag{4.101}$$

where $\alpha = (\Delta\rho/\bar{\rho})^2$. This model is still lacking in realism though, since it seems unlikely that all of the density anomalies would be concentrated at one depth.

The last approach we consider makes a less restrictive assumption about the source behavior. We simply assume that the density anomalies satisfy

$$\nabla^2 \left[R^k \rho(R,\theta,\varphi)\right] = 0 \quad , \tag{4.102}$$

where k is an integer. In this case Tscherning (1976) has shown that the variance spectrum and covariance of the density anomalies which are consistent with the potential variances V(G;n) have the form

$$V(\rho;n) = \left(\frac{2n+1}{3}\right)^2 (2n+3-k)^2 \, V(G;n) \tag{4.103}$$

$$C(\rho_i,\rho_j) = \bar{\rho}^{-2} \sum_{n=1}^{\infty} V(\rho;n) \, (\xi_i \xi_j)^{n-k} P_n(\cos(\gamma_{ij})) \quad . \tag{4.104}$$

It may be shown that the potential covariance is the convolution of the covariances of the density anomalies and the Green's function (Kautzleben *et al.*, 1977). We note also that the case of k = 0 corresponds to the density distribution of minimum variance which will produce the observed spectrum.

E. SUMMARY

In this chapter we have seen that the topographic variance spectra of the Earth, Moon, Mars and Venus are all very close to the Vening-Meinesz spectral form (4.1), in spite of vast differences in the geomorphic processes acting on these surfaces. This observation has prompted the conjecture that the solid surfaces of all planets and satellites are similarly characterized by this spectral form. Equivalently, these surfaces are conjectured to be realizations of a spherical Wiener stochastic process.

In examining a number of possible explanations for this behavior, we have found the most promising model to involve a simple equilibrium between constructional or "tectonic" processes which tend to roughen the surface uniformly at all scales, and destructional or erosive processes which tend to smooth the surface preferentially at small scales. This balance is maintained in such a way that the resultant surface is continuous almost everywhere but is differentiable almost nowhere.

This improved insight into the topographic variance spectrum may ultimately lead to a better understanding of the gravitational variance spectrum and the distribution of anomalous source masses. Another possible area for future research involves the connection between plate tectonics, elastic energy reduction and the resultant topographic variance spectrum.

REFERENCES

Allan, R.R. (1972). Depth of sources of gravity anomalies. *Nature Phys. Sci.* **236**, 22-23.

Anderson, D.L. and O'Connel, R. (1967). Viscosity of the Earth. *Geophys. J. R. Astr. Soc.* **14**, 287-295.

Au, C.K. and Shaham, J. (1971). Elastic energy and plate tectonics. *Nature* **250**, 211-213.

Baines, P.G. (1976). The stability of planetary waves on a sphere. *J. Fluid Mech.* **73**, 193-213.

Balmino, G., Lambeck, K. and Kaula, W.M. (1973). A spherical harmonic analysis of the Earth's topography. *J. Geophys. Res.* **78**, 478-481.

Beers, B.L. (1972). Harmonic analysis of analytic functions on hyperspheres. *J. Math. Phys.* **13**, 950-955.

Beers, B.L. and Dragt, A.J. (1970). New theorems about spherical harmonic expansions. *J. Math. Phys.* **11**, 2313-2328.

Bell, T.H. (1974). Representation of random noise by random pulses. *J. Appl. Phys.* **45**, 1902-1904.

Bell, T.H. (1975). Statistical features of sea floor topography. *Deep Sea Research* **22**, 883.

Bills, B.G. and Ferrari, A.J. (1977a). A harmonic analysis of lunar topography. *Icarus* **31**, 244-251.

Bills, B.G. and Ferrari, A.J. (1977b). A lunar density model consistent with topographic, gravitational, librational and seismic data. *J. Geophys. Res.* **82**, 1306-1314.

Bills, B.G. and Ferrari, A.J. (1977c). Mars topography harmonics and geophysical implications. Submitted to *J. Geophys. Res*.

Bott, M.H.P. (1971). The mantle transition zone as possible source of global gravity anomalies. *Earth Planet. Sci. Lett*. **11**, 28-34.

Bretherton, F.P. (1969). Momentum transport by gravity waves. *Q.J. Roy. Meter. Soc*. **95**, 213-243.

Bretherton, F.P. and Haidvogel D.B. (1976). Two-dimensional turbulence above topography. *J. Fluid Mech*. **78**, 192-154.

Campbell, D.B., Dyce, R.B., Ingalls, R.P., Pettengill, G.H., and Shapiro, I.I. (1972). Venus: topography revealed by radar data. *Science* **175**, 514-516.

Carson, M.A. and Kirkby, M.J. (1972). *Hillslope Form and Process*. Cambridge University Press, 467 pp.

Chandrasekhar, S. (1969). *Ellipsoidal Figures of Equilibrium.* Yale University Press, New Haven, 247 pp.

Christensen, E.J. (1975). Martian topography derived from occultation, radar, spectral and optical measurements. *J. Geophys. Res.* **80**, 2909-2913.

Chuikova, N.A. (1976). The geometrical figure of the Moon represented in the form of an expansion in spherical and sampling functions. *Sov. Astron*. **19**, 764-771.

Chung, C.L. and Scheidegger, A.E. (1968). A thermodynamic analogy for transport processes involving a non-positive definite transported quantity. *Bull. Int. Asso. Sci. Hyd*. **13**, 88-94.

Coode, A.M. (1966). An analysis of major tectonic features. *Geophys. J. Roy. Astr. Soc.* **12**, 55-66.

Coode, A.M. (1967). The spherical harmonic analysis of major tectonic features. In (S.K. Runcorn, ed.) *Mantles of the Earth and Terrestrial Planets*, Interscience, London, pp 489-498.

Cook, A.H. (1963). Sources of harmonics of low order in the external gravity field of the Earth. *Nature* **198**, 1186.

Cook, A.H. (1973). *Physics of the Earth and Planets*. John Wiley, New York, 316 pp.

Cox, C. and Sandstrom, H. (1962). Coupling of internal and surface waves in water of variable depth. *J. Ocean. Soc. Japan* **20**, 499-513.

Culling, W.E.H. (1960). Analytical theory of erosion. *J. Geol.* **68**, 336-344.

Culling, W.E.H. (1963). Soil creep and the development of hillside slopes. *J. Geol.* **71**, 127-161.

Culling, W.E.H. (1965). Theory of erosion on soil-covered slopes. *J. Geol.* **73**, 230-254.

Dietz, R.S. and Holden, J.C. (1970). Reconstruction of Pangaea: breakup and dispersion of continents, Permian to present. *J. Geophys. Res.* **75**, 4939-4956.

Duxbury, T.C. (1974). Phobos: control network analysis. *Icarus* **23**, 290-299.

Duxbury, T.C. (1976). Phobos and Deimos: geodesy. In Planetary Satellites (J.A. Burns, Ed.) University Arizona Press, Tucson, Arizona, pp. 346-362.

Fjortoft, R. (1953). On changes in the spectral distribution of kinetic energy in two dimensional non-divergent flow. Tellus **5**, 225-230.

Gilbert, G.K. (1877) Report on the Geology of the Henry Mountains U.S. Geogr. Geol. Survey, 173pp.

Goudas, C.L. (1971). Geometrical and dynamical properties of the Moon. In Physics and Astronomy of the Moon (Z. Kopal, Ed.) pp. 101-152. Academic Press, New York.

Grafarend, E.W. (1976). Geodetic applications of stochastic processes. Phys. Earth Planet. Inter. **12**, 151-179.

Grenander, U. (1975). Dynamic models of geomorphological patterns. Mathematical Geology **7**, 267-278.

Guier, W.H. and Newton, R.R. (1965). The Earth's gravity field as deduced from the Doppler tracking of five satellites. J. Geophys. Res. **70**, 4613-4626.

Halford, D. (1968). A general mechanical model for f^{α} spectral density noise. Proc. I.E.E.E. **56**, 251-258.

Hartmann, W.K. (1972). Interplanet variations in scale of crater morphology - Earth, Mars, Moon. Icarus **17**, 707-713.

Hide, R. and Horai, K. (1968). On the topography of the core-mantle interface. Phys. Earth Planet. Inter. **1**, 305-308.

Higbie, J. and Stacey, F.D. (1970). Depth of density variations responsible for features of the satellite geoid. *Phys. Earth Planet. Inter*. **4**, 145-148.

Hinze, J.O. (1959). *Turbulence*. McGraw-Hill, 586 pp.

Jenkins, G.M. and Watts, D.G. (1968). *Spectral Analysis and Its Application*. Holden-Day, 525 pp.

Johnson, T.V. and McGetchin, T.R. (1973). Topography on satellite surfaces and the shape of asteroids. *Icarus* **18**, 612-620.

Kampé de Fériet, J. (1962). Statistical mechanics of continuous media. *Proc. Symp. Appl. Math*. **13**, 165-198.

Kaula, W.M. (1967). Geophysical implications of satellite determinations of the Earth's gravitational field. *Space Sci. Rev*. **7**, 769-794.

Kaula, W.M.,Lingenfelter, R.E., Schugert, G. Sjogren, W.L. and Wollenhaupt, W.P. (1972). Analysis and interpretation of lunar laser antimetry. *Proc. Lunar Sci. Conf. 3rd* **3**, 2189-2204.

Kaula, W.M., Lingenfelter, R.E., Schubert, G., Sjogren, W.L., and Wollenhaupt, W.R. (1973). Lunar topography from Apollo 15 and 16 laser altimetry. *Proc. Lunar Sci. Conf. 4th* **3**, 2811-2819.

Kaula, W.M., Lingenfelter, R.E., Schubert, G., Sjogren, W.L. and Wollenhaupt, W.R. (1974). Apollo laser altimetry and inference as to lunar structure. *Proc. Lunar Sci. Conf. 5th*. **3**, 2049-3058.

Kautzleben, H., Harnisch, M. and Schwahn, W. (1977). The statistical description and interpretation of geophysical potential fields using covariance functions. *J. Geophys*. **43**, 163-177.

Khan, M.A. (1977). Depth of sources of gravity anomalies. *Geophys. J. R. Astr. Soc*. **48**, 197-209.

Kirkby, M.J. (1971). Hillslope process-response models based on the continuity equation in slopes: Form and process. *Inst. Brit. Geographers Special Pub*. **3**, pp. 15-30.

Kopal, Z. (1960). *Figures of Equilibrium of Celestial Bodies*. *Univ.* Wisconsin Press, Madison, 135 pp.

Krause, D.C. and Menard, H.W. (1965). Depth distribution and bathymetric classification of some sea-floor profiles. *Marine Geology* **3**, 169-193.

Lambeck, K. (1976). Lateral density anomalies in the upper mantle. *J. Geophys. Res*. **81**, 6333-6340.

Lauritzen, S.L. (1975). Random orthogonal set functions and stochastic models for the gravity potential of the Earth. *Stoch. Proc. Appl*. **3**, 65-72.

Leopold, L.B. and Langbein, W.B. (1962). The concept of entropy in landscape evolution. *U.S. Geol. Survey Prof. Paper 500-A*.

Levy, P. (1948). *Processus Stochastiques et Mouvement Brownien*. Gauthier-Villars, Paris, 365pp.

Levy, P. (1954). Le mouvement brownien. *Mem. Sci. Math*. **126**, 1-84.

Malin, M.C. and Dzurisin, D. (1977). Landform degration on Mercury, the Moon, and Mars: Evidence from crater depth/diameter relationships. *J. Geophys. Res*. **82**, 376-388.

Mandelbrot, B.B. (1967). How long is the coast of Britain? Statistical self-similarity and fractional dimension. *Science* **156**, 636-638.

Mandelbrot, B.B. (1975a). Stochastic models for the Earth's relief, the shape and fractal dimension of coastlines, and the number - area rule for islands. *Proc. Nat. Acad. Sci.* **72**, 3825.

Mandelbrot, B.B. (1975b). On the geometry of homogeneous turbulence with stress on the fractal dimension of the iso-surfaces of scalars. *J. Fluid Mech.* **72**, 401-416.

Mandelbrot, B.B. (1977). *Fractals: Form, Chance and Dimension.* W.H. Freeman, San Francisco.

Mandelbrot, B.B. and VanNess J.W. (1968). Fractional Brownian motions, fractional noises and applications. *SIAM Review* **10**, 422-437.

Marcus, A.H. (1964). A stochastic model of the formation and survival of lunar craters. I. Distribution of diameter of clean craters. *Icarus* **3**, 460-472.

Marcus, A.H. (1966). A stochastic model of the formation and survival of lunar craters. II. Approximate distribution of diameter of all observable craters. *Icarus* **5**, 165-177.

Marcus, A.H. (1967). Statistical theories of lunar and Martian craters. In *Mantles of the Earth and Terrestrial Planets* (S.K. Runcorn, Ed.) John-Wiley, New York, pp. 417-424.

Marcus, A.H. (1969). Distribution of slopes on a cratered planetary surface: Theory and preliminary applications. *J. Geophys. Res.* **74**, 5253-5267.

Marcus, A.H. (1970a). Distribution and covariance function of elevations on a cratered planetary surface. *The Moon* **1**, 297-337.

Marcus, A.H. (1970b). Comparison of equilibrium size distributions for lunar craters. *J. Geophys. Res*. **75**, 4977-4984.

McFadden, J.A. (1965). The entropy of a point process. *J. Soc. Indust. Appl. Math*. **13**, 988-994.

McKenzie, D., Roberts, J., and Weiss, N. (1973). Numerical models of convection in the Earth's mantle. *Tectonophysics* **19**, 89-103.

McQueen, H.W.S. and Stacey, F.D. (1976). Interpretation of low degree components of gravitational field in terms of undulations of mantle phase boundaries. *Tectonophysics* **34**, T1-T8.

Middleton, D. (1951). On the theory of random noise: Phenomenological models. *J. Appl. Physics* **22**, 1143-1163.

Moore, H.J. and Tyler, G.L. (1973). Comparison between photogrammetric and bistatic-radar slope-frequency distributions. *Apollo 17 Preliminary Science Report 33*: 17-26, NASA SP-330.

Naidu, P. (1968). Spectrum of the potential field due to randomly distributed sources. *Geophysics* **33**, 337-345.

Neukum, G. and Dietzel, H. (1971). On the development of the crater population on the Moon with time under meteorite and solar wind bombardment. *Earth Planet. Sci. Lett*. **12**, 59-66.

Parker, R.L. (1974). Best bounds on density and depth from gravity data. *Geophysics* **39**, 644-649.

Parker, R.L. (1975). The theory of ideal bodies for gravity interpretation. *Geophys. J.R. Astr. Soc*. **42**, 315-334.

Parzen, E. (1962). *Stochastic Processes*. Holden-Day, San Francisco 324 pp.

Pettengill, G.H., Counselman, C.C., Rainville, L.P. and Shapiro, I.I. (1969). Radar measurements of Martian topography. *Astron. J.* **74**, 461-482.

Pike, R.J. and Rozema, W.J. (1975). Spectral analysis of landforms. *Ann. Asso. Amer. Geogr.* **65**, 499-516.

Pines, D. and Shaham, J. (1973). Quadrupolar analysis of storage and release of elastic energy in the Earth. *Nature Phys. Sci.* **243**, 122-127.

Prey, A. (1922). Darstellung der höhen und tiefenverhältnisse der erde. *Abh. Ges. Wiss. Göttingen* **11**, 1-35.

Runcorn, S.K. (1965). Changes in the convection pattern in the Earth's mantle and continental drift. *Phil. Trans. Roy. Soc.* **A258**, 228-251.

Runcorn, S.K. (1967). Convection in the Moon and the existence of a lunar core. *Proc. Roy. Soc. Lond.* **A296**, 270-384.

Scheidegger, A.E. (1967). A complete thermodynamic analogy for landscape evolution. *Bull. Int. Asso. Sci. Hydrology* **12**, 57-62

Scheidegger, A.E. and Chaudhari, N.M. (1964). Some statistical properties of certain geophysical transport equations. *Pure Appl. Geophys.* **59**, 45-57.

Shannon, C.E. (1948). A mathematical theory of communication. *Bell System Tech. J.* **27**, 379-423.

Shapiro, I.I., Pettengill, G.H., Sherman, G.N., Rogers, A.E.E., and Ingalls, R.P. (1973). Venus: Radar determination of gravity potential. Science 179, 473-476.

Smith, W.B., Ingalls, R.P., Shapiro, I.I. and Ash, M.E. (1970). Surface-height variations on Venus and Mercury. Radio Science 5, 411-423.

Soderblom, L.A. (1970). A model for small-impact erosion applied to the lunar surface. J. Geophys. Res. 75, 2655-2661.

Tscherning, C.C. (1976). A mass covariance function consistent with the covariance function of the anomalous potential. Bollettino di Geodesia e Scienze Affini 35, 161-172.

Tyler, G.L., Simpson, R.A. and Moore, H.J. (1971). Lunar slope distributions: Comparison of bistatic-radar and photographic results. J. Geophys. Res. 76, 2790-2795.

Vening-Meinesz, F.A. (1951). A remarkable feature of the Earth's topography. Proc. Kon. Ned. Akad. V. Wet. B54, 212-228.

Vening-Meinesz, F.A. (1962). Thermal convection in the Earth's mantle. In Continental Drift (S.K. Runcorn, Ed.), Academic Press pp 145-176.

Walzer, U. (1971). Convection currents in the Earth's mantle and the spherical harmonic development of the topography of the Earth. Pure Appl. Geophys. 87, 73-92.

Walzer, U. (1973a). A quantitative kinematic theory of convective currents in the Earth's mantle. Pure Appl. Geophys. 105, 669-695.

Walzer, U. (1973b). Discussion of the new kinematic mantle convection theory. *Pure Appl. Geophys.* **105**, 696-712.

Warren, B.A. (1973). Transpacific hydrographic sections at lats. 43°S and 28°S. *Deep-sea Res.* **20**, 9-38.

Wells, R.A. (1971). Martian surface harmonics and continental drift. *Phys. Earth Planet. Int.* **4**, 273-285.

Woronow, A. (1977). Crater saturation and equilibrium: A Monte-Carlo simulation. *J. Geophys. Res.* **82**, 2447-2356.

Yaglom, A.M. (1962). *Stationary Random Functions*. Dover, New York, 235 pp.

V. APPENDICES

A. SPHERICAL HARMONICS

We will mainly be concerned with functions whose domain of definition is the surface of a sphere. Points on the sphere will usually be identified by their latitude (θ) and longitude (φ) relative to some coordinate system. Angular distance between points is better expressed in terms of colatitude (γ) or direction cosine ($\mu = \cos(\gamma)$) of one point relative to the other. We will occasionally interchange the coordinate pairs (θ,φ) and (μ,φ), where now $\mu = \sin(\theta)$, as the argument of a function while retaining the same symbol for the function, e.g., $F(\theta,\varphi) = F(\mu,\varphi)$. This should cause no confusion.

The family of functions on the sphere which are continuous almost everywhere (i.e., except on a set of measure zero) may be converted into a Hilbert space by introduction of a scalar product

$$\left\langle F,G\right\rangle = \frac{1}{4\pi}\int_{o}^{2\pi}\int_{-1}^{1} F(\mu,\varphi)\ G(\mu,\varphi)\ d\mu\ d\varphi \quad . \qquad A.1$$

The associated norm is given by

$$\|F\| = \left\langle F,F\right\rangle^{1/2} \qquad A.2$$

Any function for which $\|F\| < \infty$ will be said to be square integrable.

It will often prove convenient to express a function defined over the surface of a sphere as a product of a dimensionsl scale factor times a non-dimensional sum of orthogonal functions - the surface spherical harmonics. This summation, sometimes referred to as a Fourier-Legendre series, is the analogue on the sphere S^2 of a simple Fourier series on the circle S^1, and shares many of its properties. For example, the topography of a planet with mean radius R_o might be represented as

$$\begin{aligned} F(\mu,\varphi) &= R_o\left(1+\sum_{n=1}^{\infty}\sum_{m=0}^{n}\overline{P}_{nm}(\mu)\ [C_{nm}\cos(m\varphi)+S_{nm}\sin(m\varphi)]\right) \\ &= R_o\sum_{n=0}^{\infty}\sum_{m=0}^{n} F_{nm}^{T}\,\Lambda_{nm}(\mu,\varphi) \end{aligned} \qquad \text{A.3}$$

where

$$F_{nm}=\begin{pmatrix}F_{nm1}\\ F_{nm2}\end{pmatrix}=\begin{pmatrix}C_{nm}\\ S_{nm}\end{pmatrix}=\frac{1}{R_o}\left\langle F,\Lambda_{nm}\right\rangle$$

is the vector of harmonic coefficients or Fourier-Legendre transforms, of degree n and order m. The superscript T (as in F_{nm}^T) denotes transposition and

$$\Lambda_{nm}(\mu,\varphi)=\begin{pmatrix}\Lambda_{nm1}(\mu,\varphi)\\ \Lambda_{nm2}(\mu,\varphi)\end{pmatrix}=\overline{P}_{nm}(\mu)\begin{pmatrix}\cos(m\varphi)\\ \sin(m\varphi)\end{pmatrix},$$

the vector of normalized surface harmonic functions, is the product of a normalized Legendre function in latitude times a trigonometric (Fourier) vector in longitude. The Legendre polynomials $P_n(\mu)$ and associated Legendre functions $P_{nm}(\mu)$ are solutions of the differential equation (see e.g., MacRobert, 1967)

$$\frac{d}{d\mu}\left[(1-\mu^2)\frac{dP_{nm}}{d\mu}\right] + \left[(n)(n+1) - \frac{m^2}{1-\mu^2}\right]P_{nm} = 0 . \qquad \text{A.4}$$

In the un-normalized form, they satisfy the initial condition

$$P_{nm}(1) = \begin{cases} 1 & m = 0 \\ 0 & n \neq 0 \end{cases} \qquad \text{A.5}$$

and are given by

$$\begin{aligned} P_{nm}(\mu) &= (1-\mu^2)^{m/2}\frac{d^m P_n}{d\mu^m}(\mu) \\ &= (1-\mu^2)^{m/2}\frac{d^{n+m}(\mu^2-1)^n}{d\mu^{n+m}} \end{aligned} \qquad \text{A.6}$$

The normalized form is denoted by a bar $\overline{P}_{nm}(\mu)$ and is given by

$$\overline{P}_{nm}(\mu) = N_{nm}\, P_{nm}(\mu) \qquad \text{A.7}$$

where the normalization factor

$$N_{nm}^{2} = (2-\delta_{m0})(2n+1)\frac{(n-m)!}{(n+m)!}$$

is chosen so as to make the harmonics orthonormal over the sphere i.e.

$$\left\langle \Lambda_{nmi}, \Lambda_{n'm'j} \right\rangle = \delta_{nn'}\,\delta_{mm'}\,\delta_{ij} \quad . \qquad \text{A.8}$$

The rate of convergence of a Fourier-Legendre series depends on the smoothness of the function F being represented, i.e., smooth functions have rapidly convergent series representations. The individual harmonic coefficients F_{nm} depend, not only on the function F, but also on the particular orientation of the coordinate system. However, the sum of the squares of all the coefficients of a given degree

$$V\ (F;n) = \sum_{m=0}^{n} F_{nm}^{T} F_{nm} \qquad \text{A.9}$$

is invariant under rotation (Kaula, 1967) and is thus better suited to discussions of convergence. Using the facts that

$$\begin{aligned} &\nabla^2 \Lambda_{nm} + (n)(n+1)\ \Lambda_{nm} = 0 \\ &\|\ \Lambda_{nmi}\ \|^2 = 1 \qquad \text{A.10} \\ &\|\ \nabla\Lambda_{nmi}\ \|^2 = (n)(n+1) \end{aligned}$$

where ∇ and ∇^2 are the gradient and Laplacian differential operators, respectively, it may be shown (Beers and Dragt, 1970) that if the p-th derivative of F exists and is square integrable, i.e., if

$$\|\nabla^p F\| < \infty$$

then

$$V(F;n) = \mathcal{O}\left(\frac{1}{[(n)(n+1)]^{p+1}}\right) \quad . \qquad \text{A.11}$$

A more general result (Beers, 1972) is that, for a function F defined on the hypersphere S^k (S^1 is a circle, S^2 is a sphere, etc.) with a square integrable p-th derivative,

$$V(F;n) = \mathcal{O}\left(\frac{1}{[(n)(n+k-1)]^{p+1}}\right) \qquad \text{A.12}$$

where now V(F;n) is the sum of the squares of all

$$M(n,k) = (2n+k-1)\ \frac{(n+k-2)!}{(n)!\,(k-1)!}$$

hyperspherical harmonic coefficients of degree n, and (n)(n + k - 1) is an eigenvalue of the Laplacian on S^k. Thus, for functions with bounded variation, but which are not differentiable almost everywhere, we have

$$V(F;n) = \mathcal{O}\left(\frac{1}{n^2}\right) \qquad F: S^1 \to R$$
$$V(F;n) = \mathcal{O}\left(\frac{1}{(n)(n+1)}\right) \quad F: S^2 \to R \qquad \text{A.13}$$

on circles and spheres, respectively. On the other hand, infinitely differentiable functions give rise to harmonic coefficients which fall off faster than any inverse power of n, i.e., they decrease exponentially

$$V(F;n) = \mathcal{O}\left(e^{-\alpha(n)(n+k-1)}\right), \quad F: S^k \to R \qquad \text{A.14}$$

for some $\alpha > 0$.

Functions whose domain of definition extends beyond the surface of a sphere to include its interior and exterior may be expressed as a sum of solid spherical harmonics. For example, the gravitational potential exterior to a planet might be represented as

$$\Phi(R,\theta,\varphi) = \frac{GM}{R_o}\left[\frac{R_o}{R} + \sum_{n=1}^{\infty}\left(\frac{R_o}{R}\right)^{n+1}\sum_{m=0}^{n} G^T_{nm}\,\Lambda_{nm}(\theta,\varphi)\right], \quad R \ge R_o \qquad \text{A.15}$$

whereas, the potential interior to a homogeneous planet would be

$$\Phi(R,\theta,\varphi) = \frac{GM}{R_o}\left[\frac{3-(R/R_o)^2}{2} + \sum_{n=1}^{\infty}\left(\frac{R}{R_o}\right)^{n}\sum_{m=0}^{n} G^T_{nm}\,\Lambda_{nm}(\theta,\varphi)\right], \quad R \le R_o \qquad \text{A.16}$$

where G is the gravitational constant and M is the planetary mass.

In many applications, we will be more concerned with the angular distance

$$\mu = \cos(\gamma) = \left(\frac{\cos(\Delta\varphi) + 1}{2}\right) \cos(\Delta\theta) + \left(\frac{\cos(\Delta\varphi) - 1}{2}\right) \cos(2\theta + \Delta\theta) \qquad \text{A.17}$$

between the points (θ,φ) and $(\theta',\varphi') = (\theta + \Delta\theta,\ \varphi + \Delta\varphi)$, than with the specific location of the points. In such situations, we will invoke the so-called addition theorem of spherical harmonics (see e.g., Heiskanen and Moritz, 1967) which states that:

$$P_n(\mu) = \frac{1}{2n+1} \sum_{m=0}^{n} \Lambda_{nm}^{T}(\theta',\varphi')\ \Lambda_{nm}(\theta,\varphi) \quad . \qquad \text{A.18}$$

We will also have occasion to use the convolution theorem, which states that convolution in the spatial domain is equivalent to multiplication in the transform domain, and conversely. Thus, if

$$F(\theta,\varphi) = A(\theta,\varphi) * B(\theta,\varphi)$$

$$\equiv \frac{1}{4\pi} \int_0^{2\pi} \int_{-\pi/2}^{\pi/2} A(\theta',\varphi')\ B(\theta - \theta',\varphi - \varphi')\ \cos(\theta') \qquad \text{A.19}$$

$$\cdot\ d\theta' d\varphi'$$

then

$$F_{nm} = A_{nmi}\ B_{nmj}\ \delta_{ij} \qquad \text{A.20}$$

A simplification occurs if B has no azimuthal variation, i.e.,

$$B(\theta-\theta',\varphi-\varphi') = B(\gamma) = \sum_{n=0}^{\infty} (2n+1)\ B_n\ P_n(\cos(\gamma)) \qquad \text{A.21}$$

where now

$$B_n = \frac{1}{4\pi} \int_0^{2\pi} \int_{-1}^{1} B(\mu)\ P_n(\mu)\ d\mu d\varphi = \frac{1}{2} \int_{-1}^{1} B(\mu) P_n(\mu) d\mu \qquad \text{A.22}$$

is the Legendre transform of B. In that case,

$$F_{nm} = A_{nm}\ B_n\ . \qquad \text{A.23}$$

We will now consider some particularly useful examples of such azimuthally symmetric functions. Our first example is a delta function of magnitude M

$$B(\gamma) = M\ \delta(\gamma) \qquad \text{A.24}$$

for which

$$B_n = \frac{M}{2} \quad .$$

The result of convolving a function of (θ', φ') with a unit delta function located at (θ, Ψ) is simply,

$$\frac{1}{4\pi} \int_0^{2\pi} \int_{-\pi/2}^{\pi/2} A(\theta', \varphi')\ \delta(\theta - \theta', \varphi - \varphi')\ \cos(\theta')\ d\theta' d\varphi' \qquad \text{A.25}$$

$$= A(\theta, \varphi) \quad ,$$

the original function evaluated at (θ, φ). This relocation property of delta functions under convolution will prove quite useful in the sequel.

A rather wide class of azimuthally symmetric spherical functions can be obtained as solutions of the diffusion equation

$$\frac{\partial F}{\partial t} + \alpha^2\ \nabla^2 F = 0 \qquad \text{A.26}$$

and the wave equation

$$\frac{\partial^2 F}{\partial t^2} + \beta^2 \ \nabla^2 F = 0 \qquad \text{A.27}$$

by suppressing the radial and azimuthal dependence of the Laplacian differential operator so that it has the form

$$\nabla^2 = \frac{\partial}{\partial\mu}\left[(1-\mu^2)\ \frac{\partial}{\partial\mu}\right] \quad . \qquad \text{A.28}$$

We first consider the diffusion equation

$$\frac{\partial F(\mu,t)}{\partial t} + \alpha^2\ \nabla^2\ F(\mu,t) = 0 \qquad \text{A.29}$$

subject to the initial condition

$$F(\mu,0) = A(\mu) \quad .$$

Taking Legendre transforms of these equations, we obtain:

$$\frac{\partial F_n(t)}{\partial t} + \alpha^2 (n)(n+1)\ F_n(t) = 0 \qquad \text{A.30}$$

$$F_n(0) = A_n \quad .$$

The solution of this transformed system is

$$F_n(t) = A_n\ e^{-(n)(n+1)\alpha^2 t} \qquad \text{A.31}$$

so that the solution of the original system is

$$F(\mu,t) = \sum_{n=1}^{\infty} A_n\ e^{-(n)(n+1)\alpha^2 t}(2n+1)\ P_n(\mu) \qquad \text{A.32}$$

The process of diffusion is seen to act as a low-pass filter, since it attenuates the high degree harmonics of the initial condition. In the important case where the initial condition corresponds to a unit delta function, we find

$$F_n(t) = \frac{1}{2} e^{-(n)(n+1)\alpha^2 t} \quad . \tag{A.33}$$

This is the spherical analogue of the normal or Gaussian probability density of variance $\sigma^2 = 4\alpha^2 t$ (Roberts and Ursell, 1960). Obviously, when $\sigma^2 = 0$, this reduces to the original unit delta function.

We now consider the wave equation

$$\frac{\partial^2 F(\mu,t)}{\partial t^2} + \beta^2 \nabla^2 F(\mu,t) = 0 \tag{A.34}$$

subject to the initial conditions

$$F(\mu,0) = A(\mu)$$

$$\frac{\partial F(\mu,0)}{\partial t} = B(\mu)$$

Transforming these equations, we obtain the system

$$\frac{\partial^2 F_n(t)}{\partial t^2} + \beta^2 (n)(n+1) F_n(t) = 0 \tag{A.35}$$

$$F_n(0) = A_n$$

$$\frac{\partial F_n(0)}{\partial t} = B_n$$

whose solution is

$$F_n(t) = \begin{cases} A_o + B_o t & , \quad n = 0 \\ A_n \cos(\omega t) + B_n \dfrac{\sin(\omega t)}{\omega} & , \quad n \neq 0 \end{cases} \tag{A.36}$$

where $\omega^2 = \beta^2 (n)(n+1)$. In a time averaged sense, the displacement field of such a wave preserves the spectral character of its displacement initial condition $[A(\mu)]$, but is smoother than its velocity initial condition $[B(\mu)]$, since it attenuates the high degree harmonics.

Another important class of azimuthally symmetric functions is represented by the binary pulse

$$B(\gamma,\gamma_o) = \begin{cases} 1 & \gamma \le \gamma_o \\ 0 & \gamma > \gamma_o \end{cases} \qquad \text{A.37}$$

This will alternatively be denoted $B(\mu,\mu_o)$, where $\mu = \cos(\gamma)$ and $\mu_o = \cos(\gamma_o)$.

In the evaluation of the Legendre transform of this and similar functions, we will use the relation (Erdelyi, 1953, p. 170)

$$\int_\alpha^\beta P_n\, P_m\, d\mu = \left.\frac{(1-\mu^2)[P_n P_m' - P_n' P_m]}{(n-m)(n+m+1)}\right|_\alpha^\beta \qquad \text{A.38}$$

where the prime denotes differentiation. Applying this formula, we find that the Legendre transform of the unit impulse is

$$B_n(\mu_o) = 2\pi \int_{-1}^{1} B(\mu,\mu_o)\, P_n(\mu)\, d\mu = 2\pi \int_{\mu_o}^{1} P_n(\mu_o)\, d\mu \qquad \text{A.39}$$

$$= \frac{2\pi(1-\mu_o^2)\;P_n'(\mu_o)}{(n)(n+1)}$$

In some applications, it will be more convenient to use a simple binary pulse Z with the added property that

$$\int_{-1}^{1} Z(\mu,\mu_o)\, d\mu = 0 \qquad \text{A.40}$$

The functional form of this zero-sum pulse is

$$Z(\gamma,\gamma_o) = \begin{cases} 1 \ , & \gamma \leq \gamma_o \\ -\left[\dfrac{1-\mu_o}{1+\mu_o}\right] , & \gamma > \gamma_o \end{cases} \qquad \text{A.41}$$

and its Legendre transform is

$$Z_n(\mu_o) = 2\pi \int_{-1}^{1} Z(\mu,\mu_o)\ P_n(\mu)\ d\mu$$

$$= 2\pi \left[\int_{\mu_o}^{1} P_n(\mu)\ d\mu - \left(\frac{1-\mu_o}{1+\mu_o}\right) \int_{-1}^{\mu_o} P_n(\mu)\ d\mu \right] \qquad \text{A.42}$$

$$= \frac{4\pi(1-\mu_o)\ P_n'(\mu_o)}{(n)\,(n+1)}$$

B. PROBABILITY DENSITIES

In much of our analysis, we will be concerned with probabilistic arguments. Therefore, in this section we briefly introduce some of the basic notions and terminology which will be employed elsewhere. Most of this material is quite well known and unless otherwise noted can be found in standard texts (e.g., Gallager, 1968; Middleton, 1960; Thomasian, 1969).

A probability density is a real-valued function $p: \Omega \rightarrow R$, defined on some set Ω and satisfying the conditions:

$$p(\omega) \geq 0, \quad \text{for all } \omega \in \Omega \qquad \text{B.1}$$

$$\int_{\Omega} p(\omega) d\omega = 1 \quad . \qquad \text{B.2}$$

The set Ω is called the sample space, an element ω of Ω is called a sample point, and each subset of Ω is called an event. The probability of an event A

$$P(A) \equiv \int_{A} p(\omega) d\omega \qquad \text{B.3}$$

is thus a real-valued function whose domain is the class of events in Ω. The function P and the ordered pair (Ω, P) are called the probability measure and the probability space, respectively, corresponding to the probability density $p: \Omega \rightarrow R$. A random variable with associated probability space (Ω, P) is any real-valued function $F: \Omega \rightarrow R$.

If A and B are events in Ω, with $P(A) > 0$, then the conditional probability of A, given B, is defined

$$P(A|B) = P(AB)/P(A) \quad . \tag{B.4}$$

The events A and B are said to be independent, if and only if

$$P(AB) = P(A)\ P(B) \quad . \tag{B.5}$$

The n-th moment of a density is defined as

$$M_n(p) \equiv \int_\Omega \omega^n\ p(\omega)d\omega \quad . \tag{B.6}$$

All densities are normalized so that $M_0 = 1$. We will be concerned mainly with the mean (first moment)

$$E(\omega) = \int_\Omega \omega\ p(\omega)d\omega = M_1 = \mu_\omega \tag{B.7}$$

where $E(\cdot)$ is the expectation operator, and the variance (second moment about the mean)

$$V(\omega) = E(\omega - \mu_\omega)^2 = M_2 - M_1^2 = \sigma_\omega^2 \quad . \tag{B.8}$$

In predicting the value of a random variable, a highly concentrated probability distribution conveys more information than a relatively uniform distribution. To quantify this notion, we introduce the self-information

$$I(\omega) = - \ln\,[p(\omega)] \tag{B.9}$$

and the average information or entropy

$$H(\omega) = E[I(\omega)] = -\int_\Omega \ln\,[p(\omega)]\ p(\omega)d\omega \tag{B.10}$$

The entropy, thus defined, depends not only on the probability distribution, but also on the coordinate system used. If we have a joint probability distribution $p(X)$ for the variables $X = (x_1, x_2, \ldots, x_n)$ and then change variables to $Y = (y_1, y_2, \ldots y_n)$, the new distribution is

$$q(Y) = p(X) \left| \frac{\partial Y}{\partial X} \right| \qquad \text{B.11}$$

where

$$\left| \frac{\partial Y}{\partial X} \right| = \left| \frac{\partial y_i}{\partial x_j} \right|$$

is the Jacobian determinant of the transformation, and therefore

$$H(Y) = H(X) - \int \ln \left[\left| \frac{\partial Y}{\partial X} \right| \right] p(X)\, dX \qquad \text{B.12}$$

In spite of this dependence on the coordinate system, entropy is a useful way to characterize probability distributions, since we will be mostly interested in relative entropies. In fact, many of the distributions we will encounter can be obtained by seeking the distribution with maximum entropy subject to constraints such as fixed mean or variance. This approach ensures that the distribution so obtained incorporates all of our prior knowledge about the system of interest, but no more.

In the remainder of this section, we will introduce the one dimensional forms (i.e., $\Omega = R$) of some elementary probability densities which we will need later.

The simplest form we consider is the uniform density, which is the maximum entropy solution subject only to the constraints that

$$\int_{-\infty}^{\infty} p(X)dX = 1 \qquad \text{B.13}$$

$$p(X) = 0 \quad \text{unless} \quad \alpha \le X \le \beta \qquad \text{B.14}$$

It thus arises in the situation where a random variable is certain to lie in the interval (α, β), but nothing is known further about its location. The functional form of the uniform density is

$$p(X) = \begin{cases} (\beta - \alpha)^{-1} , & \alpha \le X \le \beta \\ 0 & \text{otherwise} \end{cases} \qquad \text{B.15}$$

and its moments and entropy are

$$M_1 = \frac{\alpha + \beta}{2} \qquad M_2 = \frac{\alpha^2 + \alpha\beta + \beta^2}{3}$$
$$V = \frac{(\beta - \alpha)^2}{12} \qquad H(X) = \ln\,(\beta - \alpha) \qquad \text{B.16}$$

The normal or Gaussian density arises in the analysis of the sums of independent random variables. In fact, the central limit theorem asserts that under quite general conditions, the standardized sum of independent random variables has an approximately normal distribution. The normal density with the two parameters, μ and σ^2 has the form

$$p(X) = \left[2\pi\sigma^2 \, e^{\left(\frac{X-\mu}{\sigma}\right)^2} \right]^{-1/2} , \quad -\infty \le X \le \infty \qquad \text{B.17}$$

and its moments and entropy are

$$M_1 = \mu \qquad M_2 = \mu^2 + \sigma^2$$
$$V = \sigma^2 \qquad H(X) = \frac{1}{2}\left[1 + \ln 2\pi\sigma^2\right]$$

The normal distribution has the maximum entropy of any distribution with the same mean and variance. We will occasionally use the symbol

$N(\mu,\sigma^2)$ to indicate that a random variable is normal with mean μ and variance σ^2.

The Rayleigh distribution characterizes the fluctuations in amplitude of the sum of independent random variables. Thus, if

$$A \cos (m\varphi) + B \sin (m\varphi) = J \cos (m\varphi + \Delta\varphi) \qquad \text{B.19}$$

where A and B are independent $N(0,\beta^2)$ random variables, then J and $\Delta\varphi$ are independent random variables, $\Delta\varphi$ is uniformly distributed on the interval $(0,2\pi)$ and J is Rayleigh distributed with probability density

$$p(X) = \begin{cases} \dfrac{X}{\beta^2}\, e^{-1/2\left(\frac{X}{\beta}\right)^2} & X \geq 0 \\ 0 & X < 0 \end{cases} \qquad \text{B.20}$$

The Rayleigh distribution has a single parameter β, and its moments are

$$M_1 = \left(\frac{\pi}{2}\right)^{1/2} \beta \qquad M_2 = 2\beta^2$$
$$V = \left(\frac{4-\pi}{2}\right) \beta^2 \qquad \text{B.21}$$

If $\{X_i\colon\ i = 1,2,\ldots,2n\}$ are independent $N(0,\sigma^2)$ random variables, then

$$\chi^2_{2n} = \sum_{i=1}^{2n} \left(\frac{X_i}{\sigma}\right)^2$$

has a chi-square density with 2n degrees of freedom. The functional form of the density is:

$$p(X) = \begin{cases} [2\Gamma(n)]^{-1} (X/2)^{n-1} e^{-X/2} & , \quad X \geq 0 \\ 0 & , \quad X < 0 \end{cases} \qquad \text{B.23}$$

where the gamma function takes the values

$$\Gamma(n) = \begin{cases} (n-1)! & , \quad 2n = 2,4,6,\ldots \\ \left(\frac{\pi}{4^{2n-1}}\right)^{1/2} \frac{(2n-1)!}{\left(\frac{2n-1}{2}\right)!} & , \quad 2n = 1,3,5,\ldots \end{cases} \qquad \text{B.24}$$

The chi-square distribution has a single parameter, 2n and its moments are

$$M_1 = 2n \qquad M_2 = 4n(n+1)$$
$$V = 4n \qquad \text{B.25}$$

If independent random events occur at a constant mean rate X, the probability that k events occur in an interval of length X is Poisson distributed with discrete density

$$p(k) = \begin{cases} \frac{e^{-\alpha x} (\alpha x)^k}{(k)!} & k = 0,1,2,\ldots \\ 0 & \text{otherwise} \end{cases} \qquad \text{B.26}$$

Since this is a discrete density, its moments are defined in terms of sums rather than integrals:

$$M_n \equiv \sum_{k=0}^{\infty} k^n p(k) \quad . \qquad \text{B.27}$$

The Poisson distribution has a single parameter, αx, and its first two moments, variance and entropy are

$$M_1 = \alpha x \qquad M_2 = \alpha x + (\alpha x)^2$$
$$V = \alpha x \qquad H(X) = \alpha x \, [1 - \ln(\alpha)] \qquad \text{B.28}$$

Of all point processes with intensity α, the Poisson process has the maximum entropy rate $dH(x)/dx$ (McFadden, 1965).

C. STOCHASTIC PROCESSES

A stochastic process is, roughly speaking, an ensemble of random functions, all governed by the same probability law. More precisely (Parzen, 1962; Thomasian, 1969), a stochastic process consists of a probability space (Ω, P), a non-empty set G, called the parameter set, and a random variable, $F_g: \Omega \rightarrow R$, assigned to each $g \in G$. The only parameter sets we will explicitly consider are the real line R, the positive reals R^+, the circle S^1, and the sphere S^2.

For any $\omega \in \Omega$, the function $H_\omega: G \rightarrow R$, defined by

$$H_\omega(g) = F_g(\omega) \qquad \text{for all } g \in G \qquad \text{C.1}$$

is called a realization, or sample function, of the stochastic process. For any $(g,h) \in G \times G$, the function $\Delta F_{g,h}: G \times G \rightarrow R$, defined by

$$\Delta F_{g,h} = F_h - F_g \qquad \text{C.2}$$

is called the increment of F from g to h.

A very important class of processes are those with stationary and independent increments. The increments of a process are said to be stationary if the distribution of $\Delta F_{g,h}$ depends on g and h only through their difference $|h - g|$. If the parameter set G is a sphere, this difference is just the angular distance γ between the points $g = (\theta, \varphi)$ and $h = (\theta + \Delta\theta, \varphi + \Delta\varphi)$. The increments of a process are independent if the random variables $\Delta F_{g,h}$ and $\Delta F_{g',h'}$ are independent whenever the intervals (g,h) and (g',h') are disjoint. The only processes we will actually encounter in this analysis are the Poisson and Wiener processes and some of their generalizations. All of these processes have stationary and independent increments.

1. Poisson Process

The Poisson process is basically a counting process. We define a counting function as any non-decreasing function N whose range is restricted to the non-negative integers $\{0,1,2,\ldots\}$ and which assumes every value in its range less than N_0, if it assumes the value N_0. We then define a Poisson process N_g with parameter α as any process with stationary independent increments such that the random variable N_g induces a Poisson density with mean αg, and every realization of the process is a counting function.

A process X_g is said to be a filtered Poisson process if it can be represented by

$$X_g = \sum_{n=1}^{N_g} B(g,h_n,A_n) \qquad \text{C.3}$$

where N_g is a Poisson process with intensity α, $\{A_n\}$ is a sequence of indentically distributed random variables, independent of one another and of N_g, and $B(g,h,A)$: $G^2 \times R \rightarrow R$ is the response function. We may interpret $B(g,h,A)$ as the value at g of a response of magnitude A to an impulse at h. X_g is thus the value at g of N_g such responses.

2. Weiner Process

The Weiner process is obtained as the limit of a random walk as the step size decreases to zero. Specifically, a Weiner process W(g) with parameter σ^2 is any stationary independent increment process such that the random variable $W(g)$ induces a normal $N(0,\sigma^2)$ density, and every realization of the process is a continuous function. Thus, if $\gamma = |h - g|$ is the length of the interval (g,h) in the parameter set G, then the increment $\Delta W(g,h;\omega)$ is normally distributed as $N(0,\gamma\sigma^2)$. Although realizations of a Weiner process are continuous, they are almost nowhere differentiable, i.e., for any $g \in G$, the set of realizations which have a derivative at g has probability zero.

The Wiener process has a number of other interesting properties. For example, it might be supposed that in a typical interval, the fraction (X) of the interval over which the process is positive, would be normally distributed about its mean 0.5. However, as first shown by Levy (1948, pg. 216) the probability density is minimum at its mean and is concentrated toward the extremes 0 and 1. In fact, the density is

$$p(X) = \frac{1}{\pi} \frac{1}{\sqrt{(X)(1-X)}} \qquad \text{C.4}$$

and therefore the probability

$$P[X \le u^2] = \frac{1}{\pi} \int_0^{u^2} \frac{dX}{\sqrt{(X)(1-X)}} \qquad \text{C.5}$$

$$= \frac{2}{\pi} \sin^{-1}(u) \quad , \quad 0 \le u \le 1.$$

This arc-sine law obviously also gives the distribution of the fraction $(1-X)$ of the interval over which the process is negative.

The points at which the process assumes its mean value are also of interest. Let γ_k be the length of the k-th interval between consecutive returns to the mean. Short intervals are more frequent than long ones. In particular, when the parameter set is the real line or the positive reals, $G \in \{R, R^+\}$, the probability distribution of γ_k is

$$P[\gamma_k = u] = \left(\frac{8}{\pi}\right)^{1/2} \quad u^{-3/2}$$

This distribution is approximately the same when the parameter set is the circle or sphere, $G \in \{S^1, S^2\}$, if the intervals considered are sufficiently short, i.e., $\gamma \ll 2\pi$ This is also true of a number of the other properties we will consider below.

We now consider a generalization of the Wiener process whose increments are a moving average of the increments of the standard Wiener process. Following Mandelbrot and Van Ness (1968), we define a fractional Wiener process $W_\beta(g)$ with parameters β and σ^2 $(0 \leq \beta \leq 1,\ 0 \leq \sigma^2)$ as any stationary increment process such that all the realizations of the process are continuous and the increments $\Delta W_\beta(g,h)$ are normally distributed as $N(0, \sigma^2\gamma^{2\beta})$, where $\gamma = |h - g|$ is the distance between the points g and h in the parameter set. The increments of $W_\beta(g)$ are independent if, and only if, $\beta = \frac{1}{2}$. In that case, we merely obtain the traditional Wiener process, $W_{1/2}(g) = W(g)$. The fractional process is similar to the traditional process in that, although all its realizations are continuous, they are nowhere differentiable.

The realizations of a fractional Wiener process have a degree of invariance with respect to changes of scale. To quantify this notion, we introduce the concept of self-similarity. The increments of a random function $F(g)$ are said to be self-similar with parameter Q if for any $\gamma > 0$, and any $g \in G$,

$$\Delta F(g, g+\gamma) = \gamma^{-Q} \, \Delta F(g, g+\gamma Q) \qquad \text{C.6}$$

where the indicated equality means that the two random variables are indentically distributed. If the parameter set $G \in \{R, R^+\}$ then the fractional Weiner process $W_\beta(g)$ has self-similar increments with parameter β. If $G \in \{S^1, S^2\}$, then $W_\beta(g)$ is asymptotically self-similar for small γ.

The realizations of $W_\beta(g)$ are also characterized by their extreme irregularity. This is, of course, suggested by their lack of differentiability. However, when we consider the realizations of a process with $G \in \{R, R^+\}$, we find that in their degree of convolution and intricacy they are, in fact intermediate between a smooth rectifiable curve and a Peano curve, which passes through every point of a two dimensional region. This, in conjunction with a self-similarity parameter $0 \leq \beta \leq 1$, suggests a dimensionality D for these realizations with $1 \leq D \leq 2$. In fact, generalizing a result of Mandelbrot (1975), we suggest that if $D[G]$ is the dimension of its parameter set, the dimension of a realization of $W_\beta(g)$ satisfies

$$D[W_\beta(g)] = D[G] + \beta \qquad \text{C.7}$$

Thus, for example, if $G = S^1$ or S^2, then $D[W_\beta(g)] = 1+\beta$ or $2+\beta$ respectively.

3. Ornstein-Uhlenbeck Process

We now consider another extension of the Wiener process. If $W(g)$ is a standard Wiener process, then

$$U(g) = e^{-\beta g}\, W(\alpha e^{2\beta g}) \tag{C.8}$$

is called the Ornstein-Uhlenbeck process (Uhlenbeck and Ornstein, 1930; Doob, 1942) with parameters $\alpha > 0$ and $\beta > 0$. It is a stationary normal process with zero mean and covariance

$$C(U;\gamma) = \alpha\, e^{-\beta\gamma} \quad . \tag{C.9}$$

Whereas the Wiener process is obtained from a random walk in the limit as the step length goes to zero, the Ornstein-Uhlenbeck process is derived by a similar limiting procedure from a random walk subjected to a restoring force. Thus, the Ornstein-Uhlenbeck process is stationary, whereas the Wiener process is not.

D. COVARIANCE FUNCTIONS

In much of what follows, it will be useful to consider functions on the sphere $F(\theta,\varphi)$ which are realizations of homogeneous stochastic processes. A process is said to be homogeneous if its first and second moments are invariant under the group of rotations of the sphere. This is equivalent (Roy, 1973) to stationarity, i.e., constancy of the mean $E[F(\theta,\varphi)]$ and isotropy of the covariance function $E[F(\theta,\varphi)F(\theta',\varphi')]$, i.e., the covariance depends only on the angular separation γ, between the points (θ,φ) and (θ',φ').

If we now consider two functions $A(\theta,\varphi)$ and $B(\theta,\varphi)$, we may calculate the expected value of the product $A(\Gamma)\cdot B(\Gamma+\gamma)$, where $\Gamma = (\theta,\varphi)$ and $\Gamma + \gamma = (\theta',\varphi')$ are any two points on the sphere which are an angular distance γ apart. This mean product is known as the cross-correlation of A and B (Middleton, 1960). In the case where $E(A) = E(B) = 0$, it is known as the cross-covariance and is designated

$$C(A,B;\gamma) = E[A(\Gamma)\cdot B(\Gamma+\gamma)] \quad . \tag{D.1}$$

The requirement that $E(A) = E(B) = 0$ is easily met by defining new functions, $A' = A - E(A)$ and $B' = B - E(B)$. This is equivalent to the vanishing of the harmonic coefficients of degree zero; $A_{0,0} = B_{0,0} = 0$. For example, instead of topographic radius $R(\theta,\varphi)$, we will use topographic height; $H(\theta,\varphi) = R(\theta,\varphi) - R_0$.

The covariance of a function with itself is known as the auto-covariance, or simply the covariance, and is denoted variously as

$$C(A,A;\gamma) = C(A;\gamma) = C(\gamma) = E[A(\Gamma)\,A(\Gamma+\gamma)] \tag{D.2}$$

The (cross-) covariance of the functions A and B at separation γ has a convenient representation in terms of Legendre polynomials in $\mu = \cos(\gamma)$, and the harmonic coefficients A_{nm} and B_{nm}. Applying the addition theorem

$$P_n(\cos(\gamma)) = \frac{1}{2n+1} \sum_{m=0}^{n} \Lambda_{nm}^T(\theta,\varphi)\ \Lambda_{nm}(\theta',\varphi') \qquad \text{D.3}$$

where γ is again the angular distance between (θ,φ) and (θ',φ'), we find (Heiskanen and Moritz, 1967; Kaula, 1967)

$$C(A,B;\gamma) = R_0^{\,2} \sum_{n=1}^{\infty} V(A,B;n)\ P_n\left[\cos(\gamma)\right] \qquad \text{D.4}$$

where

$$V(A,B;n) = \sum_{m=0}^{n} A_{nm}^{\ T}\ B_{nm}$$

is the (cross-) variance spectrum of A with B. For a given n, V(A,B;n) will be referred to as the degree (cross-) variance. For further discussion of spectral analysis of random processes on the sphere, see Jones (1963) and Roy (1976).

The (cross-) covariance at zero separation is known as the (cross-) variance and has the form

$$C(A,B;0) = R_0^{\,2} \sum_{n=1}^{\infty} V(A,B;n) \qquad \text{D.5}$$

since

$$P_n\ [\cos(0)] = 1.$$

If a random variable X has mean $E(X) = \mu_x$ and variance $E(X - \mu_x)^2 = \sigma_x^2$, then (Thomasian, 1969; pp. 202-208)

$$X^* = \frac{X - \mu_x}{\sigma_x} \qquad \text{D.6}$$

is called the standardized random variable corresponding to X, and has zero mean and unit variance:

$$\begin{aligned} E(X^*) &= 0 \\ E(X^*)^2 &= 1 \quad . \end{aligned} \qquad \text{D.7}$$

If X and Y have finite, nonzero variances, then the covariance between their standardizations is called their correlation coefficient and is denoted by

$$(X,Y) = C(X^*,Y^*) = \frac{C(X,Y)}{\sigma_x \sigma_y} \quad . \qquad \text{D.8}$$

For random variables on the sphere, we also define the degree correlation coefficient

$$\rho(X,Y;n) = V(X^*,Y^*;n) = \frac{V(X,Y;n)}{[V(X;n)\ V(Y;n)]^{1/2}} \qquad \text{D.9}$$

Clearly, $-1 \leq \rho_{xy} = \rho_{yx} \leq 1$, and $\rho_{xy} = 1\ (-1)$ iff X and Y are perfectly (anti-) correlated, whereas $p_{xy} = 0$ means that X and Y are uncorrelated. Thus, ρ_{xy} is a standardized measure of the degree of statistical dependence between X and Y.

If we desire to predict the value of a random variable Y based on observations of another random variable X, we may seek the numbers α and β which minimize the error variance

$$E\left[Y - (\alpha X + \beta)\right]^2 \quad .$$

In terms of standardized variables, the solution is

$$\alpha = \rho_{xy} \qquad \beta = 0 \tag{D.10}$$

and the error variance is

$$E\ (Y^* - \rho_{xy}\, X^*)^2 = 1 - \rho_{xy}^{\ 2} \tag{D.11}$$

In terms of nonstandardized variables, the so called regression line and error variance are:

$$Y = \mu_y + \sigma_y\ \rho_{xy} \left(\frac{X - \mu_x}{\sigma_x} \right) \tag{D.12}$$

$$E\ [Y - (\alpha X + \beta)]^2 = \sigma_y^{\ 2} (1 - \rho_{xy}^{\ 2}) \quad . \tag{D.13}$$

The Wiener-Khintchine theorem (Middleton, 1960; pp. 141-144) states that under quite general conditions the (cross-) covariance function and the (cross-) variance spectrum are related by a pair of integral (or series) transforms. In the case of spherical geometry, we have a Legendre transform relationship:

$$C(\mu) = R_0^{\ 2} \sum_{n=1}^{\infty} V(n)\ P_n(\mu)$$

$$R_0^{\ 2} V(n) = \frac{2n + 1}{2} \int_{-1}^{1} C(\mu)\ P_n(\mu)\ d\mu \tag{D.14}$$

Thus we can deal with whichever quantity is more convenient or gives greater insight into a problem. A case of particular interest is the spherical Wiener process, which is representative of the stochastic component of the topography of the terrestrial planets:

$$V(H;n) = \frac{V(H;0)}{(n)(n+1)} \quad . \tag{D.15}$$

The covariance in this case is

$$C(H;\gamma) = R_0^{\,2}\, V(H;0) \sum_{n=1}^{\infty} \frac{P_n[\cos(\gamma)]}{(n)(n+1)} \tag{D.16}$$

We can obtain a closed-form expression for this series by noting that

$$\frac{1}{(n)(n+1)} = \frac{1}{n} - \frac{1}{n+1} \tag{D.17}$$

and (Wheelon, 1968; pg. 53)

$$\sum_{n=1}^{\infty} \frac{P_n[\cos(\gamma)]}{n} = -\left(\ell n[\sin(\gamma/2)] + \ell n[1+\sin(\gamma/2)]\right) \tag{D.18}$$

$$\sum_{n=1}^{\infty} \frac{P_n[\cos(\gamma)]}{n+1} = -\left(1 + \ell n\,[\sin(\gamma/2)] - \ell n\,[1+\sin(\gamma/2)]\right) \tag{D.19}$$

Therefore, we find that:

$$\begin{aligned} C(H;\gamma) &= R_0^{\,2}\, V(H;0) \left[\sum_{n=1}^{\infty} \frac{P_n[\cos(\gamma)]}{n} - \sum_{n=1}^{\infty} \frac{P_n[\cos(\gamma)]}{n+1} \right] \\ &= R_0^{\,2}\, V(H;0) \left(1 - 2\ell n\,[1+\sin(\gamma/2)]\right) \quad . \end{aligned} \tag{D.20}$$

When $\gamma = 0$, this has the form

$$C(H;0) = R_0^{\,2}\, V(H;0) \tag{D.21}$$

since

$$P_n[\cos(0)] = 1$$

and

$$\sum_{n=1}^{\infty} \frac{1}{(n)(n+1)} = 1.$$

Similarly, for a fractional Wiener process W_β on a circle, the variance spectrum is

$$V(W_\beta;n) = V(W_\beta;0)\ n^{-(2\beta+1)} \quad . \tag{D.22}$$

Campbell's theorem (Rice, 1944) gives convenient expressions for the mean and covariance function of those filtered Poisson processes which can be expressed as

$$X(g) = \sum_{n=1}^{N} A_n\ B(g-h_n) \tag{D.23}$$

where N is a Poisson process of intensity α, A_n is the amplitude of the n-th pulse, and $B(g-h_n)$ is the response at g to a unit pulse at h_n. If the parameter set of the process is G, then

$$\begin{aligned} E(X) &= \alpha\ E(A) \int_G B(g)\ dg \\ C(X;\gamma) &= \alpha\ E(A)^2 \int_G B(g)\ B(g+\gamma)\ dg \quad . \end{aligned} \tag{D.24}$$

As the intensity α is increased, the process $X(g)$ approaches a normal distribution with mean $E(X)$ and variance $C(X;0)$, as given above.

As an application of the convolution theorem to the calculation of variance spectra and covariance functions, we note that, if the function F is a convolution of A and B,

$$F(\theta,\varphi) = \frac{1}{4\pi} \int_{0}^{2\pi} \int_{-\pi/2}^{\pi/2} A(\theta',\varphi')\ B(\theta - \theta',\varphi - \varphi')\ \cos(\theta')\ d\theta' d\varphi' \qquad \text{D.25}$$

and if B has no azimuthal variation, then the variance spectrum of F is simply

$$V(F;n) = B_n^{\ 2}\ V(A;n) \qquad \text{D.26}$$

and the covariance function is

$$C(F;\gamma) = R_0^{\ 2} \sum_{n=1}^{\infty} B_n^{\ 2}\ V(A;n)\ P_n[\cos(\gamma)] \quad . \qquad \text{D.27}$$

E. VISCO-ELASTIC DEFORMATION

The response of a planet to applied stress depends on the size and composition of the planet as well as the spatial and temporal distribution of the stresses. We will restrict our attention here to planets composed of homogeneous, incompressible, linear visco-elastic materials. This considerably simplifies the analysis while retaining many of the behavioral features of a more complex substance. A planet will thus be characterized by its radius R_0[cm], either mass M [gm] or density [gm cm^{-3}], rigidity μ [dyne cm^{-2}] and either kinematic viscosity ν[stoke = $\mathrm{cm}^2\ \mathrm{sec}^{-1}$] or dynamic viscosity $\eta = \rho\nu$ [poise = gm $\mathrm{cm}^{-1}\ \mathrm{sec}^{-1}$].

The relationship between applied stress σ [dyne cm^{-2}] and consequent deformation, as expressed in terms of either strain ϵ [dimensionless] or strain rate $\dot{\epsilon} \equiv d\epsilon/dt$ [sec^{-1}], depends on the material being deformed. For linear elastic, linear viscous and Maxwell visco-elastic materials, the relations are:

$$\epsilon = \sigma/\mu \qquad \text{(elastic)} \qquad \text{E.1}$$

$$\dot{\epsilon} = \sigma/\eta \qquad \text{(viscous)} \qquad \text{E.2}$$

$$\dot{\epsilon} = \dot{\sigma}/\mu + \sigma/\eta \qquad \text{(visco-elastic)} \qquad \text{E.3}$$

This latter form is only one of many possible models for linear visco-elastic behavior, but we focus on it because of historical precedent (Maxwell, 1868; Darwin, 1879) and analytical simplicity. Furthermore, it is apparently a reasonable model in many situations of geophysical interest (McKenzie, 1967).

A Maxwell material subjected to a constant stress σ, initially undergoes an elastic deformation $\epsilon = \sigma/\mu$, but also commences creeping at a rate $\dot{\epsilon} = \sigma/\eta$. After a time $t = \tau_M$, known as the Maxwell relaxation time, the viscous deformation $\epsilon = \sigma t/\eta$ exceeds the initial elastic deformation. Thus, for short time periods ($t < \tau_M$) the material is essentially elastic, whereas, for long time periods ($t > \tau_M$), the behavior is predominantly viscous.

We will now examine the short time or elastic limit in the behavior of visco-elastic planets under stress. When subjected to a disturbing potential

$$\Phi(R,\theta,\varphi) = \frac{GM}{R_0} \sum_{n=1}^{\infty} \left(\frac{R_0}{R}\right)^{n+1} \sum_{m=0}^{n} \Phi_{nm}^{T} \Lambda_{nm}(\theta,\varphi) \qquad \text{E.4}$$

an elastic sphere suffers a surface distortion proportional to the disturbing potential

$$U(\theta,\varphi) = R_0 \sum_{n=1}^{\infty} \sum_{m=0}^{n} \Phi_{nm}^{T} U_{nm}(\theta,\varphi) \qquad \text{E.5}$$

where $U_{nm}(\theta,\varphi)$ is a vector spherical harmonic whose components in the direction of the unit vectors $(\hat{e}_R, \hat{e}_\theta, \hat{e}_\varphi)$ are:

$$\begin{aligned} \hat{e}_R \cdot U_{nm}(\theta,\varphi) &= h_n \Lambda_{nm}(\theta,\varphi) \\ \hat{e}_\theta \cdot U_{nm}(\theta,\varphi) &= \ell_n \frac{\partial}{\partial\theta} \Lambda_{nm}(\theta,\varphi) \\ \hat{e}_\varphi \cdot U_{nm}(\theta,\varphi) &= \frac{\ell_n}{\cos(\theta)} \frac{\partial}{\partial\varphi} \Lambda_{nm}(\theta,\varphi) \end{aligned} \qquad \text{E.6}$$

This redistribution of mass gives rise to a further disturbance of the potential whose harmonic coefficients are

$$\Delta\Phi_{nm} = k_n \; \Phi_{nm} \quad . \qquad \text{E.7}$$

These constants of proportionality $L_n = (k_n, h_n, \ell_n)$ are known as Love numbers (Love, 1927, pp. 257-299; Munk and MacDonald, 1960, pp. 29-31), and their functional form depends on the nature of the disturbing potential. For a potential which does not load the surface, such as a rotational or tidal potential, acting on a homogeneous elastic sphere

$$\begin{aligned} k_n &= \frac{3}{2(n-1)} \left(\frac{1}{1 + N(n)\ \mu/P_c} \right) \\ h_n &= \left(\frac{2n+1}{3} \right) k_n \\ \ell_n &= \left(\frac{1}{n} \right) k_n \end{aligned} \qquad \text{E.8}$$

where

$$P_c = \frac{3GM^2}{8\pi R_0^{\,4}} \quad , \qquad \text{E.9}$$

the hydrostatic pressure at the center of the planet, is a measure of the gravitational resistance to deformation, μ is the elastic rigidity, and

$$N(n) = \frac{2(n+1)^2 + 1}{2n} \qquad \text{E.10}$$

is a purely geometrical factor related to the boundary conditions for the sphere. In a fluid planet $\mu = 0$, and the restoring force is purely gravitational. Since $N(n)$ is an increasing function of n, the elastic response is clearly more important for small features.

If the perturbing potential is due to a surface load of material of the same density as the rest of the planet, and the height of the surface load is

$$H(\theta,\varphi) = R_0 \sum_{n=1}^{\infty} \sum_{m=0}^{n} H'^{T}_{nm} \Lambda_{nm}(\theta,\varphi) \qquad \text{E.11}$$

then the potential harmonics are

$$\left(\frac{2n+1}{3}\right) \Phi_{nm} = H'_{nm} \quad . \qquad \text{E.12}$$

In this case, the deformation due to the normal stress applied by the load is opposed by the gravitational attraction of the planet by the load. The corresponding Love numbers are thus

$$L'_n = \left[1 - \frac{2n+1}{3}\right] L_n \qquad \text{E.13}$$

where L_n are the Love numbers for a potential which does not load the surface. Thus, we have explicitly

$$\begin{aligned} k'_n &= \left(\frac{1}{1 + N(n)\ \mu/P_c}\right) \\ h'_n &= \left(\frac{2n+1}{3}\right) k'_n \\ \ell'_n &= \left(\frac{1}{n}\right) k'_n \quad . \end{aligned} \qquad \text{E.14}$$

If a load of initial height H'_{nm} were placed on a sphere, the original surface would deform by $h'_n\ \Phi_{nm}$, and the final height of the load would be

$$H_{nm} = H'_{nm} + h'_n\ \Phi_{nm} \quad . \qquad \text{E.15}$$

However, since

$$H'_{nm} = \left(\frac{2n+1}{3}\right) \Phi_{nm}$$
$$h'_n = \left(\frac{2n+1}{3}\right) k'_n \qquad \text{E.16}$$

this can be rewritten as

$$H_{nm} = (1+k'_n)\, H'_{nm} \quad . \qquad \text{E.17}$$

Clearly, if the body were perfectly fluid, so that $\mu = 0$, then we would have $k'_n = -1$ and thus $H_{nm} = 0$.

The Love numbers have the following asymptotic behavior in the limit of small wavelength features:

$$\lim_{n\to\infty} \begin{bmatrix} nh_n \\ n^2 k_n \\ n^3 \ell_n \end{bmatrix} = \frac{P_c}{\mu} \begin{bmatrix} 1 \\ 3/2 \\ 3/2 \end{bmatrix} \qquad \text{E.18}$$

$$\lim_{n\to\infty} \begin{bmatrix} h'_n \\ nk'_n \\ n^2 \ell'_n \end{bmatrix} = \frac{P_c}{\mu} \begin{bmatrix} 2/3 \\ 1 \\ 1 \end{bmatrix} \qquad \text{E.19}$$

Darwin (1879) solved the problem of purely viscous deformation of a homogeneous sphere by a surface load. If the load has the same density as the sphere, and the initial height of the load is characterized by harmonic coefficients

$$H_{nm}(0) = A_{nm} \qquad \text{E.20}$$

then, at a later time t, the load height harmonics will be attenuated to

$$H_{nm}(t) = A_{nm}\, e^{-t/\tau_n} \qquad \text{E.21}$$

where the relaxation time for degree n is

$$\tau_n = \left[\frac{N(n)}{P_c}\right] \eta \qquad \text{E.22}$$

and η is the dynamic viscosity. Since τ_n is an increasing function of n, the proportional attenuation of laterally extensive features is more rapid than for small features. This is just opposite the behavior of diffusion processes.

The deformation of a Maxwell sphere due to a surface load was also determined by Darwin (1879) and is essentially identical to the behavior of a purely viscous sphere. The only difference is that the relaxation times are uniformly increased to (McKenzie, 1967; Peltier, 1974)

$$\begin{aligned} \tau_n' &= \left[\frac{N(n)}{P_c} + \frac{1}{\mu}\right] \eta \\ &= \tau_n + \tau_M \end{aligned} \qquad \text{E.23}$$

where τ_n is the viscous spherical relaxation time, and τ_M is the Maxwell relaxation time of the material.

F. POTENTIAL ENERGY

The configuration of lowest energy for an isolated mass of homogeneous material is a sphere. Any departure from sphericity thus represents an increase in potential energy, both elastic and gravitational. We will now estimate the energy corresponding to harmonic surface loads and use the constraint of finite total energy to place bounds on possible surface configurations. We will first consider elastic energy.

1. Elastic Energy

The elastic energy density, which is the work done per unit volume in elastically deforming the material, is given by

$$e = \frac{1}{2} \sum_{i=1}^{3} \sum_{j=1}^{3} \sigma_{ij} \, \varepsilon_{ij} \qquad \text{F.1}$$

where σ_{ij} and ε_{ij} are the stress and strain tensors respectively. The constitutive relation between stress and strain for an incompressible material is

$$\sigma_{ij} = \mu \, \varepsilon_{ij} \qquad \text{F.2}$$

and thus the energy density simplifies to

$$e = \frac{\mu}{2} \sum_{i=1}^{3} \sum_{j=1}^{3} \varepsilon_{ij} \, \varepsilon_{ij} \quad . \qquad \text{F.3}$$

In a system with coordinate axes X_i, the strain tensor is obtained from the displacement vector U_i by the formula

$$\varepsilon_{ij} = \frac{1}{2}\left(\frac{\partial U_i}{\partial X_j} + \frac{\partial U_j}{\partial X_i} \right) \quad . \qquad \text{F.4}$$

In spherical coordinates, the strain components are:

$$\begin{aligned}
\epsilon_{RR} &= \frac{\partial U_R}{\partial R} \\
\epsilon_{\theta\theta} &= \frac{1}{R}\left[U_R + \frac{\partial U_\theta}{\partial\theta}\right] \\
\epsilon_{\varphi\varphi} &= \frac{1}{R}\left[U_R + \tan(\theta)\, U_\theta + \frac{1}{\cos(\theta)}\,\frac{\partial U_\varphi}{\partial\varphi}\right] \\
\epsilon_{R\theta} = \epsilon_{\theta R} &= \frac{1}{2R}\left[\frac{\partial U_R}{\partial\theta} + R\,\frac{\partial U_\theta}{\partial R} - U_\theta\right] \\
\epsilon_{R\varphi} = \epsilon_{\varphi R} &= \frac{1}{2R}\left[\frac{1}{\cos(\theta)}\,\frac{\partial U_R}{\partial\varphi} + R\,\frac{\partial U_\varphi}{\partial R} - U_\varphi\right] \\
\epsilon_{\theta\varphi} = \epsilon_{\varphi\theta} &= \frac{1}{2R}\left[\frac{1}{\cos(\theta)}\,\frac{\partial U_\theta}{\partial\varphi} + \frac{\partial U_\varphi}{\partial\theta} - \tan(\theta)\, U_\varphi\right] .
\end{aligned} \qquad \text{F.5}$$

Substituting the displacement due to a single harmonic disturbing potential

$$\Phi(R,\theta,\varphi) = \frac{GM}{R_0}\left(\frac{R}{R_0}\right)^n \Phi^T_{nm}\, \Lambda_{nm}(\theta,\varphi) \quad , \quad R \le R_0 \qquad \text{F.6}$$

into the above equations we obtain

$$\epsilon_{ij}(R,\theta,\varphi) = \left(\frac{R}{R_0}\right)^n \Phi^T_{nm}\, \epsilon'_{ij}(\theta,\varphi) \qquad \text{F.7}$$

where

$$\begin{aligned}
\epsilon'_{RR} &= n\, h_n\, \Lambda_{nm} \\
\epsilon'_{\theta\theta} &= h_n\, \Lambda_{nm} + \ell_n\, \frac{\partial^2 \Lambda_{nm}}{\partial\theta^2} \\
\epsilon'_{\varphi\varphi} &= \left[h_n - \frac{m^2 \ell_n}{\cos^2(\theta)}\right]\Lambda_{nm} + \ell_n\, \tan(\theta)\, \frac{\partial\Lambda_{nm}}{\partial\theta}
\end{aligned}$$

$$2\epsilon'_{R\theta} = \left[h_n + (n-1)\,\ell_n\right] \frac{\partial \Lambda_{nm}}{\partial \theta}$$

$$2\epsilon'_{R\varphi} = \left[h_n + (n-1)\,\ell_n\right] \frac{1}{\cos(\theta)} \frac{\partial \Lambda_{nm}}{\partial \varphi}$$

$$2\epsilon'_{\theta\varphi} = \frac{\ell_n}{\cos(\theta)} \frac{\partial}{\partial \varphi} \left[2 \frac{\partial \Lambda_{nm}}{\partial \theta} - \tan(\theta)\ \Lambda_{nm}\right]$$

where the form of the Love numbers depends on the nature of the disturbing potential, i.e., whether it loads the surface or not.

As our principal interest is in the asymptotic behavior of the energy density for large n, we can neglect the terms in ℓ_n, since

$$\ell_n = \left(\frac{3}{2n+1}\right) \frac{h_n}{n} \tag{F.8}$$

Using the approximation $\ell_n = 0$ and the facts

$$\frac{1}{4\pi}\int_s (\Lambda_{nm})^2\ dS = 1 \tag{F.9}$$

$$\frac{1}{4\pi}\int_s \left(\frac{\partial \Lambda_{nm}}{\partial \theta}\right)^2 dS = (n)(n+1) - \frac{(2n+1)(m)}{2} \tag{F.10}$$

$$\frac{1}{4\pi}\int_s \frac{1}{\cos^2(\theta)} \left(\frac{\partial \Lambda_{nm}}{\partial \varphi}\right)^2 dS = \frac{(2n+1)(m)}{2} \tag{F.11}$$

(Lowes, 1966), we find that

$$\frac{1}{4\pi}\int_s \sum_{i=1}^{3} \sum_{j=1}^{3} \epsilon'_{ij}\ \epsilon'_{ij}\ dS = \left[n^2 + 2 + \frac{(n)(n+1)}{2}\right] h_n^2 \tag{F.12}$$

$$= \left(\frac{3n^2+n+4}{2}\right) h_n^2$$

Therefore, the total elastic energy corresponding to the harmonic disturbance Φ_{nm} is $E_{nm} = 4\pi R_0^{\ 3}\ e_{nm}/3$, or

$$E_{nm} = \frac{\mu}{2}\left(\frac{3n^2+n+4}{2}\right)h_n^2\,\Phi_{nm}^2\left(\frac{4\pi R_0^3}{3}\right)\int_0^1 \xi^{2n+2}\,d\xi \qquad \text{F.13}$$

$$= \frac{\pi\mu R_0^3}{3}\left(\frac{3n^2+n+4}{2n+3}\right)h_n^2\,\Phi_{nm}^2$$

where $\xi = R/R_0$.

If we consider the surface topography of a planet

$$H(\theta,\varphi) = R_0\sum_{n=1}^{\infty}\sum_{m=0}^{n} H_{nm}^T\,\Lambda_{nm}(\theta,\varphi) \qquad \text{F.14}$$

to be the result of the emplacement of a surface load $H'(\theta,\varphi)$ and the subsequent deformation of the original surface, we can calculate the total elastic energy stored during the deformation. In this case,

$$\left(\frac{2n+1}{3}\right)\Phi_{nm} = H'_{nm} = \frac{H_{nm}}{1+k'_n} \qquad \text{F.15}$$

so that a sum over all $2n+1$ terms of degree n in the harmonic expansion of the surface load yields

$$E_n = 3\pi\mu R_0^3\,\frac{3n^2+n+4}{(2n+3)(2n+1)^2}\left(\frac{h_n'}{1+k_n'}\right)^2 V(H;n) \qquad \text{F.16}$$

where

$$V(H;n) = \sum_{m=0}^{n} H_{nm}^T\,H_{nm}$$

is the topographic degree variance. The total elastic energy due to the topography is thus simply

$$E_{e1} = \sum_{n=1}^{\infty} E_n = \frac{4\pi R_0^3}{3} \sum_{n=1}^{\infty} e_n \qquad \text{F.17}$$

However, since

$$\lim_{n \to \infty} \left(\frac{h_n'}{1 + k_n'} \right) = \frac{2P_0}{3\mu} \qquad \text{F.18}$$

Therefore,

$$\lim_{n \to \infty} (2n+1)\ e_n = \frac{3P_0^{\ 2}}{4\mu}\ V(H;n) \qquad \text{F.19}$$

i.e., the elastic energy density per harmonic degree converges to zero more rapidly than the topographic degree variances. It would thus be possible to have infinite topographic variance and finite elastic energy.

2. Gravitational Energy

We now direct our attention to the gravitational energy associated with the surface topography of a planet. The gravitational energy density is just the work done per unit volume against the gravitational field in assembling the configuration from some reference state. It is calculated from

$$e = \frac{1}{2}\ \rho\ \Phi\ . \qquad \text{F.20}$$

where, as before, ρ is the mass density and Φ is the gravitational potential. We have already seen that the potential of a homogeneous spheroid with mean radius R_0 and mass M has the form

$$\Phi_i(R,\theta,\varphi) = \frac{GM}{R_0}\left[\left(\frac{3 - (R/R_0)^2}{2}\right) + \sum_{n=1}^{\infty}\left(\frac{R_0}{R}\right)^{n+1} \sum_{m=0}^{n} \Phi_{nm}^{\ T}\ \Lambda_{nm}(\theta,\varphi)\right] \qquad \text{F.21}$$

for interior points ($R \le R_0$), and

$$\Phi_e(R,\theta,\varphi) = \frac{GM}{R_0}\left[\frac{R_0}{R} + \sum_{n=1}^{\infty}\left(\frac{R_0}{R}\right)^{n+1}\sum_{m=0}^{n}\Phi_{nm}^T\,\Lambda_{nm}(\theta,\varphi)\right] \qquad \text{F.22}$$

for exterior points $R \geq R_0$, where

$$\left(\frac{2n+1}{3}\right)\Phi_{nm} = H_{nm}$$

and H_{nm} are the harmonic coefficients fo the topographic heights. If we denote the potential of a homogeneous sphere by $\Phi_0(R)$, then the gravitational energy of such a spherical configuration is

$$E_0 = \frac{1}{2}\int_0^{2\pi}\int_{-1}^{1}\int_0^{\infty}\rho(R)\,\Phi_0(R)\,R^2 dR\,d\mu\,d\varphi \qquad \text{F.23}$$

However, since $\rho(R) = 0$ for $R > 0$, this can be written

$$E_0 = \frac{GM}{2R_0}\int_0^{2\pi}\int_{-1}^{1}\int_0^{R_0}\left[\frac{3-(R/R_0)^2}{2}\right]R^2\,dR\,d\mu\,d\varphi$$

$$= \frac{GM}{2R_0}\left[\frac{3}{2}\left(\frac{4\pi R_0^3}{3}\right) - \frac{1}{2R_0^2}\left(\frac{4\pi R_0^5}{5}\right)\right] \qquad \text{F.24}$$

$$= \frac{3GM^2}{5R_0} \quad .$$

The effect of surface topography $H(\mu,\varphi)$, is found from the integral

$$E = \frac{1}{2}\int_0^{2\pi}\int_{-1}^{1}\int_0^{\infty}\rho(R)\,\Phi(R,\mu,\varphi)\,R^2\,dR\,d\mu\,d\varphi \qquad \text{F.25}$$

where now $\Phi(R,\mu,\varphi)$ includes the topographic perturbations. We will evaluate this interval over three disjoint regions: 1) the interior of the sphere, $R < R_0$, 2) an infinitesimal shell at the surface $R = R_0$, where we let $dR = H(\mu,\varphi)$, and 3) the exterior of the sphere $R > R_0$, where $\rho(R) = 0$. The desired integral will be the sum of these three parts.

The first integral is

$$E' = \frac{1}{2}\rho \int_0^{2\pi} \int_{-1}^{1} \int_0^{R_0} \Phi_i(R)\ R^2\ dR\ d\mu\ d\varphi$$

$$= E_0 + \frac{GM_\rho}{2R_0} \sum_{n=1}^{\infty} \left(\frac{R_0^{\ 3}}{n+3}\right) \sum_{m=0}^{n} \Phi_{nm}^{\ T} \int_0^{2\pi} \int_{-1}^{1} \Lambda_{nm}(\mu,\varphi) d\mu\ d\varphi\ , \qquad \text{F.26}$$

but this last term is zero due to the orthogonality of Λ_{nm}. Thus,

$$E' = E_0\ . \qquad \text{F.27}$$

The second part, or integral over the surface shell is

$$E'' = \frac{1}{2}\rho \int_0^{2\pi} \int_{-1}^{1} \Phi(R_0,\mu,\varphi)\ H(\mu,\varphi)\ R_0^{\ 2}\ d\mu\ d\varphi$$

$$= \frac{GM\rho}{2R_0} \left[4\pi\ R_0^{\ 3} \sum_{n=1}^{\infty} \sum_{m=0}^{n} \Phi_{nm}^{\ T}\ H_{nm}\right] \qquad \text{F.28}$$

$$= E_0\ \frac{15}{2} \sum_{n=1}^{\infty} \sum_{m=0}^{n} \frac{H_{nm}^T H_{nm}}{2n + 1}\ ,$$

where we have used the relationship between Φ_{nm} and H_{nm} to simplify the last expression. The third integral is trivially $E''' = 0$, since $\rho(R) = 0$ for $R > R_0$.

Thus, the effect of surface topography on a homogeneous planet is to increase the gravitational energy above the spherical value of $E_0 = 3GM^2/5R_0$ to

$$E = E_o \left[1 + \frac{15}{2} \sum_{n=1}^{\infty} \sum_{m=0}^{n} \frac{H_{nm}^T H_{nm}}{2n+1} \right] \qquad \text{F.29}$$

where

$$E_n = \frac{15}{2} \sum_{m=0}^{n} \frac{H_{nm}^T H_{nm}}{2n+1}$$

is the contribution of harmonic degree n to the total. The gravitational energy is similar to the elastic energy in that their increments per degree both decrease with increasing degree more rapidly than the corresponding increments in topographic variance, and, in fact, the asymptotic convergence rates of the two energies are identical.

G. SLOPES

Given a representation of the topographic heights on a planet $H(\theta,\varphi)$, we now desire a characterization of the slopes on the surface. We will first develop expressions for the mean square slope of given slope length, and criteria for the establishment of isotropy of the topography, and then we will consider the problem of mechanical stability of the slopes. In much of this analysis, we will consider the topography to be a realization of a homogeneous stochastic process.

The slope of the secant line between any two points a distance $L = R_0\gamma$ apart is

$$\frac{\Delta H}{L} = \frac{|H(\Gamma+\gamma) - H(\Gamma)|}{R_0\gamma} \quad , \tag{G.1}$$

and the mean square slope with slope length L is

$$\begin{aligned} S^2(L) &\equiv E\left(\left[\frac{H(\Gamma+\gamma) - H(\Gamma)}{R_0\gamma}\right]^2\right) \\ &= \frac{E[H^2(\Gamma+\gamma)] - 2E[H(\Gamma+\gamma)H(\Gamma)] + E[H^2(\Gamma)]}{(R_0\gamma)^2} \quad . \end{aligned} \tag{G.2}$$

However, by the assumed stationarity of the topography

$$E[H^2(\Gamma+\gamma)] = E[H^2(\Gamma)] \tag{G.3}$$

and, we already have

$$E[H^2(\Gamma)] = C(H;0) \tag{G.4}$$

and

$$E[H(\Gamma+\gamma)\ H(\Gamma)] = C(H;\gamma) \tag{G.5}$$

Therefore, the mean square slope of length L is

$$S^2(L) = \frac{2[C(H;0) - C(H;\gamma)]}{L^2}$$

$$= 2 \sum_{n=1}^{\infty} V(H;n) \left[\frac{1 - P_n(\cos(\gamma))}{\gamma^2} \right] \qquad \text{G.6}$$

As the slope length goes to zero and the secants defining the slope approach tangency (if the surface is, in fact, differentiable), we obtain

$$S^2(0) = \sum_{n=1}^{\infty} V(H;n) \ (n)(n+1) \qquad \text{G.7}$$

since

$$\lim_{\gamma \to 0} \left[\frac{1 - P_n(\cos(\gamma))}{\gamma^2} \right] = \frac{(n)(n+1)}{2} \quad .$$

In the important case where

$$V(H;n) = \frac{V(H;0)}{(n)(n+1)} \qquad \text{G.8}$$

we obtain the closed form expression

$$S^2(L) = 2 \ V(H;0) \sum_{n=1}^{\infty} \left[\frac{1 - P_n(\cos(\gamma)}{(n)(n+1)} \right]$$

$$4 \ V(H;0) \ \frac{\ln[1 + \sin(\gamma/2)]}{\gamma^2} \qquad \text{G.9}$$

(see Appendix D for more details). When the slope length is small, we have approximately

$$S^2(L) \doteq 2\,\frac{V(H;0)}{\gamma} \qquad \text{G.10}$$

since

$$\sin(x) = x - \frac{x^3}{3!} + \frac{x^5}{5!} - \ldots$$

$$\ell n(1+x) = x - \frac{x^2}{2!} + \frac{x^3}{3!} - \ldots$$

so that

$$\ell n[1 + \sin(x/2)] = \frac{x}{2} - \frac{x^2}{8} + \frac{x^3}{48} - \ldots$$

1. Isotropy of Slopes

Though we have assumed isotropy of covariance (and therefore of slopes) in modeling the topography as a realization of a homogeneous stochastic process, it is possible to check the validity of this assumption. We first recall that the differential arc length is given by

$$dL^2 = R_0^2\,[d\theta^2 + \cos^2(\theta)\,d\varphi^2] = R_0^2\,d\gamma^2 \quad . \qquad \text{G.11}$$

We then calculate the mean square infinitesimal slopes facing east-west

$$S_\theta^2(0) = \frac{1}{4\pi}\int_A \left(\frac{\partial H}{\partial L}\right)_\theta^2 dA \qquad \text{G.12}$$

and similarly for north-south facing slopes

$$S_\varphi^2(0) = \frac{1}{4\pi}\int_A \left(\frac{\partial H}{\partial L}\right)_\varphi^2 dA \qquad \text{G.13}$$

where the subscript indicates which coordinate is held fixed and the integration is over the entire surface of the sphere. We note that

$$\left(\frac{\partial H}{\partial L}\right)_\theta = \left(\frac{\partial H}{\partial \varphi}\right)\left(\frac{\partial \varphi}{\partial L}\right) = \sum_{n=1}^{\infty}\sum_{m=0}^{n} \frac{H^T_{nm}}{\cos(\theta)} \frac{\partial\, \Lambda_{nm}(\theta,\varphi)}{\partial \varphi} \qquad \text{G.14}$$

and

$$\left(\frac{\partial H}{\partial L}\right)_\varphi = \left(\frac{\partial H}{\partial \theta}\right)\left(\frac{\partial \theta}{\partial L}\right) = \sum_{n=1}^{\infty}\sum_{m=0}^{n} H^T_{nm} \frac{\partial\, \Lambda_{nm}(\theta,\varphi)}{\partial \theta} \qquad \text{G.15}$$

The required integrals are (Lowes, 1966)

$$\frac{1}{4\pi}\int_A \frac{1}{\cos^2(\theta)} \left(\frac{\partial \Lambda_{nm}}{\partial \varphi}\right)^2 dA = \frac{(2n+1)(m)}{2} \qquad \text{G.16}$$

and

$$\frac{1}{4\pi}\int_A \left(\frac{\partial \Lambda_{nm}}{\partial \theta}\right)^2 dA = (n)(n+1) - \frac{(2n+1)(m)}{2} \quad . \qquad \text{G.17}$$

Therefore, the mean square east-west slope is

$$s^2_\theta(0) = \sum_{n=1}^{\infty} T_\theta(n) \qquad \text{G.18}$$

and the mean square north-south slope is

$$s^2_\varphi(0) = \sum_{n=1}^{\infty} T_\varphi(n) \qquad \text{G.19}$$

where the degree tilts are

$$T_\theta(n) = \sum_{m=0}^{n} \left[\frac{(2n+1)(m)}{2}\right] H^T_{nm} H_{nm}$$

$$T_\varphi(n) = \sum_{m=0}^{n} \left[(n)(n+1) - \frac{(2n+1)(m)}{2}\right] H^T_{nm} H_{nm} \quad . \qquad \text{G.20}$$

The total mean square slope at zero slope length is simply

$$\begin{aligned} S^2(0) &= \sum_{n=1}^{\infty} T_\theta(n) + T_\varphi(n) \\ &= \sum_{n=1}^{\infty} (n)(n+1)\ V(H;n) \end{aligned} \qquad G.21$$

as previously established.

Our desired criterion for mean square isotropy of a function $H(\theta,\varphi)$ on a sphere is thus

$$T_\theta(n) = T_\varphi(n) \qquad G.22$$

or equivalently

$$(2n+1) \sum_{m=0}^{n} (m)\left[H^T_{nm}\ H_{nm}\right] = (n)(n+1) \sum_{m=0}^{n} H^T_{nm}\ H_{nm}$$

for all n. Here H_{nm} are the normalized Fourier-Legendre transforms of $H(\theta,\varphi)$.

2. Slope Stability

Physical slopes are limited in height by the strength of their constituent materials. The stability of a slope in soil is dependent upon characteristics of the soil [density (ρ), cohesion (c) and internal friction angle (φ)], characteristics of the slope [height (H), length (L) and inclination (i)] and a characteristic of the planetary surface on which the slope resides, [the local gravity (g)]. If a slope of constant inclination is extended in height, the shear stress (τ) will eventually exceed the shear resistance of the material and the slope will fail. A common failure criterion is the Mohr-Coulomb relation

$$\tau = c + \sigma \tan(\varphi) \qquad \text{G.23}$$

which expresses a linear increase in shear stress at failure with increasing normal stress (σ). The general determination of slope stability is a difficult variational problem (Revilla and Castillo, 1977), but in the case of shallow slopes the failure surface is essentially planar and the analysis of Culmann (1866) is adequate (see e.g., Terzaghi, 1943). According to this analysis the maximum height attainable in a slope of length L is

$$H(L) = \frac{4c}{\rho g}\left[\frac{\sin(i)\ \cos(\varphi)}{1 - \cos(i - \varphi)}\right] \quad . \qquad \text{G.24}$$

In many situations the effects of internal friction are negligible, so we shall assume $\varphi = 0$, and

$$H(L) = \frac{4c}{\rho g}\left[\frac{\sin(i)}{1 - \cos(i)}\right] \quad . \qquad \text{G.25}$$

In a rectilinear slope segment, we also obviously have

$$H(L) = L \tan(i) \qquad \text{G.26}$$

so that

$$\cos(i) = \left[1 + \frac{4c}{\rho g L}\right]^{-1} \quad . \qquad \text{G.27}$$

Thus, the squared height is

$$H^2(L) = \frac{8cL}{\rho g}\left(1 + \frac{L_o}{L}\right) \qquad \text{G.28}$$

where

$$L_o = \frac{2c}{\rho g}$$

However, on the Moon, for example

$$\left.\begin{aligned} c &\doteq 0.1 \text{ bar} \\ \rho &\doteq 3.0 \text{ gm cm}^{-3} \\ g &\doteq 160 \text{ gal} \end{aligned}\right\} \Rightarrow L_o = 4\text{m} \qquad \text{G.29}$$

Thus, to a good approximation

$$H^2(L) = \frac{8cL}{\rho g} \qquad L \gg L_o \quad , \qquad \text{G.30}$$

i.e., the squared height of a stability limited slope is proportional to the length of the slope.

It is interesting to note an analogous behavior exhibited by the Wiener process. If we consider the slope profile to be a realization of a Wiener process on the positive reals with parameter $\sigma^2 = 3c/\rho g$ and $W(0) = 0$ then

$$E[W^2(L)] = \sigma^2 L = \frac{8cL}{\rho g} \quad , \qquad \text{G.31}$$

i.e., the variance of the process is proportional to the length of the slope.

The spherical Wiener process also exhibits this type of behavior for sufficiently short slopes ($\gamma \ll 2\pi$). Since the covariance has the form

$$\begin{aligned} C(H;\gamma) &= C(H;0) \sum_{n=1}^{\infty} \frac{P_n[\cos(\gamma)]}{(n)(n+1)} \\ &= C(H;0) \left[1 - 2\ln[1 + \sin(\gamma/2)]\right] \quad , \end{aligned} \qquad \text{G.32}$$

the mean square range over a distance $L = R_0\gamma$ is

$$E\left(\left[H(\Gamma+\gamma) - H(\Gamma)\right]^2\right) = 2\left[C(H;0) - C(H;\gamma)\right] \qquad G.33$$

$$= 4C(H;0)\ \ell n\ [1+\sin(\gamma/2) \quad .$$

For short distances, this reduces to

$$E\left(\left[H(\Gamma+\gamma) - H(\Gamma)\right]^2\right) = 2C(H;0)\ \gamma \quad , \quad \gamma \ll 2\pi \quad , \qquad G.34$$

i.e., the mean square slope height is proportional to slope length. If we let $C(H;0) = 4c\ R_0/\rho g$, we recover the slope stability result exactly.

REFERENCES

Beers, B.L. (1972). Harmonic analysis of analytic functions on hyperspheres. *J. Math. Phys.* **13**, 950-955.

Beers, B.L. and Dragt, A.J. (1970). New theorems about spherical harmonic expansions. *J. Math. Phys.* **11**, 2313-2328.

Culmann, K. (1866). Die graphische static. In *Theorie der Stütz und Futtermauern*, Meyer and Zeller, Zürich, 564 pp.

Darwin, G.H. (1879). On the bodily tides of viscous and semi-elastic spheroids. *Phil. Trans. Roy. Soc.* **170**, 1-35

Doob, J.L. (1942). The Brownian movements and stochastic equations. *Ann. Math.* **43**, 351-369.

Erdelyi, A. (1953). *Higher Transcendental Functions, vol. I.*, McGraw-Hill, New York.

Gallager, R.G. (1968). *Information Theory and Reliable Communication.* Wiley, New York, 588 pp.

Heiskanen, W.A. and Moritz, H. (1967). *Physical Geodesy*. W.H. Freeman, San Francisco, 364 pp.

Jones, R.H. (1963). Stochastic processes on a sphere. *Ann. Math. Statist.* **34**, 213-218.

Kaula, W.M. (1967). Theory of statistical analysis of data distributed over a sphere. *Rev. Geophys.* **5**, 83-107.

Levy, P. (1948). *Processus Stochastiques et Mouvement Brownien.* Gauthier-Villars, Paris, 365 pp.

Love, A.E.H. (1927). *A Treatise on the Mathematical Theory of Elasticity*. Dover, New York, 643 pp.

Lowes, F.J. (1966). Mean-square values of spherical harmonic vector fields. *J. Geophys. Res*. **71**, 2179.

MacRobert, T.M. (1967). *Spherical Harmonics*. Pergamon Press, New York, 345 pp.

Mandelbrot, B.B. (1975). Stochastic models for the Earth's relief, the shape and fractal dimension of coastlines, and the number-area rule for islands. *Proc. Nat. Acad. Sci*. **72**, 3825 - 3828.

Mandelbrot, B.B. and Van Ness, J.W. (1968). Fractional Brownian motions, fractional noises and applications. *SIAM Review* **10**, 422-437.

Maxwell, J.C. (1868). On the dynamical theory of gases. *Phil. Mag*. **35**, 129-145.

McFadden, J.A. (1965). The entropy of a point process. *J. Soc. Indust. Appl. Math*. **13**, 988-994.

McKenzie, D.P. (1967). The viscosity of the mantle. *Geophys. J. Roy. Astr. Soc*. **14**, 297-305.

Middleton, D. (1960). *An Introduction to Statistical Communication Theory*. McGraw-Hill, New York, 1140 pp.

Munk, W.H. and MacDonald G.J.F. (1960). *The Rotation of the Earth*. Cambridge Univ. Press, London, 323 pp.

Parzen, E. (1962). *Stochastic Processes*. Holden-Day, San Francisco 324 pp.

Peltier, W.R. (1974). The impulse response of a Maxwell Earth. *Rev. Geophys. Space Phys*. **12**, 649-669.

Revilla, J. and Castillo E. (1977). The calculus of variations applied to stability of slopes. *Geotechnique* **27**, 1-11.

Rice, S.O. (1944). Mathematical analysis of random noise. *Bell System Tech. Jour*. **23**, 282-332.

Roberts, P.H. and Ursell, H.D. (1960). Random walk on a sphere and on a Riemannian manifold. *Phil. Trans. Roy. Soc. London* A **252**, 317-356.

Roy, R. (1973). Estimation of the covariance function of a homogeneous process on the sphere. *The Annals of Statistics* **1**, 780-785.

Roy R. (1976). Spectral analysis for a random process on the sphere. *Ann. Inst. Stat. Math*. **28**, 91-97.

Terzaghi, K. (1943). *Theoretical Soil Mechanics*. John Wiley, New York, 510 pp.

Thomasian, A.J. (1969). *The Structure of Probability Theory with Applications*. McGraw-Hill, New York, 746 pp.

Uhlenbeck, G.E. and Ornstein, L.S. (1930). On the theory of the Brownian motion. *Phys. Rev*. **36**, 823-841.

Wheelon, A.D. (1968). *A Short Table of Summable Series*. Holden-Day, San Francisco, 86 pp.